

AD-A218 244

DTIC FILE COPY

REPORT DOCUMENTATION PAGE

Form Approved
OMB 0704-0188

1a. REPORT SECURITY CLASSIFICATION UNCLASSIFIED		1b. RESTRICTIVE MARKINGS NONE	
2a. SECURITY CLASSIFICATION AUTHORITY		3. DISTRIBUTION/AVAILABILITY OF REPORT APPROVED FOR PUBLIC RELEASE DISTRIBUTION UNLIMITED.	
2b. DECLASSIFICATION/DOWNGRADING SCHEDULE		4. PERFORMING ORGANIZATION REPORT NUMBER(S)	
6a. NAME OF PERFORMING ORGANIZATION AFIT STUDENT AT TX A&MUNIV		6b. OFFICE SYMBOL (If applicable)	5. MONITORING ORGANIZATION REPORT NUMBER(S) AFIT/CI/CIA- 89-148
6c. ADDRESS (City, State, and ZIP Code)		7. NAME OF MONITORING ORGANIZATION AFIT/CI	
8a. NAME OF FUNDING/SPONSORING ORGANIZATION		8b. OFFICE SYMBOL (If applicable)	9. ADDRESS (City, State, and ZIP Code) Wright-Patterson AFB OH 45433-6583
8c. ADDRESS (City, State, and ZIP Code)		10. SOURCE OF FUNDING NUMBERS	
		PROGRAM ELEMENT NO.	PROJECT NO.
		TASK NO.	WORK UNIT ACCESSION NO.
11. TITLE (Include Security Classification) (UNCLASSIFIED) A VIDEO-BASED EXPERIMENTAL INVESTIGATION OF WING ROCK			
12. PERSONAL AUTHOR(S) STEVEN LYNN MORRIS			
13a. TYPE OF REPORT THESIS/DISSERTATION	13b. TIME COVERED FROM TO	14. DATE OF REPORT (Year, Month, Day) 1989	15. PAGE COUNT 237
16. SUPPLEMENTARY NOTATION APPROVED FOR PUBLIC RELEASE IAW AFR 190-1 ERNEST A. HAYGOOD, 1st Lt, USAF Executive Officer, Civilian Institution Programs			
17. CLOSING CODES		18. SUBJECT TERMS (Continuation on reverse if necessary and identify by block number)	
FIELD	GROUP	SUB-GROUP	
19. ABSTRACT (Continue on reverse if necessary and identify by block number)			

DTIC
ELECTE
S FEB 15 1990 D
B 9

**BEST
AVAILABLE COPY**

90 02 14 069

20. DISTRIBUTION/AVAILABILITY OF ABSTRACT <input checked="" type="checkbox"/> UNCLASSIFIED/UNLIMITED <input type="checkbox"/> SAME AS RPT. <input type="checkbox"/> DTIC USERS		21. ABSTRACT SECURITY CLASSIFICATION UNCLASSIFIED	
22a. NAME OF RESPONSIBLE INDIVIDUAL ERNEST A. HAYGOOD 1st Lt, USAF		22b. TELEPHONE (Include Area Code) (513) 255-2259	22c. OFFICE SYMBOL AFIT/CI

81-168

A VIDEO-BASED EXPERIMENTAL INVESTIGATION OF WING ROCK

A Dissertation

by

STEVEN LYNN MORRIS

Submitted to the Office of Graduate Studies of
Texas A&M University
in partial fulfillment of the requirements
for the degree of

DOCTOR OF PHILOSOPHY

August 1989

Major Subject: Aerospace Engineering

90 02 14 069

A VIDEO-BASED EXPERIMENTAL INVESTIGATION OF WING ROCK

A Dissertation

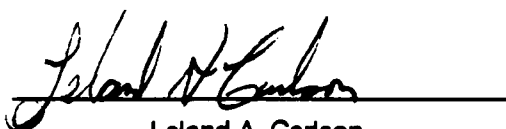
by

STEVEN LYNN MORRIS

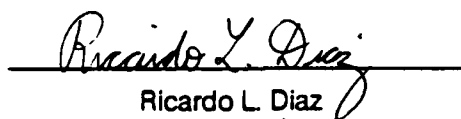
Approved as to style and content by:



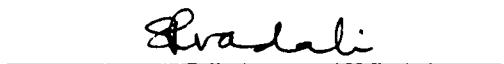
Donald T. Ward
(Chair of Committee)



Leland A. Carlson
(Member)



Ricardo L. Diaz
(Member)



Srinivas R. Vadali
(Member)



Walter E. Haisler
(Department Head)

August 1989

ABSTRACT

A Video-Based Experimental Investigation of Wing Rock

(August 1989)

Steven Lynn Morris, B.S. United States Air Force Academy

M.S., Air Force Institute of Technology

Chair of Advisory Committee: Dr. Donald T. Ward

The primary objective of this research was to develop a definitive theory on the cause of wing rock. The study was based on dynamic measurements in both a water tunnel and a wind tunnel on a sharp-edged delta wing with an 80° leading-edge sweep angle. Experimental data were compared with analytical results from a mathematical model and a fourth order Runge-Kutta integration. In the water tunnel tests, conducted at $\alpha = 35^\circ$ and Reynolds numbers from $3 \times 10^4/\text{ft}$ to $7.5 \times 10^4/\text{ft}$, the movement of the leading-edge vortices and the model motion were simultaneously tracked and analyzed using a video-based motion analysis system, ExpertVision. Quantified vortex movement data were not obtained in the wind tunnel study; however, an extensive investigation of wing rock dynamics was performed at angles of attack from 24° to 50° and Reynolds numbers from $1.09 \times 10^5/\text{ft}$ to $3.44 \times 10^5/\text{ft}$.

The initial phase of the study validated ExpertVision accuracy using stationary and forced oscillation tests on 70° and 80° delta wings. Vortex trajectory, core velocity, and burst point results from stationary tests were in good agreement with published data. Forced oscillation tests proved that ExpertVision could simultaneously track and analyze the movement of leading-edge vortices and model motion.

Wing rock is caused by the dynamic behavior of the leading-edge vortices. Specifically, the alternate lift-off and reattachment of the vortices generate an asymmetry in vortex lift and cause changes in rolling moment that initiate and sustain roll oscillations. Since wind tunnel and

water tunnel tests showed opposite direction hysteresis loops, it was concluded that roll damping could not be the primary aerodynamic mechanism that sets the limit on roll amplitude.

Wing rock dynamics were significantly different between water tunnel and wind tunnel experiments. Apparent mass terms must be included in the equations of motion when converting water tunnel acceleration data to rolling moment coefficients; with no apparent mass correction, C_l calculated from accelerations in the water tunnel were about 15 times greater than those from the wind tunnel.

Accession For	
NTIS CRAS	<input checked="" type="checkbox"/>
DTIC TAB	<input type="checkbox"/>
Unannounced	<input type="checkbox"/>
Justification	
By	
Distribution /	
Availability Codes	
Dist	Avail and/or Special
A-1	

DEDICATION

This is dedicated to the loving memory of my grandparents, Alton and Opal McCarley, to my parents, Bill and Alta Morris for their love and encouragement, and to my wife, Jacqueline, and sons, Steven and Michael, who endured with patience and love many months of neglect.

ACKNOWLEDGEMENTS

The success of the research described in this report depended heavily on many people other than the author, who gratefully acknowledges their assistance. First, I would like to express my most sincere appreciation to my graduate advisor, Dr. Donald Ward. His continuous guidance, support, and encouragement made the successful completion of this study possible. I would also like to thank Dr. Leland Carlson, Dr. Srinivas Vadali, and Dr. Ricardo Diaz for their suggestions and assistance during the course of this research. I want to thank Jorge Martinez and the personnel at the Texas A&M Low Speed Wind Tunnel for conducting the many wind tunnel tests performed during this investigation. Mike Birdsell deserves special recognition for his fabrication of the free-to-roll hardware used in the wind tunnel study. I also want to express my sincere appreciation to Jerry Malcolm, Liane Lewis, Bert Ayers, and Dan Goldfarb and the personnel at Eidetics International for their efforts in fabricating the test models and performing the water tunnel experiments. I also want to thank Paul Vied, Bryan Wallace, and Lan Pham for their assistance in the tedious task of reducing data during the early stages of this investigation. Dr. Katherine Diaz' in-depth review of the mathematical model is also greatly appreciated. The author is especially grateful to Dr. Walter Haisler, Head of the Department of Aerospace Engineering, for making the wind tunnel available for this study.

The project was funded in part by the Air Force Office of Scientific Research, Bolling Air Force Base, District of Columbia, under contract No. F49620-87-C-0069 with Captain Hank Helin serving as the contract monitor.

Finally, but by no means least important, I want to thank my wife, Jacqueline, and sons Steven and Michael, for this love, patience, and understanding during the three years they were neglected during my graduate studies.

NOMENCLATURE

Symbols

a	amplitude of roll oscillations, deg or rad
A	amplitude of limit cycle roll oscillation, deg or rad
b	wing span, ft
c	wing root chord, ft
C_L	lift coefficient
C_{ℓ}	rolling moment coefficient
C_{ℓ_0}	rolling moment coefficient at zero sideslip
\bar{C}_{ℓ_p}	$C_{\ell_p} + C_{\ell_{\dot{\beta}}} \sin \alpha_s$
C_{ℓ_p}	roll damping coefficient based on body-fixed axes
$C_{\ell_{p0}}$	roll damping coefficient at zero sideslip
$C_{\ell_{pp}}$	dimensionless variation of roll damping derivative with roll rate, $\partial C_{\ell_p} / \partial \bar{p}$
$C_{\ell_{p\beta}}$	dimensionless variation of roll damping derivative with sideslip, $\partial C_{\ell_p} / \partial \beta$
$C_{\ell_{\beta}}$	variation of rolling moment coefficient with sideslip
$C_{\ell_{\dot{\beta}}}$	variation of rolling moment coefficient with rate of change of sideslip
$C_{\ell_{\delta_A}}$	variation of rolling moment coefficient with aileron angle
C_m	pitching moment coefficient
d	roll angle conversion factor
E	energy in roll oscillation, ft-lb
f	oscillation frequency, Hz
\bar{H}	angular momentum vector, ft-lb

NOMENCLATURE

\bar{H}_B	angular momentum vector in body axes, ft-lb
I_a	apparent moment of inertia, slug-ft ²
I_{xx}	moment of inertia about body x-axis, slug-ft ²
I_{xy}	product of inertia with respect to body x- and y- axes, slug-ft ²
I_{xz}	product of inertia with respect to body x- and z- axes, slug-ft ²
I_{yy}	moment of inertia about body y-axis, slug-ft ²
I_{yz}	product of inertia with respect to body y- and z- axes, slug-ft ²
I_{zz}	moment of inertia about body z-axis, slug-ft ²
k	dimensionless reduced frequency, $\Omega b/2V_\infty$
L	rolling moment, ft-lb
L_0	$\bar{q} S b C_{\ell_0} / I_{xx}$, sec ⁻²
L_{p0}	$\bar{q} S b^2 C_{\ell_{p0}} / 2 I_{xx} V$, sec ⁻²
L_{pp}	$\bar{q} S b^3 C_{\ell_{pp}} / 4 I_{xx} V^2$, dimensionless
$L_{p\beta}$	$\bar{q} S b^2 C_{\ell_{p\beta}} / 2 I_{xx} V$, sec ⁻¹
L_{δ_A}	$\bar{q} S b C_{\ell_{\delta_A}} / I_{xx}$, sec ⁻²
M	pitching moment, ft-lb
m_a	apparent mass, slug
\bar{M}_B	moment vector in body axes, ft-lb
N	yawing moment, ft-lb
P	period of limit cycle roll oscillations, sec
p	roll rate about x-axis, rad/sec or deg/sec
\bar{p}	dimensionless reduced roll rate, pb/2V
q	pitch rate about y-axis, deg/sec or rad/sec

NOMENCLATURE

\bar{q}	dynamic pressure, lb/ft ²
r	yaw rate about z-axis, deg/sec or rad/sec
Re	Reynolds number
S	planform area, ft ²
t	time variable, sec
T	period of forced roll oscillations, sec
V	flow velocity, ft/sec or ips
V_{∞}	wind or water tunnel freestream velocity, ft/sec or ips
x	x-body axis location, inches
\bar{x}	mean vortex burst point location, inches or feet
x_b	vortex burst point, inches or feet
X	horizontal position in video frame, pixels
y	y-body axis location, inches
Y	vertical position in video frame, pixels
z	z-body axis location, inches
α	angle of attack, deg
α_c	vortex core angle of attack, deg
α_o	angle of attack at zero roll angle, deg
α_s	pitch angle or steady-state angle of attack, deg
β	sideslip angle, deg or rad
β_T	yaw angle, deg
Δ	net difference
δ_A	aileron deflection angle, deg or rad
δ_d	differential tail deflection, deg

NOMENCLATURE

θ	wing sweep half angle, deg
θ_A	apex half angle, deg
$\bar{\theta}_A$	effective apex half angle, deg
θ_c	vortex core sweep angle, deg
Λ	wing leading-edge sweep angle, deg
λ	damping of amplitude envelope in roll oscillations, sec^{-1}
ν	argument of sinusoidal function, deg or rad
ρ	fluid density, slug/ft ³
ϕ	roll or bank angle, deg or rad
τ	nondimensional time, c/V_∞
ω	frequency of roll oscillations, rad/sec
$\bar{\omega}$	angular velocity vector, rad/sec
Ω	frequency of limit cycle roll oscillation, rad/sec
μ	damping coefficient due to bearing friction
μ_1	$\bar{q}Sb^2\mu/2I_{xx}V$, sec^{-1}

Subscripts

i	instantaneous
max	maximum
min	minimum
o	initial
s	steady state

Superscripts

.	dot, derivative with respect to time
'	prime, derivative with respect to amplitude

TABLE OF CONTENTS

	Page
ABSTRACT	iii
DEDICATION	v
ACKNOWLEDGEMENTS	vi
NOMENCLATURE	vii
TABLE OF CONTENTS	xi
LIST OF TABLES	xv
LIST OF FIGURES	xvi
CHAPTER	
I INTRODUCTION	1
Problem Statement	1
Definition of Wing Rock	2
Significance of Wing Rock	3
II WING ROCK BACKGROUND AND LITERATURE REVIEW	6
Flight Observations	6
Subscale Tests on Delta Wings	13
Nguyen, Yip, and Chambers Wind Tunnel Study	13
Levin and Katz Wind Tunnel Studies	16
Jun and Nelson Flow Visualization Study	20
Computational and Analytical Studies	22
Numerical Simulation	23
Hsu and Lan Mathematical Model	24
Aerodynamic Hysteresis	26
Fluid Mechanic Analysis of Wing Rock	29
Summary	31

TABLE OF CONTENTS (continued)

CHAPTER		Page
III	EXPERIMENTAL EQUIPMENT AND TEST PROCEDURES	34
	Rationale for Experimental Approach	34
	Overview of Experiments	35
	Models and Test Facilities	35
	Test Models	35
	Water Tunnel Facility	36
	Wind Tunnel Facility	40
	Data Acquisition and Reduction System	42
	Video Cameras and Recorders	42
	Video Processor	44
	Sun 2/130 Minicomputer	45
	ExpertVision Software	45
	Data Acquisition and Analysis Procedures	47
	Water Tunnel Data Acquisition	47
	Wind Tunnel Data Acquisition	49
	Water Tunnel Data Reduction	49
	Wind Tunnel Data Reduction	54
	Mathematical Model and Simulations	55
	Mathematical Model	55
	Simulation of Wing Rock	58
	Test Matrix	58
	First Test Series	59
	Second Test Series	59
	Third Test Series	60
IV	VALIDATION TESTS AND STATIONARY WING RESULTS	64
	Stationary Model Tests	64
	Vortex Core Trajectories and Burst Points	65
	Vortex Burst Points	68
	Core Velocities and Accelerations	72
	Forced Roll Oscillations	74
	Model Motion	76
	Movement of Vortex Core and Burst Points	80
	Velocity Measurements	84
	Summary of Tests	85

TABLE OF CONTENTS (continued)

CHAPTER		Page
V	DISCUSSION OF WING ROCK RESULTS	87
	Water Tunnel Test Results	87
	Summary of Test Methods	87
	General Observations	88
	Model Motion	88
	Aerodynamic Derivative Extraction	107
	Mathematical Modeling	111
	Vortex Trajectory	119
	Summary of Water Tunnel Data	131
	Wind Tunnel Test Results	132
	Summary of Test Methods	132
	General Observations	133
	Baseline Test Condition	134
	Angle of Attack Variations	166
	Bearing Friction Tests	174
	Mass Asymmetry Tests	180
	Sideslip Tests	181
	Smoke Tests	182
	Wind Tunnel Summary	182
	Comparison of Wind and Water Tunnel Tests	183
	Similarities in Water and Wind Tunnel	183
	Water and Wind Tunnel Differences	184
	Rolling Moment Magnitudes	185
	Rolling Moment Hysteresis Directions	192
VI	CONCLUSIONS AND RECOMMENDATIONS	199
	Conclusions	199
	ExpertVision Validation	199
	Scaleability of Water and Wind Tunnel Results	200
	Wing Rock Conclusions	202
	Mathematical Model and Simulation	204
	Summary	205
	Recommendations	205
	Further Analysis of Wing Rock	206
	Dynamic Scaling Between Water Tunnel and Wing Tunnel Tests	207
	Enhancements to ExpertVision	207
	Summary	208

TABLE OF CONTENTS (continued)

	Page
REFERENCES	209
APPENDIX A APPROXIMATE ANALYTIC SOLUTION TO ONE DEGREE-OF-FREEDOM MODEL	216
APPENDIX B ENERGY ANALYSIS OF SINGLE DEGREE-OF-FREEDOM WING ROCK	232
VITA	237

LIST OF TABLES

	Page
Table 1 Data reduction procedure	53
Table 2 First test series (70 ° delta wing)	59
Table 3 First test series (80 ° delta wing)	60
Table 4 Second test series (70 ° delta wing)	61
Table 5 Second test series (80 ° delta wing)	61
Table 6 Wing rock water tunnel tests (80 ° delta wing)	61
Table 7 Wind tunnel wing rock tests	62
Table 8 Comparison of measured and calculated periods	113
Table 9 Evaluation of $\text{sgn}(\phi)$ and $\text{sgn}(\dot{\phi})$	225

LIST OF FIGURES

	Page
Fig. 1 Wing rock of the F-14. ²	3
Fig. 2 Typical wing rock response: a) roll angle history, and b) phase portrait.	4
Fig. 3 Effects of buffet and wing rock on aiming accuracy. ⁴	5
Fig. 4 F-4 damping in roll: a) $\phi = \pm 5.00^\circ$, and b) $\phi = \pm 10.5^\circ$. ⁷	7
Fig. 5 Lift curve for F-4. ⁹	7
Fig. 6 Gnat trainer: a) wing rock results, and b) damping in roll results. ⁹	9
Fig. 7 F-5 damping-in-roll. ¹³	10
Fig. 8 F-14 wing rock envelope. ²⁰	11
Fig. 9 X-29A static lateral-directional derivative and roll damping derivative. ²¹	12
Fig. 10 Free-to-roll test apparatus. ²³	14
Fig. 11 C_L versus ϕ histogram, $\alpha = 32^\circ$. ²³	15
Fig. 12 Roll damping data. ²³	15
Fig. 13 Free-to-roll models. ²⁴	16
Fig. 14 Wing rock amplitudes and frequency. ²⁴	17
Fig. 15 Canard-delta wing experiment. ²⁵	19
Fig. 16 Rolling moment histogram, $\alpha = 27.5^\circ$. ²⁵	19
Fig. 17 Region of wing rock. ²⁵	20
Fig. 18 Static vortex positions, $\alpha = 30^\circ$. ²⁶	21
Fig. 19 Vortex positions during wing rock, $\alpha = 40^\circ$. ²⁶	22
Fig. 20 Rolling moment versus roll angle. ²⁷	25
Fig. 21 Predicted versus experimental results for 80° delta wing: a) wing rock periods, and b) wing rock amplitudes. ³⁰	27
Fig. 22 Rolling moment versus roll angle comparisons. ³⁰	28

LIST OF FIGURES (continued)

	Page
Fig. 23 Roll damping coefficients versus roll angles. ³⁰	28
Fig. 24 Aerodynamic roll moment hysteresis. ³¹	30
Fig. 25 Boundaries for vortex asymmetry and vortex burst. ^{32,41}	30
Fig. 26 Effects of apex half angle on wing rock: a) vortex asymmetry, and b) vortex burst. ³²	32
Fig. 27 Delta wing models.	36
Fig. 28 Water tunnel facility.	37
Fig. 29 Delta wing mounted to forced-roll oscillation apparatus.	38
Fig. 30 Forced-roll oscillation drive apparatus.	38
Fig. 31 Free-to-roll model mounting arrangement.	39
Fig. 32 Free-to-roll bearings.	39
Fig. 33 Wind tunnel facility diagram. ⁴⁵	41
Fig. 34 Wind tunnel experimental set-up.	41
Fig. 35 Free-to-roll apparatus and mounting adapter.	43
Fig. 36 Schematic of ExpertVision.	43
Fig. 37 Orthogonal camera arrangement.	48
Fig. 38 Water tunnel flow visualization with continuous dye streams: a) planform view, and b) side view.	50
Fig. 39 Water tunnel flow visualization with pulsed dye flow.	51
Fig. 40 Vortex flow parameters: a) planform view, and b) side view.	66
Fig. 41 Vortex location parameters: a) core angle of attack, and b) average core sweep angle.	67
Fig. 42 Vortex burst point locations and α_s	68
Fig. 43 Experimental lift data versus Polhamus predictions. ⁵⁶	70

LIST OF FIGURES (continued)

	Page
Fig. 44 Vortex burst locations and β_T	71
Fig. 45 Average burst point locations and β_T	71
Fig. 46 Vortex core velocity time history.	72
Fig. 47 Vortex core acceleration time history.	73
Fig. 48 Forced oscillation parameters.	75
Fig. 49 Forced oscillation motion variables, $k = 0.26$	77
Fig. 50 Forced oscillation phase portrait, $k = 0.26$	77
Fig. 51 Rolling acceleration versus ϕ , $k = 0.26$	78
Fig. 52 Forced oscillation motion variables, $k = 1.0$	78
Fig. 53 Forced oscillation phase portrait, $k = 1.0$	79
Fig. 54 Rolling acceleration versus ϕ , $k = 1.0$	79
Fig. 55 Phasing of burst point and ϕ , $k = 0.1$	81
Fig. 56 Phasing of burst point and ϕ , $k = 0.26$	81
Fig. 57 Phasing of burst point and ϕ , $k = 1.0$	82
Fig. 58 Burst point location and reduced frequency.	83
Fig. 59 Burst point phase lag and reduced frequency.	83
Fig. 60 Forced oscillation vortex core velocity and ϕ	84
Fig. 61 Wing rock motion parameters, $V_\infty = 4$ ips (first run).	89
Fig. 62 Wing rock phase portrait, $V_\infty = 4$ ips (first run).	91
Fig. 63 Roll acceleration versus ϕ , $V_\infty = 4$ ips (first run).	92
Fig. 64 Roll acceleration versus ϕ cycle, $V_\infty = 4$ ips (first run).	92
Fig. 65 Aerodynamic rolling moment versus ϕ , $V_\infty = 4$ ips (first run).	93
Fig. 66 Wing rock motion parameters with low pass Butterworth filtering.	95

LIST OF FIGURES (continued)

	Page
Fig. 67 Rolling acceleration versus ϕ using Butterworth filtering.	95
Fig. 68 Wing rock motion parameters, $V_{\infty} = 4$ ips (second run).	97
Fig. 69 Wing rock phase portrait, $V_{\infty} = 4$ ips (second run).	97
Fig. 70 Roll acceleration versus ϕ , $V_{\infty} = 4$ ips (second run).	98
Fig. 71 Aerodynamic rolling moment versus ϕ , $V_{\infty} = 4$ ips (second run).	98
Fig. 72 Wing rock motion parameters, $V_{\infty} = 6$ ips.	99
Fig. 73 Wing rock phase portrait, $V_{\infty} = 6$ ips.	101
Fig. 74 Roll acceleration versus ϕ , $V_{\infty} = 6$ ips.	101
Fig. 75 Aerodynamic rolling moment versus ϕ , $V_{\infty} = 6$ ips.	102
Fig. 76 Wing rock motion parameters, $V_{\infty} = 10$ ips.	102
Fig. 77 Wing rock phase portrait, $V_{\infty} = 10$ ips.	104
Fig. 78 Roll acceleration versus ϕ , $V_{\infty} = 10$ ips.	104
Fig. 79 Aerodynamic rolling moment versus ϕ , $V_{\infty} = 10$ ips.	105
Fig. 80 Phase portrait comparison, water tunnel.	105
Fig. 81 Roll acceleration versus roll rate comparison, water tunnel.	106
Fig. 82 Aerodynamic rolling moment versus ϕ comparison, water tunnel.	106
Fig. 83 Wing rock frequency variation with velocity.	108
Fig. 84 Reduced frequency variation with Reynolds number.	108
Fig. 85 Roll amplitude variation with Reynolds number.	109
Fig. 86 Polynomial fit to C_{ℓ} versus β data.	109
Fig. 87 C_{ℓ_p} variation with ϕ	112
Fig. 88 Phase portrait for constant $C_{\ell\beta}$ Runge-Kutta simulation.	115

LIST OF FIGURES (continued)

	Page
Fig. 89 Rolling moment versus ϕ for constant $C_{\ell\beta}$ Runge-Kutta simulation.	115
Fig. 90 Phase portrait for time-varying $C_{\ell\beta}$ Runge-Kutta simulation.	116
Fig. 91 Rolling moment versus ϕ for time-varying $C_{\ell\beta}$ Runge-Kutta simulation.	117
Fig. 92 Roll damping derivative versus ϕ	117
Fig. 93 Phase portrait for time-varying $C_{\ell\beta}$ Runge-Kutta simulation of 10 ips test.	118
Fig. 94 Rolling moment versus ϕ for time-varying $C_{\ell\beta}$ Runge-Kutta simulation of 10 ips test.	118
Fig. 95 Vortex spanwise position: $x/c = -0.25$	120
Fig. 96 Vortex vertical displacement: $x/c = -0.25$	120
Fig. 97 Vortex core movement: $x/c = -0.25$	122
Fig. 98 Vortex spanwise position: $x/c = -0.50$	123
Fig. 99 Vortex vertical displacement: $x/c = -0.50$	123
Fig. 100 Vortex core movement: $x/c = -0.50$	124
Fig. 101 Vortex spanwise position: $x/c = -0.75$	126
Fig. 102 Vortex vertical displacement: $x/c = -0.75$	126
Fig. 103 Vortex core movement: $x/c = -0.75$	127
Fig. 104 Schematic of vortex movement.	129
Fig. 105 Vortex burst point movement during wing rock.	131
Fig. 106 Wing rock roll angle time history, $\bar{q} = 0.5$ psf.	135
Fig. 107 Wing rock roll rate time history, $\bar{q} = 0.5$ psf.	136
Fig. 108 Wing rock roll acceleration time history, $\bar{q} = 0.5$ psf.	136
Fig. 109 Wing rock phase portrait, $\bar{q} = 0.5$ psf.	137
Fig. 110 Aerodynamic rolling moment versus ϕ , $\bar{q} = 0.5$ psf.	138

LIST OF FIGURES (continued)

	Page
Fig. 111 Wing rock roll angle time history, $\bar{q} = 1.0$ psf.	139
Fig. 112 Wing rock roll rate time history, $\bar{q} = 1.0$ psf.	140
Fig. 113 Wing rock roll acceleration time history, $\bar{q} = 1.0$ psf.	140
Fig. 114 Wing rock phase portrait, $\bar{q} = 1.0$ psf.	141
Fig. 115 Average $C_{\ell\beta}$ versus α for 80° delta wing. ³⁰	142
Fig. 116 Theoretical variation of roll damping derivatives with angle of attack. ³⁰	143
Fig. 117 Aerodynamic rolling moment versus ϕ , $\bar{q} = 1.0$ psf for a) cycle A, b) cycle B, c) cycle C, and d) cycle D.	144
Fig. 118 Aerodynamic rolling moment versus ϕ , $\bar{q} = 1.0$ psf.	147
Fig. 119 Aerodynamic rolling moment versus ϕ cycle, $\bar{q} = 1.0$ psf.	148
Fig. 120 Wing rock roll angle history, $\bar{q} = 1.0$ psf, $\phi_0 = -70^\circ$	149
Fig. 121 Wing rock phase portrait, $\bar{q} = 1.0$ psf, $\phi_0 = -70^\circ$	149
Fig. 122 Wing rock phase portrait from Runge-Kutta integration.	150
Fig. 123 Aerodynamic rolling moment versus ϕ , $\bar{q} = 1.0$ psf, $\phi_0 = -70^\circ$ for a) cycle A, b) cycle B, and c) cycle C.	151
Fig. 124 Wing rock roll angle time history, $\bar{q} = 2.0$ psf.	153
Fig. 125 Wing rock roll rate time history, $\bar{q} = 2.0$ psf.	153
Fig. 126 Wing rock roll acceleration time history, $\bar{q} = 2.0$ psf.	154
Fig. 127 Wing rock phase portrait, $\bar{q} = 2.0$ psf.	155
Fig. 128 Aerodynamic rolling moment versus ϕ , $\bar{q} = 2.0$ psf, for a) cycle A, b) cycle B, c) cycle C, d) cycle D, and e) cycle E.	155
Fig. 129 Wing rock variations with Reynolds number: a) period variations, and b) frequency variations.	159
Fig. 130 Wing rock reduced frequency variation with Reynolds number.	160
Fig. 131 Wing rock roll amplitude variation with Reynolds number.	161

LIST OF FIGURES (continued)

	Page
Fig. 132 Wing rock phase portrait comparison, wind tunnel.	163
Fig. 133 Roll acceleration versus roll rate comparison, wind tunnel.	164
Fig. 134 Aerodynamic rolling moment versus ϕ comparison for a) $\bar{q} = 0.5, 1.0, 2.0$ psf, and b) $\bar{q} = 3.0, 4.0$ psf.	165
Fig. 135 Wing rock amplitude variation with angle of attack.	167
Fig. 136 Wing rock period variation with angle of attack.	169
Fig. 137 Wing rock reduced frequency variation with angle of attack.	170
Fig. 138 Wing rock phase portrait, $\alpha = 30^\circ$, $\bar{q} = 2.0$ psf.	171
Fig. 139 Aerodynamic rolling moment versus ϕ , $\alpha = 30^\circ$, $\bar{q} = 2.0$ psf.	171
Fig. 140 Wing rock phase portrait, $\alpha = 40^\circ$, $\bar{q} = 2.0$ psf.	172
Fig. 141 Aerodynamic rolling moment versus ϕ , $\alpha = 40^\circ$, $\bar{q} = 2.0$ psf.	173
Fig. 142 Bearing friction effects on wing rock response.	175
Fig. 143 Wing rock build-up with no lubrication.	176
Fig. 144 Wing rock build-up with motor oil lubrication.	176
Fig. 145 Wing rock build-up with WD-40 lubrication.	177
Fig. 146 Aerodynamic rolling moment versus ϕ , motor oil test.	178
Fig. 147 Aerodynamic rolling moment versus ϕ , grease test.	178
Fig. 148 Aerodynamic rolling moment versus ϕ , WD-40 test.	179
Fig. 149 Aerodynamic rolling moment versus ϕ : mass imbalance test.	181
Fig. 150 Angle of attack effect on roll amplitude.	184
Fig. 151 Comparison of water and wind tunnel C_{ℓ} versus ϕ	185
Fig. 152 Comparison of water and wind tunnel wing rock periods.	186
Fig. 153 Volume swept out by delta wing.	189

LIST OF FIGURES (continued)

	Page
Fig. 154 C_ℓ versus ϕ for sinusoidal motion, with phase lead.	197
Fig. 155 C_ℓ versus ϕ for sinusoidal motion, with phase lag.	197
Fig. 156 Assumed ϕ variation.	224
Fig. 157 Assumed $\dot{\phi}$ variation.	224
Fig. 158 Typical simulation of C_ℓ versus ϕ	233

CHAPTER I

INTRODUCTION

Problem Statement

Vortex flows dominate the flow field around many fighter aircraft, especially when operating at angles of attack near or above stall. In order for newer fighter configurations to exploit the additional lift that can be generated by these vortices, it is essential to fully understand their behavior. Experimental results show that this enhanced lift is quickly lost when vortex bursting occurs over lifting surfaces, diminishing the existing low pressure regions. Dynamic studies indicate that these leading-edge vortices become unstable with increasing angle of attack, α , and contribute to highly undesirable uncommanded roll oscillations known as wing rock. These limit cycle oscillations can severely limit aircraft maneuverability and pose serious safety problems during high α operations, such as in air combat maneuvering and short field landings. Wing rock can completely destroy the precision tracking ability necessary in aerial combat. Wing rock is likely to be very significant for the low-speed, high α operations of the proposed National Aero-Space Plane. Conceptual designs of that vehicle employ highly swept delta wings, which are especially prone to wing rock. In order to develop control systems to handle wing rock, it is essential to understand the mechanisms which drive it. While various experimental and computational research efforts have been performed to determine the cause of such self-induced oscillations, a universally accepted concept does not exist. The primary objective of the current research was to develop a theory identifying the cause of wing rock on slender, highly swept delta wings.

The current study leads to a detailed explanation of the cause of wing rock based on dynamic measurements in both a water tunnel and in a wind tunnel on a delta wing model with a sharp, 80° sweep angle leading edge. An extensive review of related research was also completed. The measurements were made using a commercially available, video-based motion

The citations used in this study follow the style of the *Journal of Aircraft*.

analysis tool, ExpertVision (EV).¹ The system permitted simultaneous nonintrusive measurements of the motion of an oscillating delta wing model and the movement of the leading-edge vortices in a water tunnel. Wind tunnel tests provided precise quantification of the wing dynamics from onset through steady state wing rock for a range of angles of attack and dynamic pressures. ExpertVision was used to characterize the vortex core flows over 70° and 80° swept delta wings under stationary and forced oscillation conditions. These tests not only validated the use of the diagnostic tool through excellent agreement with published data, but were the first such experimental measurements of core velocities and accelerations throughout the entire path of a leading-edge vortex. This research effort was the first known use of ExpertVision in an aerospace fluid flow application. This video system allowed the research objectives of this study to be met; without it, it would have been all but impossible to measure the dynamic relationships.

Definition of Wing Rock

Prior to discussing potential causes of wing rock, it is appropriate to define it. Wing rock is a self-induced roll-yaw oscillation which develops in the presence of some initial disturbance or asymmetry in the flow field. While yaw oscillations are present in aircraft wing rock, the motion is primarily a constant amplitude roll oscillation. Flight records of an F-14 in wing rock (Fig. 1) show that the amplitude of the roll limit cycle is significantly larger than the yaw oscillations.² Since wing rock is primarily a roll oscillation, it is also experienced in single-degree-of-freedom tests, which comprise the experiments of the current research, as well as the majority of other programs which have investigated the phenomenon. The frequency and amplitude of the oscillations are highly dependent upon aircraft or wing configuration, angle of attack, and other flow conditions, such as freestream velocity. A typical roll angle (or bank angle) time history (Fig. 2a) and phase portrait (Fig. 2b) for wing rock show the initial build-up, and subsequently, the periodicity of the limit cycle oscillation. (Throughout this report, the terms roll angle and bank angle are used interchangeably, and are represented as ϕ .) While the existence of this periodic oscillation is a well-established and worrisome fact in modern aircraft, the mechanism driving the phenomenon is still hotly debated by a wide variety of researchers.

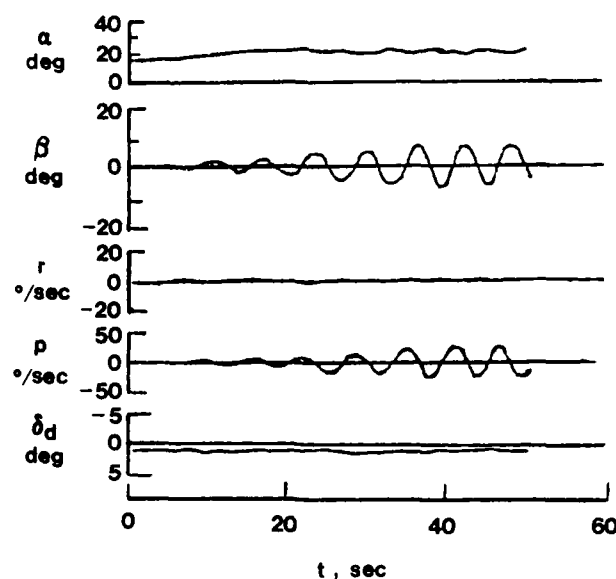
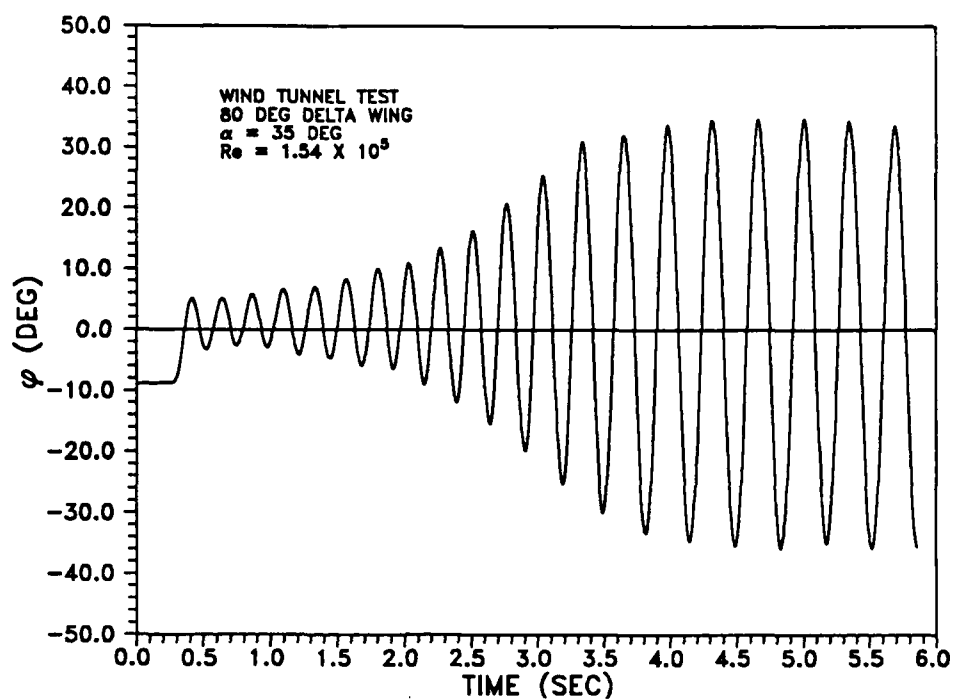


Fig. 1 Wing rock of the F-14.²

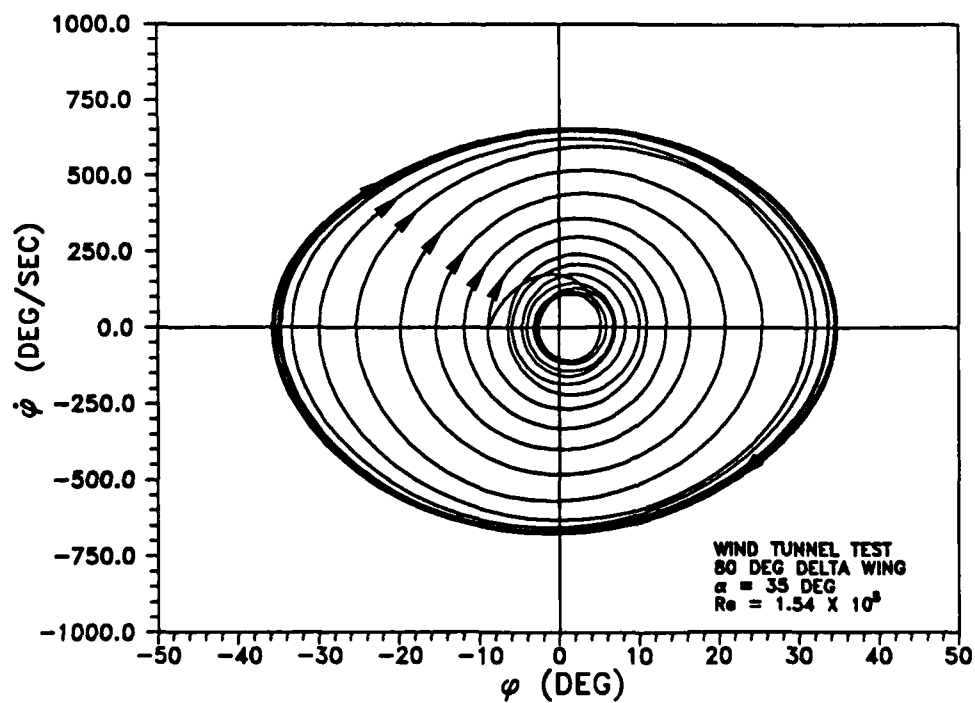
Significance of Wing Rock

Uncommanded roll oscillations during wing rock pose major limitations to the maneuverability of modern aircraft operating at high angles of attack, especially in aerial combat. Chambers, Gilbert, and Nguyen showed that these limit cycle oscillations severely limit or negate the tracking capability of fighter aircraft^{3,4} (Fig. 3). As shown on the left side of the miss distance plot, onset of buffet strongly affected aiming accuracy. Moreover, once wing rock occurred, the miss distance became very large and the pilot was unable to track the target except very briefly. This example of an unacceptable degradation in combat performance due to wing rock is extremely significant since the sustained oscillations occur at high α , near maximum lift, where modern fighter aircraft operate routinely.

Under approach and landing conditions, wing rock is a serious safety problem, especially in short field and carrier landings where aircraft must precisely maintain high angles of attack. Wing rock can cause unexpected roll rates up to 50°/sec and bank angles up to 90°, making it difficult or impossible for the pilot to precisely maneuver.³



a)



b)

Fig. 2 Typical wing rock response: a) roll angle history, and b) phase portrait.

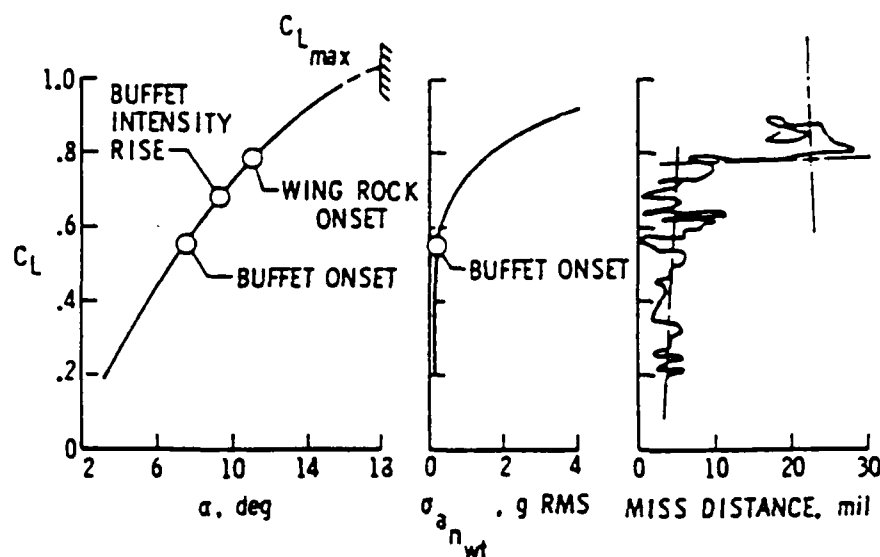


Fig. 3 Effects of buffet and wing rock on aiming accuracy.⁴

Wing rock also has a large impact on the design of aircraft control systems. Control systems designed to improve high α performance can actually aggravate or excite wing rock. For example, an aileron-to-rudder interconnect intended to eliminate adverse yaw at high angles of attack initiated wing rock due to sideslip generated by rudder inputs.^{3,4} In another case, an augmentation system designed to eliminate wing rock on a fighter configuration reduced the aircraft departure/spin resistance, a serious safety issue! Designers must consider wing rock when developing advanced control systems.

It is clear from the preceding discussion that wing rock cannot be ignored. Failure to consider the phenomenon may very well result in unacceptable and/or catastrophic safety risks on modern aircraft. Thus, it is essential to understand the mechanisms which cause self-induced and self-sustaining roll oscillations in order to control or eliminate them.

CHAPTER II

WING ROCK BACKGROUND AND LITERATURE REVIEW

While a number of experimental and analytical studies have investigated wing rock, a universally accepted theory on its cause does not exist. This chapter surveys published wing rock results and conclusions reached by other researchers. Experimentally, these efforts range from single degree-of-freedom tests on subscale models to observations and analyses of aircraft flight tests. Analytical developments range from relatively simple mathematical models to computer codes which simultaneously predict the movements of the leading-edge vortices and the motion of complete aircraft. To arrive at a logical argument explaining the driving mechanisms for self-sustaining oscillations, it is imperative to assimilate, evaluate, and compare previous research with results from the current study.

Flight Observations

One important source of information comes from flight observations and subsequent analysis of both subscale and flight test data. Since the ultimate goal is to understand and control aircraft wing rock, such data provide extremely useful information in analyzing the problem. A good example is the F-4 response. The F-4 exhibits severe wing rock at angles of attack of approximately 20° .⁵ One example of the self-induced oscillation occurred while the aircraft was in a 60° banked turn with constantly increasing angle of attack.⁶ Subsequent forced oscillation tests in a wind tunnel using a 0.13 scale model revealed an unstable roll damping coefficient $[(C_{\ell_p} + C_{\ell_{\dot{\beta}}} \sin \alpha) > 0]$ at low roll angles near the angle of attack where wing rock was experienced (Fig. 4a).⁷ At larger roll angle amplitudes, the damping in roll became "stable" (negative) at the same angle of attack (Fig. 4b), indicating a strong nonlinearity with amplitude.^{7,8} The destabilizing roll damping at small bank angles, together with its nonlinear behavior, were identified as the basic factors producing F-4 wing rock. Adding leading-edge slats to the F-4 increased the angle of attack and lift coefficient where buffet and wing rock occurred⁹ (Fig. 5),

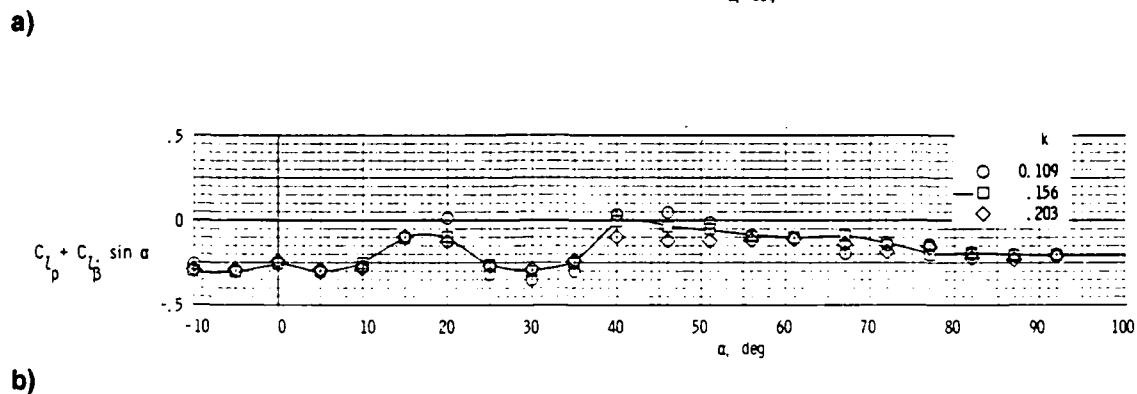
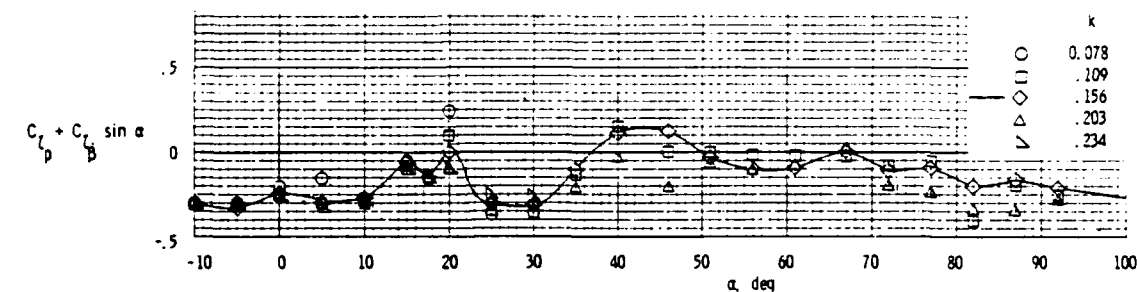


Fig. 4 F-4 damping in roll: a) $\phi = \pm 5.00^\circ$, and b) $\phi = \pm 10.5^\circ$.⁷

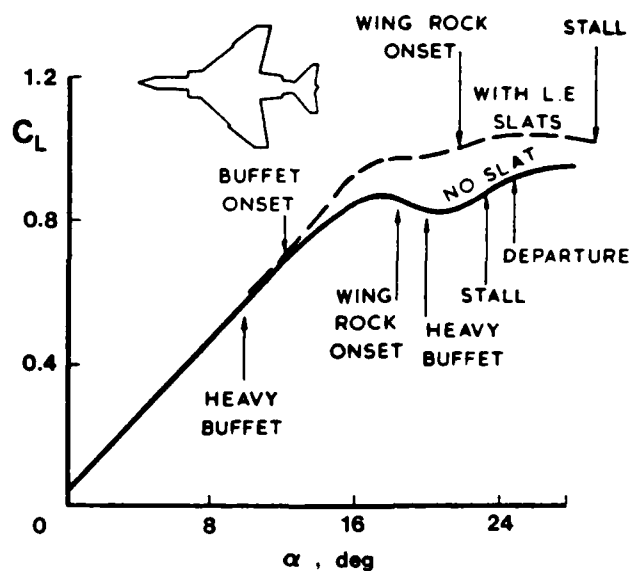


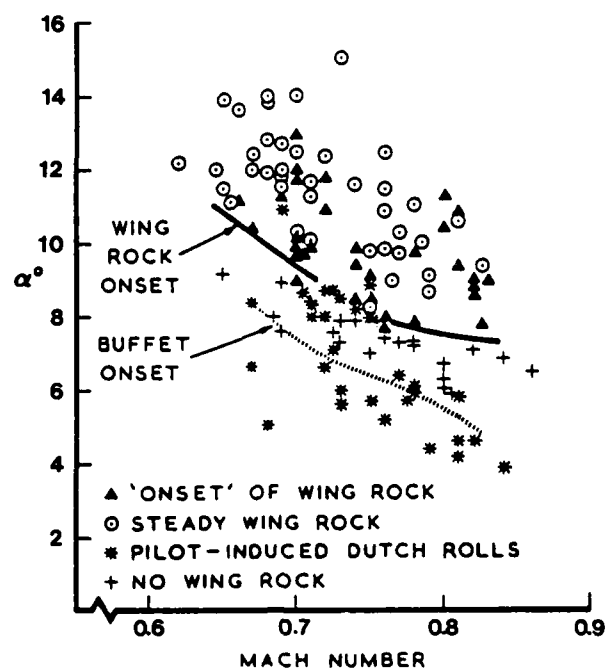
Fig. 5 Lift curve for F-4.⁹

strongly suggesting that alteration of wing aerodynamics can significantly change an aircraft's wing rock behavior.

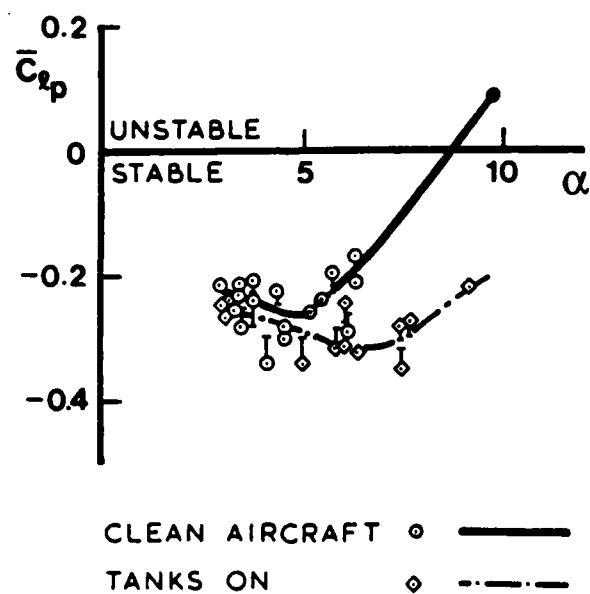
An informative series of wing rock flight tests were performed on the Gnat trainer. The program consisted of testing aircraft with and without wing fuel tanks. The clean aircraft (no tanks) consistently exhibited wing rock at specific angles of attack depending on Mach number, such that onset angle of attack decreased as Mach number increased (Fig. 6a).^{9,10} The aircraft with tanks never experienced steady wing rock, but instead demonstrated a longitudinal porpoising oscillation. Estimation of damping in roll derivatives from these flight tests clearly revealed that wing rock occurred on the clean aircraft when roll damping became positive (unstable). The aircraft carrying external tanks maintained a negative damping in roll (Fig. 6b). Ross concluded that wing tanks act like an aerodynamic fence, controlling flow separation over the wing similar to leading-edge slats on the F-4, with a resultant increase in the damping in roll.

The Handley Page 115, with a leading-edge wing sweep of 75° , was designed and built specifically to investigate handling qualities and aerodynamic characteristics of highly swept slender wings at low speed flight conditions.¹¹ The aircraft exhibited wing rock oscillations of $\pm 30^\circ$ at $\alpha = 21^\circ$, which grew to $\pm 40^\circ$ as the angle of attack was increased to 30° . At the higher angle of attack, the aircraft also experienced yaw oscillations of $\pm 3^\circ$. Simulation of both flight and subscale wind tunnel data indicated to Ross that wing rock was initiated by a nonlinear yawing moment due to sideslip, which caused a divergent Dutch roll oscillation to grow into the limit cycle.

The occurrence of wing rock at transonic flight conditions on the F-5A prompted a subscale wind tunnel program to investigate the phenomenon.¹² The wind tunnel simulation provided a lightly damped roll degree-of-freedom for the one-seventh scale model. Additionally, the flexible sting supporting the model allowed slight model oscillations in both yaw and pitch. At $M = 0.925$, the F-5A encountered wing rock at $\alpha \approx 10^\circ$. Analysis of the pressure data collected during the oscillations revealed that the primary cause of the wing rock was pressure changes on the top wing surface, especially near the wing tip. These pressure fluctuations came from motion induced changes in α and movement of the unstable shock wave. These fluctuations led to



a)



b)

Fig. 6 Gnat trainer: a) wing rock results, and b) damping in roll results.⁹

cyclic leading-edge stall and recovery. According to Hwang and Pi,¹² this cyclic change of lift on each wing produced wing rock during transonic flight.

Both the F-5E and F-5F aircraft exhibited low-speed wing rock, essentially single degree-of-freedom roll oscillations.^{13,14} Damping in roll characteristics for the aircraft (Fig. 7) revealed a strong nonlinear behavior with roll angle. At angles of attack where wing rock was experienced, roll damping was highly unstable at small roll angles and stable at large roll angles. This nonlinearity in roll damping was believed by Orlik-Ruckemann and Erickson to be the mechanism initiating and sustaining limit cycle oscillations. A water tunnel investigation of a light weight F-5E model at $\alpha = 35^\circ$ was devised to provide information on movement of the vortices during wing rock; however, the model would not exhibit the limit cycle oscillations. Flow visualization tests utilizing forced oscillations on the model in the water tunnel did reveal an oscillatory vortex pattern originating off the leading-edge extensions (LEX) which Erickson hypothesized would result in nonlinear roll damping. Other studies showed that modifying the nose or the LEX on the

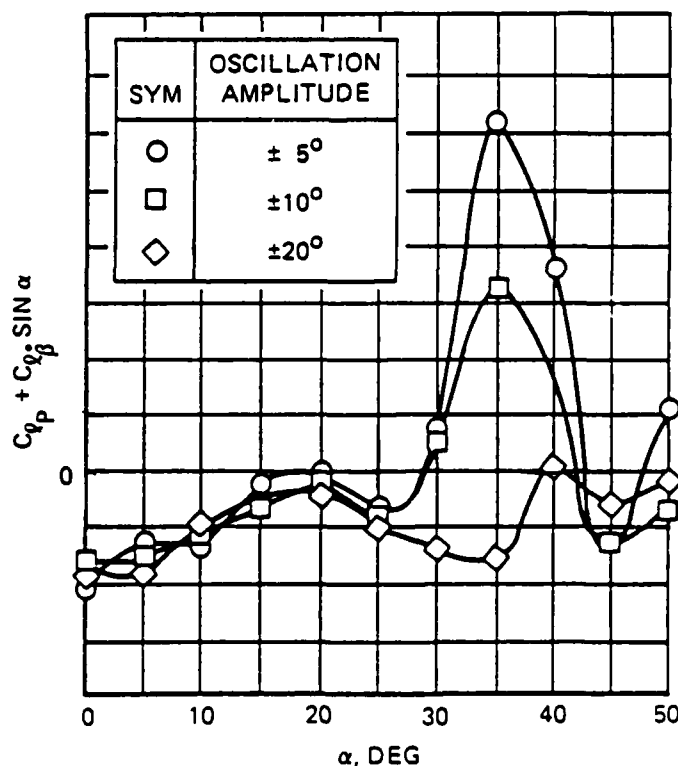


Fig. 7 F-5 damping-in-roll.¹³

F-5 substantially altered the roll damping, in addition to other aerodynamic derivatives.¹⁵⁻¹⁹ These results highlighted the importance of forebody aerodynamics on roll damping and, therefore, wing rock, for the F-5.

Wing rock of the F-14 variable-sweep fighter has been observed for angles of attack above 17° at Mach numbers up to approximately 0.65 (Fig. 8).² A typical response of the F-14 during the self-induced oscillations was shown in Fig. 1. Both flight test and wind tunnel data indicated that the F-14 wing rock occurred due to a loss of roll damping as a result of wing stall. The F-14 wing rock was manifested as large amplitude limit cycle roll oscillations at the Dutch roll frequency. The F-14 was especially noteworthy since it demonstrated strong interaction between wing rock and the design of high angle of attack control systems.²⁰ For example, the roll-to-yaw interconnect scheme, designed for roll coordination, actually interacted with wing rock to cause pilot induced oscillations during air-to-air tracking. Additionally, use of a high gain roll damper to suppress wing rock seriously degraded F-14 departure/spin resistance. An improved automatic stability and control augmentation system was designed which successfully suppressed the airplane wing rock tendency while providing a high level of departure and spin resistance.⁴

Single degree-of-freedom subscale wind tunnel tests¹⁶ (0.16 scale model) followed by unconstrained radio-controlled drop-model tests²¹ (0.22 scale model) for the X-29A revealed large amplitude wing rock with roll angles of $\pm 60^\circ$. The oscillations started as α was increased

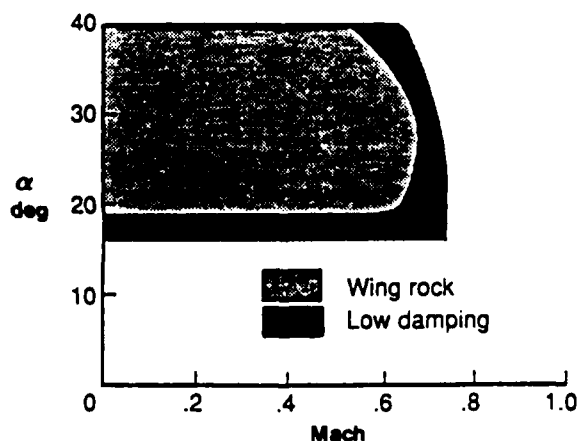


Fig. 8 F-14 wing rock envelope.²⁰

above 20° and continued to grow in amplitude up to $\alpha = 32^\circ$. Drop-model tests showed that the oscillations were almost purely about the roll axis with very small changes in yaw angle. Above $\alpha = 32^\circ$, a violent roll departure resulted. Fig. 9 shows $C_{\ell\beta} < 0$ for $\alpha > 10^\circ$. The roll damping derivative, $C_{\ell p}$, became positive at $\alpha \approx 18^\circ$, which was near the angle of attack where wing rock began. Wind tunnel tests on a 0.16 scale model of the X-29A wing planform alone demonstrated no wing rock tendencies; however, tests on the fuselage-tail configuration without the wing did exhibit limit cycle rock oscillations. These results strongly suggested that the aerodynamics of the fuselage largely created the unstable roll damping and, thereby, X-29A wing rock.

Wing rock has also been observed by Chambers, Gilbert, and Nguyen on a general aviation aircraft with a cambered, unswept wing at high angles of attack.²² These oscillations occurred at the aircraft stall prior to entering a spin. Subscale forced oscillation tests showed that the aerodynamic damping in roll ($C_{\ell p} + C_{\ell\beta} \sin \alpha$) became unstable at and beyond the stall angle of attack corresponding to the occurrence of wing rock.

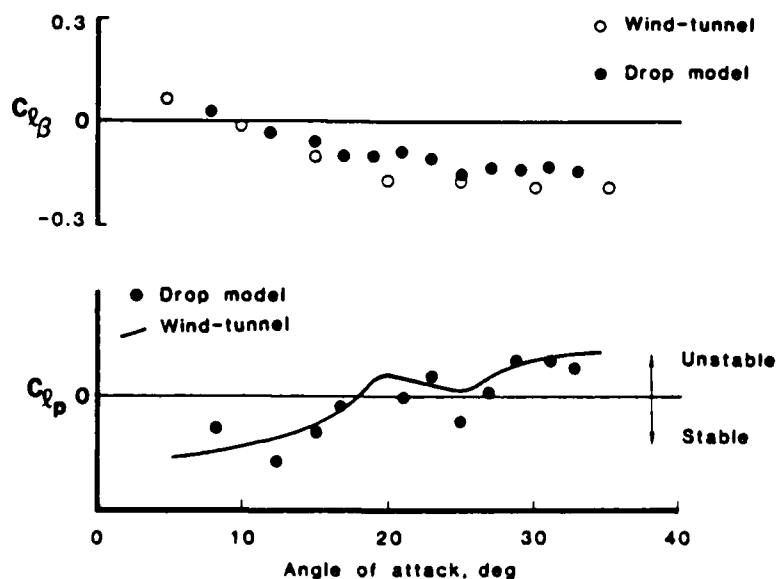


Fig. 9 X-29A static lateral-directional derivative and roll damping derivative.²¹

The preceding discussions presented some examples of wing rock observed in flight and analyzed based on flight test and subscale measurements. It is clear that there is a strong relationship between limit cycle oscillations and high angle of attack aerodynamics. Configuration changes, such as the addition of slats or wing fences, can help alleviate wing rock by altering the aerodynamics. There is also strong evidence that unstable (positive) roll damping at high angles of attack played a major role in the onset of wing rock for most of the aircraft discussed.

Subscale Tests on Delta Wings

While flight tests provide very useful wing rock data, most basic research on these periodic roll oscillations has been conducted using sharp-edged, highly swept delta wing models. Delta wings with sweep angles greater than 75° are very susceptible to wing rock. The results of these efforts are especially applicable to the current research, since an 80° delta wing was used in most of the published investigations.

Nguyen, Yip, and Chambers Wind Tunnel Study

One of the earliest and most comprehensive wing rock studies was conducted on a flat, 80° sweep sharp-edged delta wing model conducted in the NASA Langley Research Center (LaRC) $10' \times 12'$ wind tunnel.²³ These experiments included static force tests, forced oscillation, free-to-roll and rotary balance tests. Wing rock tests were conducted by mounting the model on an apparatus that was free to roll about an axis two inches below the model (Fig. 10). Roll angles were measured with a potentiometer installed in the test rig. Roll rates and roll accelerations were estimated by taking first and second derivatives of the smoothed roll angle time history. Having determined roll acceleration, aerodynamic rolling moment was calculated using

$$C_l(t_i) = \frac{I_{xx} \ddot{\phi}(t_i)}{\bar{q} S b} \quad (1)$$

This approach permitted estimation of aerodynamic rolling moments during wing rock conditions.

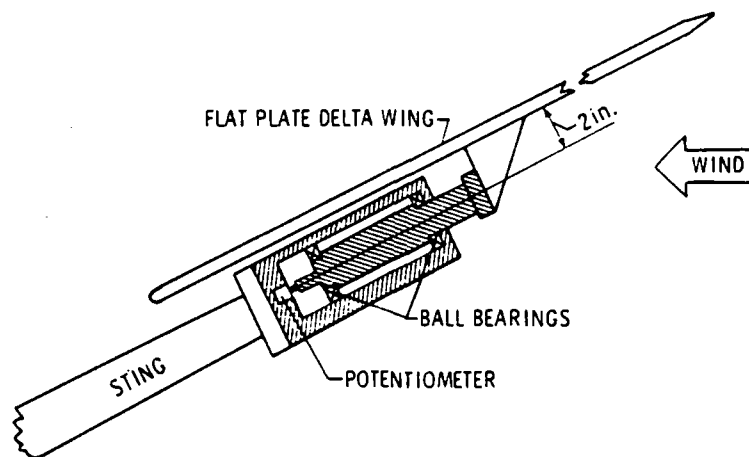


Fig. 10 Free-to-roll test apparatus.²³

Nguyen, Yip, and Chambers found that their delta wing did not experience wing rock below $\alpha = 27^\circ$. The self-induced oscillations reached maximum roll amplitudes of $\pm 40^\circ$ at $\alpha = 32^\circ$ and $\alpha = 37^\circ$. A typical rolling moment history as a function of ϕ is provided for one cycle of oscillation in Fig. 11, where the arrows on the plot indicate increasing time. The multiple values of C_{ℓ} at a given roll angle suggest hysteresis in the aerodynamic rolling moment. Based on an energy analysis (Appendix B) of the C_{ℓ} versus ϕ results the data indicated that the inner loop of the curve was destabilizing and the outer two loops were stabilizing. This LaRC report concluded that unstable aerodynamic roll damping ($C_{\ell_p} > 0$) existed at small roll angles (or sideslip angles) and stable aerodynamic roll damping ($C_{\ell_p} < 0$) existed at the larger roll angles. This hypothesis was also supported by roll damping results from forced oscillation tests (Fig. 12), which predicted unstable roll damping at the α where wing rock occurred. Unstable roll damping existed at angles of attack above $\alpha = 20^\circ$ while the free-to-roll results showed that wing rock did not start until $\alpha = 27^\circ$. Nguyen, Yip, and Chambers explained this inconsistency by inferring that the forces needed to induce wing rock were too low to overcome bearing friction in the

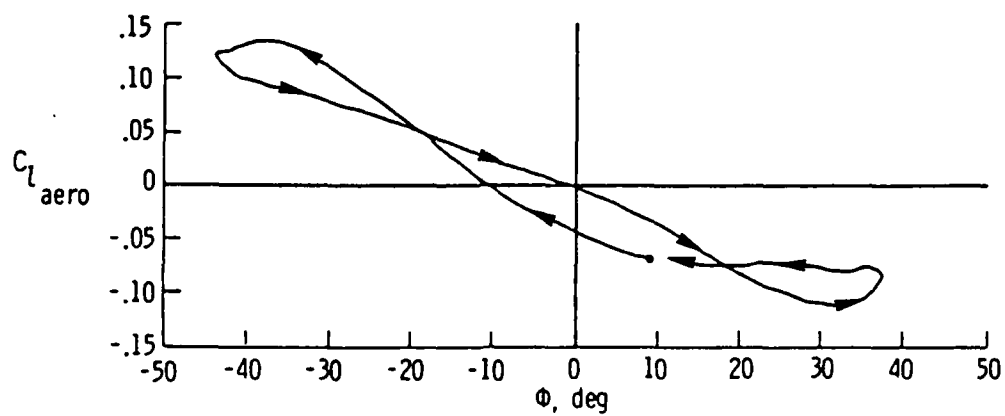


Fig. 11 C_L versus ϕ histogram, $\alpha = 32^\circ$.²³

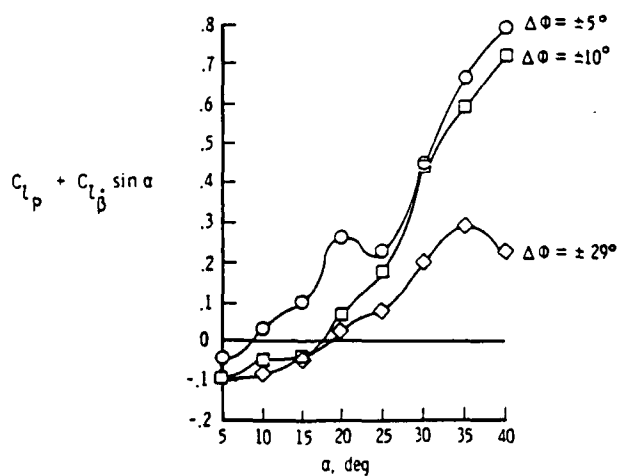


Fig. 12 Roll damping data.²³

free-to-roll apparatus until $\alpha = 27^\circ$. The results also showed that unstable roll damping decreased as roll amplitudes for the forced oscillation tests were increased.

The LaRC group attempted flow visualization using a helium bubble technique. During wing rock, the vortices varied in position above the wing such that the leeward vortex was well above the wing surface, while the windward vortex remained close to the surface. The authors concluded that the upward displacement of the leeward vortex on the up-going wing was the primary mechanism driving the wing rock and was responsible for the static restoring moment and the variations in roll damping discussed earlier.

Levin and Katz Wind Tunnel Studies

An investigation by Levin and Katz²⁴ was conducted as a follow-on to the LaRC wind tunnel study²³ to gain further insight into the wing rock phenomenon. They tested two sharp-edged delta wings with leading-edge sweeps of 76° and 80° , corresponding to aspect ratios of 1.0 and 0.71, respectively. The models for these tests were mounted on a sting-balance such that they could rotate freely about the body axes in pure roll (Fig. 13). As a result of this

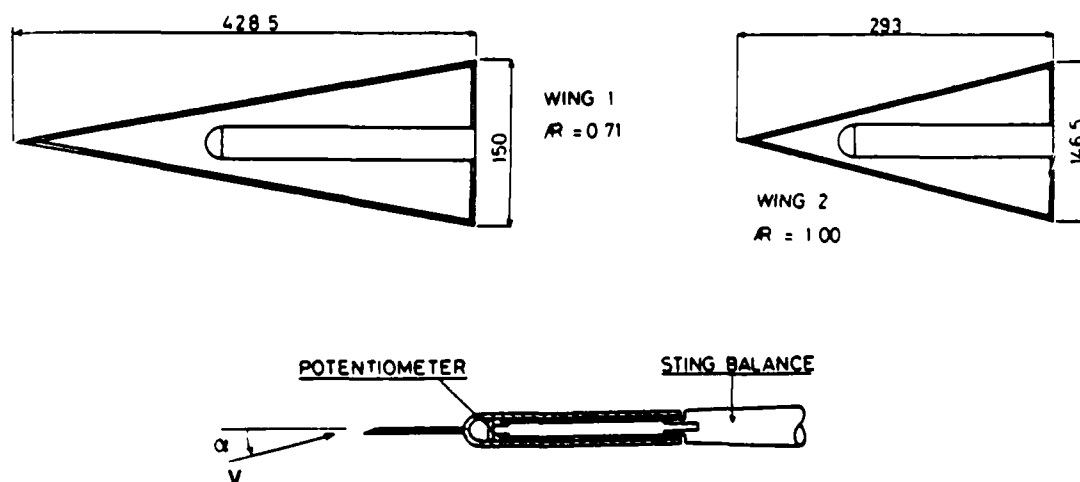


Fig. 13 Free-to-roll models.²⁴

mounting configuration, the models had a large bulge along the centerline of the wing. The study consisted of static tests, free-to-roll tests, and helium bubble flow visualization.

One of the more interesting results from this test series was that the 80° swept wing experienced self-induced oscillations while the 76° wing never did. Even when the 76° wing was perturbed with initial roll angles as high as 40° , wing rock did not occur. This fact was especially notable since the static forces for the two wings were not significantly different. The conclusions from these results were that in order for wing rock to occur under similar Reynolds numbers, bearing friction, and moment of inertia, the aspect ratio must be less than one. Levin and Katz hypothesized that the lower aspect ratio wing had lesser roll damping and was, therefore, more susceptible to wing rock.

These experiments also demonstrate that the 80° delta wing underwent wing rock for angles of attack of 19.5° to 51° (Fig. 14). For angles of attack between 19.5° and 25° , flow disturbances in the wind tunnel alone were not adequate to initiate the limit cycle so the model angle of attack was increased until wing rock started and then decreased to the value where it was to be maintained. At $\alpha > 51^\circ$, any rolling moment caused by a wind tunnel disturbance was quickly damped out and the roll angle returned to its initial value. The maximum roll amplitude

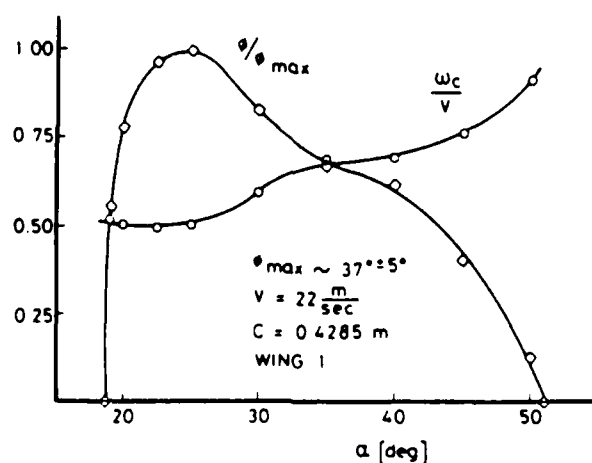


Fig. 14 Wing rock amplitudes and frequency.²⁴

was approximately $\pm 37^\circ$ at $\alpha \approx 25^\circ$. The data also showed that the wing rock frequency of oscillation increased with angle of attack for a given freestream velocity or Reynolds number for $\alpha > 25^\circ$.

Helium bubble flow visualization was used to detect the motions of the vortex cores during limit cycle oscillations. The helium tests showed that vortex breakdown (or burst location) moved with the roll oscillations. As one side of the wing rolled down, the burst point of the vortex on that side moved forward so that it was closest to the apex of the wing near the maximum downward position. The tests also showed that the burst points in the dynamic tests were closer to the apex than the breakdown locations on the stationary wing under the same flow conditions. This difference in burst point locations partially accounted for the fact that the measured normal forces were substantially less during the wing rock tests than in the static measurements.

The study concluded that wing rock occurred when the destabilizing vortex interactions "due to reduced distance between the up-moving semi-span and the leading-edge vortex"²⁴ were sufficient to overcome wing damping moments. Furthermore, the study suggested that the increased damping of the 76° delta wing was enough to prevent self-induced oscillations.

A second study conducted by Levin and Katz²⁵ investigated wing rock tendencies of a 76° swept delta wing with and without a small canard. The roller bearings and potentiometer were modified such that the bearing friction was reduced from the first study. With this reduced friction, the 76° wing experienced wing rock for angles of attack from 25° to 39° , though it never did in the previous investigation. However, a disturbance had to be introduced in the flow field in order to initiate the oscillations for most of the experiments.

The 76° delta wing was also tested with a small 80° delta wing canard mounted ahead of it (Fig. 15). Wing rock was observed for angles of attack of 19° to 44° . The presence of the canard evidently initiated self-induced oscillations with no other flow disturbance. The increased angle of attack range for wing rock was attributed to the two strong vortices generated by the canard and their interaction with the wing. A typical C_L versus ϕ plot (Fig. 16), derived using the same method employed by Nguyen,²³ indicated hysteresis with destabilizing roll damping at small roll angles (clockwise loop) and stabilizing roll damping at larger roll angles (two

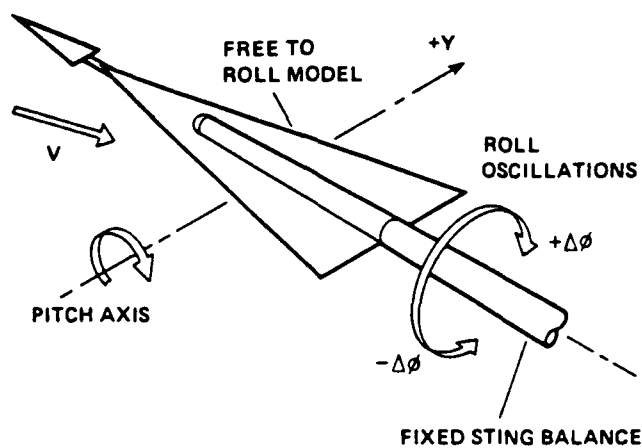


Fig. 15 Canard-delta wing experiment.²⁵

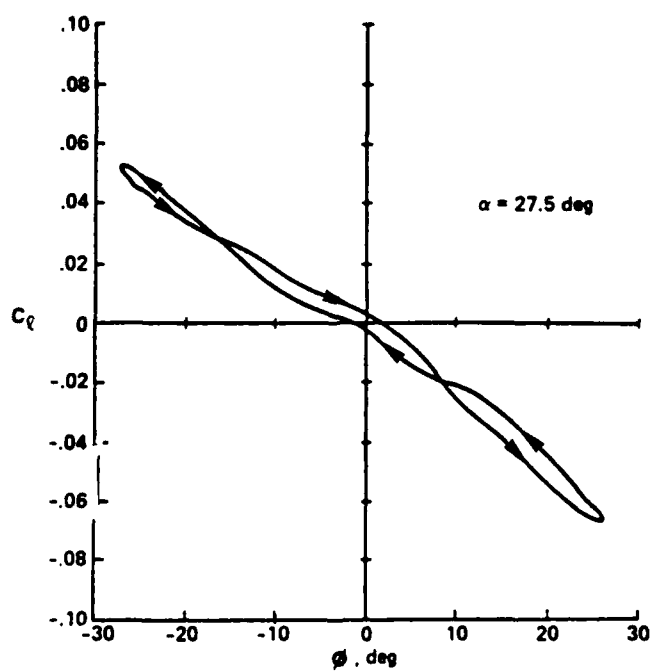


Fig. 16 Rolling moment histogram, $\alpha = 27.5^\circ$.²⁵

counterclockwise loops) during the limit cycle. In addition to symmetrical wing rock oscillations, asymmetrical oscillations existed at angles of attack between 44° and 46° and random small-amplitude oscillations occurred for $47^\circ < \alpha < 51^\circ$ (Fig. 17).

Helium bubble flow visualization showed that the two vortices of the canard and the two vortices from the wing combined into a concentrated vortex pair for the angle of attack range where symmetrical wing rock occurred (Fig. 17). The asymmetric and random oscillations were believed to be due to a much more complex interaction between the four vortices of the canard and wing. These experiments supported the hypothesis that wing rock on slender wings results from the dynamic interactions between the lifting surface and the vortices and the resultant effect on roll damping.

Jun and Nelson Flow Visualization Study

A flow visualization study was conducted by Jun and Nelson²⁶ to analyze dynamic behavior of leading-edge vortices of an 80° swept delta wing undergoing wing rock in a wind

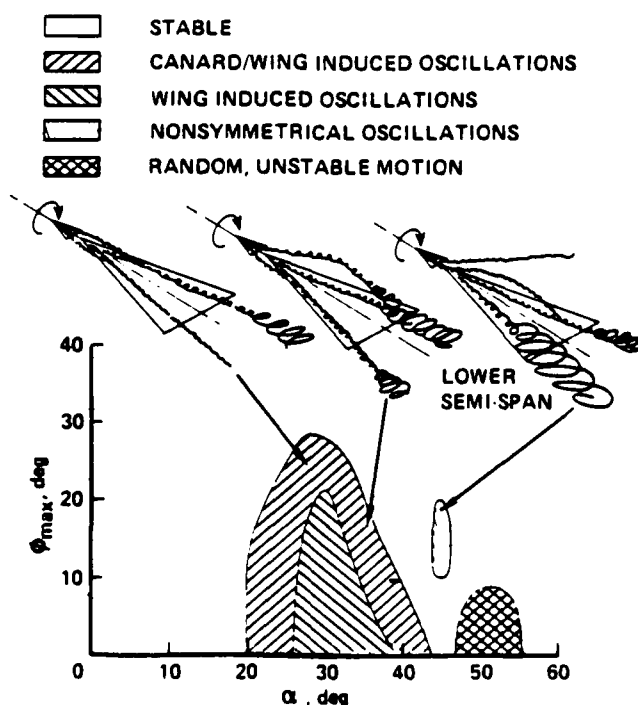


Fig. 17 Region of wing rock.²⁵

tunnel. The vortices were illuminated using smoke and a laser light sheet and thin cross sections were filmed from the rear of the model in the body axis system. The experiments consisted of both static and dynamic tests at a Reynolds number of 315,000 based on the root chord. In all tests, the positions of the vortices were measured at stations located 0.25, 0.5, and 0.75 of the root chord from the apex of the wing. The positions of the vortices with respect to the wing were determined by reducing the high-speed film data (128 frames per second) with a digitizing table connected to a minicomputer.

Static tests provided the vortex positions at angles of attack of 30° , 35° , and 40° at roll angles of 0° to 40° . Fig. 18 shows the static positions of the vortex cores on each side of the wing for $\alpha = 30^\circ$. Note that S in Fig. 18 is the local wing span. As the model rolled in either direction, the leading-edge vortices became asymmetric, with the vortex on the side of the down wing semi-span closer to the surface and more inboard than the opposite vortex. This asymmetry in vortex position with roll angle appeared to create moments necessary to initiate wing rock. At angles of attack of 35° and 40° , vortex breakdown was observed over the wing. The chordwise location of the burst point moved as the roll angle changed.

Dynamic tests were conducted using an apparatus which permitted the model to roll freely about the longitudinal body axis. The tests were performed at zero sideslip and angles of

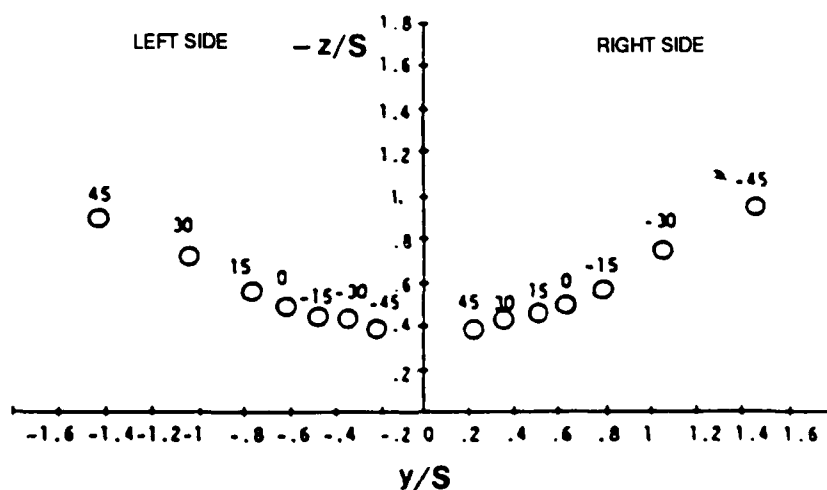


Fig. 18 Static vortex positions, $\alpha = 30^\circ$.²⁶

attack of 30° , 35° , and 40° . Frequency, amplitude, and movement of the leading-edge vortices were determined for the limit cycle oscillations. The frequency of oscillation was 2.17 Hz, corresponding to a reduced frequency of 0.091. For the dynamic tests, vortex positions at a given roll angle differed from the static locations. Additionally, vortex positions depended upon direction of roll. When the wing rolled toward a given vortex, the vortex was closer to the wing than when the wing rolled away from it (Fig. 19). The data clearly showed the dependency of vortex position on roll angle and direction of motion. This hysteresis in the vortex location underscored a lag in the flow field due to wing oscillations and vortex interactions. The study concluded that movement of the vortices during the rolling motion caused a change in the rolling moment which reversed the direction of motion. It was this dynamic interaction between the vortices and the wing which generated and sustained wing rock.

Computational and Analytical Studies

The results presented in the preceding discussions comprise the major experimental investigations of wing rock reported in the literature. These measurements have not only resulted in various interpretations as to the cause of wing rock, but have also been compared with

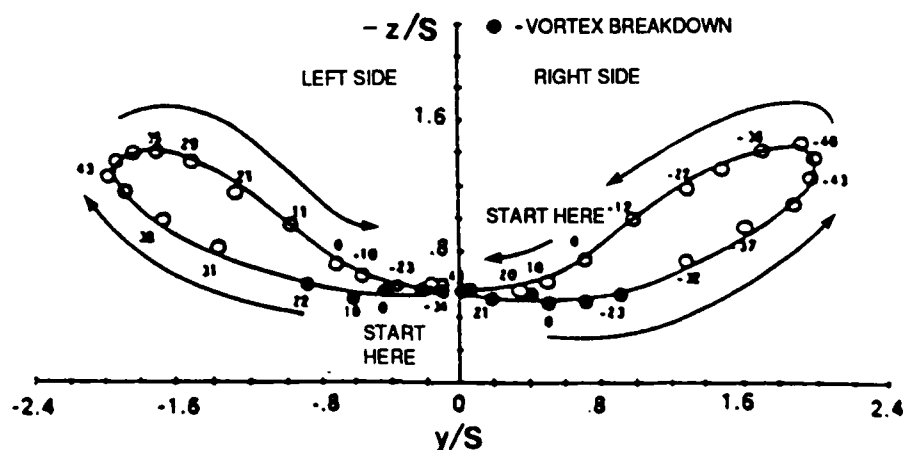


Fig. 19 Vortex positions during wing rock, $\alpha = 40^\circ$.²⁶

computational results. Additionally, information obtained in these studies has helped formulate simple mathematical models used to approximate wing rock limit cycles. This section highlights the key computational and analytical efforts performed to simulate and understand wing rock. The major contributions include a numerical simulation developed by Konstadinopoulos, Mook, and Nayfeh,^{27,28} a single degree-of-freedom mathematical model refined by Hsu and Lan,^{29,30} an analysis by Schmidt,³¹ and fluid mechanic analyses by Ericsson.^{32,33,34,35,36}

Numerical Simulation

The most sophisticated computational investigation of wing rock in slender delta wings was performed by Konstadinopoulos, Mook, and Nayfeh.^{26,27} They conducted a numerical simulation of the experiments conducted by Nguyen, Yip, and Chambers²³ and Levin and Katz.²⁴ They simultaneously simulated the time histories of the delta wing motion and the flow field. Aerodynamic loads were computed with an unsteady vortex-lattice method and the equation of motion was integrated with a predictor-corrector scheme to provide wing motions.

The analysis examined an 80° delta wing with an axis of rotation either below or on the centerline of the model as tested in the studies of Nguyen and Levin and Katz, respectively. The equation of motion used in the study had the form

$$I_{xx} \ddot{\phi} = \left(\frac{1}{2} \rho c S V^2 \right) C_{\ell} - \mu \dot{\phi} \quad (2)$$

where c was the root chord, S the planform area, V the freestream velocity, C_{ℓ} the aerodynamic rolling moment coefficient and μ the friction coefficient which accounted for damping in the bearings of the free-to-roll apparatus. The method treated the wing and the wake adjoining its leading and trailing edges as a sheet of vorticity, while the wing was modeled as a bound vortex and the wake as a free vortex. Given initial conditions and the motion of the wing, calculations marched forward in time to compute both the generalized aerodynamic forces on the wing and a description of the wake.

The numerical results were compared to data from two experimental studies.^{23,24} In both cases, the level of agreement between numerical calculations and experimental results depended strongly upon the choice of the friction coefficient. Once a proper choice of bearing friction had been made, calculations agreed well with experimental data for angles of attack below 30° . The authors claimed that at $\alpha \geq 30^\circ$, vortex bursting observed in the experiments led to significant disagreement between the numerical and experimental results since the numerical algorithms did not include vortex bursting.

Konstadinopoulus, Mook, and Nayfeh^{26,27} described a wing rock cycle based on the calculated positions of the leading-edge vortices from the simulation. At small roll angles, the motion of the wing caused the upward-moving semi-span to compress the vortex system and the downward-moving side to stretch it. The spanwise positions of the cores changed very little during this process. As a result, the vorticity caused a larger velocity on the upward-moving side which created a rolling moment in the direction of motion. This destabilizing moment favored a continuation of the rolling. As the roll angle increased, the compressed vortex moved outboard and the stretched system moved inboard due to a change in the incoming velocity. As the compressed vortex was blown outboard, the tangential velocity component on the wing was reduced while the normal velocity component, downwash, increased. This increase in downwash reduced the effective α , resulting in a loss of lift and a stabilizing moment. The stabilizing moment reversed the direction of rotation and perpetuated the wing rock. Their simulation also showed that hysteresis in vortex positions caused a hysteresis in rolling moment variation with roll angle (Fig. 20).

Hsu and Lan Mathematical Model

As opposed to the complex computer code discussed above, relatively simple mathematical models have been developed which reasonably predict both the frequency and amplitude of wing rock for slender delta wings, given estimates of the aerodynamic derivatives. Hsu and Lan^{29,30} developed one and three degrees-of-freedom models based on the Beecham-Titchener asymptotic method.³⁷ Of particular interest to the present research was their single

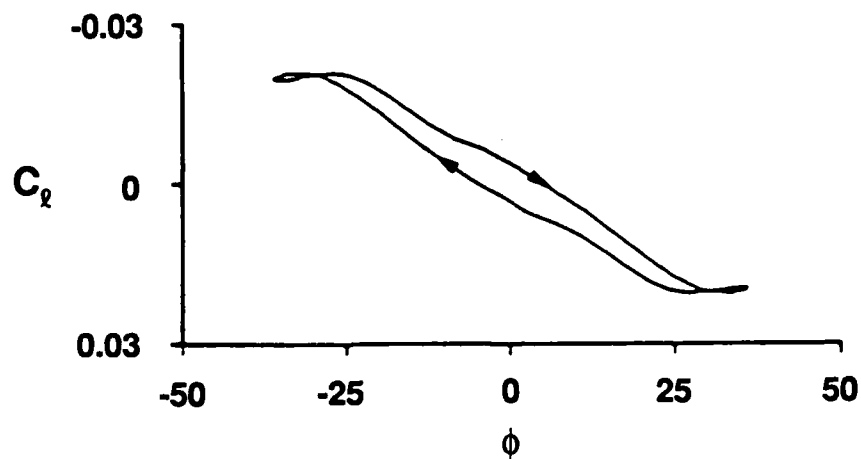


Fig. 20 Rolling moment versus roll angle.²⁷

degree-of-freedom model. Their model was similar to one presented by Nguyen, Yip, and Chambers²³; however, Hsu and Lan included a variation in roll damping with roll rate, $C_{\ell_{pp}}$, in the representation of the rolling moment. The function used in the mathematical model was

$$C_{\ell} = C_{\ell_0} + C_{\ell_{\beta}} \beta + C_{\ell_p} \bar{p} + C_{\ell_{\delta_A}} \delta_A \quad (3)$$

where

$$C_{\ell_p} = C_{\ell_{p0}} + C_{\ell_{p\beta}} |\beta| + C_{\ell_{pp}} |\bar{p}| \quad (4)$$

Equations (3) and (4) were combined with equation (1) to derive an expression for the frequency and amplitude of wing rock using the Beecham-Titchener approach. The frequency and amplitude relationships obtained were

$$\Omega = \left[-\frac{\bar{q} S b}{I_{xx}} \sin \alpha_s C_{\ell_{\beta}} \right]^{1/2} \quad (5)$$

and

$$A = -\frac{3\pi}{4} \frac{C_{\ell p0}}{\sin \alpha_s C_{\ell p\beta} + \frac{\Omega b}{V} C_{\ell pp}} \quad (6)$$

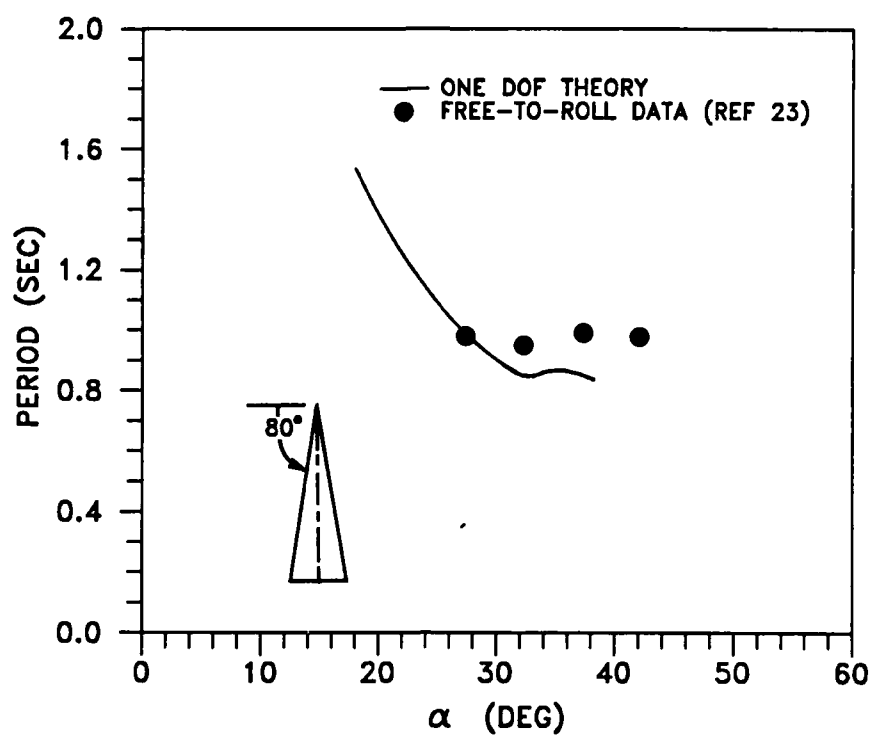
where Ω is the frequency in radians per second and A is the amplitude in radians. Equations (5) and (6) are verified in Appendix A; however, the current study included bearing friction in the equation of motion, which resulted in the amplitude equation (A70) instead of equation (6). Note that if $\mu = 0$ in equation (A70), it is identical to equation (6). The inclusion of friction did not change the frequency result, so equation (5) is the same as equation (A68).

Success in accurately predicting frequency and amplitude was dependent upon the proper choice of the averaged aerodynamic derivatives, $C_{\ell\beta}$, $C_{\ell p0}$, $C_{\ell p\beta}$, and $C_{\ell pp}$. Hsu and Lan obtained $C_{\ell\beta}$ from experimental data and calculated the remaining derivatives using a computer code developed by Lan.^{38,39} The code included corrections in the derivatives meant to account for vortex bursting and provided converged solutions up to $\alpha = 38^\circ$. Comparisons of the mathematical model approximations for wing rock period and amplitude with experimental data indicated reasonable to good agreement (Fig. 21). A typical simulation of the rolling moment versus roll angle history revealed reasonable agreement with experimental results from Nguyen, Yip, and Chambers²³ (Fig. 22).

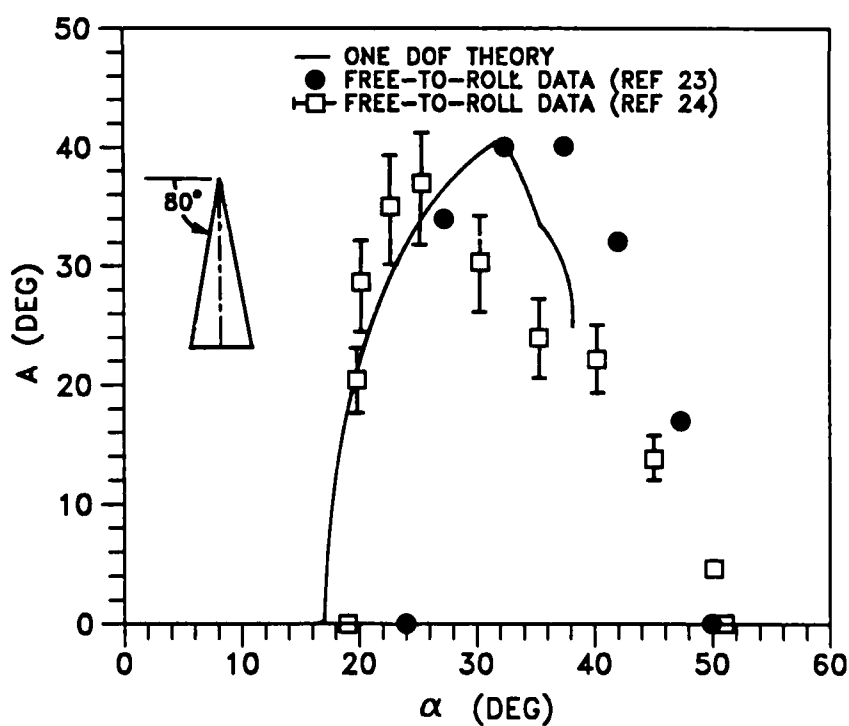
Examination of the nonlinear roll damping derivative, $C_{\ell p}$, in equation (4), indicated that the damping was unstable at small roll angles and stable at large roll angles (Fig. 23). The study concluded that it was this nonlinear variation in roll damping which sustained the steady state wing rock experiments.

Aerodynamic Hysteresis

Schmidt³¹ showed that aerodynamic hysteresis described by a relay action can produce limit cycles like those of wing rock. Schmidt modeled the rolling moment as



a)



b)

Fig. 21 Predicted versus experimental results for 80 delta wing: a) wing rock periods, and b) wing rock amplitudes.³⁰

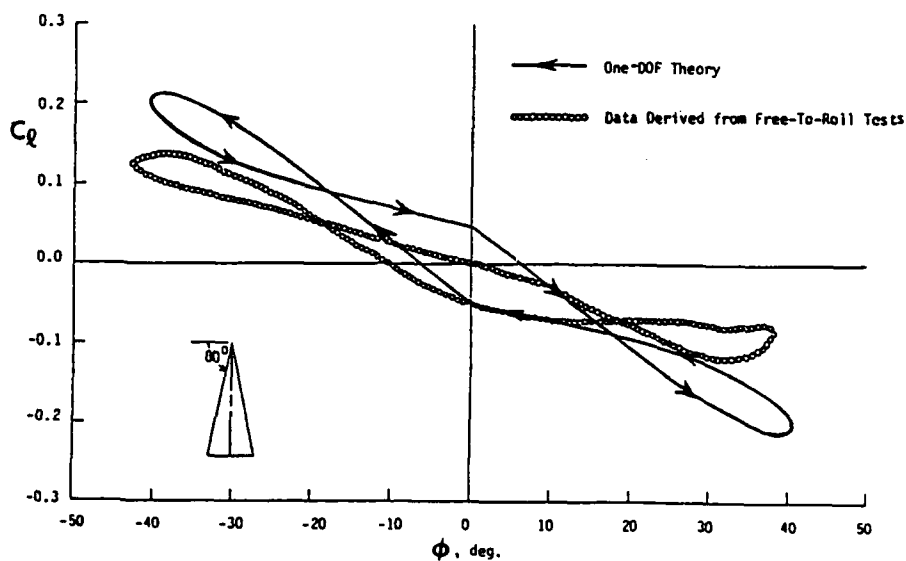


Fig. 22 Rolling moment versus roll angle comparisons.³⁰

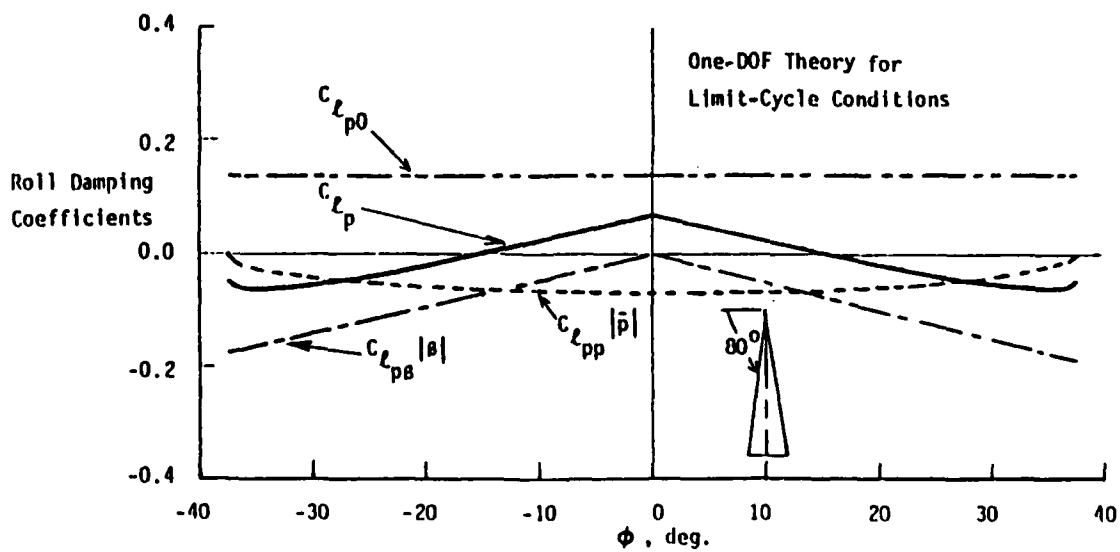


Fig. 23 Roll damping coefficients versus roll angles.³⁰

$$C_{\ell}(\beta) = C_{\ell\beta} \beta + \Delta C_{\ell} \operatorname{sgn}(\dot{\beta}) \quad (7)$$

where $\Delta C_{\ell} \operatorname{sgn}(\dot{\beta})$ causes the value of the rolling moment at a given β (or ϕ) to be a function of the direction of motion (Fig. 24). Schmidt claimed that this nonlinearity in rolling moment sustained steady state wing rock. Other studies have also stated that aerodynamic hysteresis in rolling moment needs to be included in mathematical models describing the limit cycle oscillations.⁴⁰ While Schmidt's analysis indicated the ability to produce wing rock with aerodynamic hysteresis, he did not suggest an explanation related to fluid motion for the cause of the hysteresis.

Fluid Mechanic Analysis of Wing Rock

A detailed explanation of the cause of wing rock based on fluid dynamics was developed and presented in a series of papers by Ericsson.^{32,33,34,35,36} He showed that wing rock was caused by an asymmetry in the leading-edge vortices based on a comprehensive review and analysis of the experimental studies of Nguyen, Yip, and Chambers²³ and Levin and Katz.²⁴ His analysis was based on delta wing results of Polhamus⁴¹ which related vortex asymmetry and vortex breakdown to α and the apex half angle of the wing, Θ_A (Fig. 25). To analyze the effects of sideslip angle and roll angle, he formulated an effective apex half-angle, $\bar{\Theta}_A$, for the left and right wing semi-spans. He obtained the expressions (for $\Theta_A \leq 15^\circ$ and $\beta \leq 15^\circ$)

$$\bar{\Theta}_A = \Theta_A + \Delta\Theta_A \quad (8)$$

where

$$(\Delta\Theta_A)_{R,L} = \pm \tan(\alpha_O) \sin \phi \quad (9)$$

or

$$(\Delta\Theta_A)_{R,L} = \pm \beta / \cos(\alpha_O) \quad (10)$$

where the \pm signs refer to the right and left wing semi-spans, respectively.

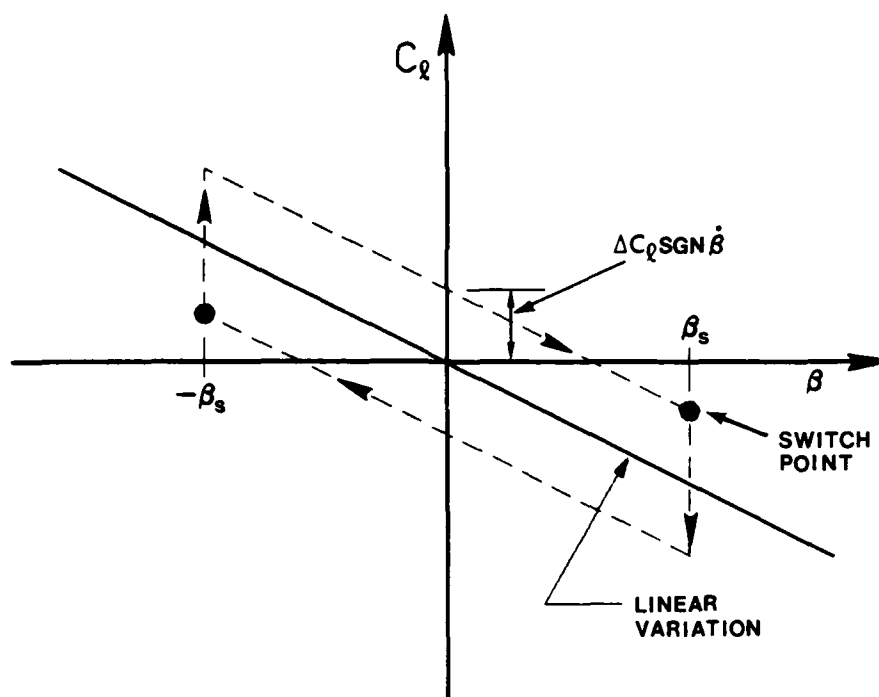


Fig. 24 Aerodynamic roll moment hysteresis.³¹

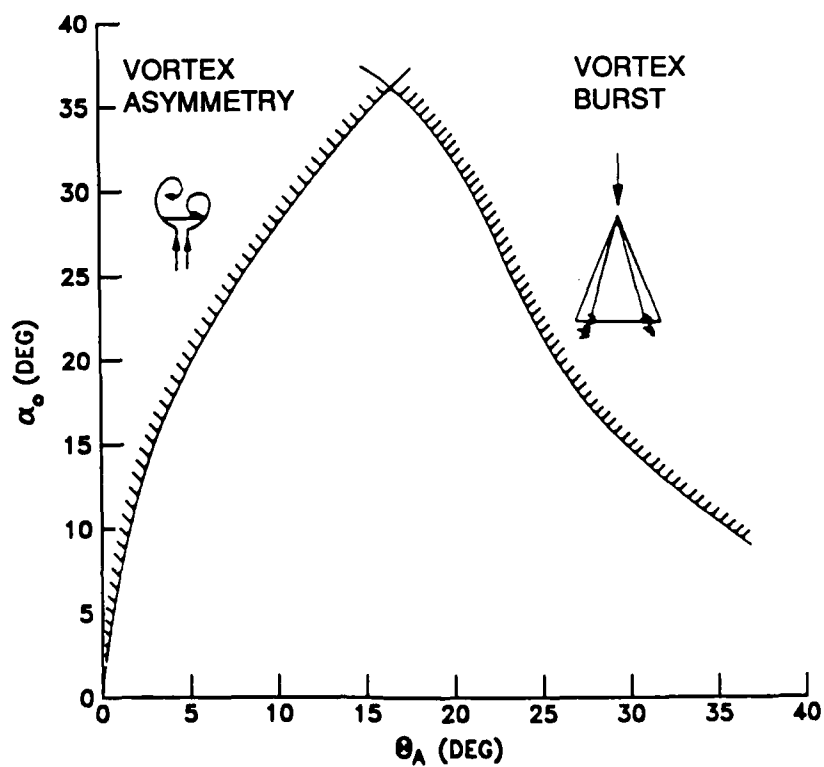


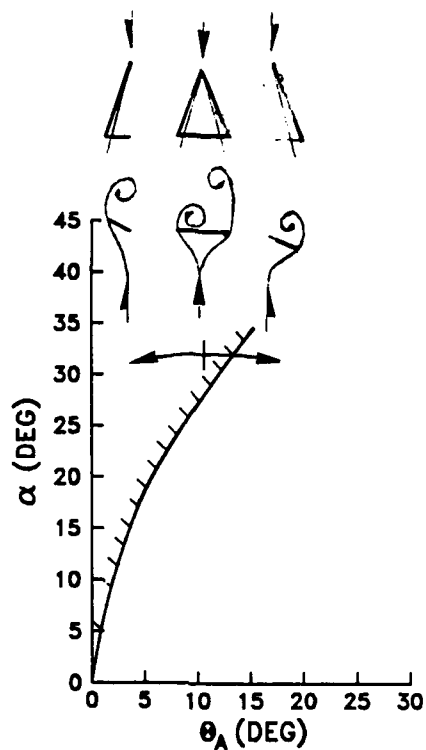
Fig. 25 Boundaries for vortex asymmetry and vortex burst.^{32,41}

Ericsson used Fig. 26 to provide an explanation of wing rock based on fluid mechanics. At a given α - θ_A combination where vortex asymmetry was experienced, the wing semi-span with the lifted-off vortex lost lift and dipped down rotating about the roll axis. As the roll angle increased, the effective apex angle $\bar{\theta}_A$ increased, as shown by equations (8) and (9), and the vortex reattached to the wing (Fig. 26a). The reattached vortex generated an increased lift providing the restoring rolling moment needed to reverse the direction of motion. As a result of a convective time lag, the wing remained dynamically unstable in roll until the limit cycle amplitude was reached.

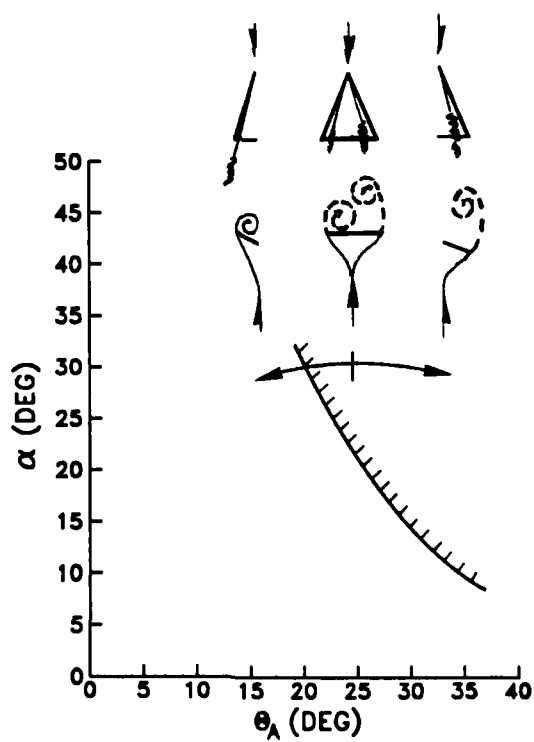
Additionally, Ericsson used Fig. 26b to show that vortex burst cannot cause wing rock. If asymmetric vortex bursting exists on the wing, the wing semi-span with the most forward burst point must lose lift and drop down, resulting in an increase in the effective apex angle. The increased apex angle would cause the wing semi-span to drop further into the vortex burst region, without generating the restoring moment needed for a limit cycle oscillation. At the same instance, the opposite semi-span must move out of the vortex burst region due to the decreased semi-apex angle. This movement results in an increased lift which favors roll divergence instead of wing rock. Ericsson concluded that while vortex bursting does not cause wing rock, its presence does affect the amplitude of the limit cycle. In fact, Ericsson postulated that vortex bursting actually limits the maximum wing rock amplitude as the angle of attack is increased.³⁴ He stated that while asymmetric leading-edge vortices initiate the limit cycle oscillations of slender delta wings, most conventional aircraft wing rock results from asymmetric vortices originating from the slender forebody.^{33,36} While it is asymmetric vortex shedding from the forebody which initiates wing rock, it is the interaction of these vortices with the wings which sustains the limit cycle.

Summary

This chapter has reviewed previous wing rock research. Flight test data, subscale testing, and analytical studies have provided insight into potential causes of wing rock; however,



a)



b)

Fig. 26 Effects of apex half angle on wing rock: a) vortex asymmetry, and b) vortex burst.³²

considerable disagreement still exists on the primary mechanism driving the limit cycle oscillations. A number of studies observed that unstable roll damping existed at the onset of wing rock; however, they provided little information as to the cause of it. Nguyen²³ and Hsu³⁰ both hypothesized that the oscillations resulted from unstable roll damping at small roll angles and stable damping at large roll angles. Nguyen also indicated that the change in damping was directly related to the movement of the leading-edge vortices, but did not have sufficient flow visualization to prove it. Levin and Katz²⁴ stated that the positions of the leading-edge vortices were important in wing rock, though they also lacked detailed information on the movement of the vortices. Ericsson provided a fluid dynamic explanation, showing that wing rock was produced by alternate lift-off and reattachment of the vortices. Jun and Nelson quantified the positions of the vortices at several chordwise locations, but did not have dynamic information on the motion of model, so no information on rolling moments was available. Schmidt postulated that rolling moment hysteresis with roll angle generated wing rock, but provided no explanation for the cause of the hysteresis. So while the various studies have shown the existence of unstable roll damping at wing rock onset, the presence of hysteresis, asymmetry in the leading-edge vortices, and the occurrence of vortex bursting, none have conclusively determined the cause of the periodic oscillations.

While a considerable amount of piecemeal information exists, none of the experimental studies simultaneously quantified the motion of the wing or aircraft and the leading-edge vortices throughout the entire wing rock cycle. Since previous research efforts have postulated that vortices are important in initiating and sustaining wing rock, the need to correlate movement of the vortices with vehicle motion clearly exists. It is this lack of information and the acquisition of a unique tool for measuring fluid and rigid body motion which motivated the current study. The following chapter summarizes the project and describes the experimental hardware and data acquisition system.

CHAPTER III

EXPERIMENTAL EQUIPMENT AND TEST PROCEDURES

Rationale for Experimental Approach

As summarized at the end of Chapter II, previous experiments and computations have led to observations regarding wing rock that are not totally consistent. Analytical studies²⁷⁻³⁶ have shown that wing rock can be produced by either static nonlinear aerodynamics, loss of roll damping, or aerodynamic hysteresis. Experimentalists²³⁻²⁶ have concluded that limit cycle oscillations are closely related to the dynamics of the leading-edge vortices and the effects they have on roll damping. While the experimental studies obtained information on either wing dynamics or the position of the vortices during wing rock, none have quantified both motions simultaneously. Considering the observed relationship between the dynamic behavior of the vortices and the model motion itself, the current study was designed to fill that void in the data base and, thereby, more fully understand the mechanisms driving the limit cycle oscillations. This rather ambitious objective provided the motivation for using a video-based motion analysis scheme, ExpertVision,^{1,42} to analyze wing rock.

ExpertVision allowed the motion of multiple objects captured on videotape to be digitized for detailed analysis on a minicomputer using internal software or user-developed programs. This nonintrusive technique permitted the relative movement of the leading-edge vortices and the oscillating model to be determined during wing rock tests in a water tunnel. A detailed wind tunnel study was also performed on the same 80° delta wing undergoing self-induced oscillations; however, quantified flow visualization of the vortex motion was not obtained. In addition to the free-to-roll wing rock tests, vortex flows over 70° and 80° were characterized under stationary and forced oscillation conditions. These tests not only expanded the data base on such wings, but also validated the use of ExpertVision. This research was the first known use of ExpertVision to quantify fluid trajectories. Therefore, this report documents successful use of video imaging to simultaneously sense fluid and model dynamics in water tunnel experiments.

This chapter describes the experimental hardware, facilities, and data acquisition and reduction system used in the study. It also discusses the overall research approach and outlines the procedures employed.

Overview of Experiments

The experimental data obtained in this research effort consisted of both water tunnel and wind tunnel tests conducted in three separate test series performed over an eighteen month period of time. The first test series examined 70° and 80° delta wings under stationary and forced oscillation conditions in the water tunnel with the primary objective of either validating or repudiating the use of ExpertVision for studies of this type. Leading-edge vortices were visualized in the water tunnel by injecting black dye into the vortex cores at the apex of the wing. The second series consisted of water tunnel tests on the same two models under stationary and forced oscillation conditions using newly acquired 200 Hz high speed video cameras instead of the 60 Hz cameras used in the first series. This series also included free-to-roll tests on the 80° delta wing at $\alpha = 35^\circ$ and at flow velocities of 4, 6, and 10 inches per second (ips). Wing rock data were collected at this point in the effort since the capability to track model motion and vortex movement had been successfully demonstrated in previous forced oscillation tests. The third set of experiments consisted of free-to-roll tests in the wind tunnel using the same 80° delta wing model. These tests analyzed model dynamics over a wide range of angles of attack and dynamic pressures. Some flow visualization was attempted using a smoke wand; however, only a limited amount of qualitative information was obtained.

Models and Test Facilities

Test Models

Two delta wing models with leading-edge sweep angles of 70° and 80° were fabricated and tested (Fig. 27). Each model had a root chord of 10 inches and a single 20° bevel cut from the lower leading edges. The models were constructed from one-eighth inch aluminum and were instrumented with dye ports on each side of the apex of the delta wing. The models were painted

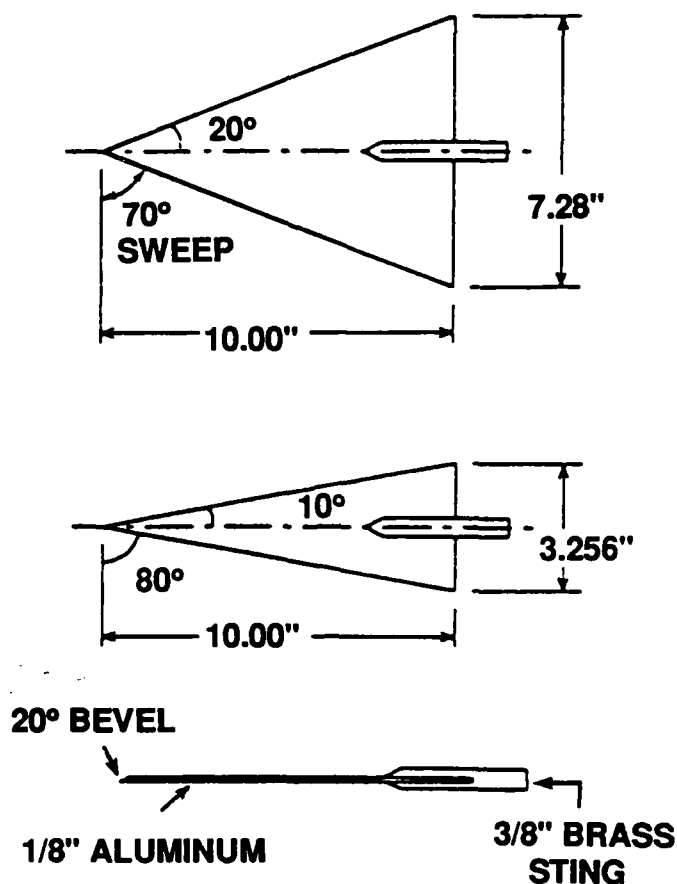


Fig. 27 Delta wing models.

flat gray to achieve good contrast with the black dye pulses and streams used for flow visualization. Three reference dots were also painted on the models for scaling of the video-measured distances. A small pin with a one-eighth inch diameter black head was attached to each wing tip for the forced and the free-to-roll dynamic tests to allow tracking of the model during the roll oscillations.

Water Tunnel Facility

The water tunnel tests were conducted in the Eidetics International Visual Aerodynamics Division 1520 Flow Visualization Water Tunnel.^{43,44} The facility is a continuous horizontal flow tunnel with a test section 20" high x 15" wide x 60" long (Fig. 28). The test section was

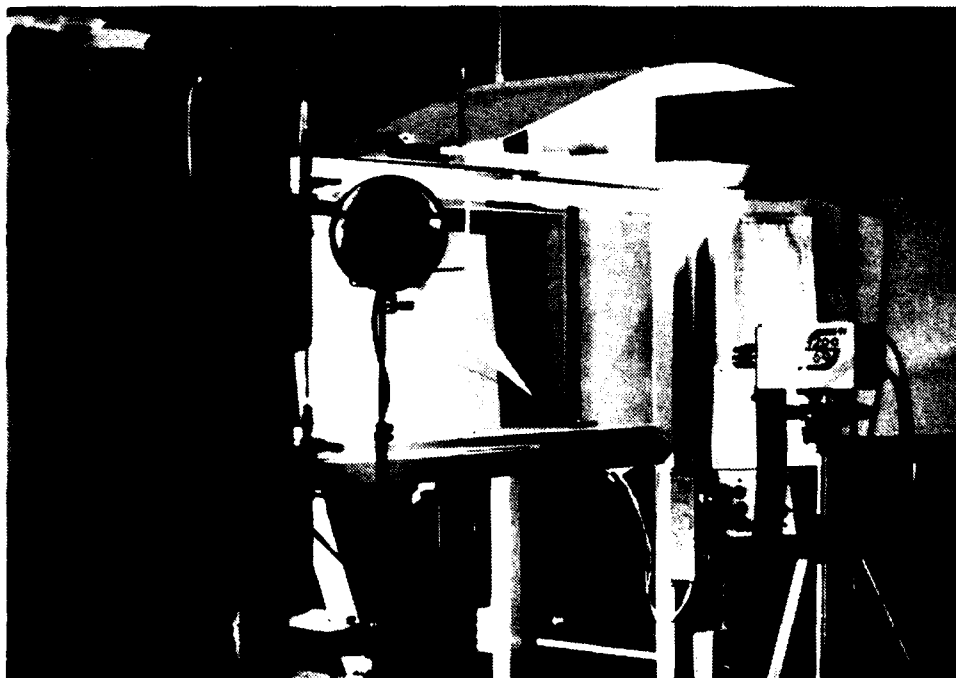


Fig. 28 Water tunnel facility.

constructed of tempered glass permitting both the side and planform of the model to be viewed. Test section flow velocities were varied from 0 to 10 ips. All stationary and forced oscillation tests were run at a freestream velocity of 4 ips ($Re = 3 \times 10^4/ft$), while free-to-roll tests ranged from 4 to 10 ips (corresponding to a Reynolds number of $3 \times 10^4/ft$ to $7.5 \times 10^4/ft$). In stationary and forced oscillation tests, models were mounted in an inverted position (Fig. 29) on a forced-roll oscillation apparatus (Fig. 30) capable of providing roll amplitudes of $\pm 50^\circ$, and frequencies from 0 to 0.22 Hz. For stationary tests, the model was locked in place. The mount was attached to an adjustable turntable which allowed yaw angle, β_T , variations of $\pm 30^\circ$. The angle of attack was adjustable up to 60° . For wing rock tests, the 80° model was mounted inverted in the tunnel (Fig. 31) to a bracket containing two concentric steel ring bearings (Fig. 32). With this mounting arrangement, the model was free-to-roll about its longitudinal body axis.

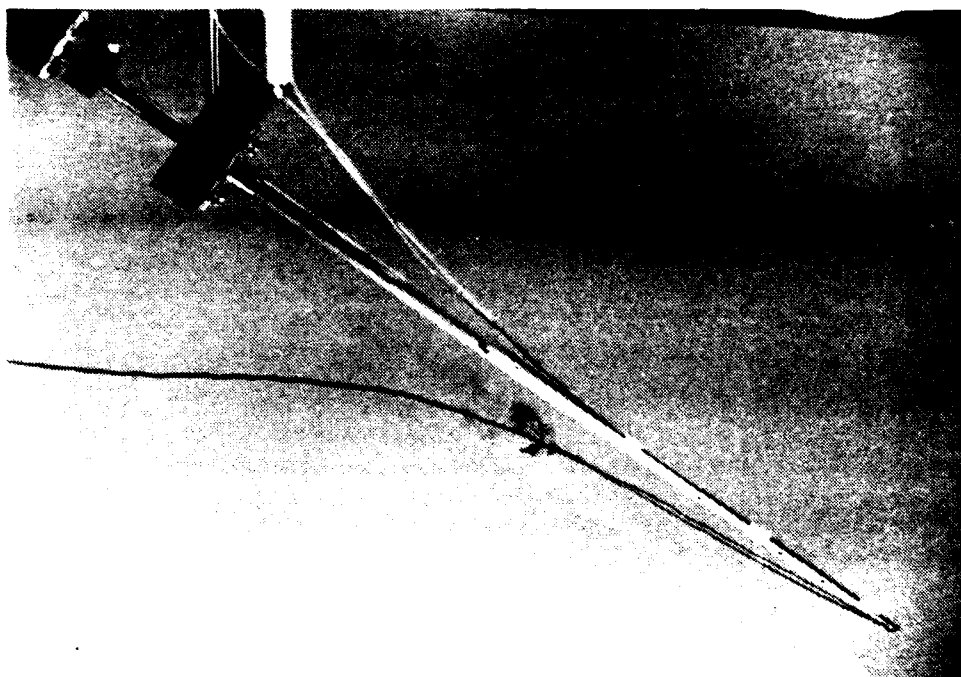


Fig. 29 Delta wing mounted to forced-roll oscillation apparatus.

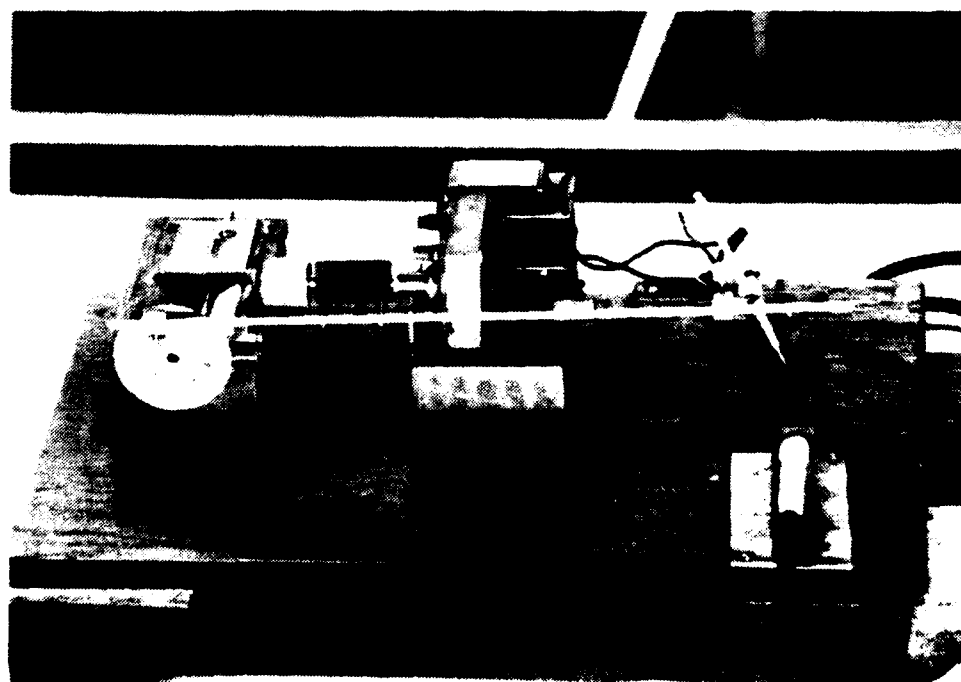


Fig. 30 Forced-roll oscillation drive apparatus.

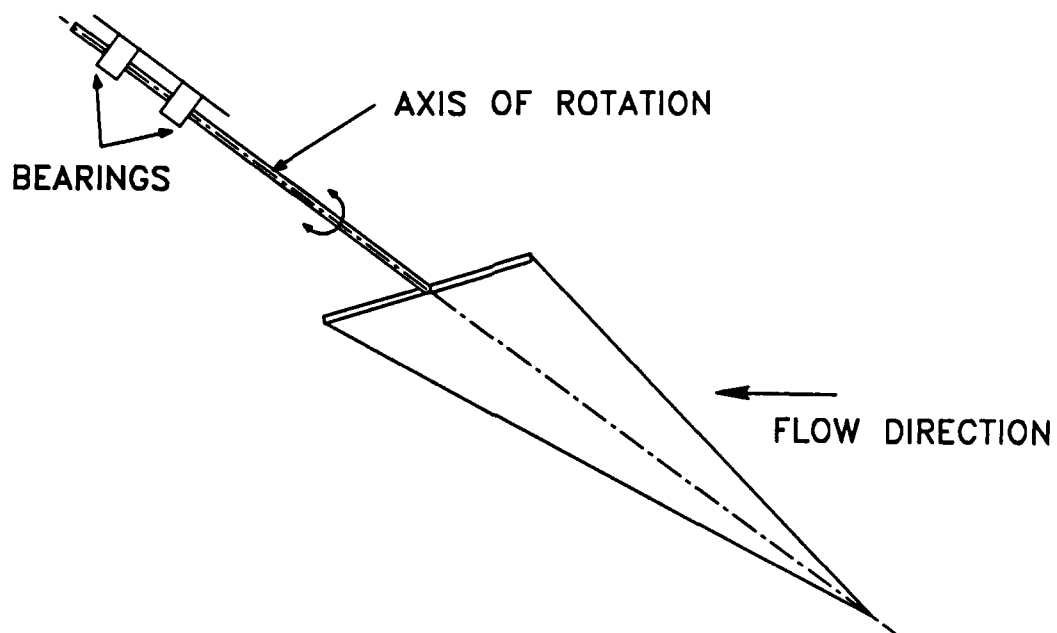


Fig. 31 Free-to-roll model mounting arrangement.

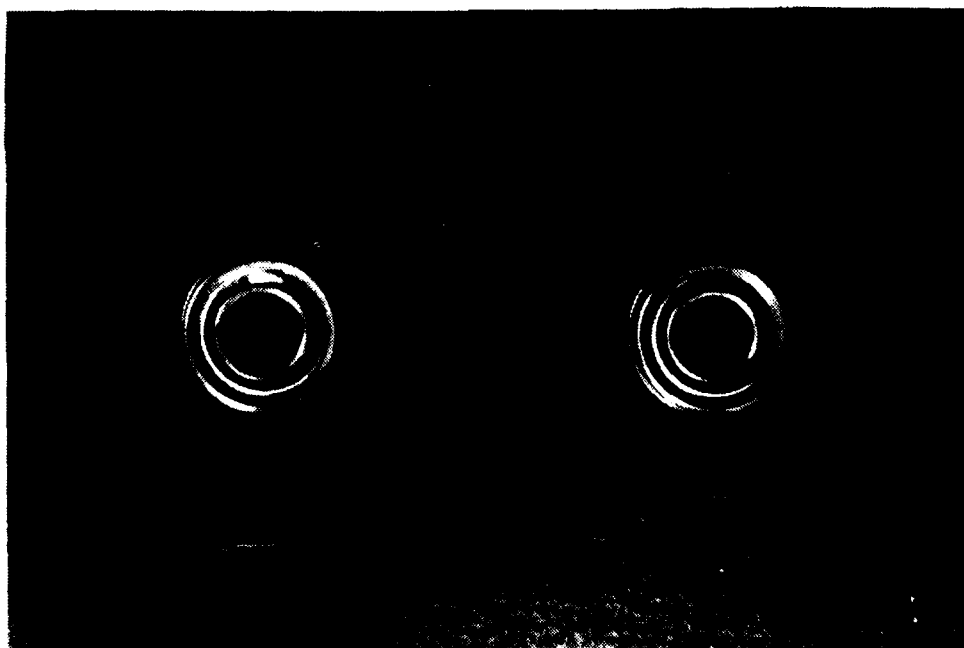


Fig. 32 Free-to-roll bearings.

The Eidetics water tunnel had its own dye system for visualizing the vortices. System pumps delivered various colors of dye to the model in the test section through Tygon feed lines. While a solenoid valve was designed and built for pulsing the dye, manually squeezing and releasing the pliable feed lines provided reliable and repeatable dye packets.

Providing adequate contrast between the model, the background, and the black dye highlighting the leading-edge vortices was essential to the success of ExpertVision. Matte gray models with black reference dots provided excellent contrast with black dye in the leading-edge vortices. A suitable background for videotaping was a photographically neutral (18% gray) poster board. This simple background provided a slight contrast with the model and allowed an excellent view of dye streams or pulses. Lighting was one of the most critical aspects of the tests and considerable time was spent in adjusting both intensity and incidence angles. Unfortunately, it was highly configuration-dependent and had to be readjusted at each new α and β_T . It was especially difficult to maintain a satisfactory contrast level during dynamic tests since the lighting varied as the model rolled. Most of the set-up time was spent in obtaining adequate contrast levels; however, failure to have done so would have made accurate data reduction impossible.

Wind Tunnel Facility

A third test series was performed in the Texas A&M Low Speed Wind Tunnel,⁴⁵ a closed circuit, single return system with a 7' wide by 10' high by 12' long high-test section (Fig. 33). Plexiglass and glass windows permitted videotaping of the side and planform views of the model. A newly developed robotic sting allowed α variations from 0° to 90° to be controlled by a personal computer and software in the control room of the wind tunnel (Fig. 34). As the angle of attack was changed, the sting readjusted its position to keep the model roughly in the center of the test section. A turntable, built into the bottom of the floor, allowed the model to be rotated in yaw.

The wind tunnel produced dynamic pressures of up to 100 pounds per square foot (psf) or flow velocities of up to 290 feet per second (fps). Dynamic pressures could be resolved to ± 0.05 psf. The current study was performed at dynamic pressures of 0.5 psf to 10 psf, (Reynolds

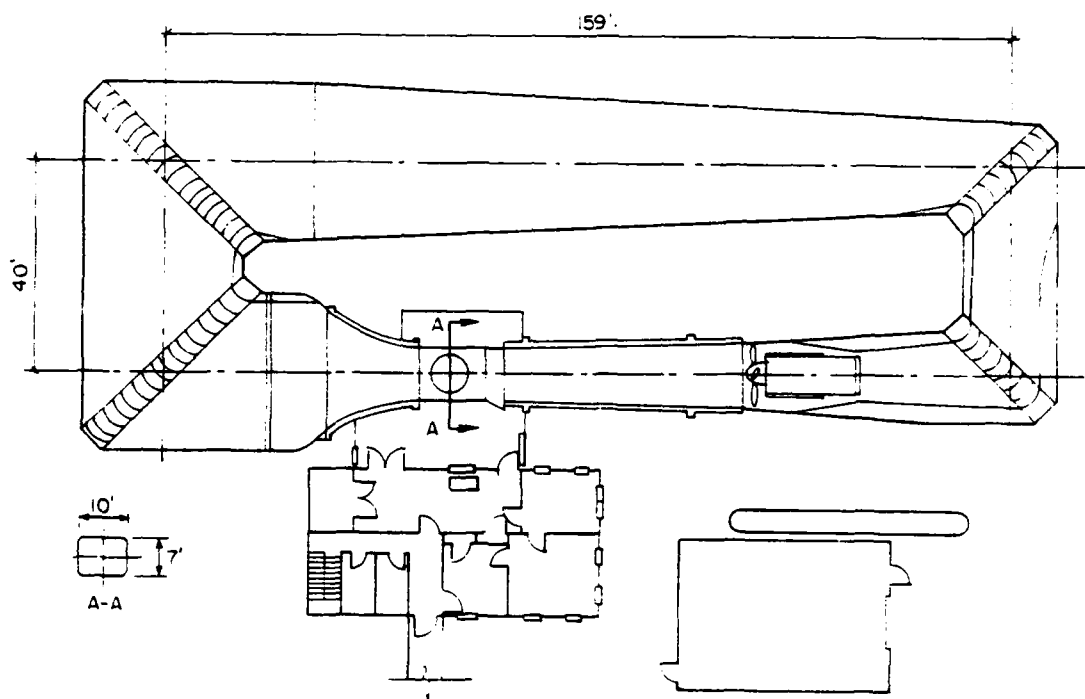


Fig. 33 Wind tunnel facility diagram.⁴⁵

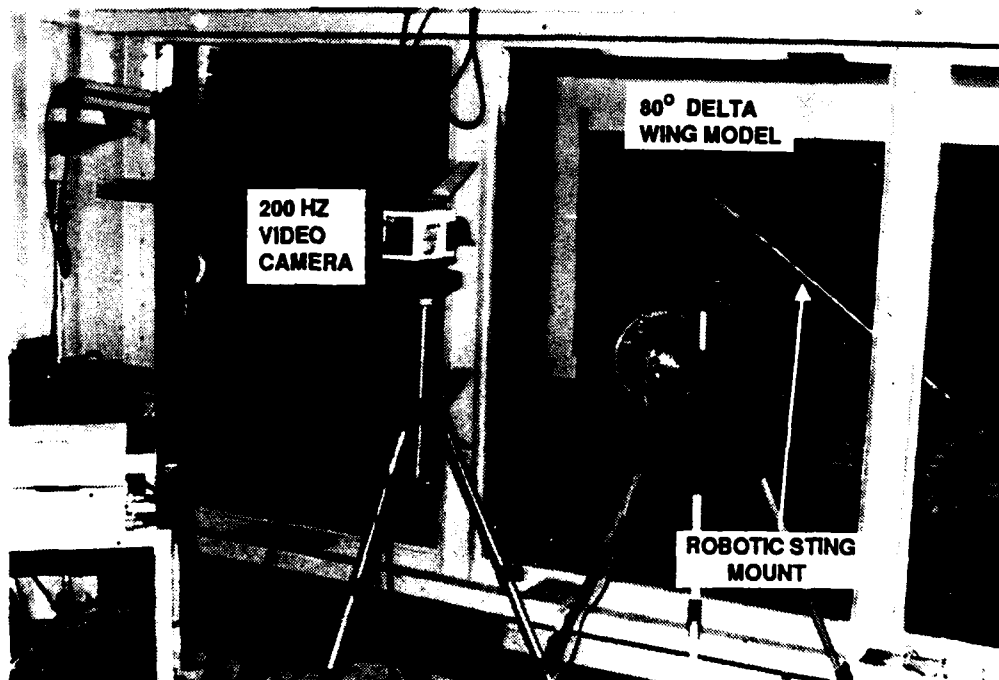


Fig. 34 Wind tunnel experimental set-up.

numbers of 1.09×10^5 to 4.86×10^5). Lower dynamic pressures were attempted in order to match the upper water tunnel Reynolds number; however, wing rock could not be sustained. A smoke generator and various wands were available in the wind tunnel for visualizing local flow regions. Unfortunately, only a limited amount of flow visualization of the leading-edge vortices was obtained. The testing provided some gross information on movement of the vortices; however, no results on vortex positions and burst points were quantified.

A special free-to-roll apparatus was fabricated at the Texas A&M University Flight Mechanics Laboratory for the wind tunnel wing rock tests. The fixture housed the same two bearings used in the water tunnel study (Fig. 32) and adapted to the end of the robotic sting (Fig. 35). The assembly permitted easy removal, cleaning, and lubrication of the bearings.

Data Acquisition and Reduction System

The data acquisition and reduction system used in this research effort was ExpertVision (EV),^{1,42} developed by the Motion Analysis Corporation. ExpertVision is a general purpose video-based motion analysis system which acquires, digitizes, processes, and displays the motion characteristics of selected subjects. The version of EV used for this study captured and analyzed data in two dimensions, requiring at least two near-orthogonal camera planes to provide information in all three dimensions. The manufacturer advertised that the system could track over 200 passive targets simultaneously. Once target data were digitized and stored on the Sun minicomputer, they could be interactively examined, edited, analyzed, and plotted using the customized software that is part of EV. The system configuration used included two video cameras, at least two video recorders, a high resolution monitor, the proprietary VP-110 video processor, a Sun minicomputer, the installed ExpertVision software, and a dot matrix printer/plotter (schematic shown in Fig. 36).

Video Cameras and Recorders

Two different sets of video cameras were used in the course of the research. During the first water tunnel test series, experiments were videotaped with two RCA video cameras

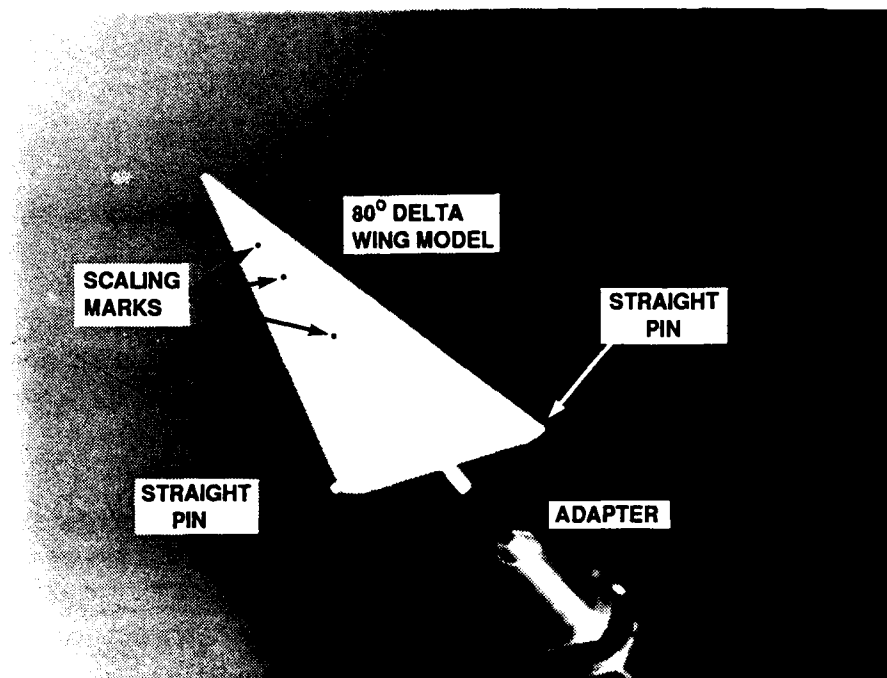


Fig. 35 Free-to-roll apparatus and mounting adapter.

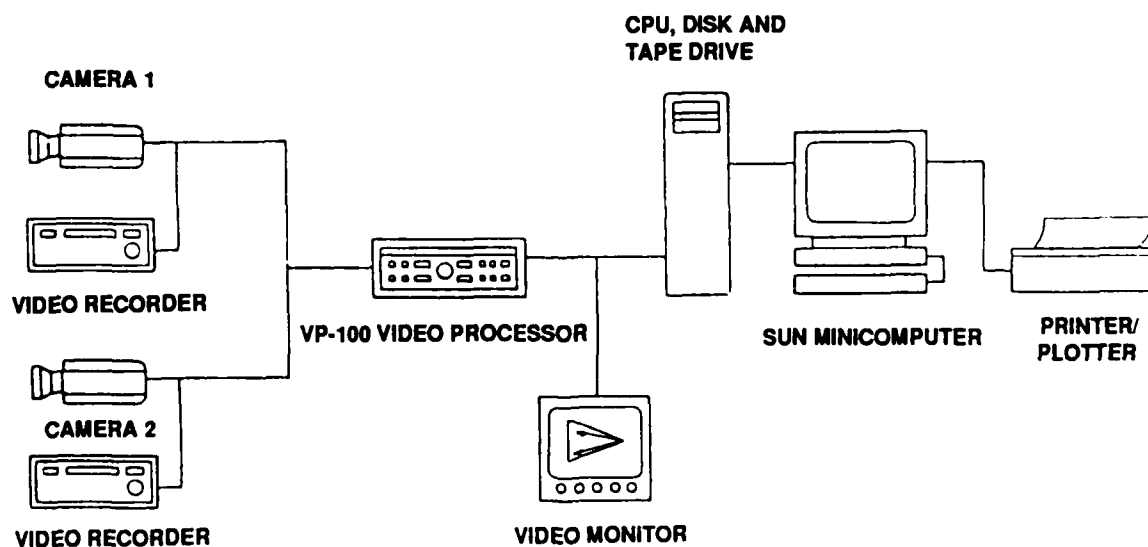


Fig. 36 Schematic of ExpertVision.

collecting data at 60 frames per second. The data were recorded on one-half inch videotapes using two standard VHS video cassette recorders (VCRs). The second series of water tunnel tests and the wind tunnel experiments were videotaped using two NAC 60/200 Hz high speed cameras, operating at 200 frames per second. Data were recorded on standard VHS tapes using two NAC 200 Hz video recorders acquired as part of the high speed camera system. In all three test series, videotapes were played back on a 60 Hz Panasonic AG-6300 video cassette recorder for analog-to-digital (A/D) conversion using the ExpertVision VP110 video processor and a Sun 2/130 minicomputer.

Video Processor

The nucleus of the ExpertVision system was a proprietary VP110 video processor produced by the Motion Analysis Corporation. The video processor allowed the user to identify the outlines of objects to be tracked, eliminate unwanted information and noise, and perform the A/D conversion of the video data for subsequent analysis on the Sun minicomputer. These functions were performed by a combination of analog and digital hardware. Unwanted noise introduced during the taping process or resulting from uneven lighting was filtered out by a user-controlled band-pass filter in the video processor. The user determined the outlines of selected targets by either "absolute thresholding" or "dynamic contrasting," both of which are hardware-based edge detection procedures.^{1,42} With these methods the user could select any combination of vertical and horizontal edges to describe the object being tracked. Typically, either a single leading edge or all four edges of the subject were selected for A/D conversion and subsequent analysis on the Sun minicomputer.

The outlines or perimeters of a target had a raw video resolution of 256 horizontal pixels by 240 vertical pixels. However, the position of the object could be determined to a much higher resolution since coordinates of its centroid were calculated to within fractions of pixels using ExpertVision algorithms on the Sun minicomputer.

Sun 2/130 Minicomputer

An integral part of the ExpertVision motion analysis system was a Sun 2/130 minicomputer. The Unix-based software used in transferring, editing, reducing, and analyzing the video data was installed on this Sun computer. Additionally, a hardware interface between the VP110 video processor and the computer allowed A/D conversion of the raw video data for subsequent digital processing. The Sun computer had both a hard disk and a tape back-up system for storing raw and reduced digitized test data.

ExpertVision Software

Software modules that make up the EV system provided a variety of data processing and analysis capabilities. Rather than listing detailed descriptions of all available software features, only major algorithms used for this project will be discussed.

The VIDE routine was used in A/D conversion of videotaped data. It was employed in conjunction with the VP110 video processor. One option allowed the user to specify the time duration of the videotape segment to be digitized. The user could also specify whether every frame or some increment of frames was to be digitized. For example, if the user wanted to digitize only every fifth frame of a videotape sequence, he could do so. If the camera frame rate of the digitized data were 60 Hz, then the default time scaling embedded in EV software would be correct for data analysis. If the camera frame rate were 200 Hz, the ENVIR routine was used to set appropriate time scaling.

The CENTROID module calculated X and Y pixel locations for the geometric center of all objects in each video frame. The user selected a rectangular neighborhood defined by pixel height and width. CENTROID then centered the neighborhood over an arbitrary pixel in the first frame of the video file. By definition, all pixels lying within the specified neighborhood belonged to a given object. The neighborhood was then centered over each of the other pixels in the included region which increased the number of pixels belonging to the object. This "neighborhood search" was applied repeatedly until all pixels in the object had served as the center of a neighborhood. This set of pixels described the complete object for which the

centroid was computed. The same process was repeated for other pixels in the video frame which were not associated with the first object until all pixels had been examined. This procedure was performed for each video frame of data. The resulting output was a file consisting of the centroids of all objects being tracked for each video frame. A proper choice of neighborhood size was essential for tracking multiple distinct objects. If the selected neighborhood were too large, multiple objects could be viewed as a single object. If it were too small, a single object could be incorrectly identified as multiple targets.

The PATH module was used to determine the translational movement of a centroid with time. This information provided the time history of an object's motion by connecting the movement of a centroid from frame to frame. The user specified a square mask size to define the region of search for a centroid in the next video frame. If two centroids fell within the mask size, the software automatically selected the centroid closest to the object's position in the previous frame. The user could also specify the number of frames to look ahead should a centroid be missing from the region of search in the next series of frames. If this option was exercised, missing centroids were supplied using linear interpolation. The user had to exercise care in selecting mask size, especially when multiple objects were being tracked in the same series of video frames.

Once an object's path was determined, the SPLIT option allowed the user to separate that path into X and Y trajectory time histories. Scaling factors to convert pixel locations into physical coordinates could also be input. In the current study, time histories of Y position from the side camera view were used to compute roll angles by applying appropriate trigonometry relations.

The DIF routine took the X or Y position time histories and determined the time rate of change by computing central differences for the inputs. This routine was used once in determining roll rate and a second time in calculating roll acceleration. The frame rate was a user-specified option required for proper time scaling.

Another important algorithm was SMOOTH. This routine eliminated or reduced local irregularities in either the path or time series data. Smoothing was accomplished by replacing

each data element with a weighted average of itself and its immediate neighbors. The user specified the number of immediate neighbors to be used in the calculation by specifying a "window width." The elements falling within the window were included in computing the moving average. The weights prescribed in the calculation were taken from the "Tukey window," a function that weighted elements with a normal distribution. Therefore, weights applied to an element decreased with increasing distance from the central element. This process acted as a low-pass filter, suppressing high frequency deviations due to noise or target "twinkle." This routine was applied to the Y time history data prior to calculation of roll rates and roll accelerations. Failure to smooth roll angle measurements resulted in taking derivatives of noise and led to large fluctuations in roll acceleration.

The EV software package also included several editors used to eliminate unwanted noise or information when the filtering and masking capabilities of the video processor were unable to do so. Use of these algorithms, such as the MASK frame by frame editor, was very laborious and time-consuming; however, it was often essential in order to obtain high quality reduced data.

Other useful EV routines included PLOT and LIST. PLOT was used to graphically display data files to the screen. This feature provided the capability to quickly analyze results during the data reduction process. The LIST command wrote EV data files to disk in ASCII format, permitting them to be analyzed on other computer systems. While videotape data were converted to useful data files with EV hardware and software, much of the analysis was performed with user-generated and commercially available programs on an IBM-compatible PC/AT.

Data Acquisition and Analysis Procedures

Water Tunnel Data Acquisition

Each test was photographed from both the side and the bottom (top or planview of the model) of the water tunnel with video cameras arranged orthogonally (Fig. 37). Since each view of the model represented a plane, three-dimensional movement of an object was obtained by correlating the two data planes utilizing the X water tunnel axis as a common dimension. For the test series using the 200 Hz NAC cameras, this correlation was relatively easy since the elapsed

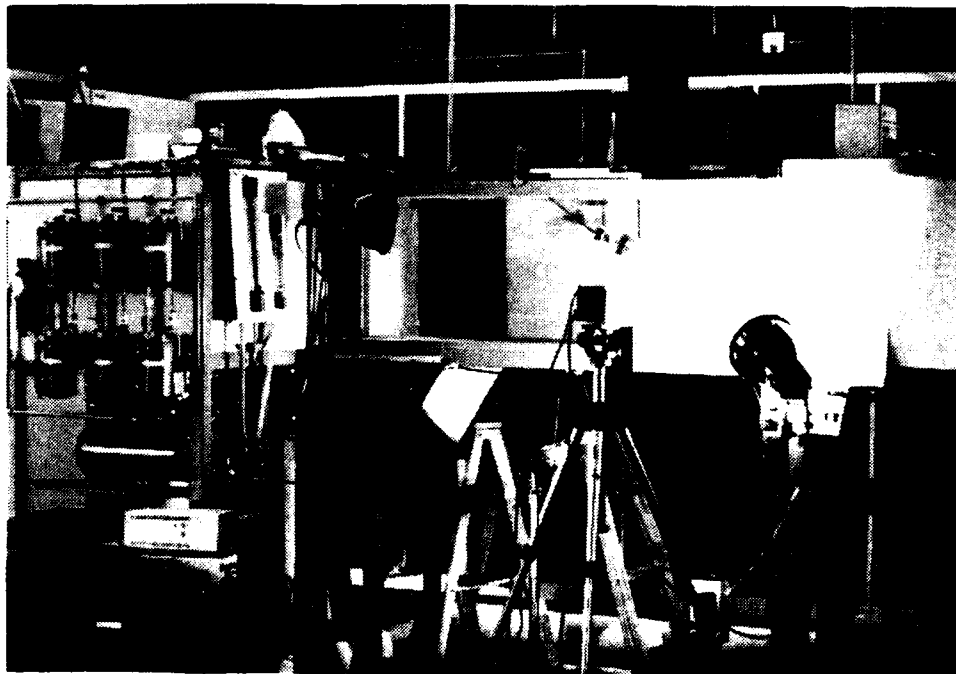


Fig. 37 Orthogonal camera arrangement.

recording time was encoded at the top of each video frame. Both cameras were started simultaneously, so the two planar views could be combined to provide three-dimensional information by matching encoded times. The 60 Hz cameras did not display an internal timer, so considerably more effort was required to match the frames from the two views. Despite this complication, a fairly good time correlation was achieved by identifying a common event in the two views and making it the first frame of the digitized data. The appearance of a dye pulse at the leading edge of the wing was an excellent reference point and served as the initial frame for each of the two views in the pulsed dye experiments. In the forced oscillation tests, matching frames at maximum roll angles from the two views provided a means of correlating two data files. After the first frames had been time-matched manually, the remaining frames were automatically synchronized since the frame rates of the two cameras were identical.

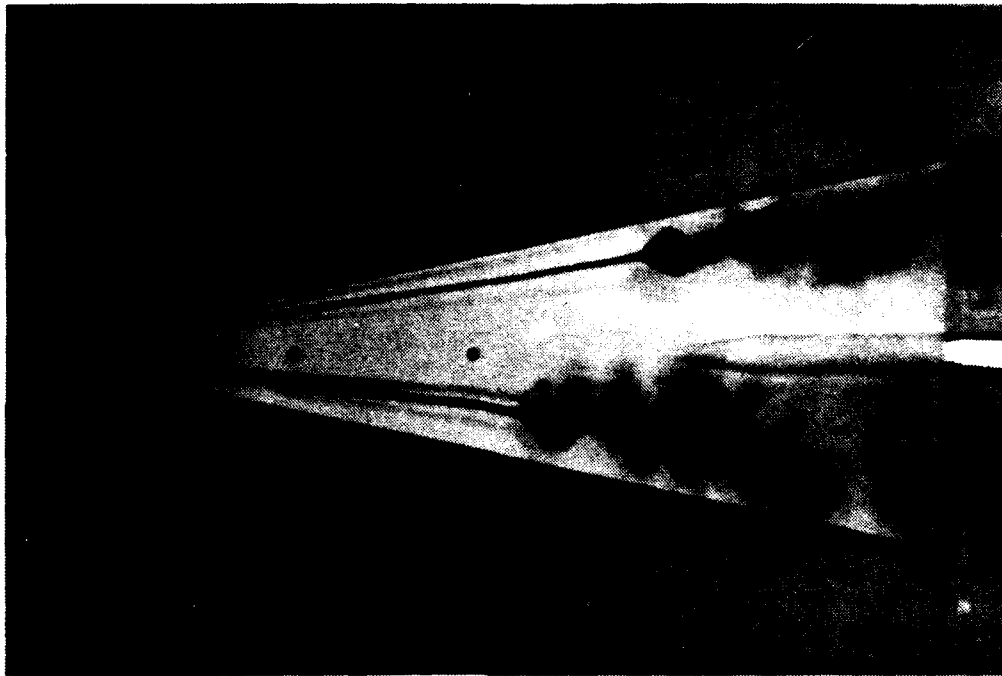
Vortex flows were visualized in the water tunnel tests by injecting either continuous dye streams or pulsed dye elements into the leading-edge vortices at the apex of the wing. Continuous dye filaments (Fig. 38) were very useful in determining vortex trajectories and burst points. This process required that only a few frames of data be digitized, edited, and analyzed for those test segments with a stationary wing. Continuous dye streams were essential to accurately track vortex trajectory and burst point movement during both forced and free roll oscillation tests; however, the editing required for this phase of data reduction was extensive. Due to the large variances in lighting during the wing's rolling motion, frame-by-frame digitization of videotape images was required. This process was extremely time-consuming. Pulsed dye packets (Fig. 39) were essential for calculating the velocities and accelerations associated with these vortical flows. Since individual elements of fluid had to be tracked from frame to frame, editing these paths made this task a demanding part of the data reduction, also.

Wind Tunnel Data Acquisition

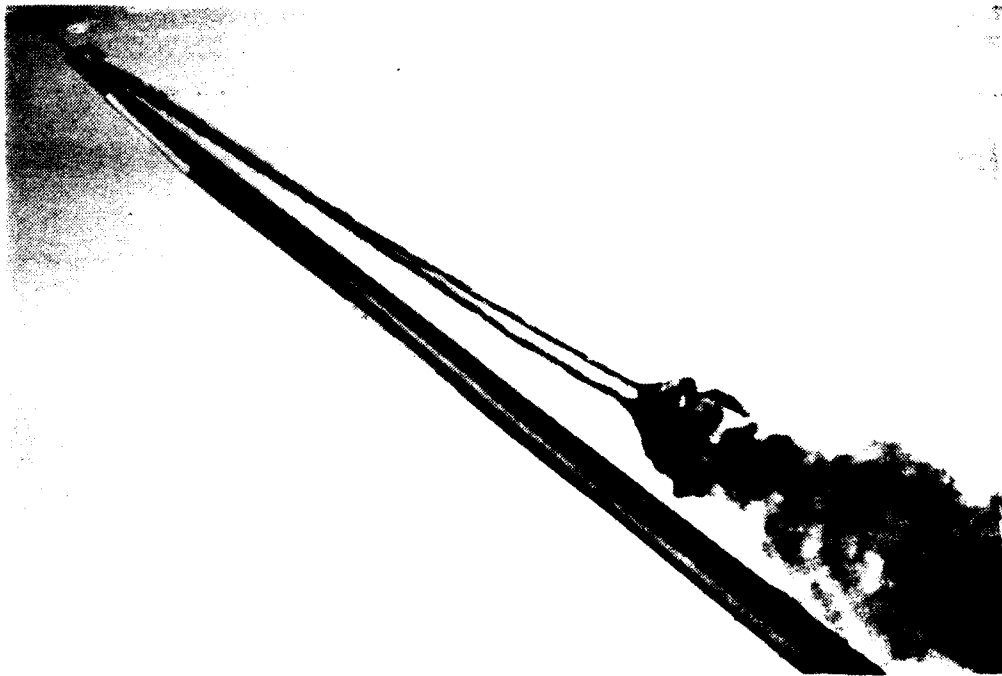
Wind tunnel tests were videotaped from the side and planview of the model with the 200 Hz cameras. Since very little flow visualization was obtained, the top camera view had a very limited application for these tests. The side camera view alone gave wing motion and the roll angle time histories. Flow visualization of leading-edge vortices using a smoke wand was attempted (with little success) on the last few wind tunnel runs. While the vortices were recorded on videotape, a much clearer indication of their motion was obtained by visually observing the tests from inside the wind tunnel.

Water Tunnel Data Reduction

The reduction of the water tunnel data was significantly more involved than originally anticipated. The major difficulty experienced in the water tunnel data reduction was associated with the leading-edge vortices. Determination of velocities and accelerations on the stationary tests was rather time-consuming as a result of the need for manual editing; however, it was relatively simple compared to simultaneously tracking the motion of the wing and the movement



a)



b)

Fig. 38 Water tunnel flow visualization with continuous dye streams: a) planform view, and b) side view.

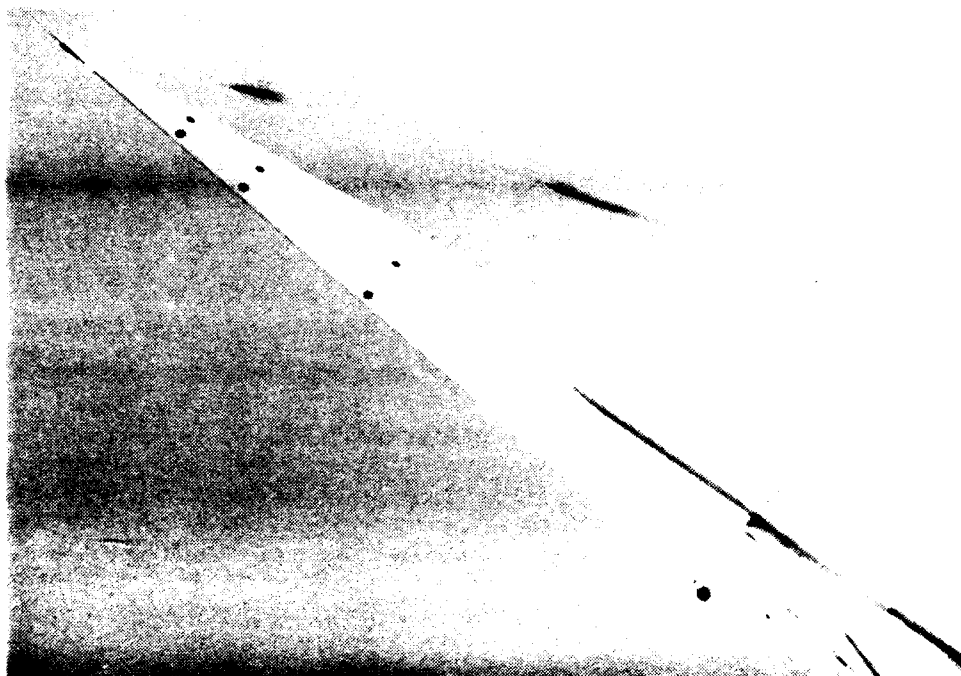


Fig. 39 Water tunnel flow visualization with pulsed dye flow.

of the vortices. Unfortunately, as the model rolled, the lighting on the model changed, resulting in a continual change in the contrast level between the model and the vortices. While these changes did not significantly increase the difficulty in tracking model motion throughout the roll oscillations, it was impossible to track the leading edge using a single contrast threshold value during the A/D conversion. As a result, it was necessary to digitize and edit the videotape images one frame at a time in order to track both the vortices and the model motions. This laborious procedure permitted the contrast levels to be changed at different roll angles by adjusting the contrast threshold on the video processor.

To analyze the movement of the vortices, an x/c location along the model was selected and the y and z positions in the body axes were determined at that chordwise location from the two video views. Manual editing was required to obtain the desired information. To transform vortex locations to the body axis system of the oscillating model, appropriate geometry had to be

incorporated into the data conversion routine. To shorten the time spent reducing data, only a fraction of the videotape frames were analyzed. Experience showed that examining data frames every 0.1 seconds was adequate to capture vortex movement.

Reduction of raw digitized video data was accomplished using the software routines discussed on pages 45-47. Table 1 summarizes the procedure followed to obtain roll angle, roll rate, and roll acceleration time histories. The process included both EV algorithms and user-generated routines.

Roll angles were determined from the Y positions from the side camera, which were converted to roll angles by taking into account that the wing tip actually travelled in an arc in and out of the plane rather than as a line in the plane as it appeared on the monitor. Due to this out-of-plane motion, a change in Y distance represented different roll angles depending on the position of the wing; that is,

$$Y = d \sin \phi \quad (11)$$

related roll angle to Y position, where d was hypothetically the wing semi-span. Rather than using the semi-span value as d, which requires a precise scaling of the video frame in physical units to have the correct units for Y, the value of d was measured experimentally from a series of calibration tests. The relationship between the Y data and the roll angle was determined by setting the wing at a precisely measured roll angle and videotaping it. Reduction of the video data yielded Y values which corresponded to known roll angles. The value of d was then calculated from equation (11). Some slight variations were found in the value of d when determined for different known roll angles; however, the variations were always less than 2%. Closer agreement would have been unrealistic since setting and measuring the calibrated roll angles could not be done perfectly. Additionally, some error in the Y positions was expected since the reference point traveled in and out of the video plane. As a result, at certain positions in the rolling motion, the reference point on the wing was closer to the camera than at others. However, the calibration tests showed that this effect was negligible and within the ability to

Table 1 Data reduction procedure

Desired Information	EV Software	Remarks
A/D conversion of videotape data	VIDE	VP110 and software used to create and digitize target outlines
Remove noise from digitized video file	MASK	Editor used to remove unwanted information and noise
Target centroids	CENTROID	Calculation of target centroids for each frame of video data
Target trajectories	PATH	Creation of the paths of each target's movements
X and Y data time histories	SPLIT	Breaks path into X and Y trajectories
Roll angle time history		IBM PC program converts Y data history to roll angle history
Smoothed roll angles	SMOOTH	Eliminates high frequency noise from Y data history and IBM PC converts to roll angle history
Roll rate time history	DIF	Central differencing of smoothed Y data history and IBM PC converts to roll rate history
Alternate method for roll angle time history		Central differencing of smoothed roll angle history on IBM PC
Roll acceleration	DIF	Central differencing of Y velocity data history and IBM PC converts to roll accelerations
Alternate method for roll acceleration time history		Central differencing of roll rate history on IBM PC

Note: IBM PC refers to an IBM PC/AT compatible computer.

measure the roll angle. The value of Y corresponding to the known $\phi = 0^\circ$ wing position was also required in accurately converting from Y location data to roll angles.

The roll rates were determined both with and without the EV central difference algorithm DIF. To calculate roll rates, the roll angle time history was smoothed using the SMOOTH algorithm. The Y time history was first smoothed and then converted to roll angle using the personal computer. Other smoothing routines were also used and yielded similar results (as will be discussed in Chapter 5). In the first method of computing roll rate, the time variation of the Y data was calculated with the DIF algorithm in EV. Just as the Y data had to be converted to roll angles using the appropriate trigonometry and scaling relations, such was the case with the Y velocity data to obtain roll rates. The second method was to central difference the smoothed roll angle data outside EV. As anticipated, both methods yielded the same results within round-off errors. Roll accelerations were determined in the same way. First, DIF was applied to the Y velocity, yielding Y acceleration data. These values were then converted to roll accelerations. An alternate method central differenced the roll rates to obtain roll accelerations on the IBM PC.

The aerodynamic rolling moments were calculated using equation (1)

$$C_{\ell}(t_i) = \frac{I_{xx} \ddot{\phi}(t_i)}{\bar{q} S b} \quad (12)$$

as discussed in Chapter II. Analysis of the C_{ℓ} results indicated that while use of this relation is valid in wind tunnel studies, the equation must include apparent mass terms for water tunnel tests. This point will be discussed in detail in Chapter V. The methods used to determine aerodynamic derivatives from the data will also be discussed in that chapter.

Wind Tunnel Data Reduction

Wind tunnel data acquisition was much less time-consuming than water tunnel data since smoke flow visualization did not provide quantifiable vortex core locations. Determination of the model motion variables and aerodynamic rolling moments was accomplished using the same procedure employed in the water tunnel data reduction. Unlike the water tunnel results,

equation (12) provided rolling moments which were in good agreement with other published data for 80° delta wings.

Mathematical Model and Simulations

While the experimental measurements gave an excellent ability to observe and analyze wing rock behavior, further insight was gained from comparing that data with predictions from mathematical models and simulations. The mathematical model used for this project was selected because it had provided reasonable simulations of prior experimental tests and it was simple. Its simplicity allowed the analyst to immediately assess the effects that different aerodynamic derivatives have on limit cycle characteristics. Additionally, a good simulation of wing rock response was obtained by numerically integrating the nonlinear equation of motion using a fourth order Runge-Kutta algorithm.

Mathematical Model

The mathematical model used in this study was initially developed and presented by Nguyen, Yip, and Chambers.²³ It was later extended by Hsu and Lan^{29,30} to include roll damping variations with roll rate. In both cases, an approximate analytic solution of the one degree-of-freedom model was determined using the Beecham-Titchener method.³⁷ The current research used the same approach to rederive the model, including the effects of bearing friction. While bearing friction is irrelevant for unconstrained motion in flight, it is present in all single degree-of-freedom wind and water tunnel free-to-roll tests. A summary of the mathematical model is provided here; however, the complete derivation is available in Appendix A.

Since wing rock in wind and water tunnel experiments was a single degree-of-freedom rolling motion, the aircraft equations of motion reduced to equation (12). Equation (12) was modified in the current study to include the effects of bearing friction so that

$$C_{\ell}(t_i) = \frac{I_{xx} \ddot{\phi}(t_i)}{\bar{q} S b} + \frac{\mu \dot{\phi}}{\bar{q} S b} \quad (13)$$

where μ is a damping term due to bearing friction. To develop a nonlinear differential equation describing the wing rock motion, the aerodynamic rolling moment, C_ℓ , was represented by

$$C_\ell = C_{\ell_0} + C_{\ell_\beta} \beta + C_{\ell_p} \bar{p} \quad (14)$$

where

$$C_{\ell_p} = C_{\ell_{p0}} + C_{\ell_{p\beta}} |\beta| + C_{\ell_{pp}} |\bar{p}| \quad (15)$$

The terms included were based on observations of static force, forced oscillation, rotary, and free-to-roll tests conducted on an 80° delta wing in the wind tunnel.^{29,30} Hsu obtained reasonable simulations of the wind tunnel results of Nguyen, Yip, and Chambers²³ using equations (14) and (15). The absolute values take into account that $C_{\ell_{pp}}$ and $C_{\ell_{p\beta}}$ change sign during an oscillation. Equations (13), (14), and (15) were combined with kinematic relations

$$\beta = \sin^{-1} (\sin \alpha_s \sin \phi) \quad (16)$$

and

$$p = \dot{\phi} \quad (17)$$

to form a nonlinear second order equation, where α_s is the angle of attack at zero yaw angle. The nonlinear equation was simplified by approximating equation (16) as

$$\beta \approx \phi \sin \alpha_s \quad (18)$$

The approximation in equation (18) created errors which increased with ϕ (up to a 7.3% error at $\phi = 37^\circ$); however, the assumption was needed to formulate the approximate math model. The resulting differential equation was

$$\begin{aligned} \frac{I_{xx}}{\bar{q} S b} \ddot{\phi} + \frac{\mu}{\bar{q} S b} \dot{\phi} = & C_{\ell_0} + \sin \alpha_s C_{\ell_\beta} \phi + \dots \\ & \dots + (C_{\ell_{p0}} + \sin \alpha_s C_{\ell_{p\beta}} |\phi| + C_{\ell_{pp}} \left| \frac{\dot{\phi} b}{2V} \right|) \left| \frac{\dot{\phi} b}{2V} \right| \end{aligned} \quad (19)$$

While in reality $C_{\ell\beta}$, $C_{\ell p0}$, $C_{\ell p\beta}$, and $C_{\ell pp}$ were time-varying derivatives, they were represented as constant averaged values in the mathematical model^{29,30} and simulations. In a more convenient form, equation (19) was rewritten as

$$\ddot{\phi} = L_0 + \sin \alpha_s L_\beta \phi + (L_{p0} + \sin \alpha_s L_{p\beta} |\phi| + L_{pp} |\dot{\phi}|) \dot{\phi} - \mu_1 \dot{\phi} \quad (20)$$

where the L_0 , L_β , L_{p0} , $L_{p\beta}$, L_{pp} , and μ_1 are defined in equation (A17) of Appendix A.

Assuming a time-varying solution of the form

$$\phi(t) = a(t) \cos(t) \quad (21)$$

and applying the Beecham-Titchener method,³⁷ approximate values for frequency, period, and amplitude of wing rock were obtained as shown in Appendix A. Wing rock frequency and period were estimated using

$$\Omega = \left[- \frac{\bar{q} S b}{I_{xx}} \sin \alpha_s C_{\ell\beta} \right]^{\frac{1}{2}} \quad (22)$$

and

$$P = 2\pi / \Omega \quad (23)$$

where Ω is the average frequency in rad/sec and P is the period in sec. The limit cycle roll magnitude was determined using

$$A = - \frac{3\pi}{4} \frac{C_{\ell p0} - \mu}{\sin \alpha_s C_{\ell p\beta} + \frac{\Omega b}{V} C_{\ell pp}} \quad (24)$$

where A is the amplitude in radians. An accurate determination of μ is extremely difficult, if not impossible, so its inclusion in equation (24) was primarily to give a qualitative feel for the effect of bearing friction.

Simulation of Wing Rock

In addition to estimating wing rock amplitude and frequency, it was of interest to approximate the time response of the system. Several different approaches were used to conduct numerical simulations. A relatively simple method was to assume a variation of roll angle and compute its first derivative to obtain roll rate. Given roll angle and roll rate, C_ℓ was approximated at each time step from equations (14) and (15). One form of the simulation assumed a sinusoidal variation in roll angle using frequency and amplitude values from equations (22) and (24). Yet another simulation was performed using experimental frequency and amplitude results in the sinusoidal roll angle variation instead of calculated values from the math model.

A more satisfying approach was to numerically integrate the nonlinear equation of motion in equation (13) (with C_ℓ represented by equations (14) and (15)), using a fourth order Runge-Kutta algorithm. This integration eliminated the requirement for the β approximation of equation (18). Both average and time-varying aerodynamic derivatives were used in the simulation. The outputs of the simulation were the time history of the motion variables and rolling moment coefficients and an estimation of limit cycle amplitude and frequency. This method was attractive since it made no initial assumption about the roll angle history. It also provided information about the stability of the limit cycle by examining the response at different initial conditions. For comparison purposes, the fourth order Runge-Kutta algorithm was also used to integrate equation (19) or (20), with β approximated by equation (18).

Test Matrix

The preceding discussion described the hardware used and the procedures followed in conducting the present study. This section lists the tests performed to meet the research objectives. Not all of the tests were analyzed with EV since it was much easier to videotape the experiments than to reduce the data. However, even the tests which were not analyzed in detail provided useful data.

First Test Series

As discussed earlier in this chapter, the first test series consisted of stationary and forced oscillation tests on both 70° and 80° delta wings in the Eidetics International water tunnel. Each test was videotaped from the planform and side view using the two 60 Hz video cameras. All of the tests in this phase of the study were conducted at a water tunnel flow velocity of 4 ips. The test matrix for the 70° delta wing is provided in Table 2. Similarly, the 80° delta wing tests are listed in Table 3.

Second Test Series

The second series of tests were also performed on the 70° and 80° delta wings in the water tunnel; however, the experiments were videotaped with the high speed 200 Hz video

Table 2 First test series (70° delta wing)

$\alpha_s (^\circ)$	$\beta_T (^\circ)$	f (Hz)	$\phi (^\circ)$	Test Type
10	0, ± 5 , ± 10	---	---	Stationary
15	0, ± 5 , ± 10	---	---	Stationary
20	0, ± 5 , ± 10	---	---	Stationary
25	0, ± 5 , ± 10	---	---	Stationary
30	0, ± 5 , ± 10	---	---	Stationary
35	0, ± 5 , ± 10	---	---	Stationary
40	0, ± 5 , ± 10	---	---	Stationary
15	0	0.0440	± 30	Forced oscillation
25	0	0.0179	± 30	Forced oscillation
25	0	0.0440	± 30	Forced oscillation
25	0	0.1760	± 30	Forced oscillation
35	0	0.0440	± 30	Forced oscillation

Table 3 First test series (80° delta wing)

α_s (°)	β_T (°)	f (Hz)	ϕ (°)	Test Type
15	0, ± 5 , ± 10	---	---	Stationary
20	0, ± 5	---	---	Stationary
25	0, ± 5 , ± 10	---	---	Stationary
30	0, ± 5 , ± 10	---	---	Stationary
35	0, ± 5 , ± 10	---	---	Stationary
40	0, ± 5 , ± 10	---	---	Stationary
25	0	0.0180	± 30	Forced oscillation
25	0	0.0440	± 30	Forced oscillation
25	0	0.1740	± 30	Forced oscillation
35	0	0.0440	± 30	Forced oscillation

cameras. Based on results from the first test series, a slightly different test matrix was followed. The 70° delta wing tests are listed in Table 4. All of these tests were conducted at a water tunnel velocity of 4 ips as in the first test series. The 80° delta wing stationary and forced oscillation tests are summarized in Table 5 and were also performed at a freestream velocity of 4 ips. The wing rock water tunnel study on the 80° delta wing was conducted during this test series. These experiments are summarized in Table 6.

Third Test Series

The third test series consisted of a detailed wind tunnel investigation of the same 80° delta wing which was tested in the water tunnel (see Table 7). These experiments were conducted over two and one-half weeks and involved three separate wind tunnel entries. The angle of attack was varied from 24° to 55° to determine the wing rock range and to assess its effects on limit cycle behavior. In addition to the wide range of angles of attack and dynamic

Table 4 Second test series (70° delta wing)

α_s (°)	β_T (°)	f (Hz)	ϕ (°)	Test Type
15	0	---	---	Stationary
25	0, ± 5 , ± 10	---	---	Stationary
35	0, ± 5 , ± 10	---	---	Stationary
25	0	0.0179	± 30	Forced oscillation
25	0	0.0440	± 30	Forced oscillation
25	0	0.1760	± 30	Forced oscillation
35	0	0.0440	± 30	Forced oscillation

Table 5 Second test series (80° delta wing)

α_s (°)	β_T (°)	f (Hz)	ϕ (°)	Test Type
25	0, ± 5 , ± 10	---	---	Stationary
25	0	0.0181	± 30	Forced oscillation
25	0	0.0448	± 30	Forced oscillation
25	0	0.1747	± 30	Forced oscillation
35	0	0.0443	± 30	Forced oscillation

Table 6 Wing rock water tunnel tests (80° delta wing)

Run No.	α_s (°)	β_T (°)	V_∞ (ips)	Re (/ft)
1	35	0	4	30,000
2	35	0	4	30,000
3	35	0	6	45,000
4	35	0	10	75,000

Table 7 Wind tunnel wing rock tests

α_s (°)	β_T (°)	\bar{q} (psf)	ϕ_0 (°)	Remarks
24	0	5	0	NL
25	0	5	0	NL
26	0	5	0	NL
27	0	5	0	NL
30	0	0.5, 1, 2, 3, 5	0	NL
30	0	0.5, 1, 2, 3, 5	-70	NL
35	0	0.5, 1, 1.5, 2, 3, 4, 5, 10	0	NL
35	0	1	-10	NL
35	0	0.5, 1, 1.5, 2	-70	NL
35	0	3	-75	NL
35	-2, 2	1, 2	0	NL
35	-4, -3, -2, 2, 3	0.5	0	NL
35	0	0.5, 1	0	Smoke, NL
35	0	0.5, 1, 2	0	MI, NL
35	0	0.5, 1, 2	-70	MI, NL
35	0	0.5, 1, 2, 3	0	WD
35	0	0.5, 1	-70	WD
35	0	0.5, 1, 2, 3	0	MO
35	0	0.5, 1	-70	MO
35	0	0.5, 1, 2, 3	0	GR
35	0	0.5, 1	-70	GR
40	0	0.5, 1, 2, 5	0	NL
40	0	0.5, 1, 2	-70	NL
45	0	1, 2, 5	0	NL
50	0	5	0	NL
51-55	0	5	0	NL

NL - No lubrication of bearings

WD - Bearings lubricated with WD-40

MO - Bearings lubricated with motor oil

GR - Bearings packed in grease

MI - Model not mass balanced

pressures examined, runs were repeated at the same conditions to assess repeatability. Wing rock transients and build-up were analyzed by setting the model at some initial roll angle and releasing it once the flow had reached steady state. Runs were also made to examine the effects of bearing friction on the self-induced oscillations. Friction was varied by changing the lubrication of the bearings in the free-to-roll apparatus. The nominal case was no lubrication. Lubricating the bearings with WD-40, motor oil, and grease permitted the amount of friction to be changed, even though the magnitude of the change could not be measured directly. After testing was conducted with each new lubricant, the bearings were thoroughly cleaned prior to application of the next lubricant. Sideslip tests were also performed to examine the effects of model misalignment on wing rock dynamics. The model was also intentionally subjected to a mass imbalance about its roll axis to evaluate effects on limit cycle oscillations. Two smoke tests were conducted at $\alpha = 35^\circ$ in an attempt to analyze the vortex movements. While well over one hundred runs were made in the wind tunnel test series, only a subset of the tests were analyzed in detail. The ability to quickly obtain large amounts of data and then selectively choose which tests to analyze were important features of the ExpertVision system.

The following chapter discusses the results of the stationary wing and forced oscillation tests on the 70° and 80° delta wing. These tests not only validated the use of ExpertVision for dynamic fluid flow applications, but also provided new information on the behavior of leading-edge vortices of slender delta wings. Chapter V provides the results of both the water tunnel and the wind tunnel wing rock experiments.

CHAPTER IV

VALIDATION TESTS AND STATIONARY WING RESULTS

This chapter presents the results of the stationary and forced oscillation tests on 70° and 80° delta wings conducted in the Eidetics International water tunnel. The objectives of these tests were twofold. First, the initial tests confirmed that ExpertVision could be utilized to conduct nonintrusive measurements of the vortex flows on highly swept delta wings. The stationary wing data gave excellent correlation with published data, demonstrating the ability to obtain quantitative information on the vortex trajectories and burst point locations. Forced oscillation data validated EV capability to simultaneously track the movement of the leading-edge vortices, specifically the vortex burst points and the motion of the model. Since the tests were conducted at known wing oscillation frequencies and roll angle amplitudes, model motion data measured by EV was compared to these parameters. Second, vortex core velocities and accelerations were derived from these measurements, extending the existing data base on delta wings. Forced oscillation tests revealed the phase relationship of vortex burst point movement and model roll angle as a function of frequency. These data were apparently the first data published relating measured phase relationships between vortex burst point location and model motion of a delta wing undergoing roll oscillations.

The tests were videotaped with both 60 Hz (first series) and 200 Hz (second series) cameras. The two test series not only examined the two camera systems, but also provided multiple tests at given run conditions to evaluate repeatability. The test matrix is provided in Tables 2 through 5 in Chapter III. For validation and comparison purposes, the results from the current study were compared to data from other references.^{13,26,46-64}

Stationary Model Tests

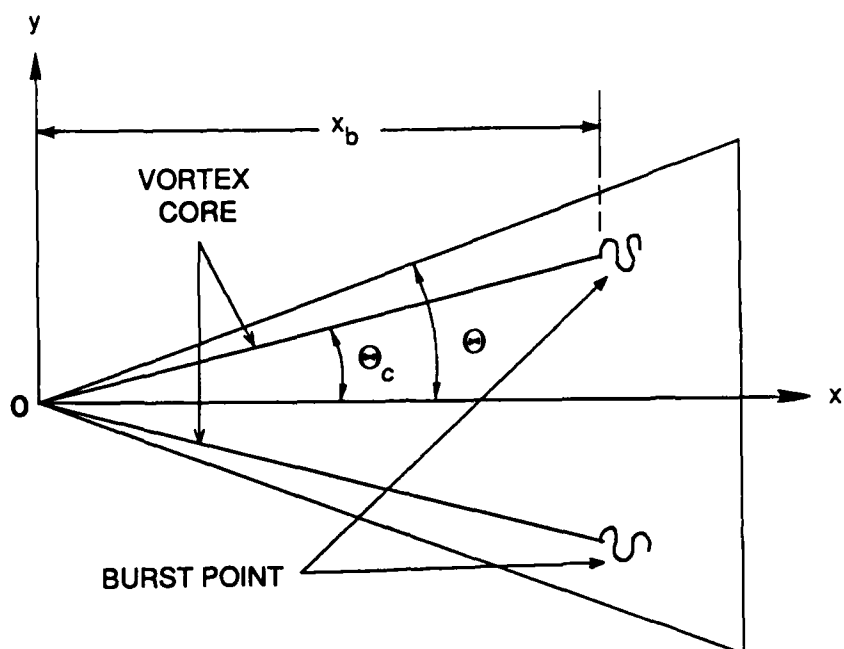
For the stationary wing tests, models were mounted in the test section and aligned to selected α_s and β_T . Black dye was injected into one or both of the dye ports near the apex of the planform so that as dye entered the water stream, it was immediately captured by the

leading-edge vortex on the appropriate side. Videotape was taken of the steady flow field once the vortices had stabilized. The steady, continuous dye stream from the first part of the taping sequence was particularly helpful in ascertaining burst point locations and trajectories. Pulsed dye tests were essential for computing the vortex core velocities and accelerations; however, these pulses required much more data reduction time since extensive frame by frame editing was required to produce a useable video file.

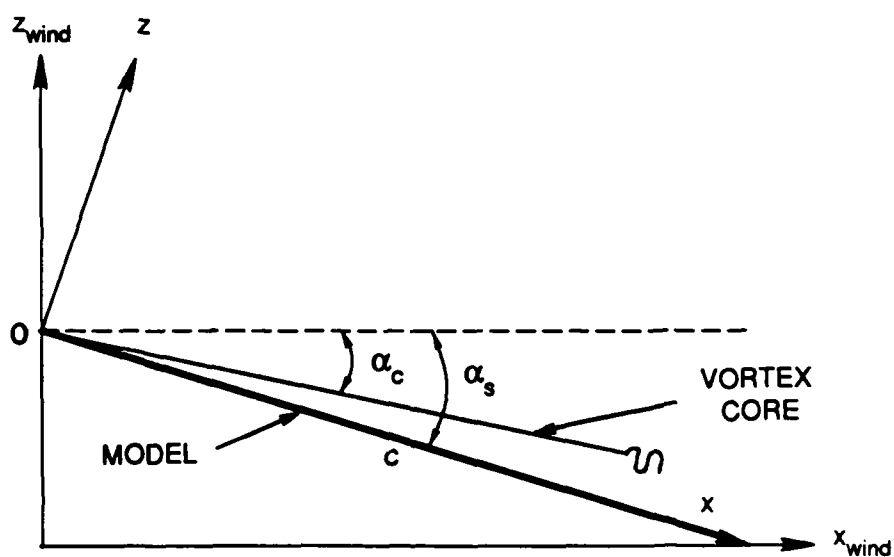
Vortex Core Trajectories and Burst Points

Vortex core locations were determined from continuous dye streams and are presented as vortex core angle of attack ($\alpha_s - \alpha_c$) and the average vortex core sweep angle ($\theta - \theta_c$) (Fig. 40). The core angle of attack was taken from the side camera view and the core sweep angle from the planform view. While this manual process of correlating information from the two cameras was time-consuming and did not utilize statistical redundancy to refine measurement accuracy, the results were consistent for different instances of time during a given test and repeatable between identical runs conducted in both test series.

For steady flows, the leading-edge vortices originated on each side of the apex of the wing and traveled in a straight path (Fig. 38). Therefore, by presenting the data as $\alpha_s - \alpha_c$ and $\theta - \theta_c$, the x, y, and z core positions in the body axis could be determined at any chordwise location by trigonometry. Fig. 41 summarized these two location parameters for the 70° and 80° delta wings as a function of α_s . Measured vortex core positions above the wing were in fairly good agreement with both theory^{13,46,47} and with previous experimental measurements^{13,48,49} (Fig. 41a). The largest discrepancies occurred at low α_s . The average vortex core sweep angle (Fig. 41b) was the average of the values for right and left vortices. The two values were not always identical, perhaps indicating a slight misalignment of the model in the test section; that is, uncertainty in either β_T or ϕ . Vortex core sweep angles were larger by approximately 15 to 20% than reported by Erickson¹³ or Lambourne and Bryer.⁴⁸ Despite the difference in magnitudes, both the measured and published $\theta - \theta_c$ data changed very little with α_s .

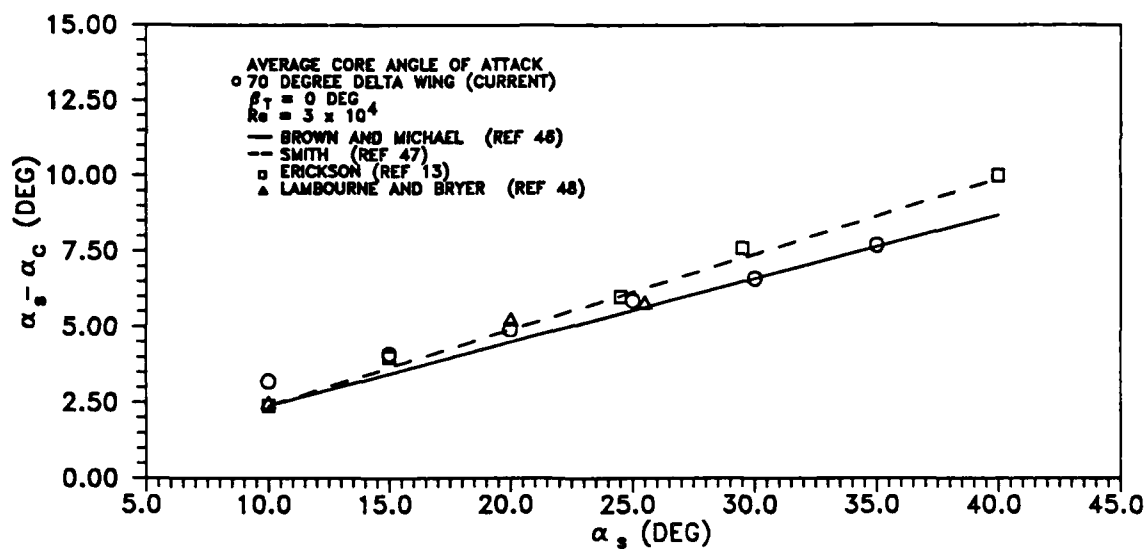


a)

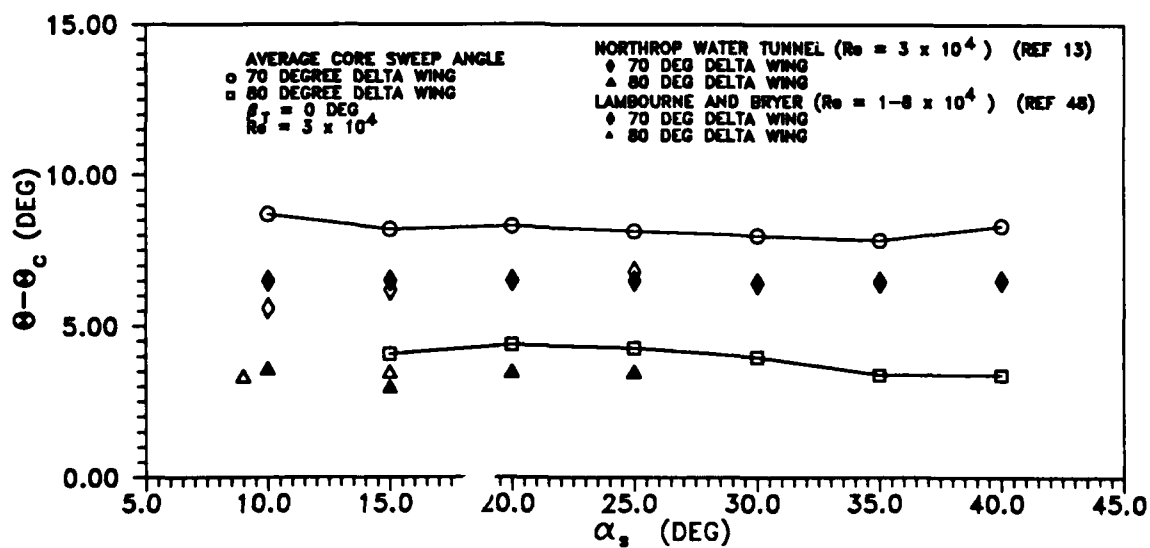


b)

Fig. 40 Vortex flow parameters: a) planform view, and b) side view.



a)



b)

Fig. 41 Vortex location parameters: a) core angle of attack, and b) average core sweep angle.

identified in Fig. 42 by the "error bars" that depict the data spread on the burst point measurements. In addition, accuracy of α_s settings could not be checked with ExpertVision, since a reference was not available in the water tunnel. Fortunately, in the second test series with the 200 Hz cameras, a horizontal reference line on the tunnel test section wall was visible in the video field of view. This reference line allowed direct measurement of α_s with ExpertVision. The measured value was 24.3° instead of the nominal 25° . The excellent agreement of the burst points from the second test series at this α_s with the ONERA data and Moore's results¹³ was encouraging, but cast further doubt on the measurements from the earlier tests. Due to the steepness of the curves in the vicinity of $\alpha_s = 25^\circ$, if the angle of attack in the first tests was actually larger than 25° , the measured burst points would have been in much better agreement with published data. For the 70° delta wing, the burst points were behind the trailing edge at $\alpha_s < 25^\circ$. These locations were outside of the video field of view and therefore could not be digitized. For identical reasons, no burst point locations were available below $\alpha_s = 35^\circ$ for the 80° delta wing. On both models, the burst point moved toward the leading-edge when α_s increased.

The good agreement of the current tests with results from both water tunnel and wind tunnel studies demonstrated the insensitivity of burst point location to Reynolds number in a steady flow.^{13,48-53} Lambourne et al.⁴⁸ found that very small differences in vortex breakdown existed between Reynolds numbers of 1×10^4 and 4.6×10^6 . Condensation trails from an F-5 showed burst point locations remarkably similar to those exhibited on a 1/72 scale model, even though the aircraft Reynolds number was over 2000 times larger than that for the model.⁵³ These results, further supported by the current tests, have permitted low speed flow visualization in the water tunnel to be correlated with wind tunnel force and moment measurements in steady flow.

Burst point locations at $\beta_T = 0^\circ$ for the 70° delta wing explained why the experimental lift data deviated from the C_L estimated using Polhamus' leading-edge suction analogy^{41,54-59} (Fig. 43). Agreement was very good between experimental data and predictions from the Polhamus analytical method until $\alpha = 25^\circ$, which corresponded to movement of the burst point forward of the trailing edge. Discrepancies grew with increasing α . Since the Polhamus

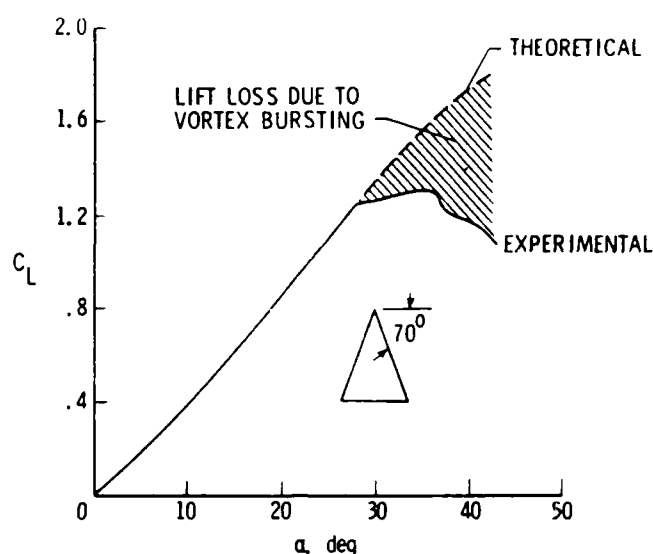
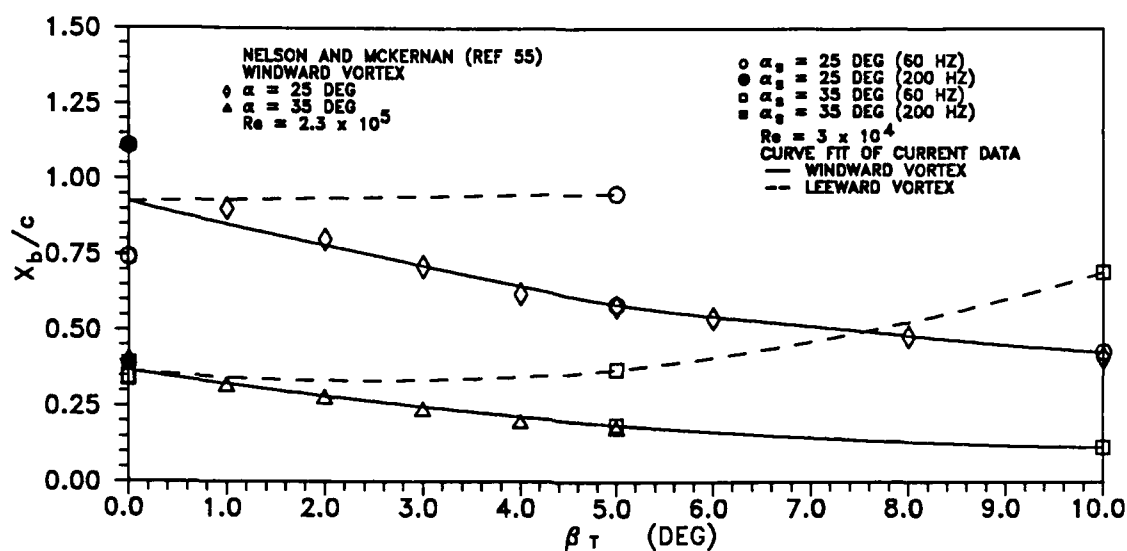
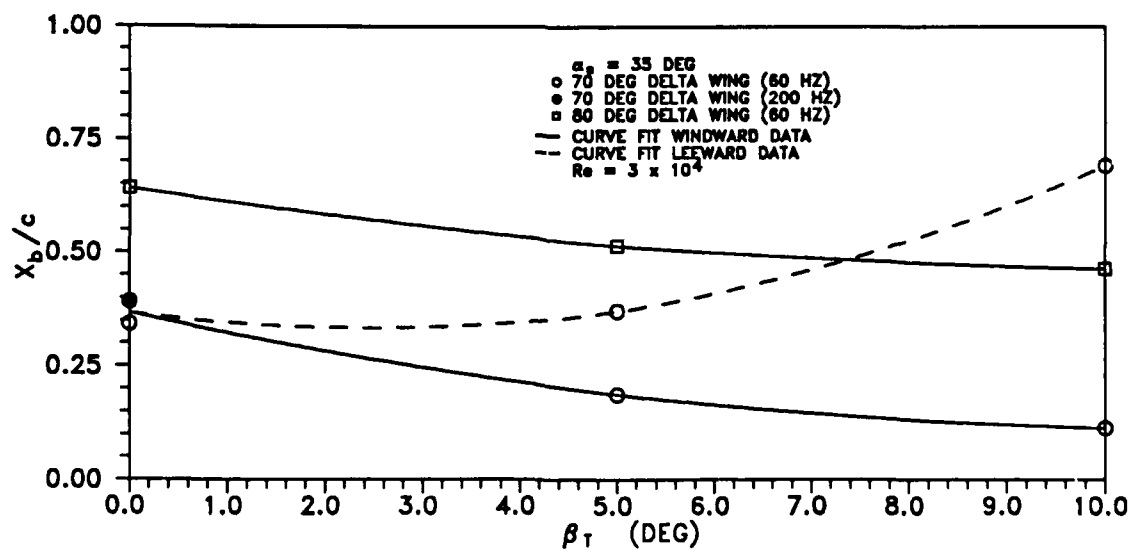


Fig. 43 Experimental lift data versus Polhamus predictions.⁵⁶

approximation did not account for vortex bursting, the more forward the burst point, the larger the error between predicted and measured lift coefficients.

The effect of flow asymmetry on vortex burst point locations was readily quantified with ExpertVision. Fig. 44 showed how both leeward and windward vortices were affected by increasing cross flow for the 70° delta wing. Two different model angles of attack were presented and burst point locations were plotted against β_T . The windward burst point varied almost linearly with β_T at $\alpha_s = 25^\circ$ and $\alpha_s = 35^\circ$. The burst point moved closer to the apex of the wing as β_T increased. The leeward vortex, however, apparently gained stability from being more nearly aligned with the flow, since it burst further downstream. The burst point occurred downstream of the trailing edge at $\alpha_s = 25^\circ$ and $\beta_T = 10^\circ$. Fig. 44 compared current data to wind tunnel results presented by McKernan and Nelson.^{55,60} These comparisons again show the largest discrepancy at α_s and $\beta_T = 0$. Agreement was very good for β_T of 5° and 10° and for $\alpha_s = 35^\circ$ and $\beta_T = 5^\circ$. Fig. 45 compared burst point behavior at $\alpha_s = 35^\circ$ for both wings for the same range of β_T as considered above. The burst points were closer to the trailing edge for the 80° wing. The leeward vortex burst point was not shown for the 80° wing because, again, it

Fig. 44 Vortex burst locations and β_T .Fig. 45 Average burst point locations and β_T .

burst behind the trailing edge and outside the field of view. The vortex burst point moved aft, apparently affected more by leading-edge sweep than by α_s .

Core Velocities and Accelerations

A primary objective of this part of the study was to demonstrate the capability of ExpertVision to determine axial core velocity profiles of individual vortices. As shown in Fig. 46, the video tracking of dye pulses, the algorithms in ExpertVision, and the editing processes provided reasonable estimates of vortex core velocity. These velocities were nondimensionalized by the freestream velocity of the water tunnel, which was 4 inches per second during the testing. Time was nondimensionalized by the time required for a fluid element traveling at freestream velocity to traverse one chord, c . The video system was used to check V_∞ at several different speeds; in every case, measurements in the test section were virtually identical to the V_∞ set by the tunnel operator. The maximum axial velocity of the core increased with increasing α_s , reaching a peak of slightly over 3 times that of the freestream at $\alpha_s = 35^\circ$. Erickson¹³ reported core velocity ratios ranging from 2 to 3, at angles of attack of 30° to 40° , quite consistent with the current measurements. Erickson's data also showed that maximum axial core velocity decreased when going from $\alpha_s = 30^\circ$ to $\alpha_s = 35^\circ$. However, these new data did not show a

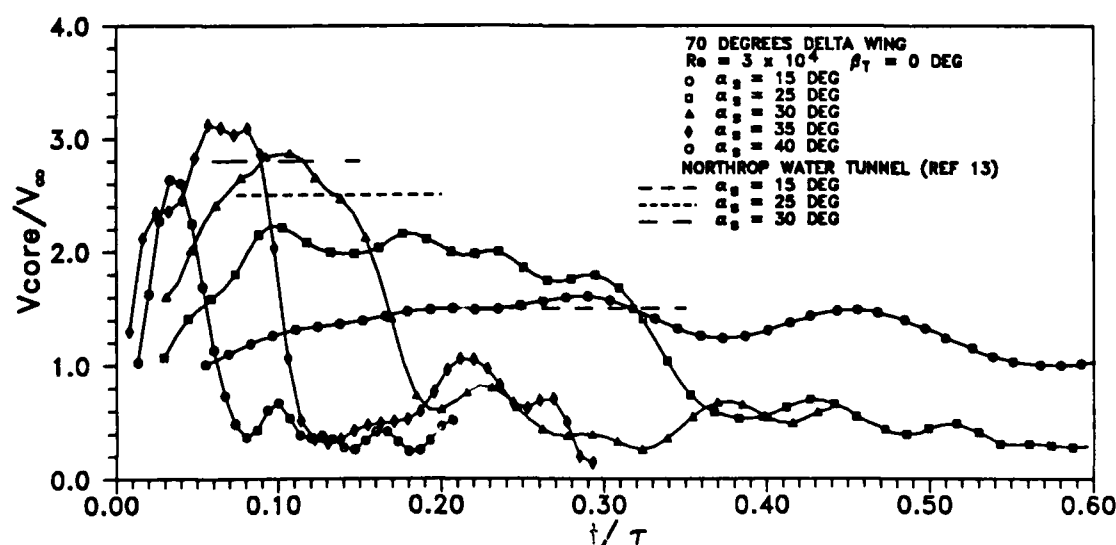


Fig. 46 Vortex core velocity time history.

decrease in peak velocity until α_s was between 35° and 40° . This result was very interesting since it correlated with the decrease in lift coefficient above $\alpha_s = 35^\circ$, shown in Fig. 43. These facts suggested that maximum lift on the delta wing may result due to both a forward movement of the burst point (Fig. 42) and a decrease in vortex core velocities. The measurements indicated that the fluid did not attain its maximum speed until a short time after dye was injected into the core flow. The velocities measured, especially at $\alpha_s = 25^\circ$, showed that core velocity was not uniform. These oscillations may be due to the helical character of the vortex as recorded on the two-dimensional video image. Redundant three-dimensional measurements might resolve some of these questions regarding the finer vortex structure.

ExpertVision derived accelerations directly by central differencing velocity profiles. An example of such accelerations is depicted in Fig. 47. Initial acceleration of the dye element, as it came out of the dye port, was shown in the first 0.04-0.05 nondimensional time units. Moreover, deceleration of the fluid element at about $0.34 t/\tau$ pinpointed vortex breakdown. Finally, average deceleration of the fluid in the vortex core was apparent from $0.15 < t/\tau < 0.63$. This average deceleration, ignoring the spike at $t/\tau = 0.34$ associated with vortex breakdown, was about 5 ips^2 . These data suggested the strength of the dissipative forces in the fluid flow field. The oscillatory nature, seen in velocity profile, was emphasized in these acceleration data.

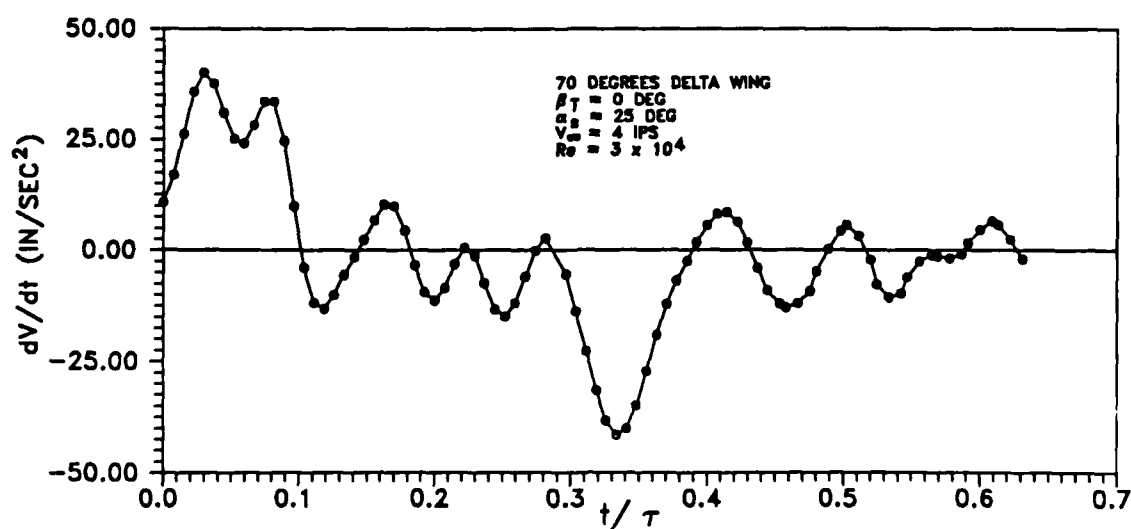


Fig. 47 Vortex core acceleration time history.

Recognizing that numerical differentiation is a process that loses information, the acceleration algorithms in ExpertVision still provided useful and unique information.

These data represented the first known measurements of velocities and accelerations throughout the entire path of a leading-edge vortex. Thus, these measurements were a significant addition to the data base and clearly illustrated the effects of α on core velocity. The ability to track a single group of particles from a Lagrangian standpoint is a major advantage of ExpertVision. This complements the use of a laser velocimeter which obtains data from an Eulerian viewpoint, requiring the system to be moved each time data is collected at a new chordwise location.

Forced Roll Oscillations

Measurements discussed in the preceding section were made with the model stationary in the water tunnel during a given run. However, delta wings provide classic examples of nonlinear dynamics associated with vortical flow structures, such as wing rock. The video system gave the experimentalist more capability to make dynamic measurements of a nonstationary model and allowed one to quantify and catalog the relationship between the motion of the lifting surface and its associated vortices. Both amplitude and phasing relationships could be studied in detail. To demonstrate this capability, a forced oscillation rig built by Eidetics International was set to produce $\phi = \pm 30^\circ$ at three different oscillation frequencies, corresponding to reduced frequencies, k , of 0.1, 0.25, and 1.0. Again, both continuous dye streams and pulsed dye streams were used to locate burst points and to calculate velocities of fluid elements entrained in the vortex flow. These measurements validated the capability of ExpertVision to capture and quantify fluid motion in the vortices, which was essential prior to undertaking the wing rock study. Terms used to analyze these dynamic data are illustrated and defined in Fig. 48. The \bar{x} is the average burst location at $\phi = 0^\circ$ and $\Delta t/T$ is the phase difference.

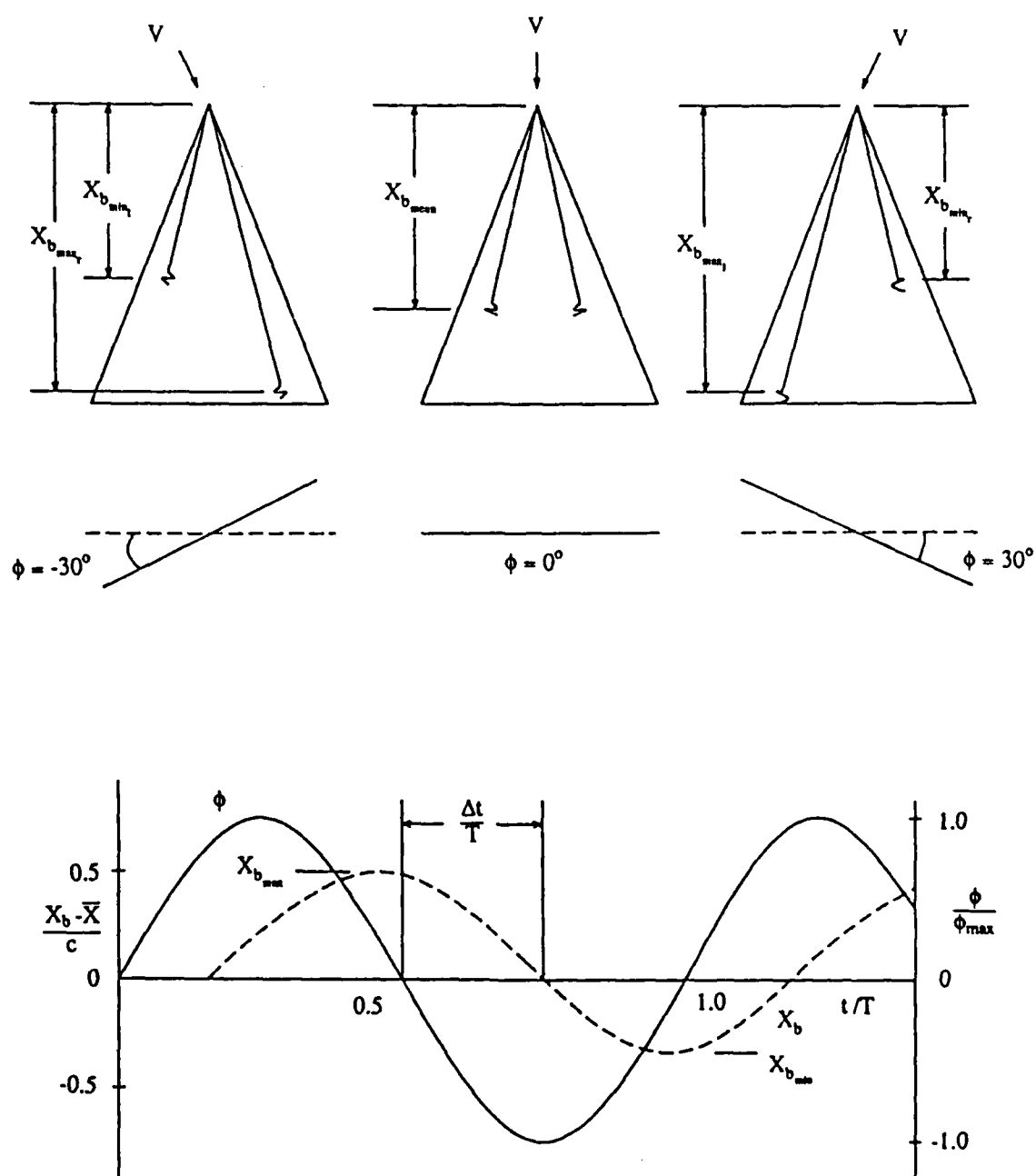
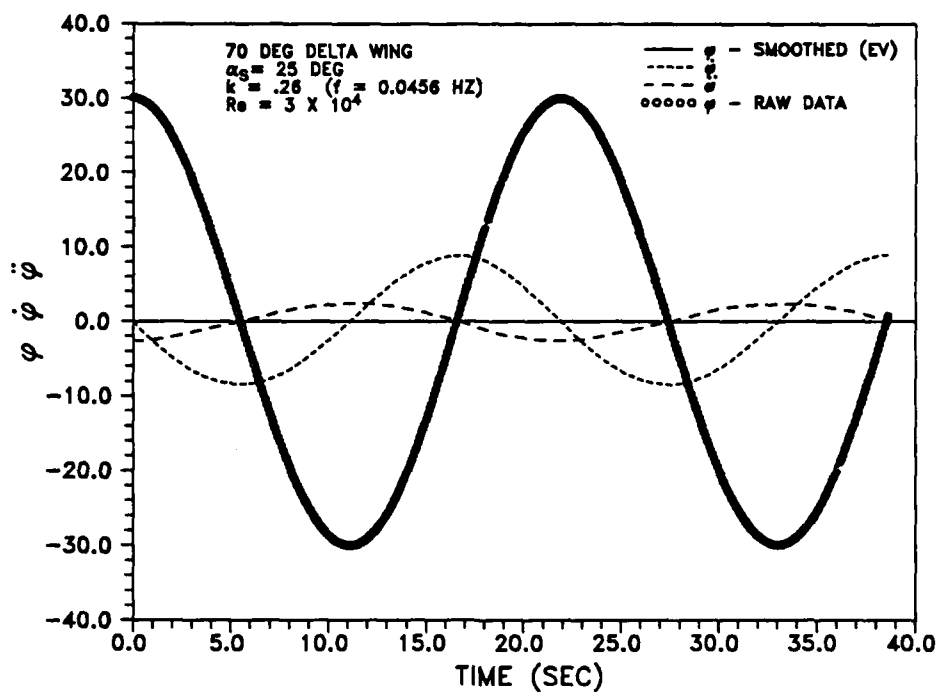
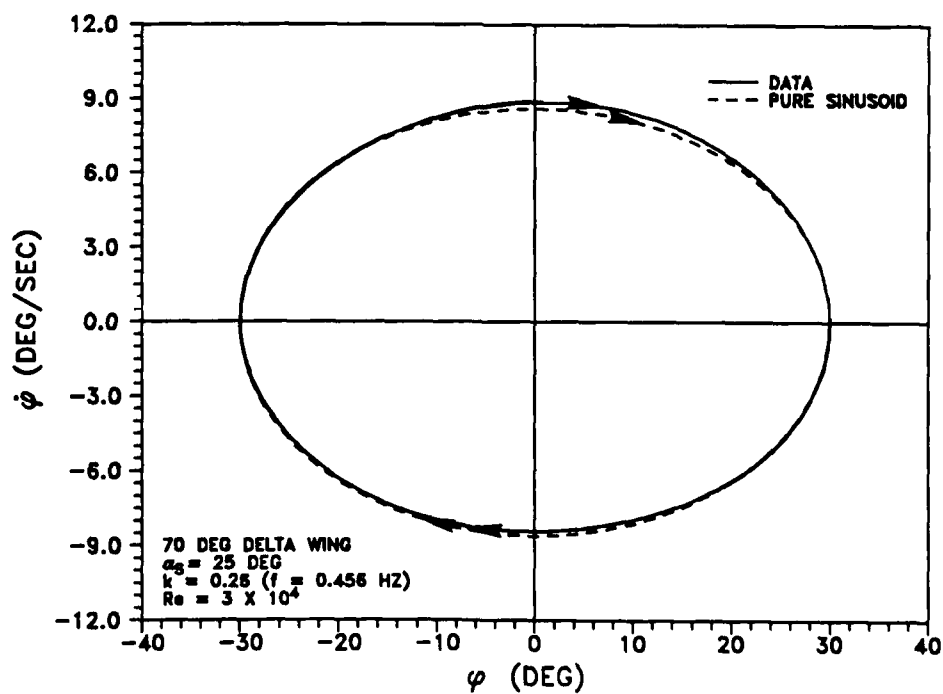
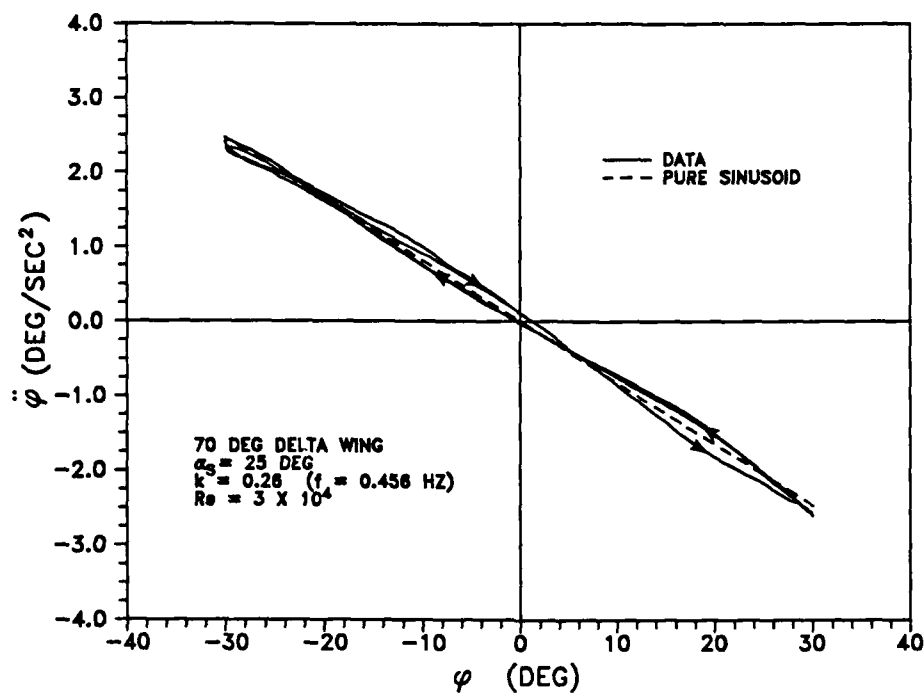
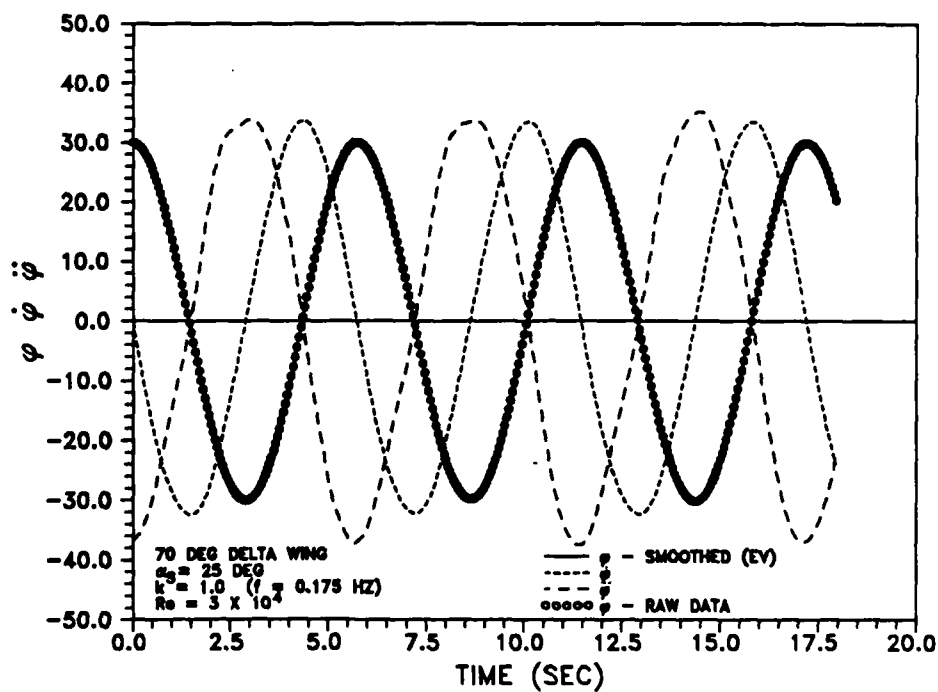


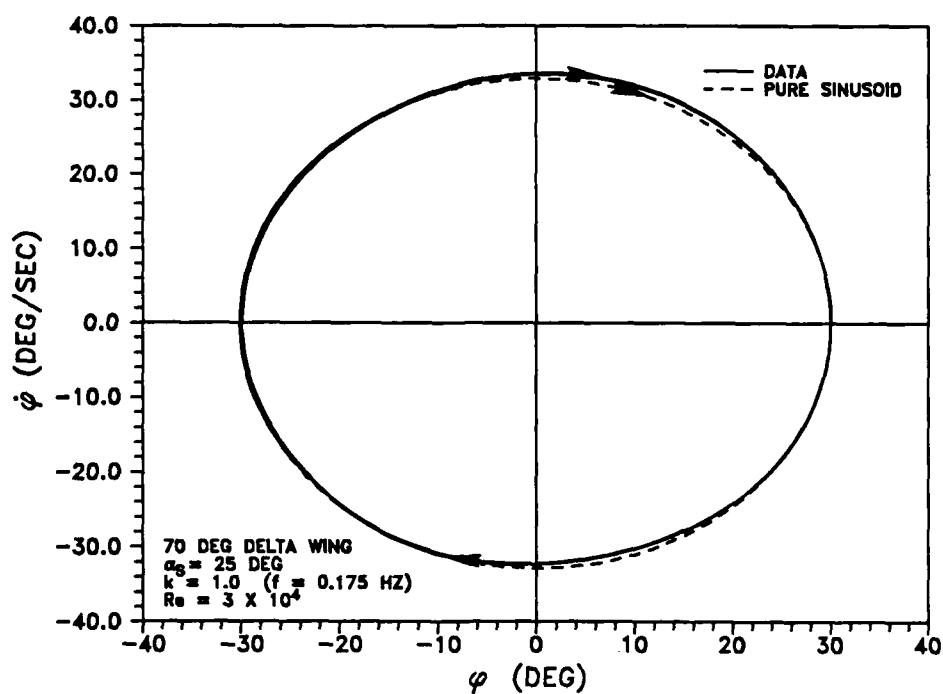
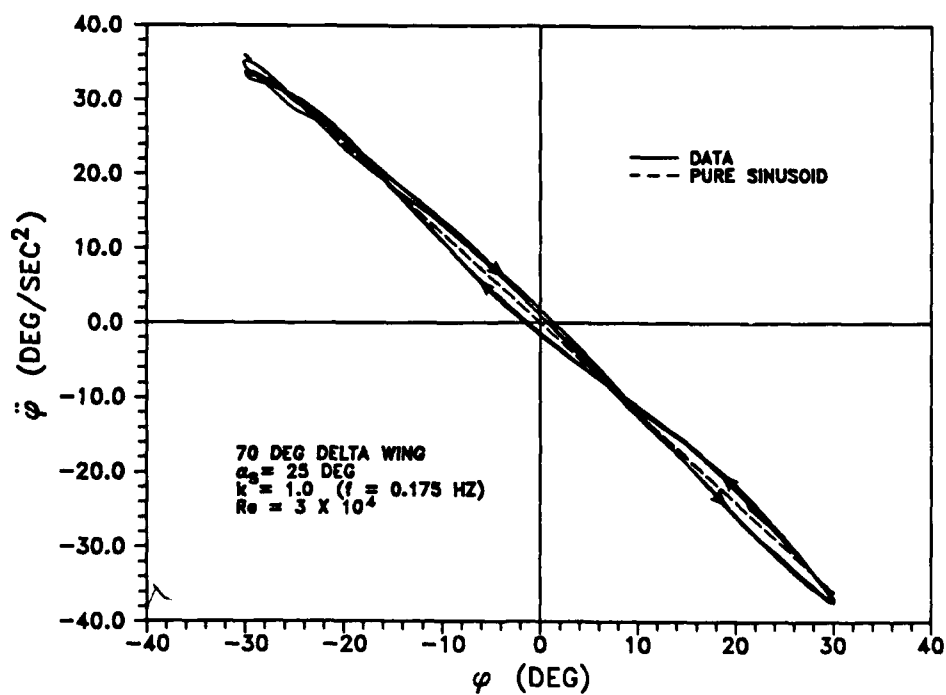
Fig. 48 Forced oscillation parameters.

Model Motion

A typical response of the model during forced roll oscillations at $\alpha_s = 25^\circ$ and $k = 0.26$ is plotted in Fig. 49. In addition to the ϕ time history, roll rate and roll accelerations are also shown. For this test, the forced oscillation rig (Fig. 30) was set to give a sinusoidal frequency of 0.444 Hz, corresponding to a reduced frequency (k) of 0.25, and bank angles of $\pm 30^\circ$. ExpertVision measured period, frequency, and reduced frequency, which were 21.93 sec, 0.456 Hz, and 0.26, respectively. The frequency was 2.7% higher than the prescribed value, certainly within the ability to set that motion parameter on the forced oscillation apparatus. The measured bank angles were $\pm 30.1^\circ$. Fig. 50 compares the actual motion of the wing to an assumed pure sinusoidal motion at the same roll amplitude and frequency. There was a slight difference in these trajectories, which was not surprising with the simple, inexpensive motor and mechanical linkages in the forced oscillation rig. It was quite unlikely that the rig produced perfect sinusoidal motion. These imperfections in the forced oscillation apparatus also resulted in hysteresis in the roll acceleration versus roll angle plot (Fig. 51). The constant average slope was very close to the curve predicted for a sinusoidal motion at the same frequency and roll amplitude. A similar set of data resulted for the forced oscillation test at 0.174 Hz (Figs. 52-54). As shown in Fig. 50, the period of the oscillation was 5.734 sec, with $\phi = \pm 30^\circ$. Therefore, the frequency and reduced frequency were 0.175 Hz and 1.0 Hz, respectively, within 0.5% of the specified value. The increased roll rates and roll accelerations due to the higher frequency were evident in comparing Fig. 52 and Fig. 49. The phase portrait comparison of the data showed good agreement between experimental results and a pure sinusoidal motion. The deviations that did exist were in the same regions of the phase plane that reflected the largest disagreements in the lower frequency test. This comparison further indicated that the deviation from sinusoidal motion was characteristic of the forced oscillation device and that it could be identified with ExpertVision. Roll acceleration versus ϕ (Fig. 54) showed very repeatable results for 3 cycles of oscillation with hysteresis loops almost identical to the $k = 0.26$ data (Fig. 51). Once again, the same characteristic of the forced oscillation rig were observed. Predicted values for a pure sinusoidal motion with the same frequency and amplitude were superimposed. The $k = 0.1$ data (not

Fig. 49 Forced oscillation motion variables, $k = 0.26$.Fig. 50 Forced oscillation phase portrait, $k = 0.26$

Fig. 51 Rolling acceleration versus ϕ , $k = 0.26$.Fig. 52 Forced oscillation motion variables, $k = 1.0$.

Fig. 53 Forced oscillation phase portrait, $k = 1.0$.Fig. 54 Rolling acceleration versus ϕ , $k = 1.0$.

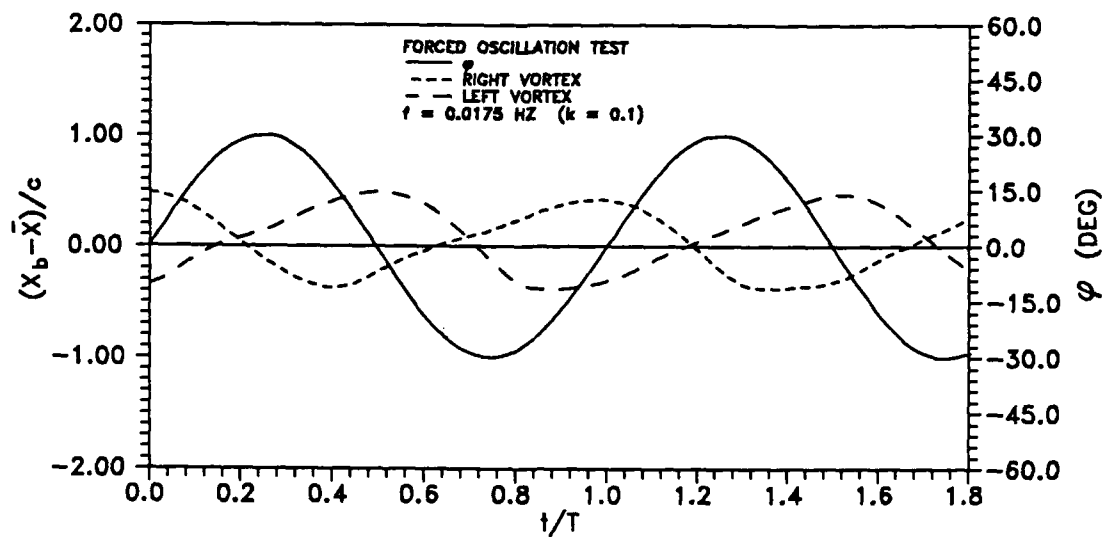
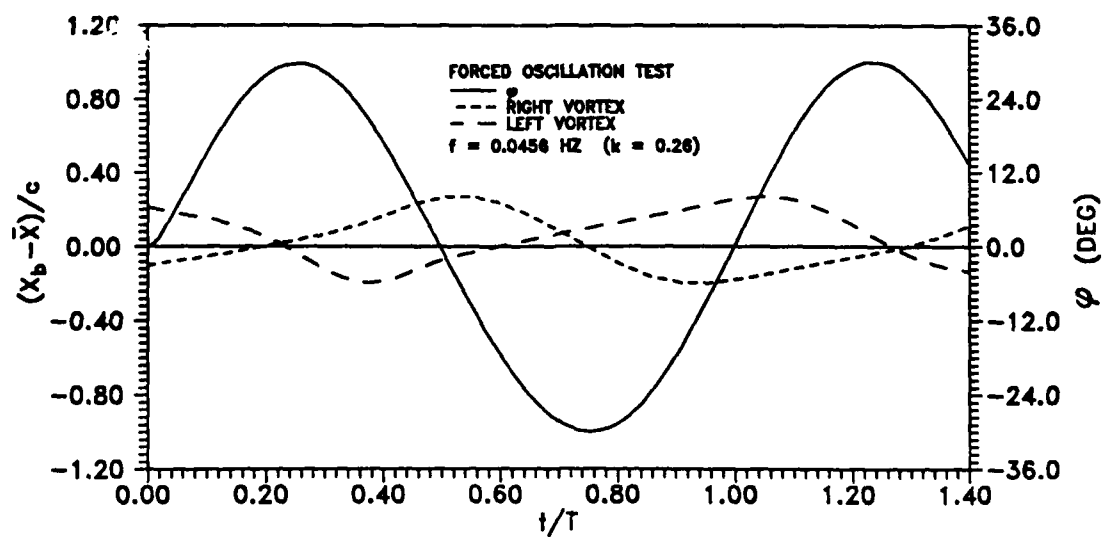
shown) revealed very similar results. The measured period was 55.8 sec, corresponding to a frequency of 0.0179 Hz and a reduced frequency of 0.1. Roll angles were measured as $\pm 30.2^\circ$.

The forced oscillation test results clearly demonstrated ExpertVision's capability to precisely measure dynamic motion from videotape information. The ability to identify secondary effects, like hysteresis in the forced oscillation mechanism, proved that the system was capable of detecting similar behavior in the wing rock experiments to follow. The excellent repeatability of roll acceleration versus ϕ and its hysteresis showed that smoothing and differentiating the ϕ time history did not mask the nonlinear effects of the motion.

Movement of Vortex Core and Burst Points

Visual observation of the vortex cores during a forced roll oscillation revealed that the fluid in the core tended to remain fixed in space initially. After a short time delay, the core was apparently influenced by the pressure field around the moving wing and began to follow the rolling motion. However, the lag in the movement of the vortex was quite noticeable and highly dependent upon the reduced frequency of oscillation.

One of the most interesting features of vortex-model interactions noted during forced roll oscillations was the relationship of the vortex burst points to ϕ . Figs. 55-57 show such data for the 70° wing operating at $\alpha_s = 25^\circ$ for three reduced frequencies. The vertical axis in these plots is the burst point location less the mean burst point location at $\phi = 0^\circ$. For the lowest frequency (Fig. 55), as the model rolled toward a vortex, the burst point moved toward the leading edge after a short time delay. This movement was consistent with static wind tunnel data presented by Jun and Nelson²⁶ which showed that the vortex burst point on the side of the downgoing wing moved closer to apex as the ϕ increased up to 30° . When the roll direction reversed, again after a short time delay (approximately 10% of the period), the burst point moved aft. For higher frequencies (Figs. 56 and 57), the time delay grew and completely altered the trend. At both higher frequencies, the burst point was still moving forward as the wing started to roll away from the vortex. Apparently, the time delay between the movement of the lifting surface and movement of the vortex core was a very important factor in this relationship and,

Fig. 55 Phasing of burst point and ϕ , $k = 0.1$.Fig. 56 Phasing of burst point and ϕ , $k = 0.26$.

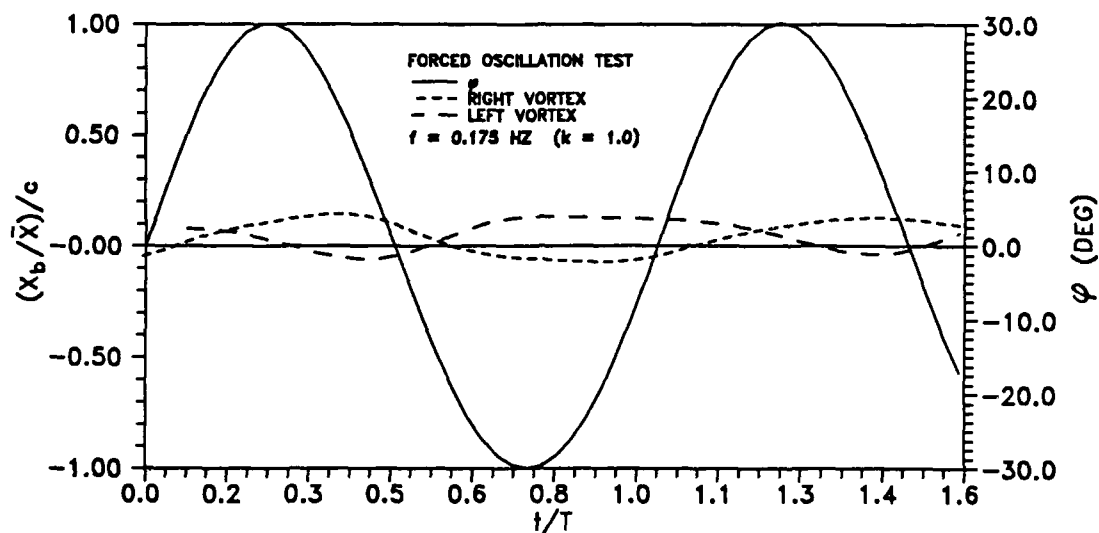


Fig. 57 Phasing of burst point and ϕ , $k = 1.0$.

therefore, may be the key to predicting this feature of vortex motion. The important point, for the purpose of validating the use of ExpertVision, was that the system readily quantified this behavior. Both time delays and amplitudes of burst movement for a given forced roll oscillation frequency were part of the information collected. The period of the burst point oscillation was roughly equal to that of the roll oscillation, as would be expected, considering the dependence of burst point on ϕ .

The amplitude of the burst point movement diminished as forcing function frequency increased. Video data quantified and confirmed that qualitative observation, with peak amplitudes decreasing as shown in Fig. 58. Additionally, the phasing between the model and the burst point location was extracted from Figs. 55-57. The phase difference was plotted in Fig. 59. If this phase increment was taken as the fraction of the roll oscillation period in each of these plots, the resulting data also showed trends that corroborated qualitative observations. At low frequencies, the burst point stayed quite close to the mean position. In Fig. 59, this behavior was

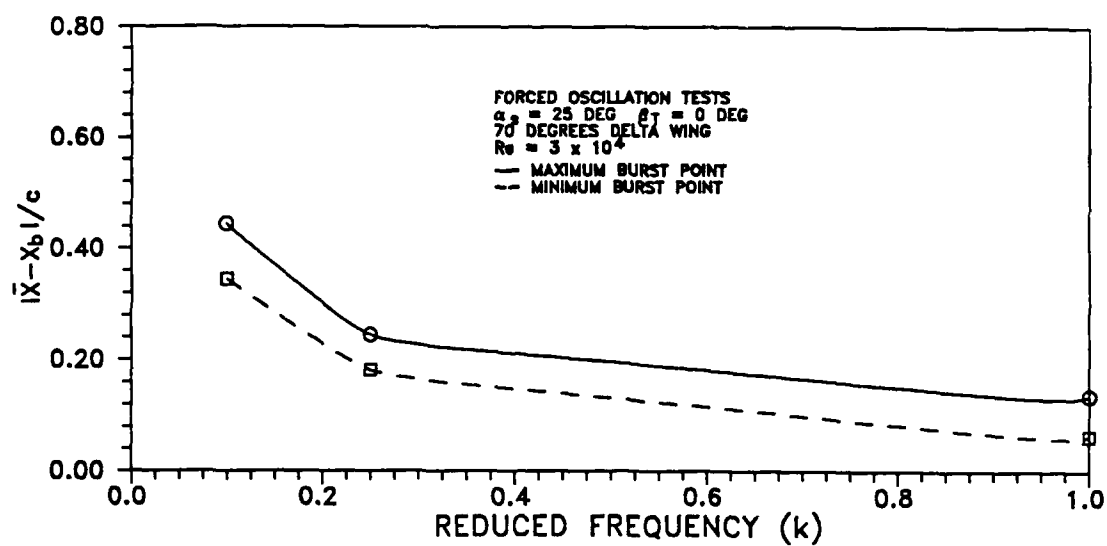


Fig. 58 Burst point location and reduced frequency.

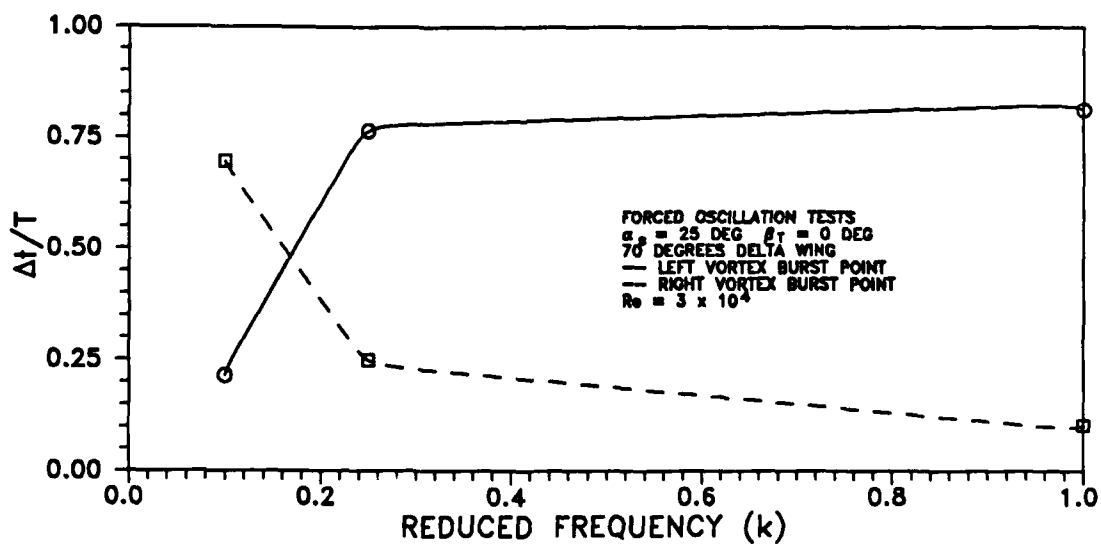


Fig. 59 Burst point phase lag and reduced frequency.

indicated by phase differences tending to either 0 or 1 (that is, with wing fixed, there would be no phase difference). However, phase shift quickly became about 20% of the oscillation period as reduced frequency increased. If k increased further, the phase shift also increased. However, as k increased above 0.25, the rate of change of phase angle dropped drastically. Obviously, to completely define these curves, forced oscillation tests at several more frequencies must be conducted. Nevertheless, the video-based motion analysis tool provided useful and thought-provoking data, which until now has not appeared in the literature.

Velocity Measurements

While measurement of vortex core velocities on a stationary delta wing was a significant achievement, such measurements were also performed during the forced oscillation tests. A sample of those measurements at given streamwise locations during the roll oscillations is given in Fig. 60. Obtaining these velocities was tedious and required the use of the 200 frames/sec video data rather than the 60 frames/sec data. Velocities were obtained during the forced

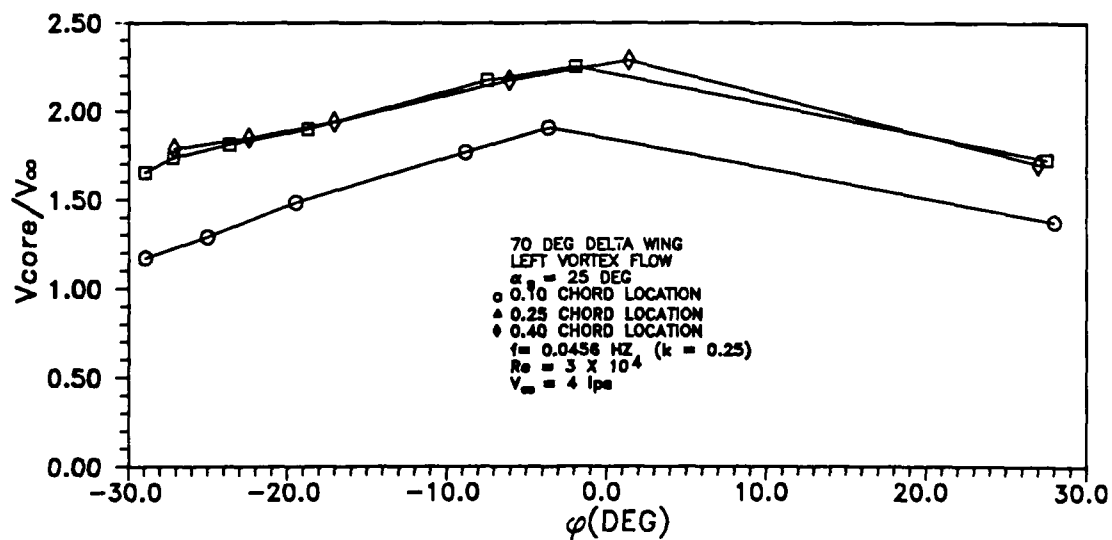


Fig. 60 Forced oscillation vortex core velocity and ϕ .

oscillation test since, at a frequency of 0.456 Hz, the model moved an average of only 0.027° in roll from one frame to the next. Therefore, the velocity calculated with the dye pulses could be assigned to a ϕ with a high degree of accuracy. The major difficulty in obtaining velocities throughout the oscillations was due to changes in the lighting during the motion. As shown in Fig. 60, there were very little data at the positive roll angles, other than near the maximum value. This loss of data was because of reflections from the 70° delta wing model at $4^\circ < \phi < 27^\circ$. While continuous dye streams used to determine vortex burst points were visible in this region, the small pulses of dye were not. This point emphasized the importance of uniform lighting to achieve optimum results and the need for redundant cameras.

Measured core velocities apparently decreased at any given location during either the downstroke or the upstroke of the wing. In fact, the change in the velocity at any of the three streamwise locations was very nearly linear during the downstroke. At all three locations, velocity decreased approximately 1.5 ips during the 30° downstroke of the left wing of the model. Velocities at 0.25c and 0.4c were virtually identical. Also, the velocities at the 0.25c and 0.40c locations at $\phi = 0^\circ$ were very similar in magnitude to the stationary data presented in Fig. 46. These curves were remarkably regular, smooth, and repeatable, lending additional credibility to the data collection and reduction process. Unfortunately, there were no other experimental or theoretical calculations found in the literature with which to compare these measurements.

Forced oscillation tests clearly demonstrated the capability of ExpertVision to quantify dynamic fluid and model motions simultaneously. This capability is particularly important since data collection is very similar to that employed in obtaining qualitative flow visualization data through video recordings. Other than taking special care to illuminate the test section to insure high contrast between the vortex flow and background throughout the range of wing motion, videotaping procedures are identical.

Summary of Tests

The stationary and forced oscillation tests thoroughly demonstrated the capability of ExpertVision to obtain high quality quantified vortex flow measurements. The position of the

vortex cores and the burst points on the static model compared reasonably well with other experimental data and with analytical predictions. The ability to obtain velocity and acceleration profiles throughout the path of the vortex core was a significant contribution to the data base for vortical flows. Forced oscillation tests demonstrated the capability to simultaneously track leading-edge vortices and motion of the model. Model motion parameters and roll angle displacements were in excellent agreement with inputs set by the tunnel operator. The system also successfully identified subtle phenomena, such as mechanical hysteresis in the forced oscillation apparatus. Altogether, these tests provided the necessary validation of the system for use in quantifying the movement of the leading-edge vortices and model motion during wing rock, with a reasonable expectation of acquiring high quality, informative data. Chapter V presents the results of that phase of the research.

CHAPTER V

DISCUSSION OF WING ROCK RESULTS

This chapter discusses the results of the wing rock study conducted on an 80° slender delta wing in both water and wind tunnels. A summary of the tests was presented in Tables 6 and 7 in Chapter III. Comparisons of the data with results from a single degree-of-freedom mathematical model are provided throughout the chapter. The water tunnel tests were all performed at $\alpha = 35^\circ$ for velocities of 4 ips to 10 ips. In these experiments, the leading-edge vortices and the model motion were simultaneously tracked. The wind tunnel study consisted of a much larger range of test conditions; however, no quantified information on the vortex movements was obtained. The discussions are presented under the three major headings of water tunnel tests, wind tunnel tests, and water and wind tunnel test comparisons.

Water Tunnel Test Results

The water tunnel study was conducted with the primary objective of simultaneously analyzing the motion of an oscillating wing and the movement of associated leading-edge vortices during wing rock. The water tunnel was ideal for such a study since the 80° delta wing experienced wing rock at high angles of attack in the water and the vortex flows could easily be illuminated with dye for flow visualization. ExpertVision provided an excellent means of nonintrusively recording and analyzing these phenomena. The ability to construct roll angle time histories without appendages built onto the model, as in the Levin and Katz^{24,25} study, or below the model, as used by Nguyen, Yip, and Chambers,²³ permitted the testing of a true delta wing configuration.

Summary of Test Methods

All of the wing rock tests were performed at $\alpha = 35^\circ$ at flow velocities of 4, 6, and 10 ips. The velocities corresponded to Reynolds numbers of $3 \times 10^4/\text{ft}$, $4.5 \times 10^4/\text{ft}$, and $7.5 \times 10^4/\text{ft}$, respectively. The motion was videotaped from the side and from the top of the wing with 200 Hz

cameras once the limit cycle had been established. A third 60 Hz camera was in place during the 4 ips test, providing a view from behind the model through the glass at the end on the water tunnel. The side camera view was used to measure roll angle as discussed in Chapter III. The rear camera also provided an excellent check on the roll angle measurements for the 4 ips test. Data were recorded at time increments as small as 0.005 seconds; however, due to the relatively low roll rates, increments of 0.025 seconds were more than sufficient. Smoothing of the data was accomplished using the Tukey window algorithm in EV, although polynomial fits and low band-pass filters were also used for comparisons. Roll rates and roll accelerations were calculated by central differencing the smoothed roll angle and roll rate time histories, respectively.

General Observations

In each of the tests, the model immediately began to oscillate and rapidly achieved the limit cycle as the flow was brought up to the desired freestream velocity. As the model oscillated in roll, there was an alternate lift-off and reattachment of leading-edge vortices. The vortices also alternately moved inboard and outboard of the wing during the oscillations. Vortex lift-off and reattachment did not occur instantaneously over the entire wing, but began at the apex and propagated back as the rolling motion continued. The vortex trajectories, therefore, were time-varying three-dimensional curves in space, rather than straight lines. Vortex bursting was also observed during wing rock and it changed chordwise locations as the model rolled. Hysteresis existed in both the vortex motions and the movement of the burst point locations. These general observations demonstrated the EV capability to simultaneously track both the model motion and vortex movements during wing rock. The following sections present the quantified results and analysis for the water tunnel experiments.

Model Motion

A considerable amount of time was expended in determining and analyzing the motion of the delta wing during wing rock in the water tunnel. It was essential to the success of this study to have confidence in the results of these initial wing rock tests since the quantification of such

experiments in the water tunnel had never been done before. As a result, the A/D conversion of videotape segments was performed many times for different threshold settings on the video processor to achieve the highest quality raw data files possible. Since the tests were allowed to run for extensive periods of time, different portions of the runs were analyzed to assess the repeatability of the phenomenon. To examine the effects of smoothing on a specific roll angle time history, the size of the Tukey window was varied to find the optimum number of points needed to achieve a satisfactory second derivative, $\ddot{\phi}$, while not eliminating important information due to oversmoothing. Too little smoothing yielded unacceptable, noisy $\ddot{\phi}$ time histories, while too much smoothing made the results appear as pure sinusoidal motions, without hysteresis in the rolling moments.

A typical roll angle time history for the 4 ips test is plotted in Fig. 61. The symbols represent every fourth raw data point and the solid line is the data smoothed with EV using a window size of 51 points. The maximum difference between the raw and smoothed data points

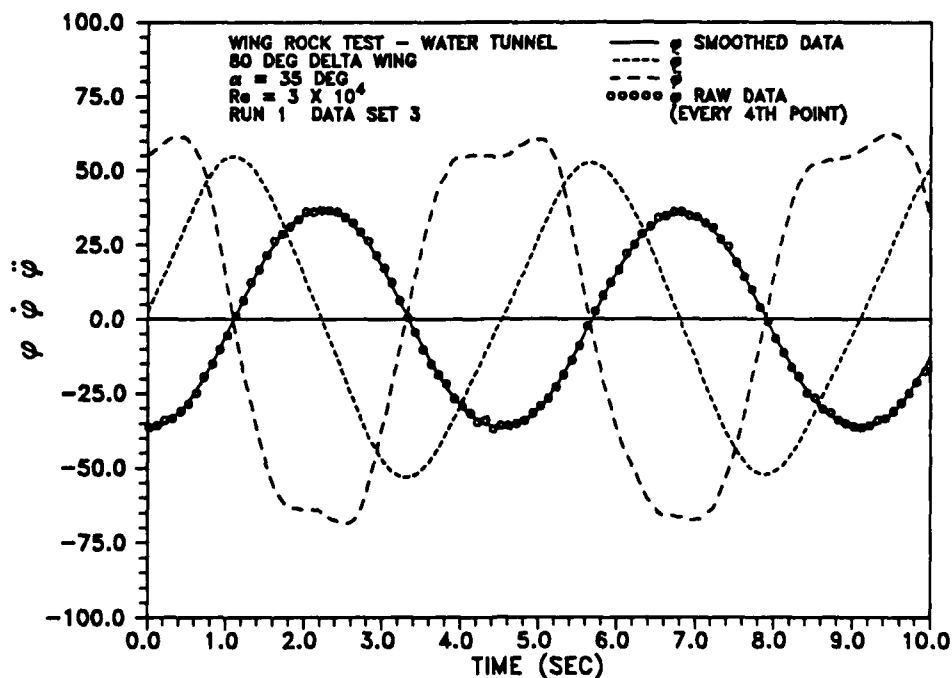


Fig. 61 Wing rock motion parameters, $V_\infty = 4 \text{ ips}$ (first run).

was 0.91° , with an average deviation for all points of 0.24° . This level of agreement was quite good and was consistent with results obtained by Katz and Levin,²⁵ who fitted their data with a cubic spline. They reported maximum differences of 1° . The average period of the oscillation was 4.55 seconds, which was very repeatable from cycle to cycle (within ± 0.05 seconds for the cycles examined). The reduced frequency, k , calculated using

$$k = \frac{\Omega b}{2 V_\infty} \quad (25)$$

(where Ω is the average frequency in radians/second) was 0.61. Roll angles varied from -37° to 37° with maximum variations usually less than 0.5° ; however, they were as large as 3.5° in one instance. In general, the oscillations were symmetric about $\phi = 0^\circ$, indicating symmetry in the model and test arrangement. Roll rate and roll acceleration histories (units of $^\circ/\text{sec}$ and $^\circ/\text{sec}^2$, respectively) determined from the smoothed roll angle data are also shown in Fig. 61. An important result which can be readily observed from the roll acceleration trace was that $\ddot{\phi}$ was larger after ϕ had passed through its maximum magnitude than before. This phase difference was indicative of a hysteresis in roll acceleration with ϕ , which will become more obvious in subsequent plots.

A phase portrait (Fig. 62) of the 4 ips data showed an isolated closed path, a classical limit cycle. Roll rates ranged from approximately $-53^\circ/\text{sec}$ to $54.7^\circ/\text{sec}$, with an average magnitude based on all cycles of $53.1^\circ/\text{sec}$. Had the roll angle history been a pure sinusoidal variation of the form

$$\phi = 37 \cos [(2\pi/4.55) t] \quad (26)$$

the roll rate would have been

$$\dot{\phi} = -51.09 \sin [(2\pi/4.55) t] \quad (27)$$

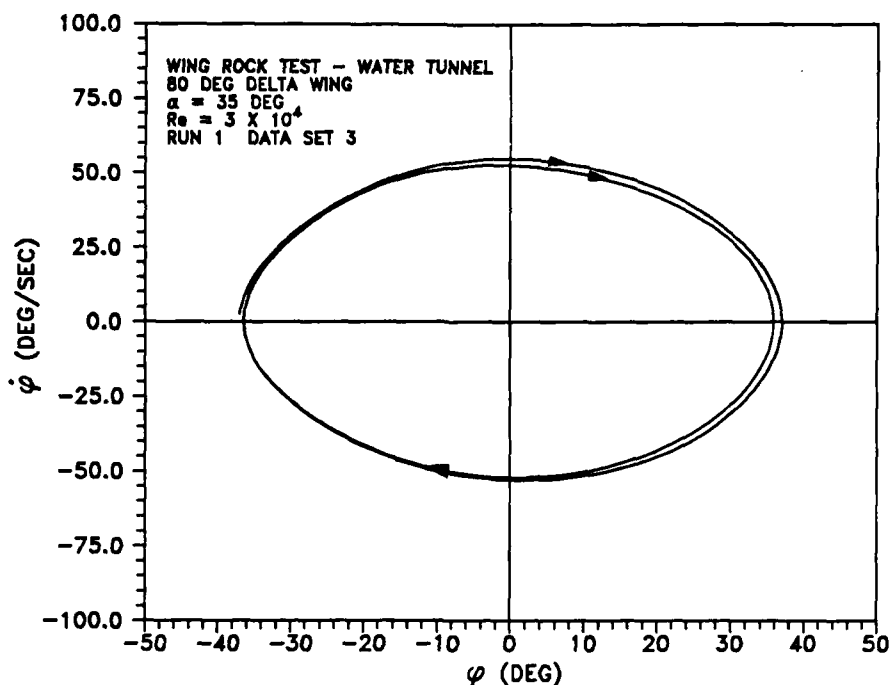


Fig. 62 Wing rock phase portrait, $V_{\infty} = 4$ ips (first run).

with a maximum roll rate magnitude of $51.09^\circ/\text{sec}$. This comparison indicated a difference of approximately 3.9% between the maximum roll rate of the measured data and the calculated value assuming a sinusoidal variation in ϕ .

A typical $\ddot{\phi}$ versus ϕ plot for a $V_{\infty} = 4$ ips test (Fig. 63) clearly revealed the hysteresis discussed earlier. The two cycles of the nearly periodic trajectory were quite close but did not coincide, which was not surprising since the $\ddot{\phi}$ points were the numerical second derivatives of measured roll angles and there were some variations noted in maximum roll angles from cycle to cycle. The arrows on the curves show the direction of motion and therefore indicate increasing time. Each cycle had three loops; that is, the curve crossed itself twice during a cycle. To more clearly describe the loops, a single cycle of the same data is presented (Fig. 64). The outer two loops at the higher ϕ were clockwise while the interior loop was counterclockwise. The outer two loops indicated that the magnitude of the acceleration was larger after it passed through the maximum positive or negative ϕ than before, as previously stated during examination of Fig. 61.

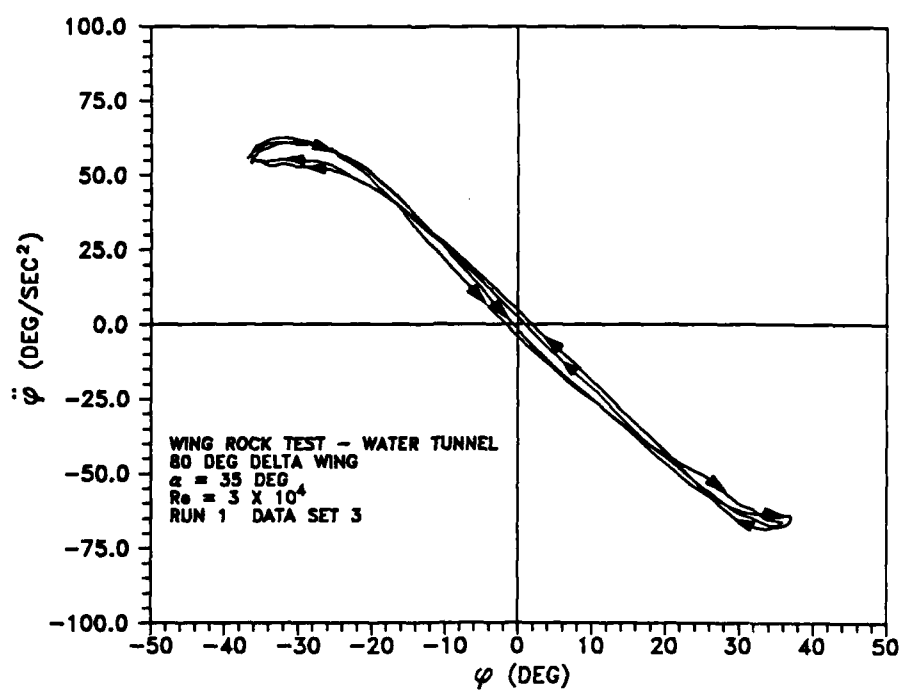


Fig. 63 Roll acceleration versus ϕ , $V_\infty = 4$ ips (first run).

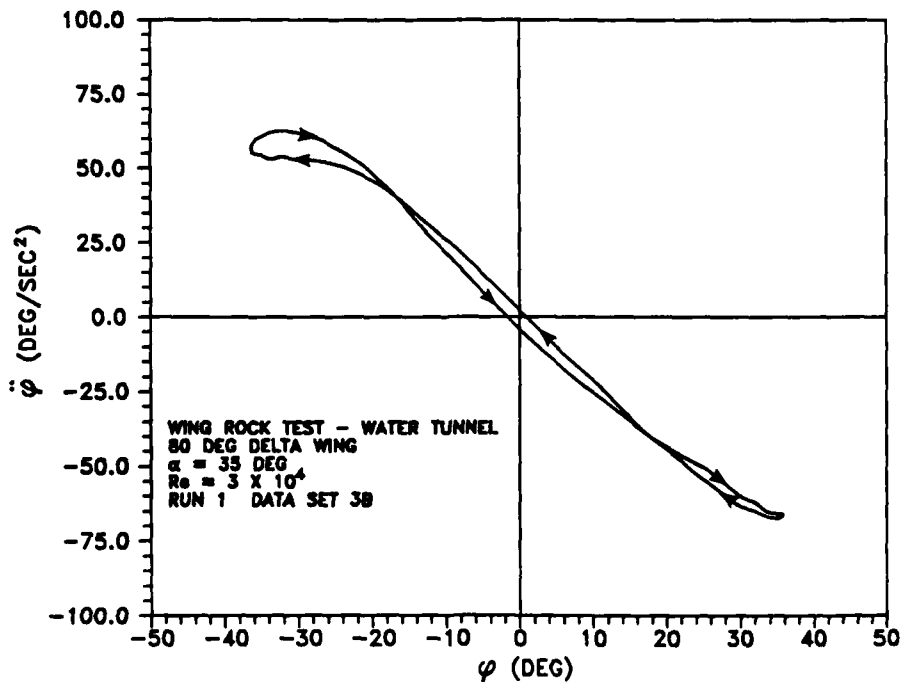


Fig. 64 Roll acceleration versus ϕ cycle, $V_\infty = 4$ ips (first run).

The interior counterclockwise loop showed that the wing had a positive acceleration at $\phi = 0^\circ$ for decreasing ϕ and a negative roll acceleration for increasing ϕ . The roll acceleration data ranged from $-66.1^\circ/\text{sec}^2$ to $62.5^\circ/\text{sec}^2$, with an average magnitude for all cycles of $64.6^\circ/\text{sec}^2$. Assuming a sinusoidal variation in ϕ as given in equations (26) and (27), the roll acceleration could be estimated as

$$\ddot{\phi} = -70.6 \cos [(2\pi/4.55)t] \quad (28)$$

where the maximum magnitude is $70.6^\circ/\text{sec}^2$. The difference between the actual data and the maximum magnitude of equation (28) was approximately 9%.

A very important calculation for this study was the rolling moment trace of the wing rock cycle, which was computed from the single degree-of-freedom equation (12). That equation directly related $\ddot{\phi}$ and aerodynamic rolling moment, C_ℓ . A typical trace for the $V_\infty = 4$ ips test (Fig. 65) showed that the results were just a scaled version of the $\ddot{\phi}$ plot (Fig. 63). Notice that these results were significantly different from Nguyen's wind tunnel data (Fig. 10).²³ Even though

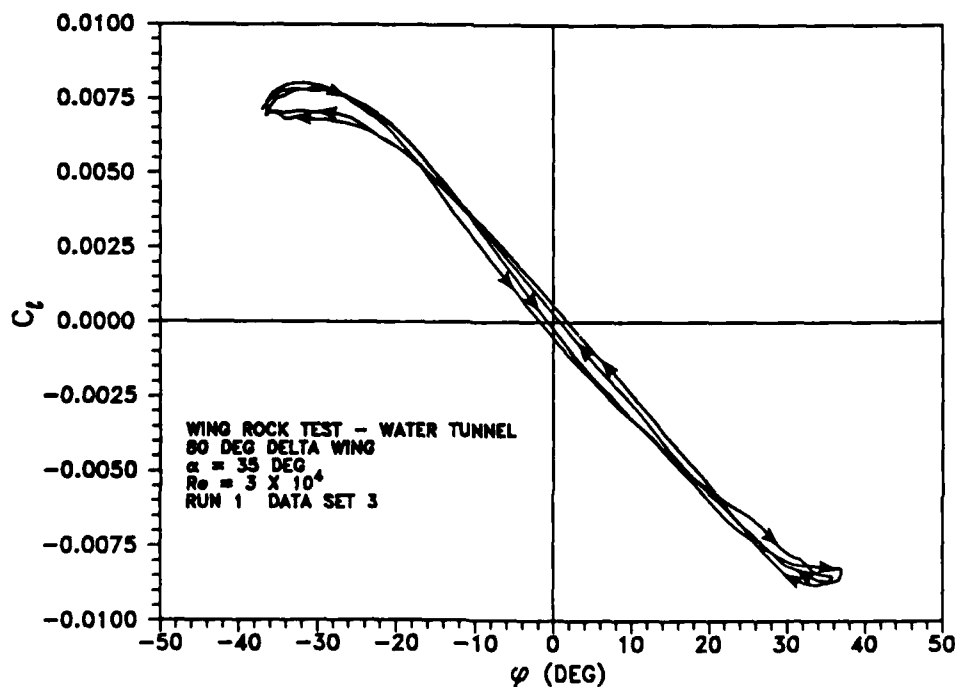


Fig. 65 Aerodynamic rolling moment versus ϕ , $V_\infty = 4$ ips (first run).

there was a 3° difference in α between the two tests and the wind tunnel experiments were performed at a Reynolds number over an order of magnitude higher, such a marked difference was surprising. Not only was the slope of the curves substantially different, but hysteresis directions were opposite. This result was extremely puzzling since both models were 80° delta wings and had quite similar limit cycle wing rock. Based on the energy analysis used by Nguyen, Yip, and Chambers²³ (Appendix B), where

$$\Delta E = q S b \int C_{\ell}(\phi) d\phi \quad (29)$$

the water tunnel results showed a stabilizing energy increment ($\Delta E < 0$) at small ϕ and a destabilizing one ($\Delta E > 0$) at large ϕ . This effect was just the opposite of the wind tunnel results and conflicted with the theory that unstable roll damping at smaller sideslip angles (or ϕ) and stable roll damping at larger sideslip angles were the primary driving mechanisms of wing rock. Despite the differences in the energy results between the water and wind tunnel tests, both sets of data supported the idea that the total energy exchanged between the flow and the wing for a complete cycle must be zero for a limit cycle to exist. This conclusion was based on the qualitative assessment that the areas of the outer two loops were approximately equal to the area of the interior loop. Clearly, a limit cycle existed in the water tunnel even though the roll damping causative explanation for the limit cycle was damaged—perhaps beyond repair. Considering the important implications of these water tunnel results, a large amount of time and effort was expended verifying that the hysteresis and the C_{ℓ} were correct.

First, the smoothing algorithm was questioned. Despite the fact that the EV smoothing routine appeared to yield good results, other smoothing techniques were employed to assess effects on hysteresis and roll magnitudes. One method filtered the raw ϕ data with a second order low pass Butterworth filter using a routine in MATRIX_x. An example of such filtering for the 4 ips run condition is shown in Fig. 66. The roll rates and roll accelerations had a few more "bumps" in the data, however, the magnitudes and general shapes were similar to those obtained with EV smoothing. The more important result was seen in the $\ddot{\phi}$ versus ϕ data (Fig. 67). While

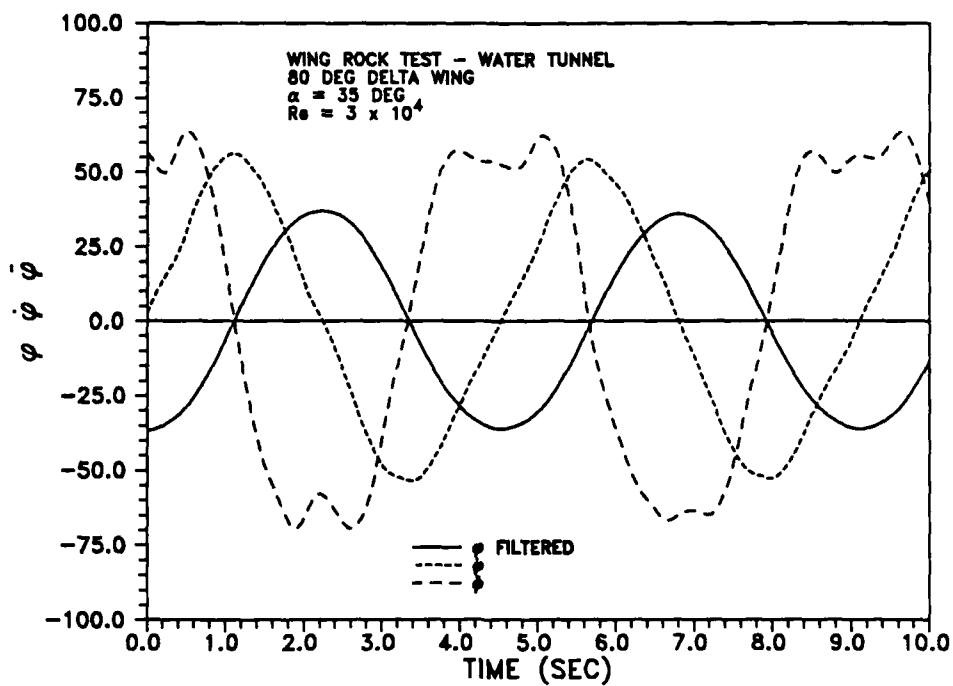


Fig. 66 Wing rock motion parameters with low pass Butterworth filtering.

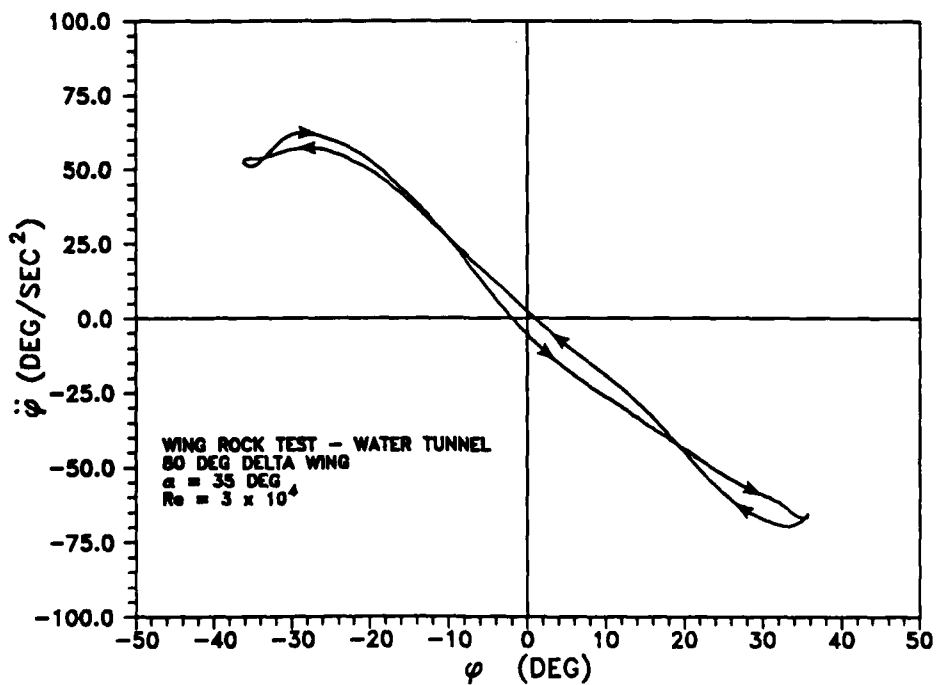


Fig. 67 Rolling acceleration versus ϕ using Butterworth filtering.

there are some differences between this plot and Fig. 63 employing EV smoothing of the ϕ , the important parameters of ϕ magnitudes and direction of hysteresis were very similar. Katz and Levin²⁵ reported similar differences in the appearance of their data when changing the order of their spline curve fit. Such changes were not at all surprising since any alteration of the ϕ history will be seen in the shapes of its first and second derivatives. The raw ϕ data were also fitted with a 10th order polynomial from which the first and second derivatives were taken to yield roll rates and roll accelerations, respectively. Using this procedure, the data was smoother than when using the other two methods; however, what little hysteresis was present in the $\ddot{\phi}$ versus ϕ and C_ℓ versus ϕ curves matched the trends in the other algorithms. The magnitudes were also in agreement with the results from the other methods of smoothing. Based on the different techniques and amount of smoothing examined, the direction of hysteresis was real and not artificially created through the smoothing process.

The C_ℓ versus ϕ information obtained for the forced oscillation tests, discussed in Chapter IV, also provided confidence in the ability to identify hysteresis in the model motion parameters. These tests demonstrated a very repeatable hysteresis (Figs. 51 and 54) due to the mechanical forced oscillation drive apparatus, which was in the opposite direction of the hysteresis in the wing rock experiments. These two different results indicated that the video-based method of determining model rolling motion readily identifies hysteresis, should it exist, in either direction.

Figs. 68-71 present data from a second wing rock run conducted at $V_\infty = 4$ ips. The smoothing parameters were the same as used on the first run, discussed above. The period of oscillation and roll angle magnitudes (Fig. 68) were identical to those in the first run, demonstrating excellent repeatability of the data. Both the phase portrait (Fig. 69) and $\ddot{\phi}$ versus ϕ data (Fig. 70) were virtually indistinguishable from the results of the earlier test at the same conditions. The C_ℓ versus ϕ plot (Fig. 71) also contained data taken from a random cycle with the 60 Hz camera positioned at the end of the water tunnel. The two curves were not from the same wing rock cycle since there was no provision made for time correlating data from the side and end camera views. This comparison was important since the end view showed similar

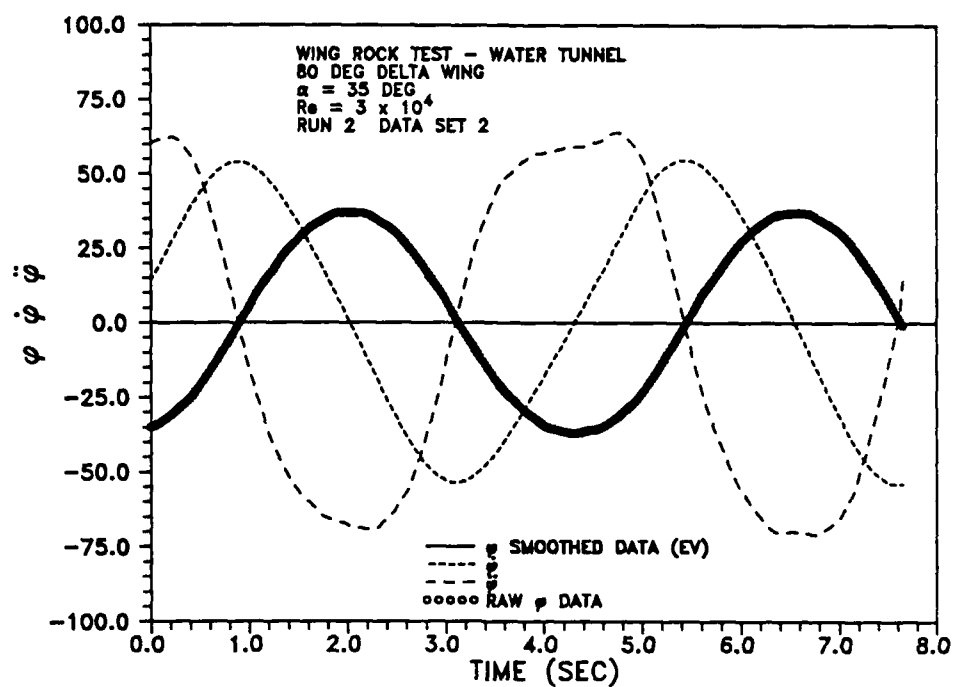


Fig. 68 Wing rock motion parameters, $V_\infty = 4$ ips (second run).

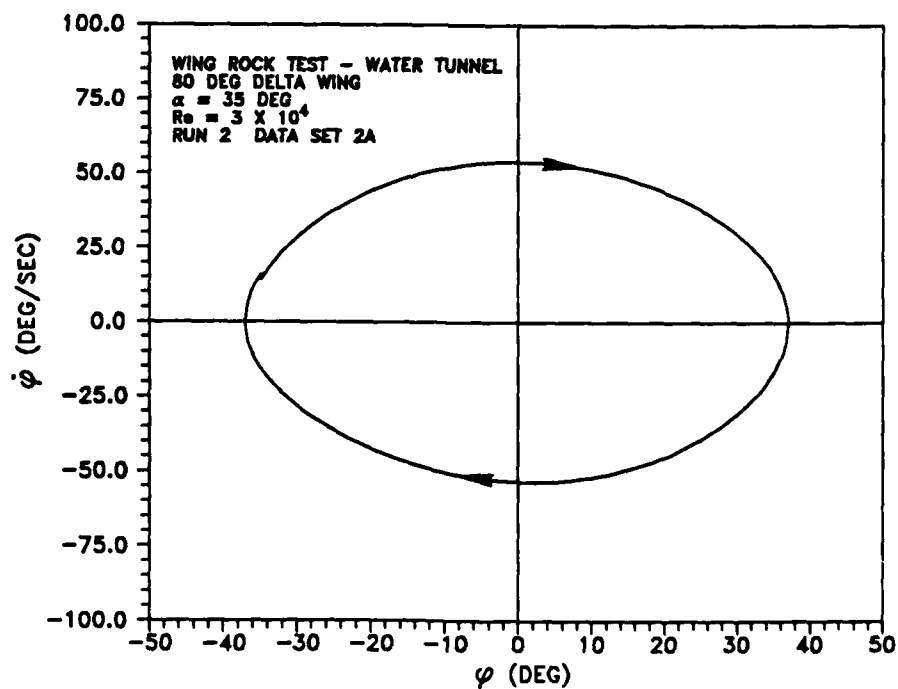


Fig. 69 Wing rock phase portrait, $V_\infty = 4$ ips (second run).

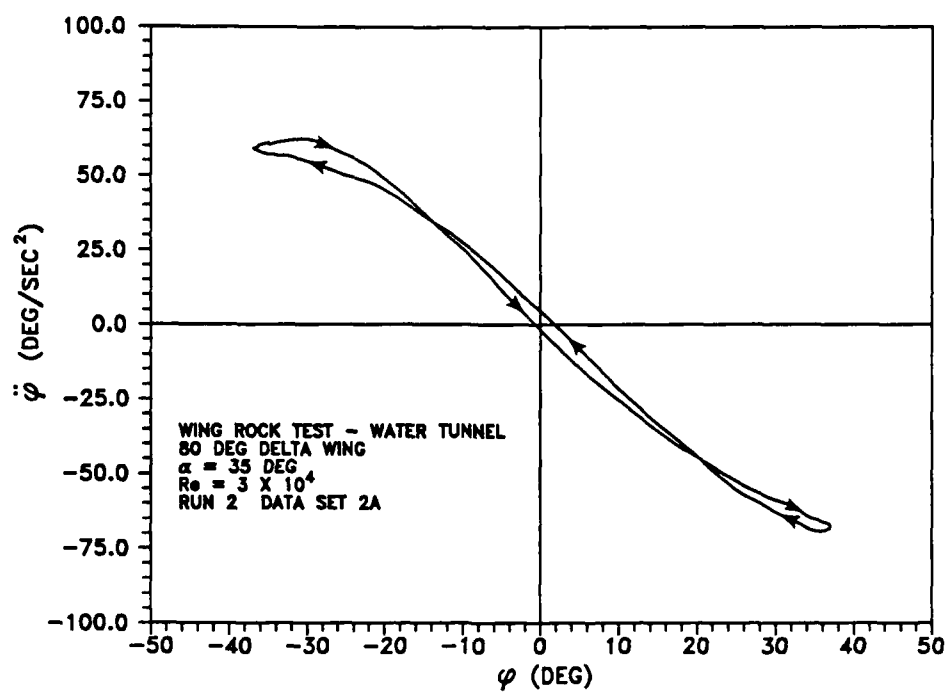


Fig. 70 Roll acceleration versus ϕ , $V_\infty = 4$ ips (second run).

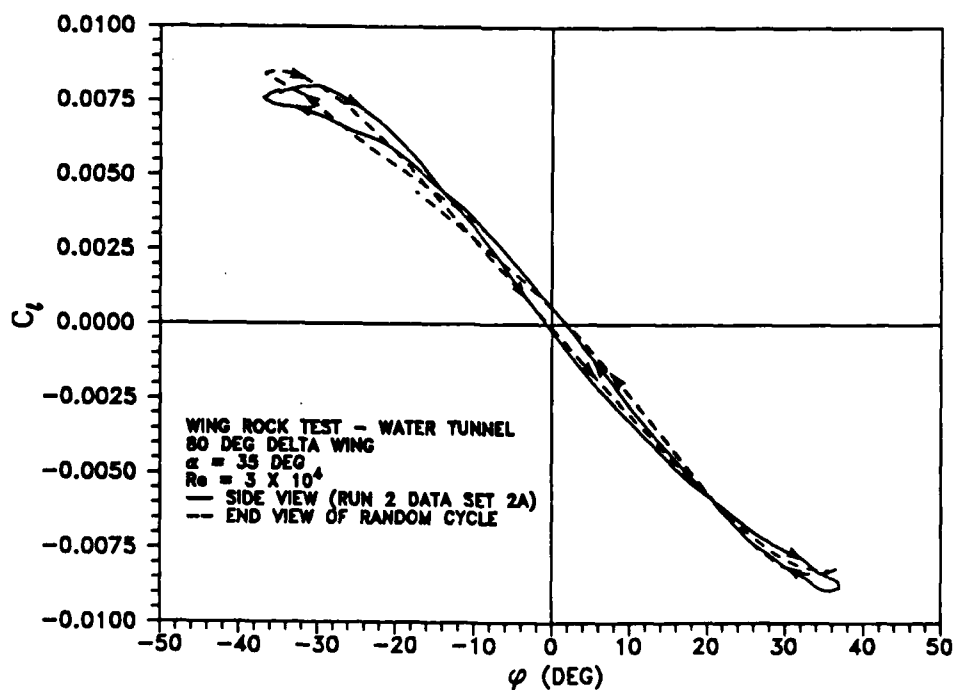


Fig. 71 Aerodynamic rolling moment versus ϕ , $V_\infty = 4$ ips (second run).

hysteresis and C_l magnitude information, even though it was taken from a completely independent perspective. This result further proved that hysteresis was not simply introduced from the optical method of obtaining ϕ data.

Wing rock motion parameters for the $V_\infty = 6$ ips test, $Re = 4.5 \times 10^4$, are shown in Fig. 72. Once again, a 51 point EV smoothing of the ϕ time history was employed in computing roll rates and roll accelerations. The obvious effect of increased flow velocity was a decrease in the period of oscillation to 2.861 seconds. This change resulted in an average frequency of oscillation, Ω , of 2.196 rad/sec compared to 1.381 rad/sec for the 4 ips test. While the actual frequency had increased by 59%, reduced frequency for the $V_\infty = 6$ ips was 0.645 compared to 0.61 for the 4 ips test, an increase of only 5.7%. Roll angles varied from -37.4° to 36.6° , with an average maximum magnitude of 36.6° . It is interesting to note that while there was a substantial difference in the period of oscillation due to the higher freestream velocity, the magnitudes of ϕ were very similar. The roll rates ranged from $-84^\circ/\text{sec}$ to $83^\circ/\text{sec}$, with an average magnitude of

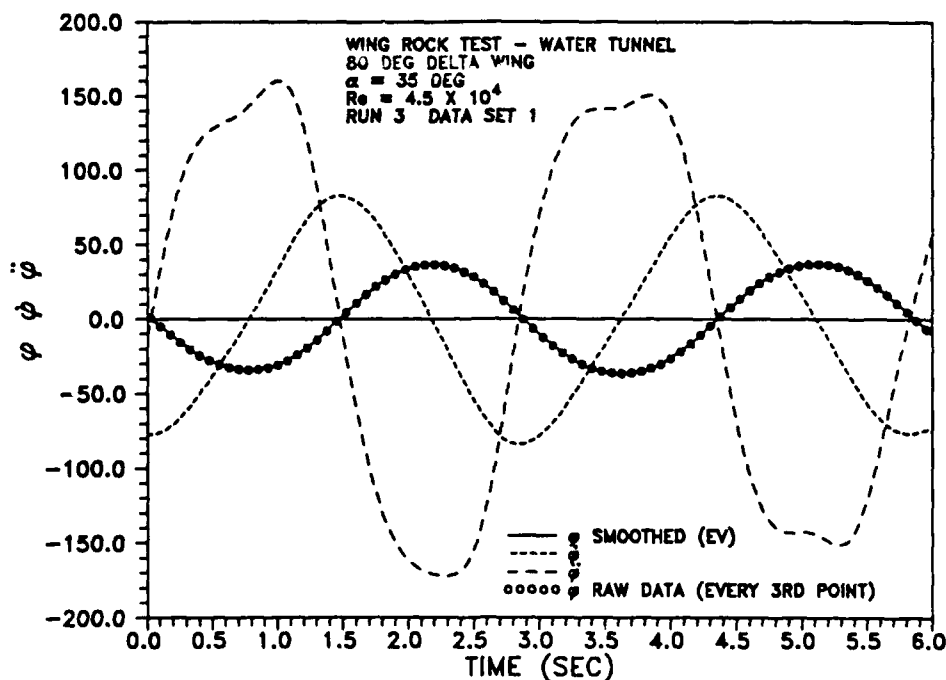


Fig. 72 Wing rock motion parameters, $V_\infty = 6$ ips.

80.7°/sec based on all the cycles examined. Had the roll angle history been a true sinusoid with the measured maximum ϕ magnitude and period, then the maximum roll rate would have been

$$|\dot{\phi}|_{\max} = A\Omega = 36.6 (2\pi/2.861) = 80.38^\circ/\text{sec} \quad (30)$$

Therefore, the average measured maximum roll rate was less than 1% higher than the value for a sinusoidal variation in ϕ . The roll accelerations varied from -172.1°/sec² to 160.4°/sec², with an average maximum magnitude of 161.2°/sec². If the rolling motion was a pure sinusoid, the maximum magnitude of the roll acceleration would have been

$$|\ddot{\phi}|_{\max} = A\Omega^2 = 36.6 (2\pi/2.861)^2 = 176.5^\circ/\text{sec}^2 \quad (31)$$

As a result, the sinusoidal rolling motion assumption yielded a maximum roll acceleration value 9.5% higher than measured experimentally.

The phase portrait (Fig. 73) showed the limit cycle behavior of the roll oscillations as expected. The roll acceleration trace (Fig. 74) had substantially larger magnitudes than were experienced in the lower velocity cases (Figs. 63 and 70). However, while there was a significant difference in $\ddot{\phi}$, a cycle of the C_L versus ϕ plot (Fig. 75) revealed rolling moment magnitudes and hysteresis directions very similar to the 4 ips results (Figs. 65 and 71). It is significant that the tests showed virtually no change in the C_L magnitudes, despite a 50% increase in the freestream velocity. The relevance of this result will become more obvious later in this chapter in the discussion of the aerodynamic derivatives.

The 10 ips velocity free-to-roll test, $Re = 7.5 \times 10^4$, also exhibited a decrease in period, or an increase in frequency, with increasing velocity (Fig. 76). The wing rock period was 1.725 seconds, corresponding to an average frequency of 3.64 rad/sec and a reduced frequency of 0.642. While the actual frequency was 66% higher than for the 6 ips test, the reduced frequency was almost the same, 0.642 as opposed to 0.645. Roll angles varied from -37.4° to 36.6° with an average maximum magnitude of approximately 36.7°, almost identical to values obtained in the 6 ips test. Roll rates ranged from -137.6°/sec to 139.1°/sec, with an average magnitude of approximately 137.8°/sec. A pure sinusoidal motion would have yielded maximum roll rates of

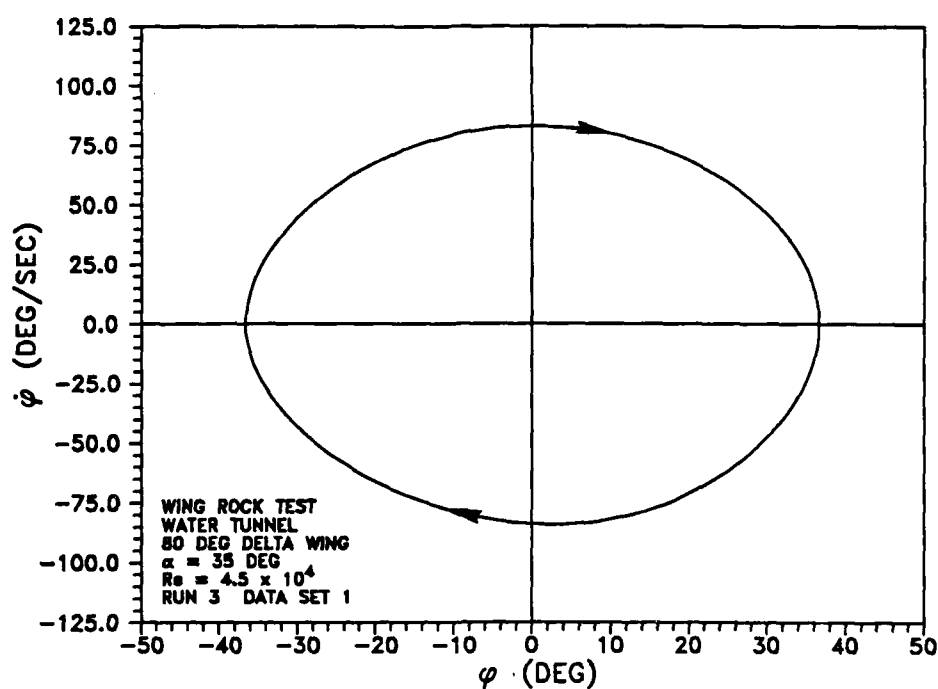


Fig. 73 Wing rock phase portrait, $V_\infty = 6$ ips.

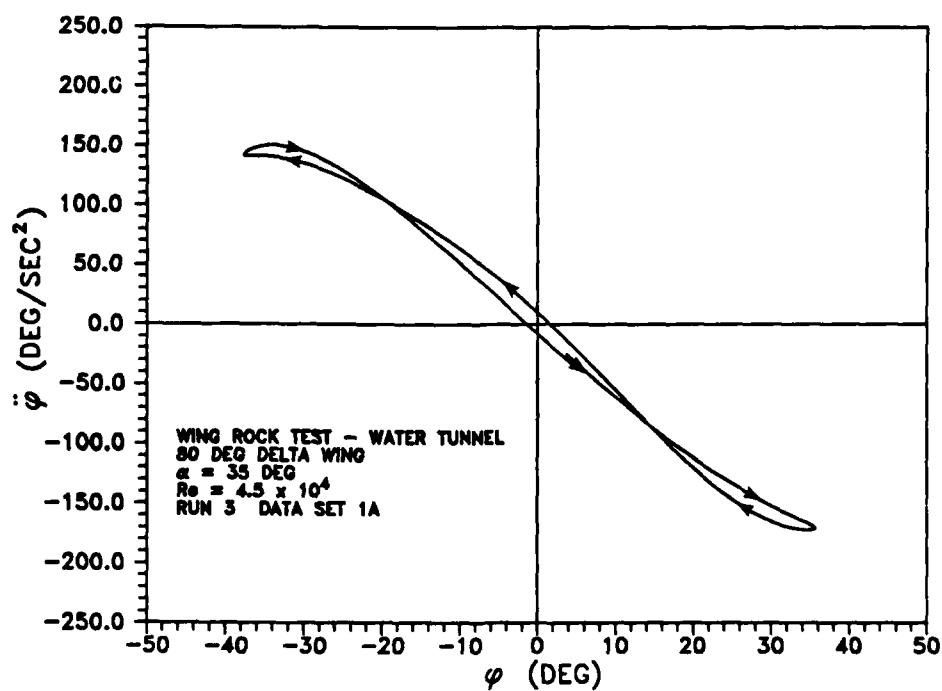


Fig. 74 Roll acceleration versus ϕ , $V_\infty = 6$ ips.

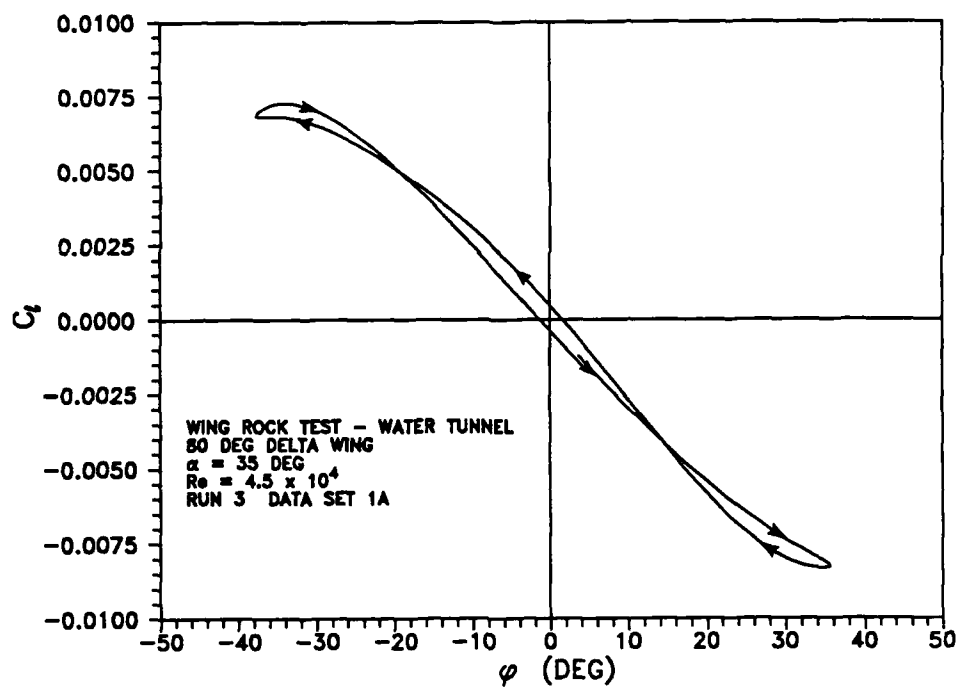


Fig. 75 Aerodynamic rolling moment versus ϕ , $V_\infty = 6$ ips.

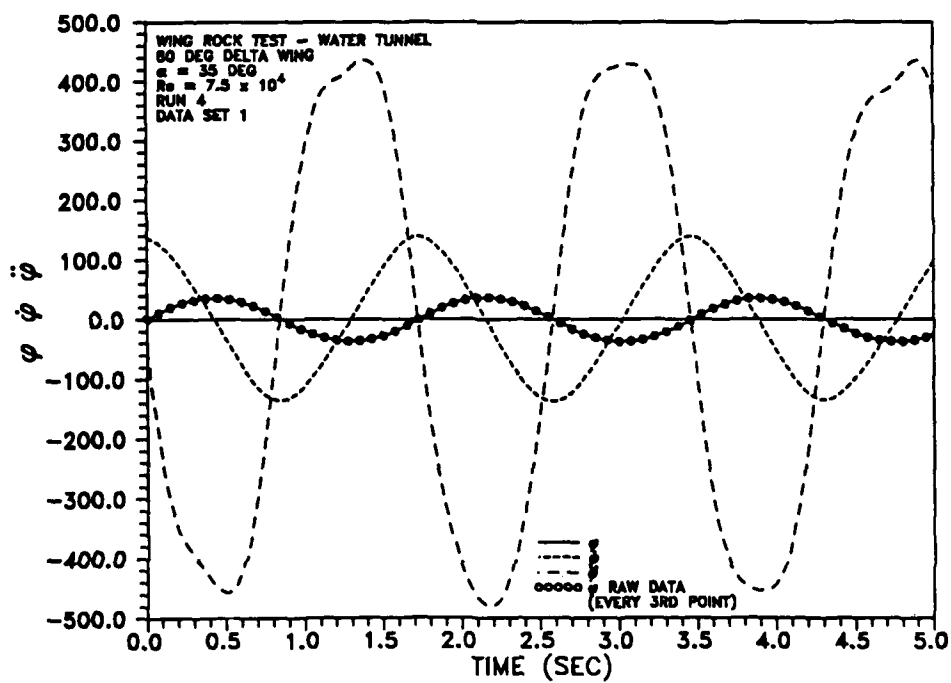


Fig. 76 Wing rock motion parameters, $V_\infty = 10$ ips.

133.7°/sec based on the average measured roll angle magnitude and frequency. The roll accelerations varied from -479.6°/sec² to 436.4°/sec², with an average magnitude of 450.7°/sec². The sinusoidal assumption would have resulted in a maximum roll acceleration magnitude of 486.9°/sec², 8% higher than the measured data.

As in the previous tests, the limit cycle behavior of the model motion could be clearly seen from the phase portrait (Fig. 77). While the magnitudes of ϕ were very similar to the lower velocity tests, roll rates were much larger. The $\ddot{\phi}$ versus ϕ data (Fig. 78) revealed a significant increase in acceleration magnitudes over the lower velocity tests, as already discussed; however, the hysteresis direction was the same. Despite the large differences in the $\ddot{\phi}$, the C_{ℓ} versus ϕ history (Fig. 79) was similar in both magnitude and hysteresis direction to the 4 ips and 6 ips tests. Therefore, C_{ℓ} appeared to be relatively insensitive to the freestream velocity from $V_{\infty} = 4$ ips to $V_{\infty} = 10$ ips.

A summary of phase portraits for the three different freestream velocities is presented in Fig. 80. This comparison showed that roll rates increased with increasing velocity while roll angle magnitudes remained essentially the same. Therefore, the increase in roll rates directly resulted from the higher frequencies. The roll acceleration versus roll rate curves shown in Fig. 81 (itself a phase plot for $\dot{\phi}$) provided another interesting comparison between the tests. This form of a phase plot showed that the closed path moved further from the origin as freestream velocity increased. While the magnitudes of the variables were different for each test, the shape of the curves were very similar. Probably the most important comparison was shown in the C_{ℓ} versus ϕ plot (Fig. 82). As stated earlier, the three curves were similar in both hysteresis direction and roll angle magnitudes. Variations between the traces did exist; however, the differences were similar to those which occurred from cycle to cycle during a given test (Fig. 64). As will be shown in a later section, the similarity between the C_{ℓ} versus ϕ plots indicated that the aerodynamic derivatives of the wing, most notably $C_{\ell\beta}$, were relatively insensitive to velocity and Reynolds number changes for the range spanned by these water tunnel tests.

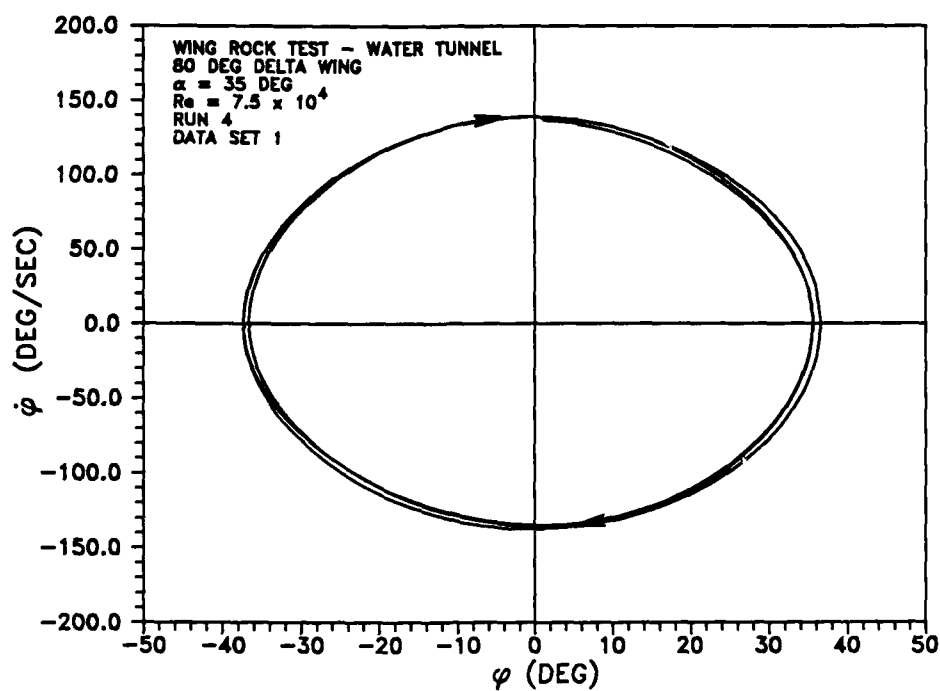


Fig. 77 Wing rock phase portrait, $V_\infty = 10$ ips.

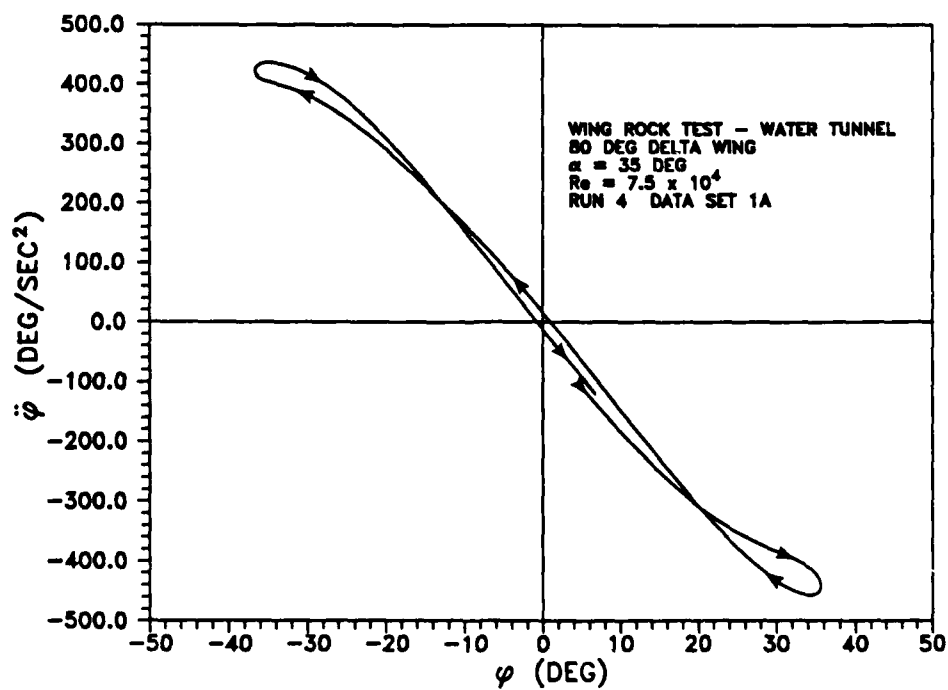


Fig. 78 Roll acceleration versus ϕ , $V_\infty = 10$ ips.

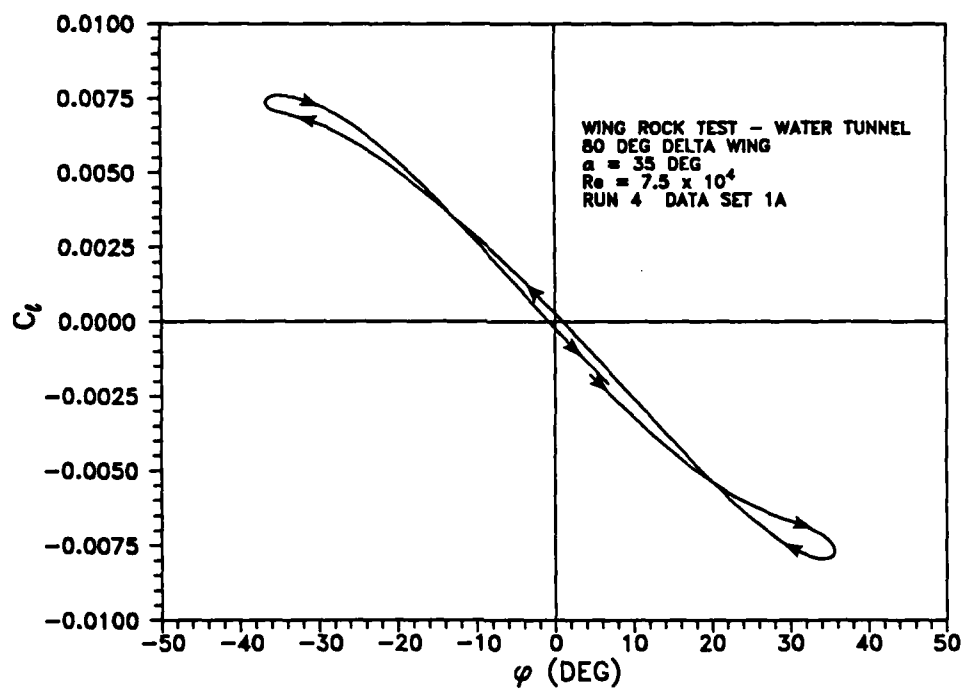


Fig. 79 Aerodynamic rolling moment versus ϕ , $V_\infty = 10$ ips.

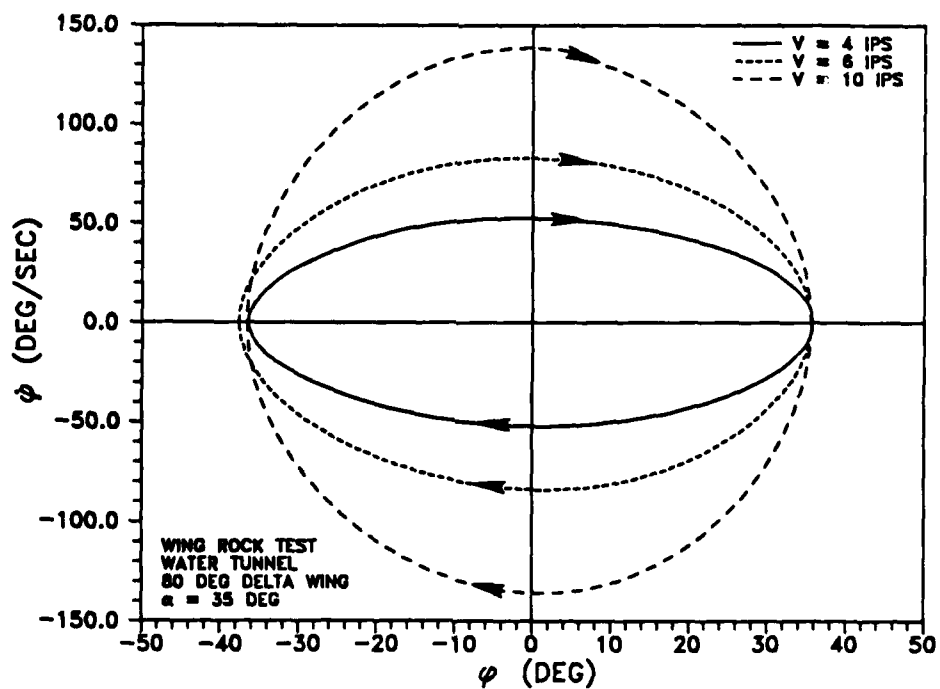


Fig. 80 Phase portrait comparison, water tunnel.

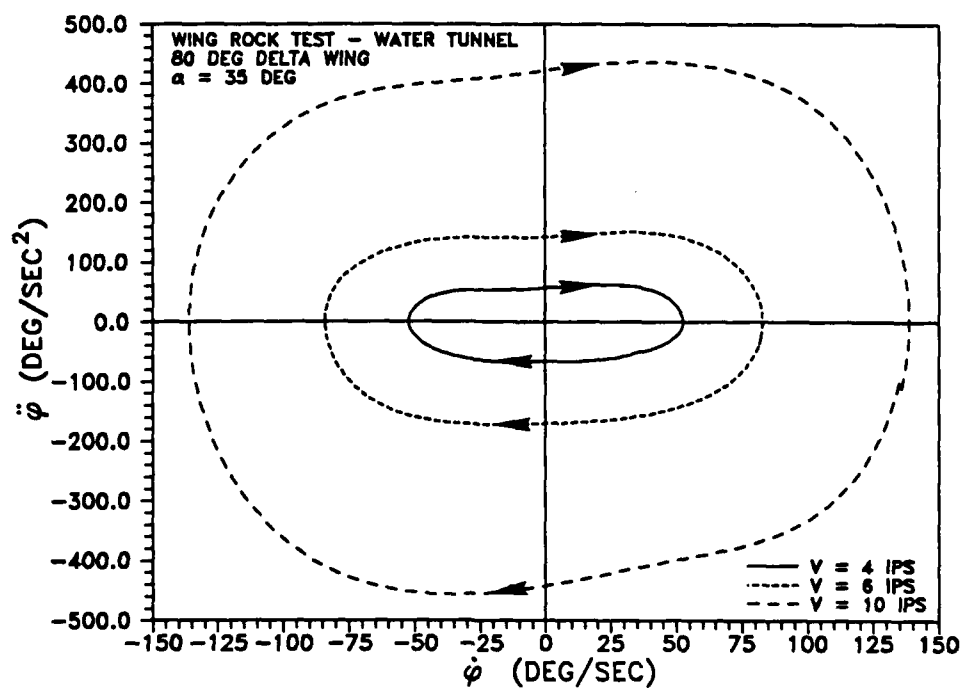


Fig. 81 Roll acceleration versus roll rate comparison, water tunnel.

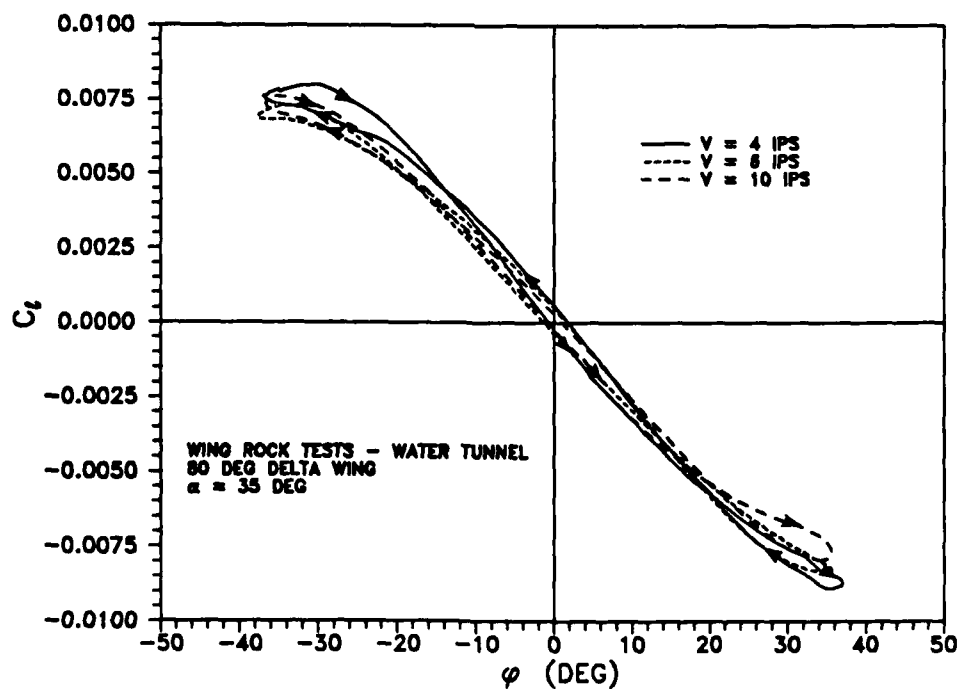


Fig. 82 Aerodynamic rolling moment versus ϕ comparison, water tunnel.

Fig. 83 shows the effects of velocity on wing rock average frequency. Figs. 84 and 85 show the variations of reduced frequency and roll amplitude with Reynolds number, respectively. Results from a NASA-sponsored study conducted in the Eidetics International⁶⁵ water tunnel using the same 80° delta wing model were also plotted on the graphs. Those data agreed very well with the current results. Additionally, wing rock data on a 78° delta wing in a different water tunnel showed similar trends in the frequency variations¹³ (Fig. 83). In summary, both the roll angle magnitudes and the reduced frequencies remained relatively constant for the range of Reynolds numbers and velocities tested in the current research.

Aerodynamic Derivative Extraction

In addition to the general wing rock behavior, important aerodynamic derivatives were extracted from the data and analyzed. Hsu³⁰ simulated wind tunnel wing rock data reasonably well using average aerodynamic derivatives for an 80° delta wing and assuming a sinusoidal variation in the rolling motion. Those simulations suggested that the slope of the C_{ℓ} versus ϕ curve was determined by the $C_{\ell\beta}$ of the wing and the hysteresis was driven by the roll damping, $C_{\ell p}$. The current research found the same result by integrating the nonlinear equation of motion with a fourth order Runge-Kutta algorithm.

The aerodynamic derivatives $C_{\ell\phi}$ and $C_{\ell\beta}$ were related directly by the one degree-of-freedom relation

$$\beta = \sin^{-1} (\sin \alpha_s \sin \phi) \quad (32)$$

where α_s is the angle of attack of the wing at zero sideslip and roll angle. Therefore, the most accurate method of finding the $C_{\ell\beta}$ from the data was to plot C_{ℓ} versus β instead of C_{ℓ} versus ϕ . $C_{\ell\beta}$ was estimated by fitting the C_{ℓ} versus β plot with a 10th order polynomial (Fig. 86) and taking its derivative. Note that the average C_{ℓ} versus β data was almost linear for a large portion of the curve and then decreased in slope at the larger sideslip angles. This change in slope at larger β was consistent with C_{ℓ} versus β data presented in the literature for 80° delta

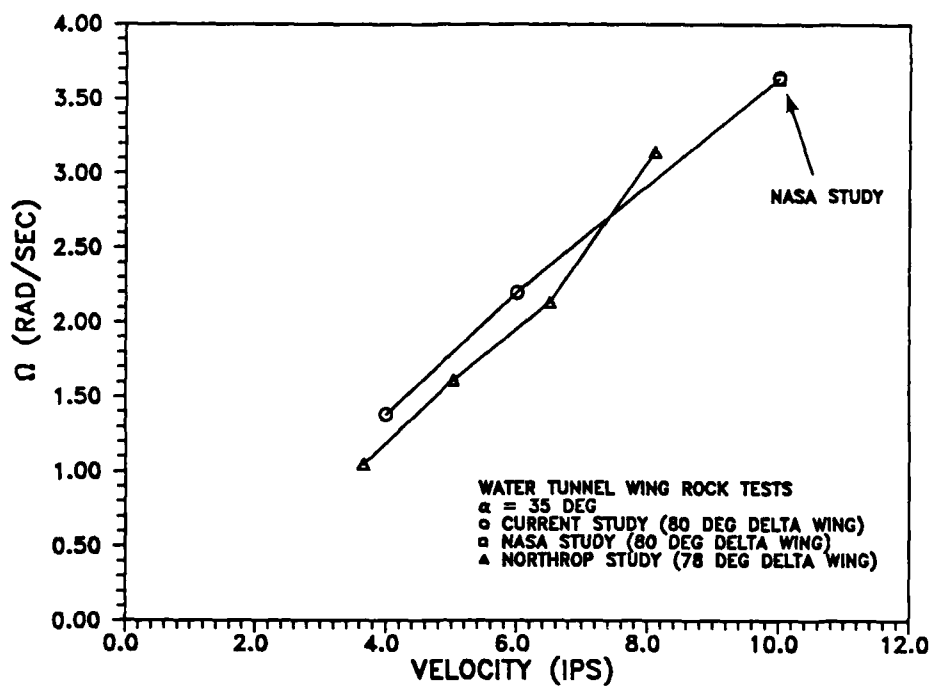


Fig. 83 Wing rock frequency variation with velocity.

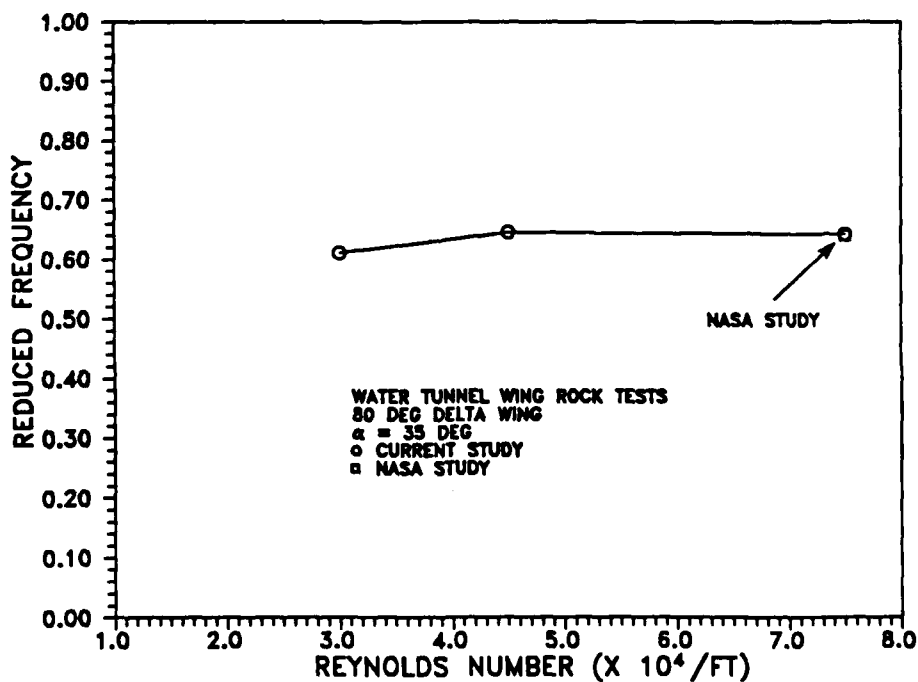


Fig. 84 Reduced frequency variation with Reynolds number.

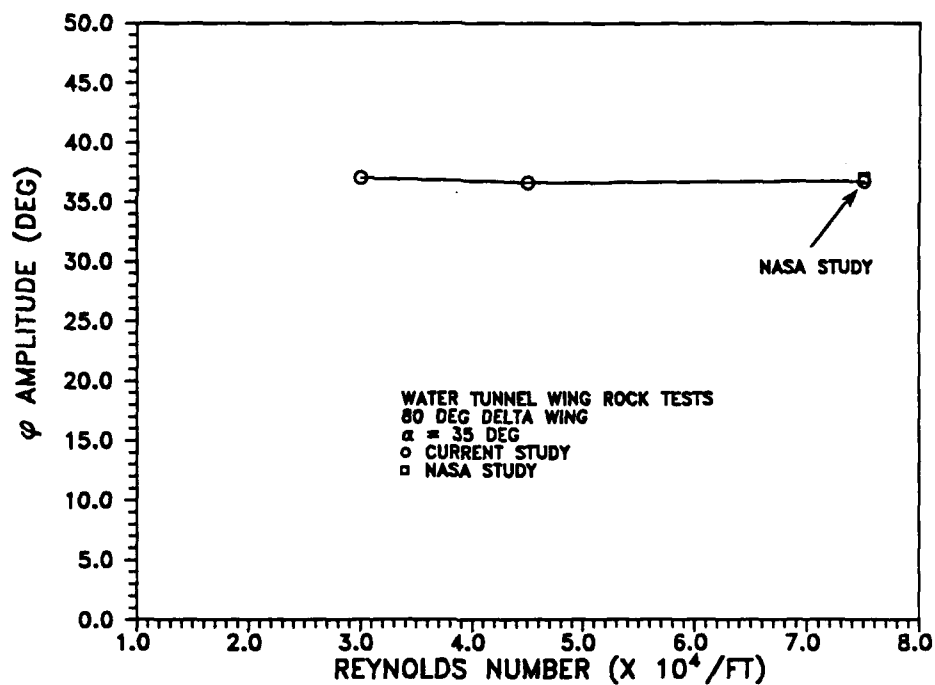
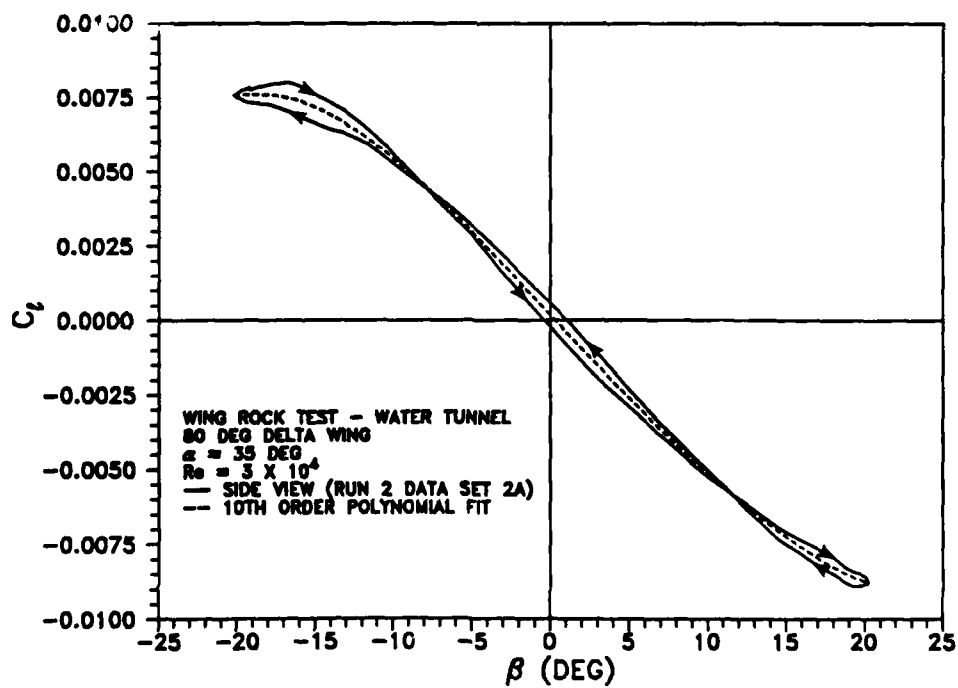


Fig. 85 Roll amplitude variation with Reynolds number.

Fig. 86 Polynomial fit to C_l versus β data.

wings.²³ An average value of $C_{\ell\beta}$ was also calculated from the polynomial for input to the mathematical model. The $C_{\ell\beta}$ determined from fitting the water tunnel data was more than 15 times smaller than the value obtained in air. Average $C_{\ell\beta}$ values determined from the test data ranged from -0.02796/rad to -0.0295/rad compared to an average wind tunnel value of -0.444/rad for an 80° delta wing at $\alpha = 35^\circ$.³⁰ This difference in the aerodynamic derivatives obtained in the two media was larger than expected; the reasons for this behavior will be discussed in detail in later sections. The $C_{\ell\beta}$ values were fairly constant for Reynolds numbers from 3×10^4 to 7.5×10^4 , as can be inferred from Fig. 82.

An approximate value of $C_{\ell\beta}$ could also be obtained directly from the C_ℓ versus ϕ data using

$$\beta \approx \phi \sin \alpha_s \quad (33)$$

Knowing the slope of the C_ℓ versus ϕ curve, $C_{\ell\phi}$, the $C_{\ell\beta}$ derivative can be estimated with

$$C_{\ell\beta} \approx C_{\ell\phi} / \sin \alpha_s \quad (34)$$

This approximation gave average values of $C_{\ell\beta}$ within 3% of the more accurate approach.

Roll damping variations were then obtained by applying the relation

$$C_\ell = C_{\ell\beta} \beta + C_{\ell p} \bar{p} \quad (35)$$

where

$$\bar{p} = \frac{b p}{2V_\infty} \quad (36)$$

and

$$p = \dot{\phi} \quad (37)$$

Since C_{ℓ} variations with β and p were known from the data and $C_{\ell\beta}$ was determined from the polynomial fit, $C_{\ell p}$ was approximated by rearranging equation (35):

$$C_{\ell p} = \frac{[C_{\ell} - C_{\ell\beta} \beta]}{\bar{p}} \quad (38)$$

It should be stressed that equations (35) and (38) assumed that all contributions to the rolling moment other than the $C_{\ell\beta}$ term were due to roll damping, $C_{\ell p}$. In reality, what is described as $C_{\ell p}$ should more precisely be represented as $(C_{\ell p} + C_{\ell\dot{\beta}} \sin \alpha_s)$, since the $\dot{\beta}$ term may not be negligible at high angles of attack.⁶⁶ It was also possible that the $C_{\ell\dot{\beta}}$ term behaved differently in water tunnel experiments than in wind tunnel measurements, accounting for apparent differences in $C_{\ell p}$; however, there was no way to examine that possibility in the current study. Additionally, any effects due to friction also showed up in the value of $C_{\ell p}$ derived from equation (38). A typical example of the calculated $C_{\ell p}$ versus ϕ results is plotted in Fig. 87. Damping was negative between roll angles of -14° and 21° and positive at magnitudes of $\phi < -14$ and $\phi > 21^\circ$. These data implied stable roll damping ($C_{\ell p} < 0$) at small roll angles ($-14^\circ < \phi < 21^\circ$) and unstable damping ($C_{\ell p} > 0$) at large roll angles ($\phi > 21^\circ$ or $\phi < -14^\circ$), just the opposite of results obtained in the wind tunnel. These $C_{\ell p}$ results were consistent with the energy analysis from equation (29). The asymmetry in the roll damping with respect to $\phi = 0^\circ$ was largely due to differences in the magnitudes of the hysteresis in the two outer loops of Fig. 71.

Mathematical Modeling

Aerodynamic derivatives were essential to predict wing rock characteristics and to implement mathematical models. As discussed in Chapter III and Appendix A, both frequency and amplitude of the roll oscillations were driven by the aerodynamic derivatives. It became clear early in the data reduction and analysis process that aerodynamic derivatives determined from both wind tunnel tests and computational codes for an 80° delta wing could not be used in either

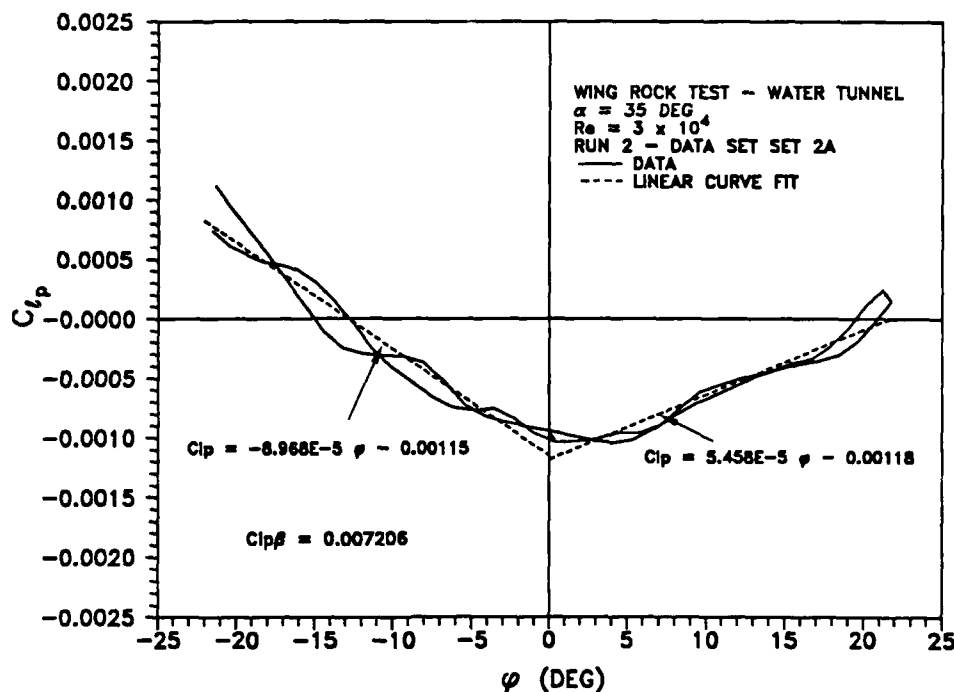


Fig. 87 C_{lp} variation with ϕ .

the mathematical model or numerical simulations to predict or to duplicate water tunnel results. Using the wind tunnel $C_{l\beta}$ for an 80° delta wing in the mathematical model yielded a predicted period of 0.99 sec for the 4 ips test, rather than the measured value of 4.55 sec. The large disagreement can be attributed to the factor of 15 difference in the $C_{l\beta}$ noted earlier between water tunnel and wind tunnel tests. However, it was possible to use aerodynamic derivatives estimated from the water tunnel data in the mathematical model to reasonably predict frequency, and amplitude (with considerably more uncertainty).

Frequencies and periods of oscillation were calculated using equations (22) and (23). Since the mathematical model developed using the Beecham-Titchener method required a constant value of $C_{l\beta}$, average values were computed for each test from a polynomial fit. Table 8 compares the results of the mathematical model for the water tunnel tests at velocities of

Table 8 Comparison of measured and calculated periods

V_{∞} (ips)	$C_{\ell\beta}$	Period (sec)		Difference (%)
		Measured	Model	
4	-0.0291	4.55	3.84	-15.6
6	-0.02796	2.863	2.612	-8.8
10	-0.0295	1.725	1.525	-11.6

4, 6, and 10 ips with the measured data. For the $V_{\infty} = 4$ ips tests, with an estimated $C_{\ell\beta}$ of -0.0291, the predicted period was approximately 84% of the measured value. For the 6 ips test, $C_{\ell\beta}$ was estimated to be -0.02796, a 4% difference from 4 ips results. Using that value and the higher velocity, the mathematical model predicted a period which was approximately 91% of the actual value. For the 10 ips test, the average $C_{\ell\beta}$ was -0.0295, which resulted in a predicted value that was 88% of the actual period. As shown, the mathematical model predicted periods which were from 9% to 16% below the experimental values. At $\alpha = 35^\circ$, Hsu³⁰ predicted a period of oscillation approximately 17% lower than the measured wind tunnel values from the Nguyen, Yip, and Chambers study²³ using equations (22) and (23).

It was more difficult to obtain the roll damping derivatives, $C_{\ell p0}$, $C_{\ell pp}$, and $C_{\ell p\beta}$ required in equation (24) to compute the roll amplitude. To obtain these derivatives from the experiments $C_{\ell pp}$ was assumed to be zero and $C_{\ell p\beta}$ was estimated from the $C_{\ell p}$ versus ϕ data (Fig. 87). The $C_{\ell p0}$ was defined as the roll damping at zero sideslip angle and was determined at the y-axis crossing. The more difficult estimate came with the determination of a reasonable single valued estimate of $C_{\ell p\beta}$. A linear fit of the $C_{\ell p}$ versus ϕ data was applied to both positive and negative ϕ 's and the magnitudes of these fits were averaged to yield a single value of $C_{\ell p\phi}$. $C_{\ell p\phi}$ was then converted to $C_{\ell p\beta}$ using the same relations discussed earlier. At $V_{\infty} = 4$ ips, $C_{\ell p0} \approx -0.00104$

and $C_{\ell_{p\beta}} \approx 0.007206$. Substituting these values into equation (24) yielded an amplitude of approximately 34.2° , 92% of the measured value of 37° . It must be emphasized that since there were variations in the size and the symmetry of the hysteresis loops, there were slight changes in the C_{ℓ_p} versus ϕ data from cycle to cycle. Therefore, there was more uncertainty in the determination of roll amplitudes than in the calculation of frequency.

The aerodynamic derivatives derived from the study were used in simulating water tunnel tests. Equations (13), (14), and (15) were combined to form a second order differential equation which was numerically integrated with a fourth order Runge-Kutta algorithm using the estimated aerodynamic derivatives. Simulations were performed using both a constant average value of C_{ℓ_β} and a time-varying C_{ℓ_β} taken from the polynomial fit of the data.

The $V_\infty = 4$ ips test was simulated using both of the methods described above. Using constant C_{ℓ_β} , the phase portrait (Fig. 88) from the Runge-Kutta integration gave a limit cycle with a roll amplitude of 34.4° and a period of 3.9 sec, which were 0.5% and 1.6% higher, respectively, than the approximation from the mathematical model using the same values of C_{ℓ_β} , $C_{\ell_{p0}}$, and $C_{\ell_{p\beta}}$. As discussed earlier, $C_{\ell_{pp}}$ was assumed to be zero. Fig. 88 also compared water tunnel data obtained at the same conditions. The roll rates were higher in the simulation due to the higher predicted frequency, even though the roll amplitude was underpredicted. The simulation of the C_ℓ versus ϕ (Fig. 89) indicated hysteresis in the same direction as the water tunnel data. The almost constant slope of the averaged simulated C_ℓ versus ϕ curve resulted from the constant value of C_{ℓ_β} used in the simulation. A second simulation was conducted with C_{ℓ_β} varying as determined from the tenth order polynomial fit. As shown in the phase portrait (Fig. 90), there was an improved agreement with the experimental data. The amplitude of the limit cycle was still approximately 34.4° ; however, the period of oscillation was 4.08 sec, approximately 90% of the actual value. As a result of the increased period, or decreased frequency, the roll rates were also closer to the data values. The C_ℓ versus

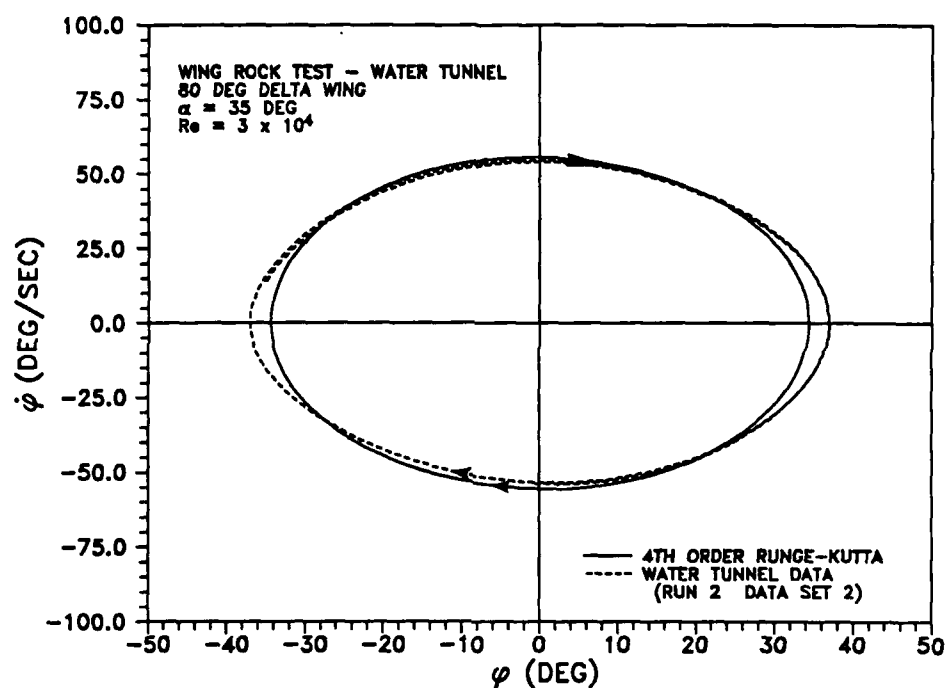


Fig. 88 Phase portrait for constant $C_{l\beta}$ Runge-Kutta simulation.

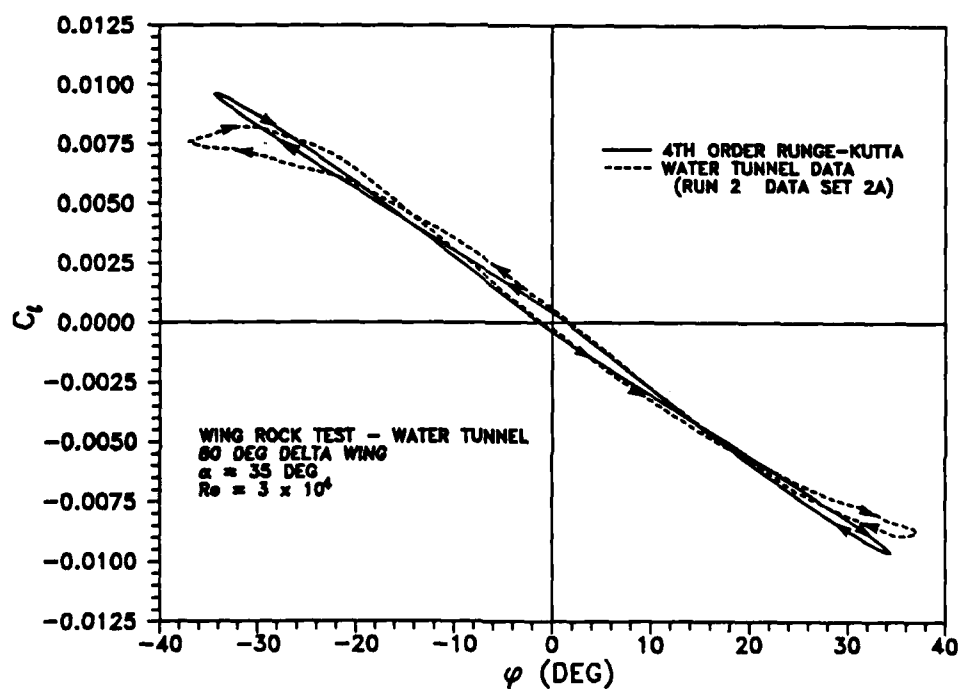


Fig. 89 Rolling moment versus ϕ for constant $C_{l\beta}$ Runge-Kutta simulation.

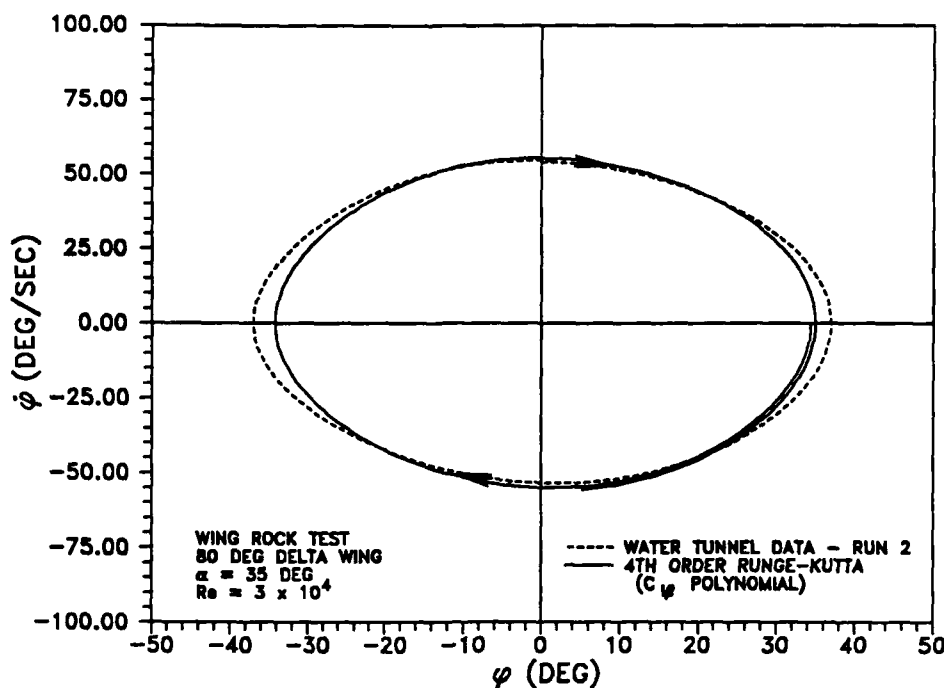


Fig. 90 Phase portrait for time-varying $C_{l\beta}$ Runge-Kutta simulation.

ϕ (Fig. 91) matched the experimental data much closer with variable $C_{l\beta}$. Since the $C_{l_{p0}}$ and $C_{l_{p\beta}}$ were still average values, the hysteresis in the outer loops was the same for both positive and negative roll angles, while it was asymmetrical in the test results (i.e., larger loop for $\phi < 0$ than for $\phi > 0$). The hysteresis at the small ϕ matched the water tunnel data very well. The approximate roll damping versus ϕ curve calculated with equation (38) is shown in Fig. 92.

The aerodynamic derivatives from the 4 ips run were also used to simulate the $V_{\infty} = 10$ ips test by changing appropriate flow conditions in the 4th order Runge-Kutta program. The phase portrait (Fig. 93) illustrated reasonable agreement between the calculations and the data, especially the roll rates. The simulated period of oscillation was 1.64 sec, only 5% below the measured value of 1.725 sec. While the average measured roll angle amplitude was 36.7° , the Runge-Kutta integration yielded a magnitude of 34.4° . Fig. 94 shows that hysteresis loops were in the same direction; however, there was a slight difference in the slopes of the C_l versus

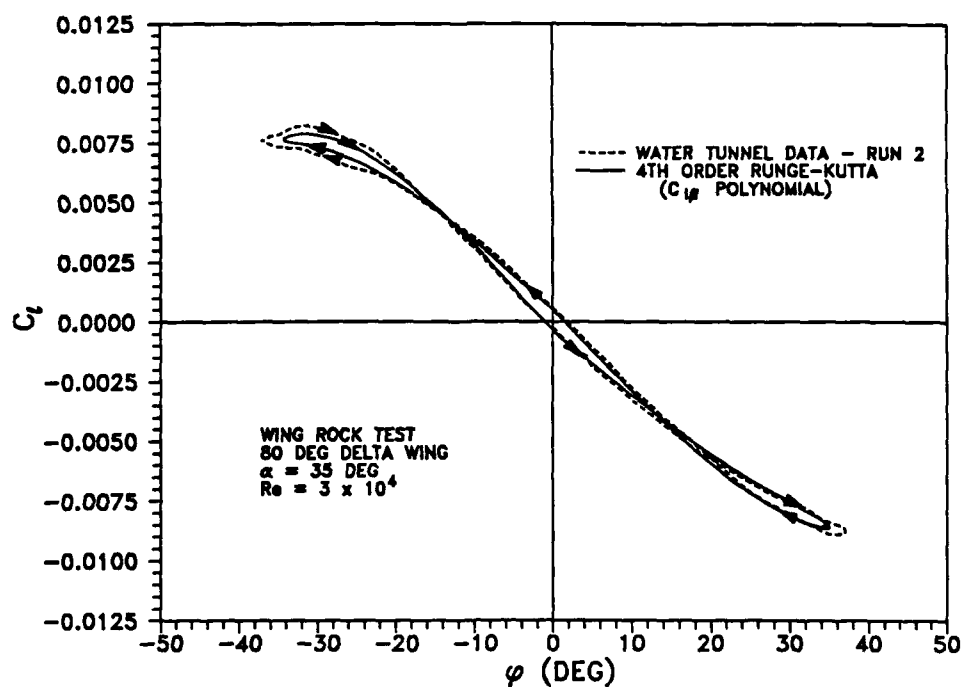


Fig. 91 Rolling moment versus ϕ for time-varying $C_{l\beta}$ Runge-Kutta simulation.

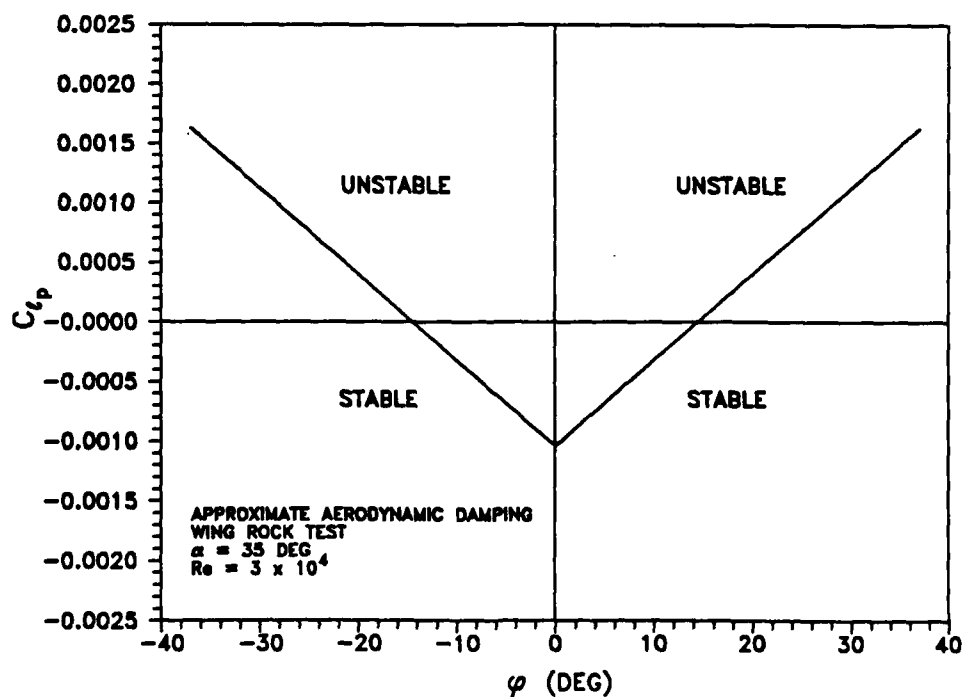


Fig. 92 Roll damping derivative versus ϕ .

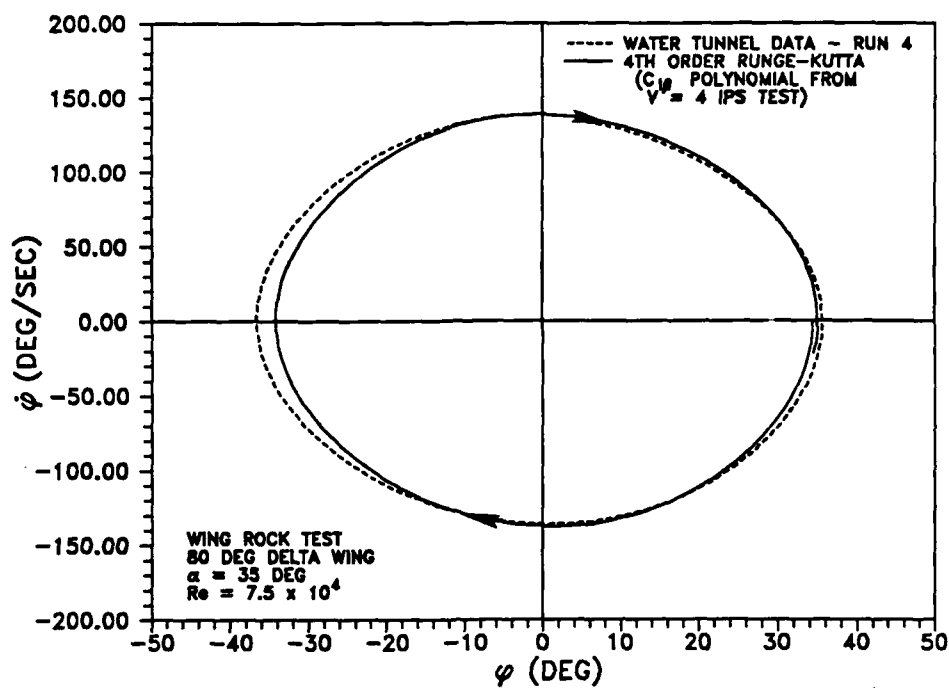


Fig. 93 Phase portrait for time-varying $C_{l\beta}$ Runge-Kutta simulation of 10 ips test.

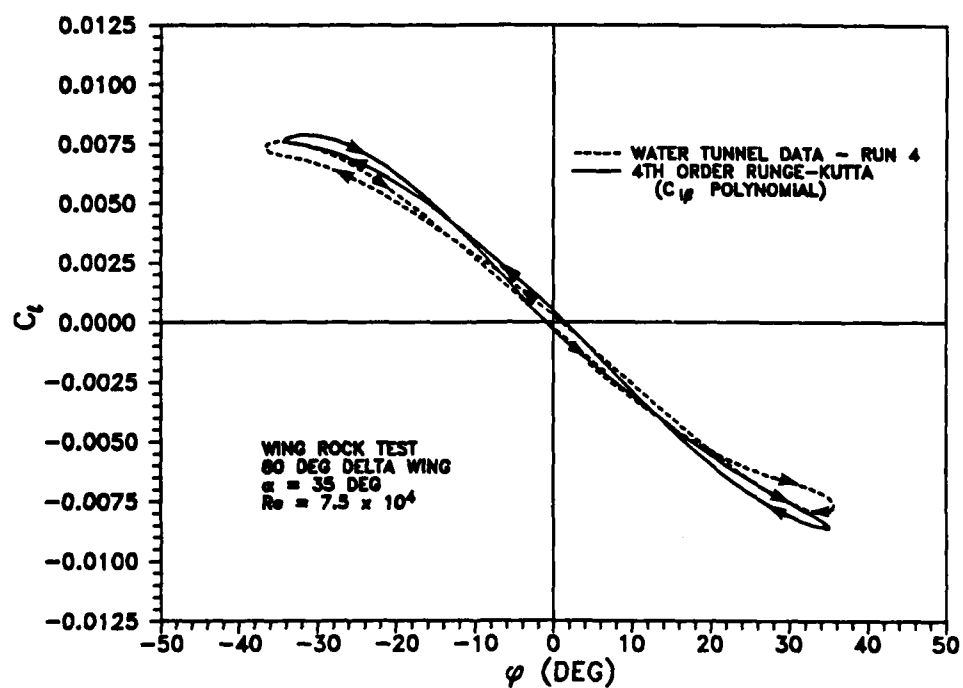


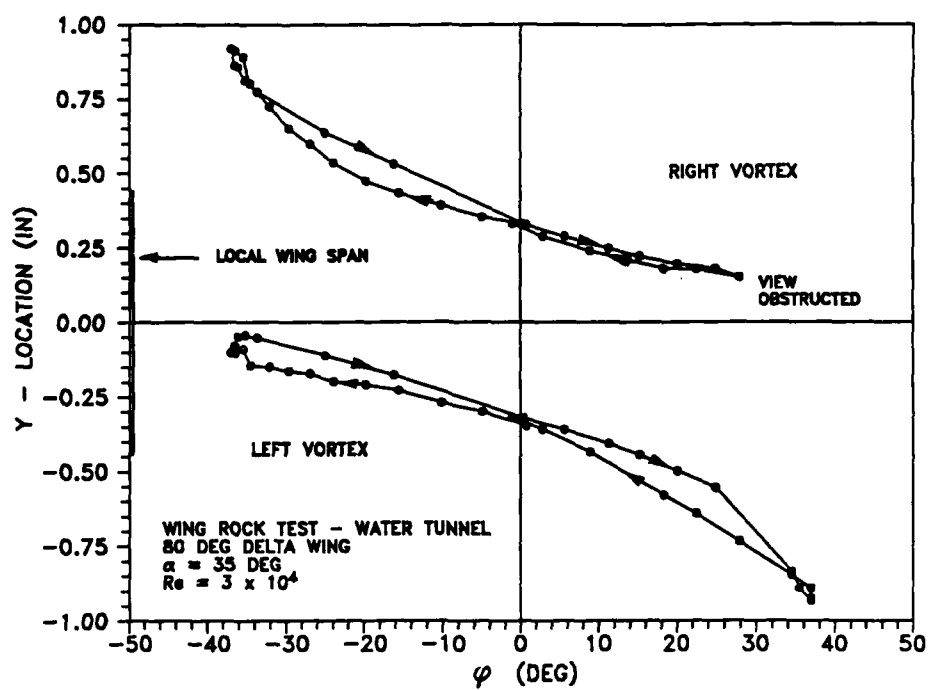
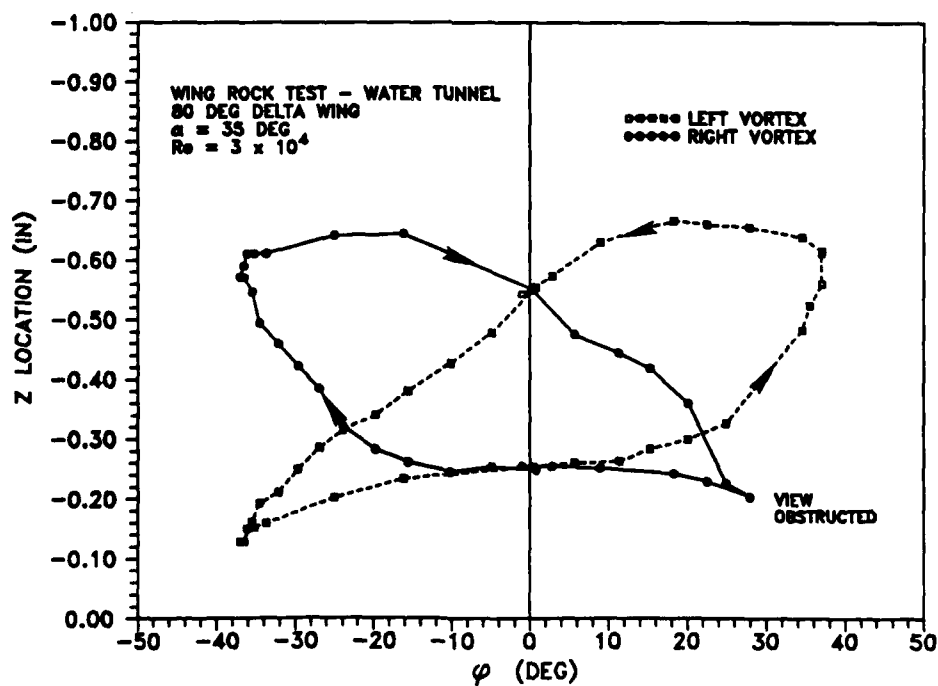
Fig. 94 Rolling moment versus ϕ for time-varying $C_{l\beta}$ Runge-Kutta simulation of 10 ips test.

ϕ curves. This deviation was expected since the values of $C_{l\beta}$ calculated from the $V_\infty = 4$ ips and $V_\infty = 10$ ips tests were not identical, as shown in Fig. 82. Equation (20) was also numerically integrated using the fourth order Runge-Kutta algorithm to examine the effects of using the β approximation given in equation (18). The estimated roll amplitudes and periods were almost in exact agreement with the math model calculations (less than 0.1% difference). This agreement showed that the Beecham-Titchener method used in the simple math model predicted wing rock periods and amplitudes almost as accurately as the fourth order Runge-Kutta integration using the same function for C_l and approximation for β .

Vortex Trajectory

A large amount of data describing the response of the model during wing rock has been presented. Up to now, no attempt has been made to relate this response to the aerodynamics of the flow-model interactions. This section presents data describing the movement of the leading-edge vortices during limit cycle oscillations and how it related to model dynamics. The vortex core positions provided useful insight into wing rock mechanics. The data presented detail vortex positions in the body axes system at the quarter-chord, half-chord, and three quarter-chord locations, $x/c = -0.25$, $x/c = -0.5$, and $x/c = -0.75$, respectively, for the $V_\infty = 4$ ips water tunnel runs. Note that the x axis is out the nose of the model, the y axis is out the right wing, and the z axis is down.

The y and z positions of the vortex cores at $x/c = -0.25$ were plotted against ϕ for a complete wing rock cycle (Figs. 95 and 96, respectively). The y position data (Fig. 95) showed that at $\phi = 0^\circ$, the spanwise locations of the vortices were the same. As the model rolled, the vortex on the side of the downward moving semi-span shifted inboard, while the vortex on the side of the upward moving semi-span shifted outboard. This shift was evident from the data when looking at $\phi = -37^\circ$, where the left vortex was close to the centerline of the wing while the right vortex was well off the wing. The data revealed hysteresis in the movement of the core with roll angle, except at $\phi = 0^\circ$. The plot also showed that the left vortex and right vortex moved

Fig. 95 Vortex spanwise position: $x/c = -0.25$.Fig. 96 Vortex vertical displacement: $x/c = -0.25$.

outside of the local wing edge at $\phi \approx 15^\circ$ ($\dot{\phi} > 0$) and $\phi \approx -15^\circ$ ($\dot{\phi} < 0$), respectively. The z position versus ϕ data (Fig. 96) showed an even greater dependence of vortex core location on the direction of the wing rolling motion. These results revealed a significant asymmetry in the vertical displacement of the leading-edge vortices at $\phi = 0^\circ$. When the wing was rolling clockwise ($\dot{\phi} > 0$), the right vortex was approximately 0.55 inches above the wing while the left vortex was only 0.25 inches from the surface. Just the opposite was true for counterclockwise motion of the wing ($\dot{\phi} < 0$). Therefore, this asymmetry in the vortex positions created an imbalance in vortex lift, forcing the model away from wings level. As the model moved further away from $\phi = 0^\circ$, the vortex on the downward semi-span moved very close to the wing surface, while the opposite vortex was displaced well above it. Data were not available for the maximum positive ϕ since the model obstructed the view of the vortex in the side camera; however, the y data and the lack of visibility of the right vortex indicated trends similar to the left vortex. The y versus z plot of the vortex positions (Fig. 97) presented the same information as the previous two plots; however, it viewed vortex movements as if looking from the aft end of the model along the x -body axis. Note that the y and z axes have approximately the same scale and the local cross-section of the model is shown on the y -axis of the graph. Some of the data points are labeled with ϕ values for reference. For example, at $\phi = -37^\circ$, the right vortex was located at $y = 0.92$ in and $z = -0.57$ in, while the left vortex was at $y = -0.1$ in and $z = -0.13$ in. From this picture, it was clear that the right vortex was not only displaced much higher above the surface, but it was also well outboard of the local edge of the wing. On the other hand, the left vortex was close to the wing surface and well inboard of the local edge of the wing. Therefore, the left half-span of the wing (lower wing half since $\phi = -37^\circ$) had a higher vortex lift than the right half-span (upper half of the wing), which resulted in a local restoring moment which favored a return to wings level. This effect was confirmed in Fig. 97 by a decrease in ϕ magnitude at the next labeled data point. The general shape of these plots and the relative positions of the vortices with respect to the wing were similar to results presented by Jun and Nelson²⁶ at $x/c = -0.75$, for both $\alpha = 30^\circ$ and

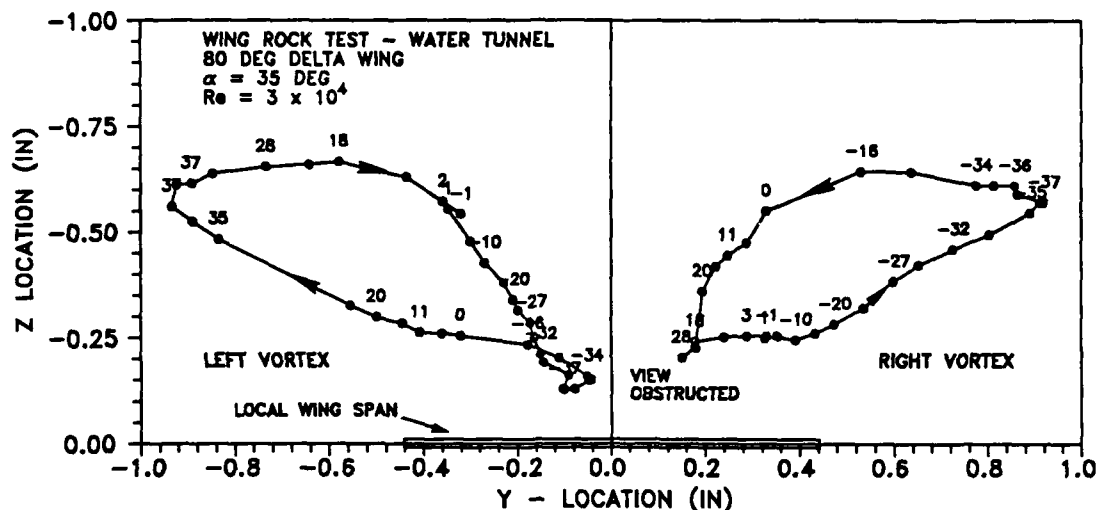
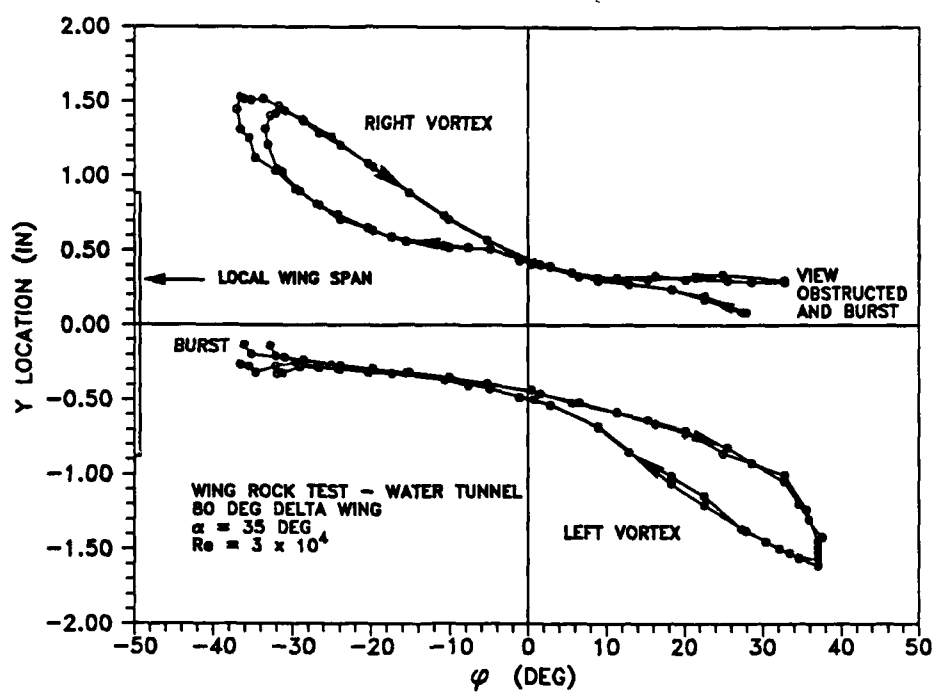
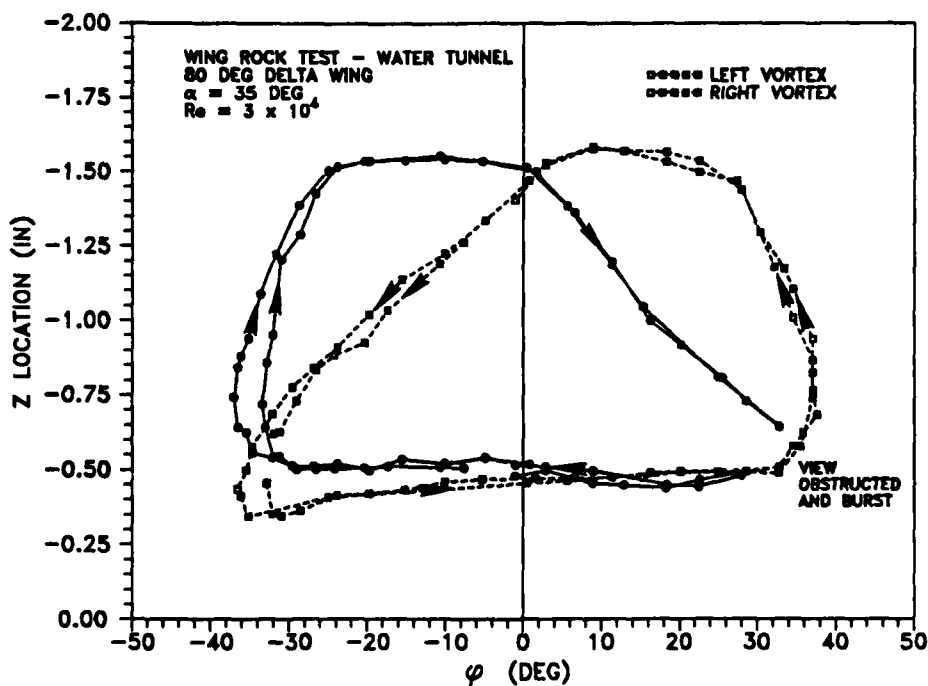


Fig. 97 Vortex core movement: $x/c = -0.25$.

$\alpha = 40^\circ$ (Fig. 18). Unfortunately, a complete data set for $\alpha = 35^\circ$ was not available in that reference; however, it could be reasonably assumed that the data were similar to that of the other two angles of attack.

The same vortex position information for $x/c = -0.5$ is shown in Figs. 98-100. Two cycles of oscillation were examined at this location to assess repeatability of the vortex position measurements. As illustrated by these results, the two cycles of data were in excellent agreement, other than the maximum negative ϕ of the model. The y position data (Fig. 98) again indicated that the spanwise locations of the two vortex cores were symmetric at $\phi = 0^\circ$. As the model rolled, the vortex on the downward side of the wing moved inboard while the opposite vortex moved well outboard. This pattern was the same as existed for $x/c = -0.25$; however, the left and right vortex moved outside of the local wing edge at $\phi \approx 29^\circ$ ($\dot{\phi} > 0$) and $\phi \approx -29^\circ$ ($\dot{\phi} < 0$), respectively. This showed that each wing half-span lost vortex lift at a different ϕ than at $x/c = -0.25$, indicating a phase shift in vortex positions. Another noticeable trend in the data was that there was significant hysteresis of the vortex positions with ϕ on the upper half-

Fig. 98 Vortex spanwise position: $x/c = -0.50$.Fig. 99 Vortex vertical displacement: $x/c = -0.50$.

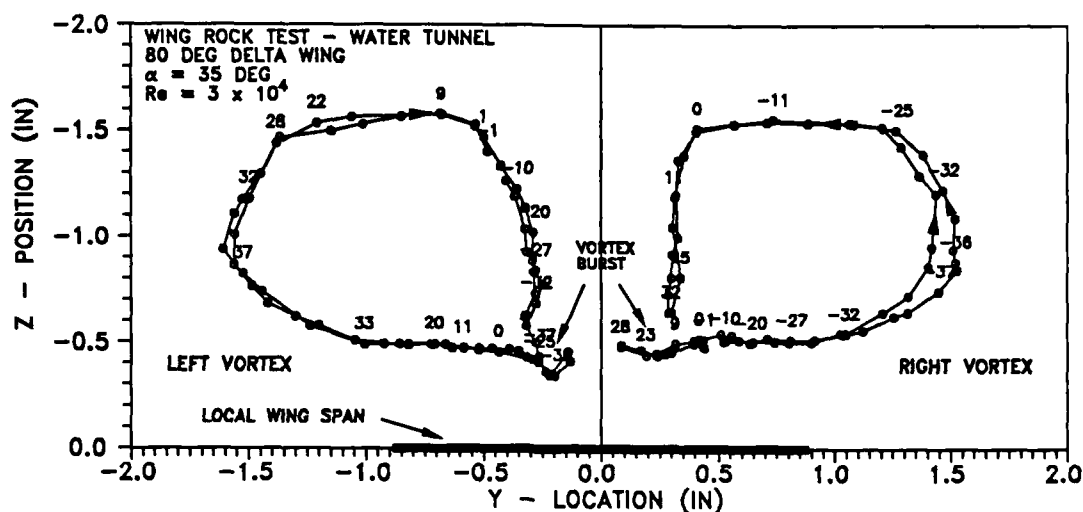
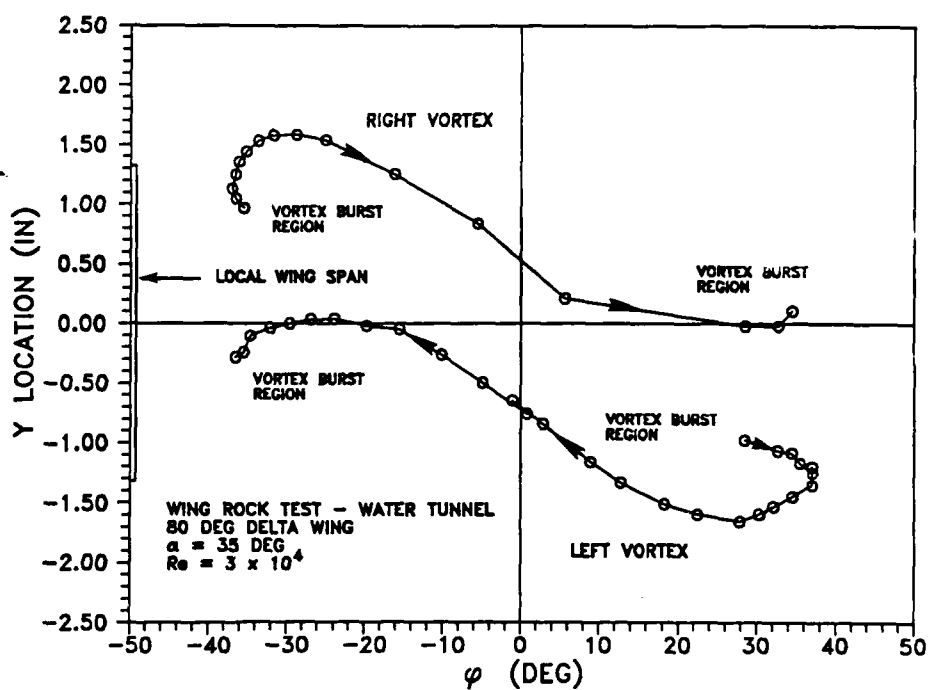
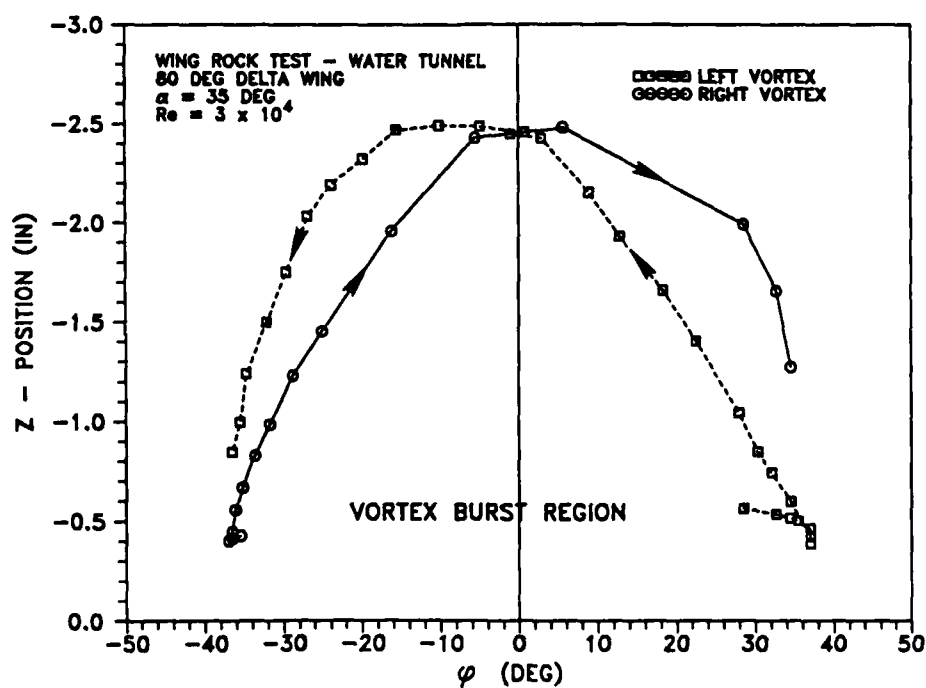


Fig. 100 Vortex core movement: $x/c = -0.50$.

span of the wing while there was considerably less hysteresis of the vortex locations on the lower half-span. The z positions (Fig. 99) also displayed a different picture than the $x/c = -0.25$ data, which further indicated that movement of the vortices were dependent on the x locations. The data showed that at maximum roll magnitudes, the z position of the vortex on the upward semi-span was approximately 50% of the maximum displacement obtained, compared to $x/c = -0.25$ where the z displacement was larger than 90% of the maximum value. Again, this indicated that the entire vortex did not move uniformly in a straight line, which was qualitatively evident from the videotapes. The y versus z plot (Fig. 100) gave an excellent view of vortex movement in the model body axes (with the cross-section of the wing superimposed). Once again, the idea that there was increased vortex lift on the downward half of the wing was strongly supported by the small displacement of the vortex above the wing surface on the downward half-span compared to the relatively large vertical displacement and outboard location of the vortex on the upward half-span. This increased vortex lift on the lower semi-span provided a restoring moment which

opposed roll divergence and bounded the wing rock. As illustrated in the discussions of Figs. 98 and 99, the vortex positions exhibited a significant phase shift when moving aft from $x/c = -0.25$ to $x/c = -0.50$. Therefore, vortex lift as a function of ϕ was different at these two locations. This effect in turn caused the local rolling moments to be out of phase between the two chordwise stations. Notice that the vortex on the lower half-span burst upstream of $x/c = -0.50$ as the wing passed through its maximum downward displacement.

The third chordwise location examined, $x/c = -0.75$, (Figs. 101-103) presented a considerably different picture. The y data (Fig. 101) still showed an inboard shift of the vortex on the lower semi-span and an outboard shift of the vortex on the upper semi-span. Symmetry in the y locations appeared to exist at $\phi = 0^\circ$ as it did for the other two chordwise locations. There was an indication of hysteresis; however, a complete cycle of vortex core movement could not be observed due to vortex bursting. The data also showed that the left and right vortex moved outboard of the local wing edge at $\phi \approx 36^\circ$ ($\dot{\phi} < 0$) and $\phi \approx -37^\circ$ ($\dot{\phi} < 0$), respectively. The z data (Fig. 102) showed that the vortex was near its maximum displacement above the wing (within 2%) at $\phi = 0^\circ$. This was different than data at $x/c = -0.25$ where at $\phi = 0^\circ$, the z distance was 83% of the maximum displacement above the surface. The difference between the core positions was much more pronounced at the maximum roll angle magnitudes ($\phi = \pm 37^\circ$). At $x/c = -0.75$, the z displacement was approximately 16% of the maximum distance above the surface, compared to 90% at $x/c = -0.25$ and 50% at $x/c = -0.75$. Equally noticeable was that the left vortex was closest to the wing when the left semi-span was at its most upward position, just the opposite of the condition at $x/c = -0.25$. The same relation appeared to be true for the right vortex and right semi-span. The data showed that once vortex burst occurred, it did not propagate aft of $x/c = -0.75$ for almost half a cycle of oscillation, so there were only a small number of roll angles where both vortices were visible over the wing at the same time. The y versus z plot (Fig. 103) displayed similar information in the body axes with the local cross-section of the wing superimposed. Note that unlike the previous two chordwise locations, the vortex

Fig. 101 Vortex spanwise position: $x/c = -0.75$.Fig. 102 Vortex vertical displacement: $x/c = -0.75$.

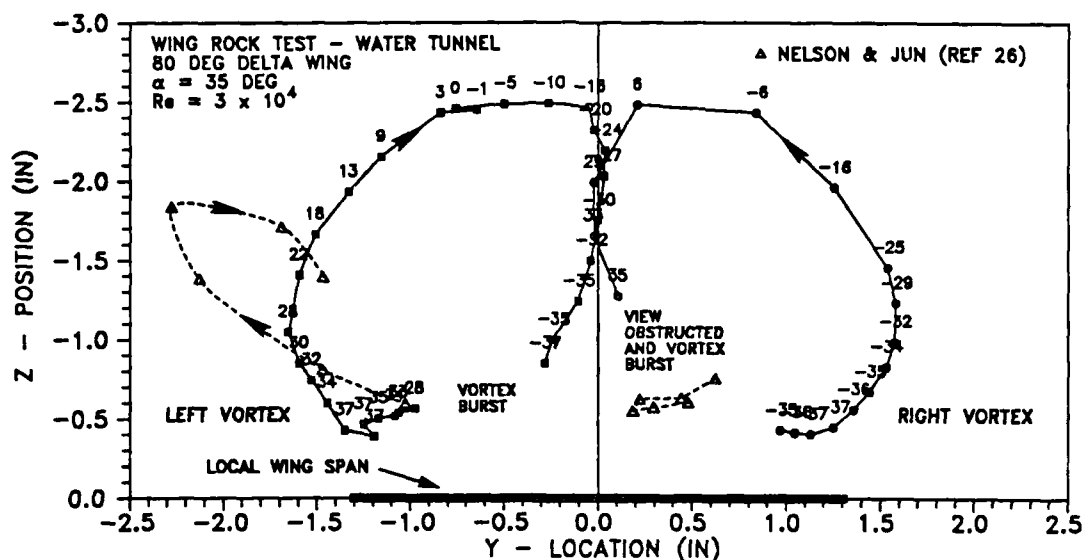


Fig. 103 Vortex core movement: $x/c = -0.75$.

positions were inside the local wing edges for a much larger portion of the oscillation. Once again, the large phase shift of the vortex positions was evident in comparing Fig. 103 with Fig. 97 and Fig. 100 from the other chordwise locations. Additionally, the vortex trajectory was markedly different from wind tunnel data presented by Jun and Nelson²⁶ at $x/c = -0.75$. Their limited wind tunnel data at $\alpha = 35^\circ$ were scaled and plotted on Fig. 103 for comparison. Note that the vortex positions from the wind tunnel tests moved further outboard, but not as high above the wing surface when compared to the water tunnel data. As previously mentioned, their data looked more like the water tunnel results at $x/c = -0.25$ (Fig. 97). A typical plot of their wind tunnel data at $\alpha = 40^\circ$ (Fig. 19) also provided an indication of vortex movements at $x/c = -0.75$, despite the higher α . As will be discussed in the comparison section, it was this large difference in the behavior of the vortices which is believed to have caused the opposite directions of hysteresis in C_l versus ϕ between the water and the wind tunnel experiments.

The phase shifts of the vortex positions with chordwise location is not surprising considering the low flow velocities in the water tunnel. Dynamic tests by Lambourne et al.⁶⁷ experimentally demonstrated that leading-edge vortices do not reach their steady state position at all chordwise locations simultaneously. Instead, the vortex positions propagated aft at the freestream velocity of the flow. Therefore, there was a convective time lag in the vortex positions which is equal to

$$\Delta t = \Delta x / V_{\infty} \quad (39)$$

For the 4 ips water tunnel test runs, it would take 1.25 seconds for the position of the vortex to move from $x/c = -0.25$ to $x/c = -0.75$. Since the period of oscillation was 4.55 seconds, the model would have rotated through 0.27 cycle during this time increment. This delay equated to an average ϕ change of about 40° ($\Delta\phi$ varies depending on $\dot{\phi}$) since the wing oscillated through 148° during one cycle. Therefore, by the time the vortex positions would have reached the $x/c = -0.75$ chordwise location, the model would have rotated to a significantly different ϕ . Since the phase difference between two chordwise locations was determined by the ratio Ω/V_{∞} the reduced frequency, k , is an important parameter. For a given model geometry, the larger the reduced frequency, the larger the phase lag of the vortex positions with x/c . The dynamic interaction between the oscillating model and the vortices are much more complicated than suggested by this simple calculation; however, this approximation helps explain the different vortex patterns at each chordwise location.

A simplified schematic of vortex movement during a half cycle of oscillation is shown in Fig. 104 for the 4 ips test. The solid circles ($x/c = -0.25$ location) and broken circles ($x/c = -0.75$) were measured from water tunnel data, while the asterisks were $x/c = -0.75$ locations from the Jun and Nelson wind tunnel data²⁶ at $\alpha = 35^\circ$. At $\phi = 0^\circ$, the $x/c = -0.25$ vortex positions were asymmetric, generating a rolling moment in the counterclockwise direction. As the wing moved to more negative roll angles, the left vortex moved more inboard and closer to the wing while the right vortex moved outboard and away from the wing. The motion

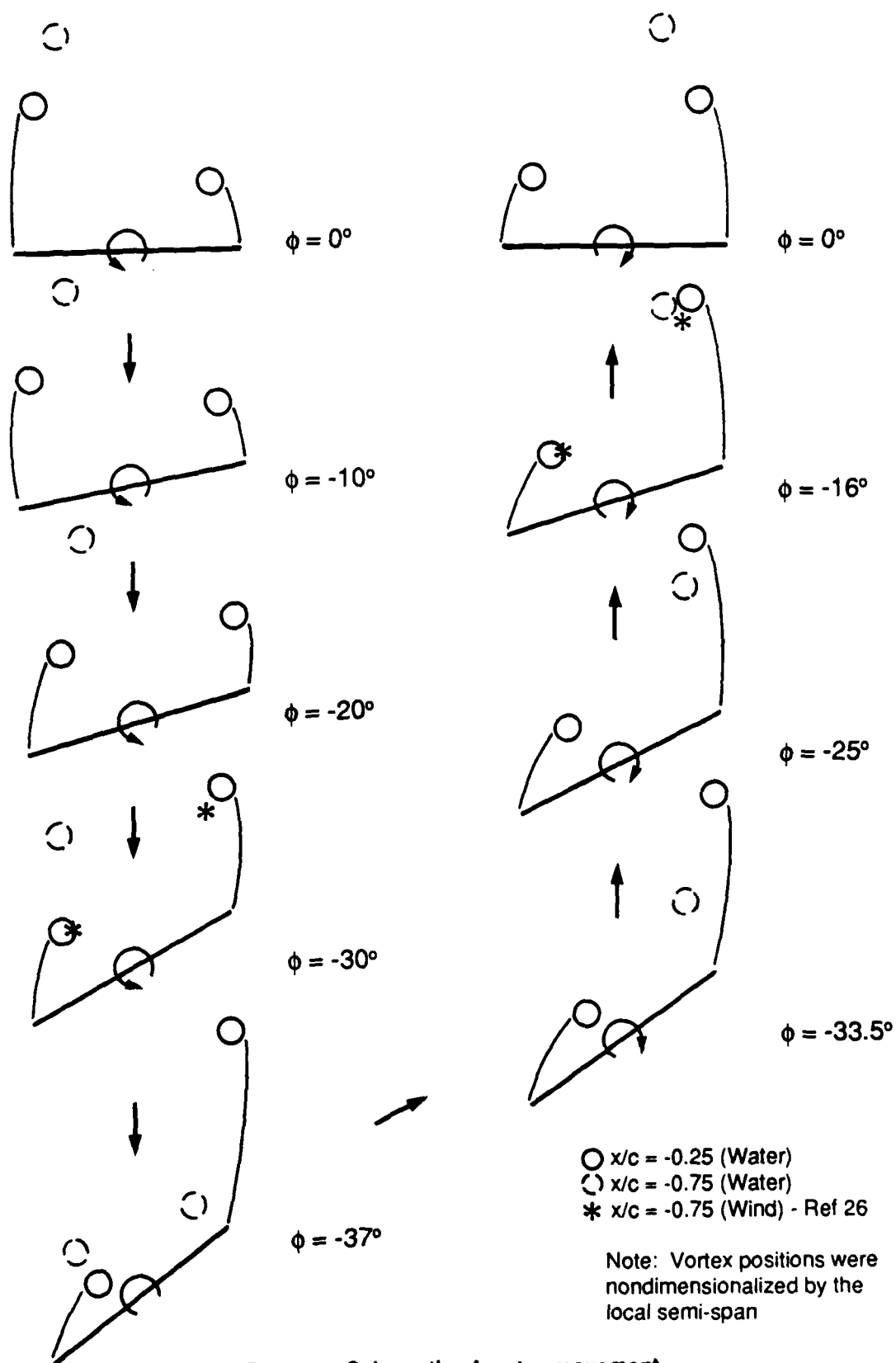


Fig. 104 Schematic of vortex movement.

continued in that direction until there was a change in the rolling moment due to lift-off of the right vortex and reattachment of the left vortex. This incremental switch in rolling moment occurred due to the increased lift on the lower wing half-span and provided the aerodynamic spring necessary to reverse the direction of motion and thus bound the limit cycle. The motion then moved clockwise due to the new positions for the vortices. When the wing returned to $\phi = 0^\circ$, the vortex positions were mirror images of the $\phi = 0^\circ$ wing position at the beginning of the half-cycle and the model was rotating in the opposite direction. While not shown in Fig. 104, the same phenomena existed for the other half of the cycle. The $x/c = -0.75$ water tunnel data reflected the phase differences in the positions of the vortices described earlier. For most of the roll angles shown at $x/c = -0.75$, only one vortex existed over the wing due to vortex bursting. At $\phi = -37^\circ$, the vortex positions at $x/c = -0.75$ actually generated a moment opposing the one generated at $x/c = -0.25$, once again illustrating the importance of this phase shift between the two chordwise locations. The limited $\alpha = 35^\circ$ wind tunnel data shown in the diagram was very similar to the $x/c = -0.25$ water tunnel data. The fact that these results appeared similar even though they were obtained at different chordwise locations for the two media suggested that there were much smaller phase differences in the vortex positions along the chord in the wind tunnel tests. This phasing was expected due to the smaller time lag predicted by equation (39) for wind tunnel measurements. For the wind tunnel test at $V_\infty = 29$ fps, the model would have only moved 0.04 cycles in the time it would take for the vortex system to move from $x/c = -0.25$ to $x/c = -0.75$. Due to much smaller phase lags in the vortex positions of the wind tunnel tests, the phase differences in local vortex lift distribution and local rolling moments as a function of x were much less than in the water test experiments. Therefore, the net rolling moment at a given ϕ was different between the water and wind tunnel tests. It was these phase differences in vortex positions, and thus C_{ℓ} , between the water tunnel and the wind tunnel studies which are believed to account for the opposite hysteresis direction in the C_{ℓ} versus ϕ plots. This point will be discussed in more detail in the comparison section of this chapter.

Burst point data (Fig. 105) showed that the left vortex burst initially and at its more forward location when the left side of the wing was near its maximum downward position. The

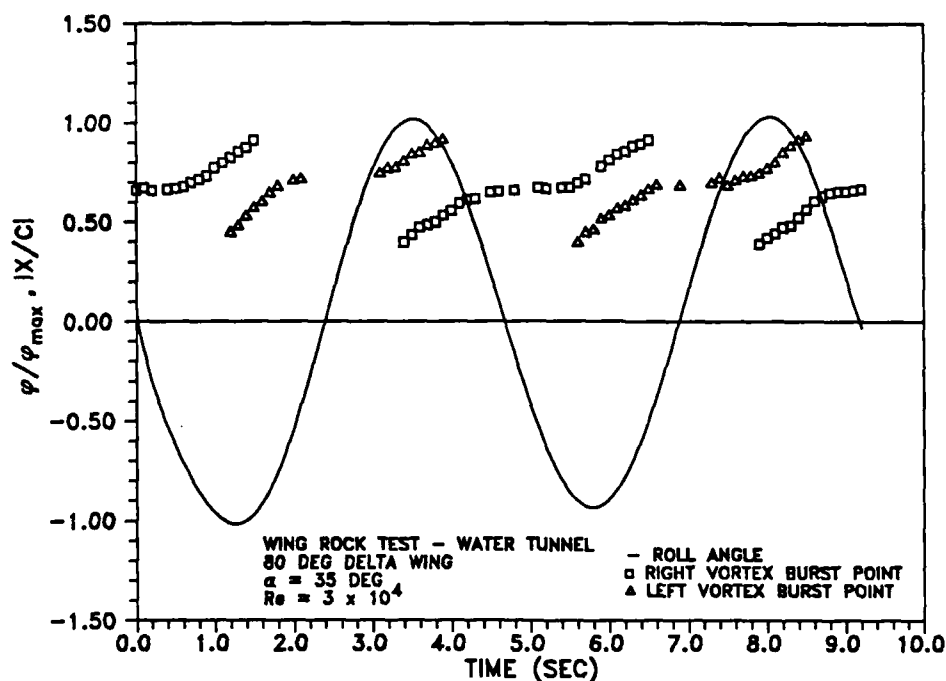


Fig. 105 Vortex burst point movement during wing rock.

same was true of the right vortex when the right side of the wing was near its maximum downward position (maximum positive ϕ). Such bursting actually decreased the lift on that side of the wing; however, this effect was overshadowed by the increased lift due to the positions of the vortex cores. These results supported Ericsson's conclusion that vortex bursting actually opposes wing rock rather than causing or perpetuating it.³²⁻³³ The aft movement of the vortex burst point with decreasing $|\phi|$, coupled with variation of vortex positions with x location, supported the results in Fig. 65, indicating that the maximum restoring moment occurred at ϕ less than the maximum positive or negative value. Note that the vortex burst point locations were consistent with the data shown for the vortex positions at each chordwise location.

Summary of Water Tunnel Data

The preceding results were especially significant in that they provided the first known data which simultaneously quantified both vortex locations and wing motion during limit cycle

oscillations. The 80° delta wing experienced sustained wing rock at high α as others have reported. However, the data also revealed significant differences between the model dynamics in the water tunnel and those reported in the wind tunnel. These differences prompted further study to evaluate wing rock behavior of the same model in the Texas A&M University Low Speed Wind Tunnel. Such a test series was the only way to verify the differences in wing rock behavior between the two media. Using the same model and bearings in the free-to-roll apparatus eliminated many of the variables which existed between the water tunnel study and other published wind tunnel wing rock results.

Wind Tunnel Test Results

The wind tunnel study provided high quality data on the wing rock behavior of the 80° delta wing for a wide range of test conditions. The results were generally similar to those reported by Nguyen, Yip, and Chambers²³ and Levin and Katz;^{24,25} however, the model examined in the present research was closer to a true delta wing configuration. While the wind tunnel study did not provide quantitative vortex positions as obtained in the water tunnel, it did yield an extensive data base describing the effects of different flow parameters on wing rock. This phase of the study fully verified that the model dynamics in the wind tunnel were significantly different from those observed in the water tunnel.

Summary of Test Methods

Over 150 runs were made in the wind tunnel during this phase of the study. Prior to conducting dynamic tests at each new α or camera arrangement, a series of calibration runs were made. In these tests, the model was precisely set at different roll angles and videotaped with the camera system. The reduced data from these calibration runs were extremely useful in scaling the dynamic video data to provide accurate ϕ time histories. The free-to-roll tests examined angles of attack from 24° to 55° and dynamic pressures of 0.5 psf to 10 psf, corresponding to Reynolds numbers of $1.09 \times 10^5/\text{ft}$ to $4.86 \times 10^5/\text{ft}$. Since comparing the wind

and water tunnel data was a primary objective of these experiments, emphasis was placed on the $\alpha = 35^\circ$ test conditions at the lower dynamic pressures of 0.5 psf and 1 psf.

All video data were taken from the side and top of the wind tunnel with the two 200 Hz camera; however, only the side view was used to quantify model dynamics. The 200 Hz cameras provided good resolution of the model dynamics up to dynamic pressures of about 4 psf. For dynamic pressures of 5 psf and above, wing rock frequency and amplitude could still be determined; however, the ability to obtain high quality C_L versus ϕ data was marginal due to the high oscillation frequencies and the smaller number of data points per cycle. The same procedures employed in the reduction and analysis of the water tunnel motion data were used for wind tunnel measurements.

General Observations

The 80° delta wing experienced wing rock for angles of attack of approximately 25° to 50° for a Reynolds number of 3.44×10^5 ($\bar{q} = 5$ psf). It was difficult to identify the upper α limit since at times the small amplitude oscillations were periodic, while in other instances they appeared to momentarily cease and start up again. Above 50° , model motions were clearly random low amplitude oscillations of a highly unsteady nature. Levin and Katz²⁴ obtained wing rock on an 80° delta wing from $\alpha = 19.5^\circ$ to $\alpha = 51^\circ$ at $Re = 4.4 \times 10^5/\text{ft}$. The Nguyen, Yip, and Chambers study²³ reported limit cycle oscillations from $\alpha = 27^\circ$ to $\alpha = 42^\circ$ at $Re = 1.09 \times 10^6/\text{ft}$; however, they did not identify an upper α limit. At lower dynamic pressures, the α range for wing rock decreased, most likely due to the inability of the smaller aerodynamic forces to overcome friction in the bearings. Additionally, at some of the lower dynamic pressures and angles of attack, the turbulence in the flow was not sufficient to initiate wing rock at $\phi_0 \approx 0^\circ$. But in many of these instances, limit cycle oscillations could be started by creating a disturbance in the flow field upstream of the model. Once started, the limit cycle was self-sustaining in most cases.

Qualitatively, wing rock amplitude and frequency of oscillation were strong functions of both α and dynamic pressure. Other than these observations of the frequency and amplitude trends, merely viewing the videotapes provided little information. The more useful quantitative wing rock data were obtained using ExpertVision.

Baseline Test Condition

Since water tunnel tests were performed at $\alpha = 35^\circ$, that angle of attack was chosen as the baseline condition for the wind tunnel study. The test conditions examined at $\alpha = 35^\circ$ were shown in Table 7. Many of these tests were duplicated as many as ten times during the investigation to examine repeatability.

To approach the water tunnel Reynolds number as closely as possible, the wind tunnel tests were conducted at the lowest possible dynamic pressure. The largest Reynolds number in the water tunnel was $7.5 \times 10^4/\text{ft}$, so wind tunnel tests were attempted at that flow condition. Unfortunately, the corresponding dynamic pressure of 0.238 psf was too low for steady wing rock to develop. Moreover, the wind tunnel had questionable flow quality at this low speed. The dynamic pressure was slowly increased until a steady, repeatable wing rock occurred at $\bar{q} = 0.5$ psf, corresponding to $V_\infty = 20.5$ fps and $Re = 1.09 \times 10^5/\text{ft}$. Therefore, at the closest flow conditions, the wind tunnel Reynolds number was approximately 45% higher than the water tunnel value.

This $\bar{q} = 0.5$ test condition was repeated on four different days over a 16-day period with almost identical results. While steady wing rock existed at this flow condition, it would not self-initiate at $\phi_0 = 0^\circ$. To start the oscillations, it was necessary to introduce a long cylindrical object into the flow approximately 5 feet upstream of the model. The object was inserted into the flow through a small hole in the top of the wind tunnel. The flow asymmetry or turbulence created by the object was sufficient to initiate wing rock. Wing rock did self-initiate when the model was released from an initial roll angle of -70° . These results strongly suggested that an asymmetry in the flow field must be large enough to generate aerodynamic forces to overcome

bearing friction before wing rock will develop. The average period of an oscillation was 0.4 sec with variances of ± 0.04 sec for the different tests. This period corresponded to an average frequency of 15.7 rad/sec and a reduced frequency of 0.113. Average roll angles varied from -28.7° to 28.7° with maximum deviations of $\pm 0.7^\circ$ from cycle to cycle. A typical time history is plotted for multiple cycles of oscillation in Fig. 106. The roll rates (Fig. 107) ranged from $-473.6^\circ/\text{sec}$ to $469.8^\circ/\text{sec}$, with an average amplitude of 466.7° . Had the roll angle been a pure sinusoidal variation with a period of 0.4 sec and an amplitude of 28.7° , the roll rate would have been $450.8^\circ/\text{sec}$, a difference of 3.5% from the measured values. A typical roll acceleration profile (Fig. 108) showed a more gradual change in acceleration after the peak value than before it. As discussed earlier, this resulted in rolling moment hysteresis with ϕ . It is interesting to compare these results with water tunnel data presented in Figs. 61, 68, 72, and 76, where the drop in acceleration after the peak was more rapid than the rise before it, just the opposite of the

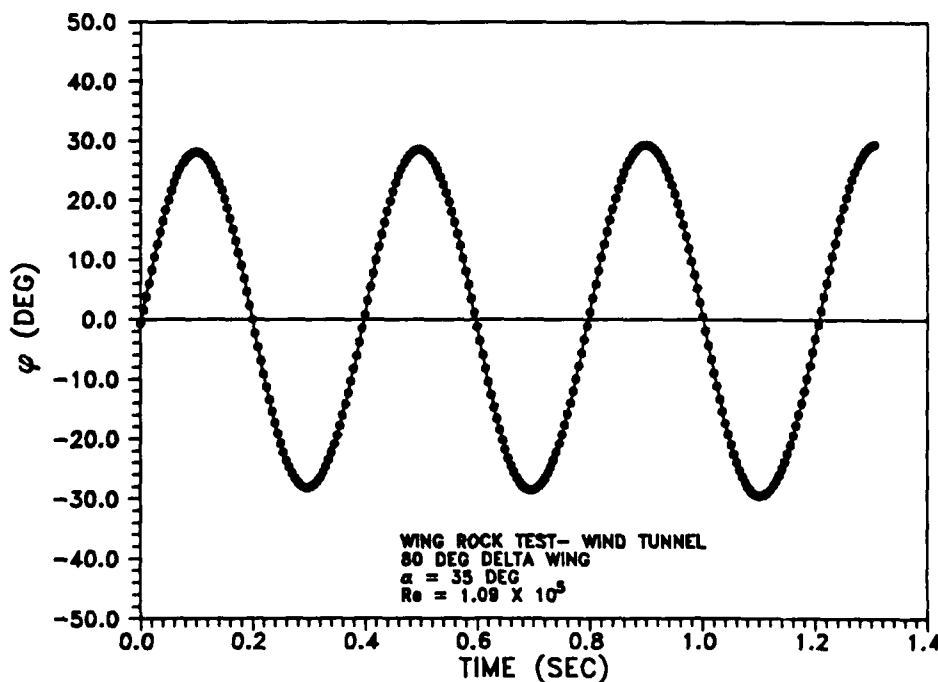


Fig. 106 Wing rock roll angle time history, $\bar{q} = 0.5$ psf.

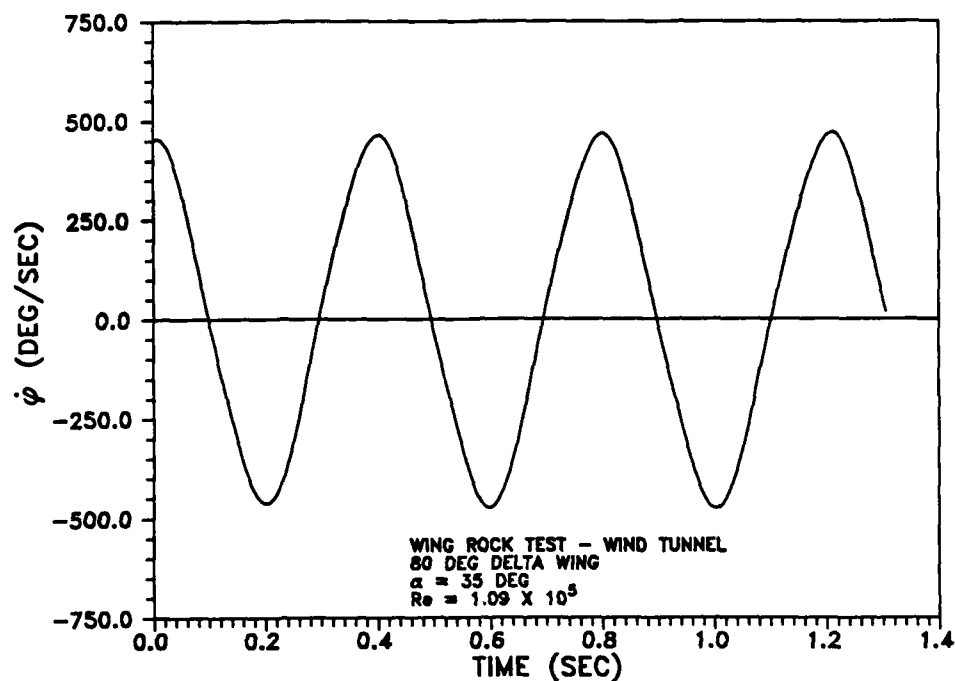


Fig. 107 Wing rock roll rate time history, $\bar{q} = 0.5$ psf.

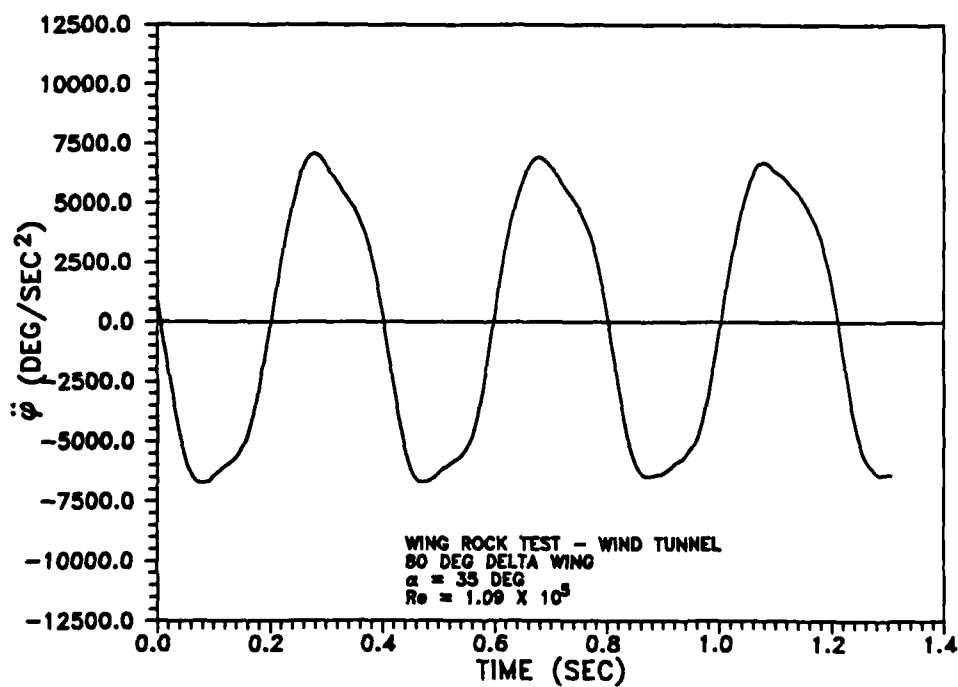


Fig. 108 Wing rock roll acceleration time history, $\bar{q} = 0.5$ psf.

wind tunnel findings. The average roll acceleration magnitude was $6716^\circ/\text{sec}^2$, compared to a predicted value of $7081^\circ/\text{sec}^2$ for a pure sinusoidal variation in ϕ . The phase portrait (Fig. 109) revealed a stable limit cycle for multiple cycles of oscillation. Also shown is a phase portrait which assumed sinusoidal variations in roll angles and roll rates with the experimental values of amplitude and frequency. Fig. 109 pictorially illustrates the deviation between a pure sinusoidal motion of the wing and the actual wing oscillations. Probably the most important result was the C_ℓ versus ϕ plot (Fig. 110), which was derived from acceleration data using equation (12). As speculated prior to the wind tunnel study, both C_ℓ magnitudes and the hysteresis directions were different from the water tunnel results (Figs. 65, 71, 75, and 79). However, it was extremely important that both the magnitudes and the hysteresis directions agreed with results presented by Nguyen, Yip, and Chambers.²³ Based on the energy approach of equation (29), the data indicated that there was unstable damping at small ϕ and stable damping at large ϕ .

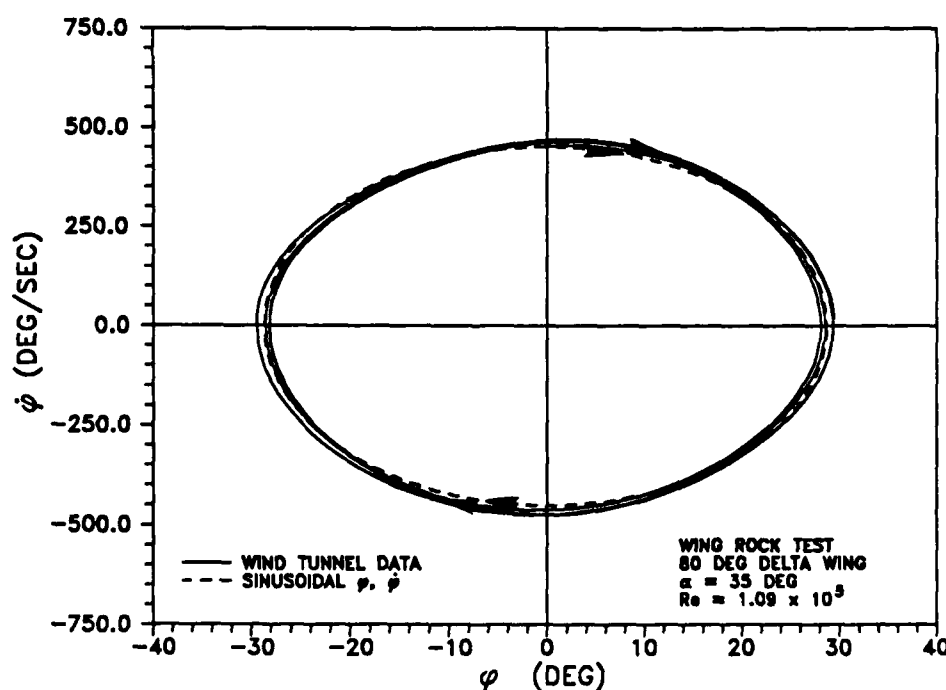


Fig. 109 Wing rock phase portrait, $\bar{q} = 0.5$ psf.

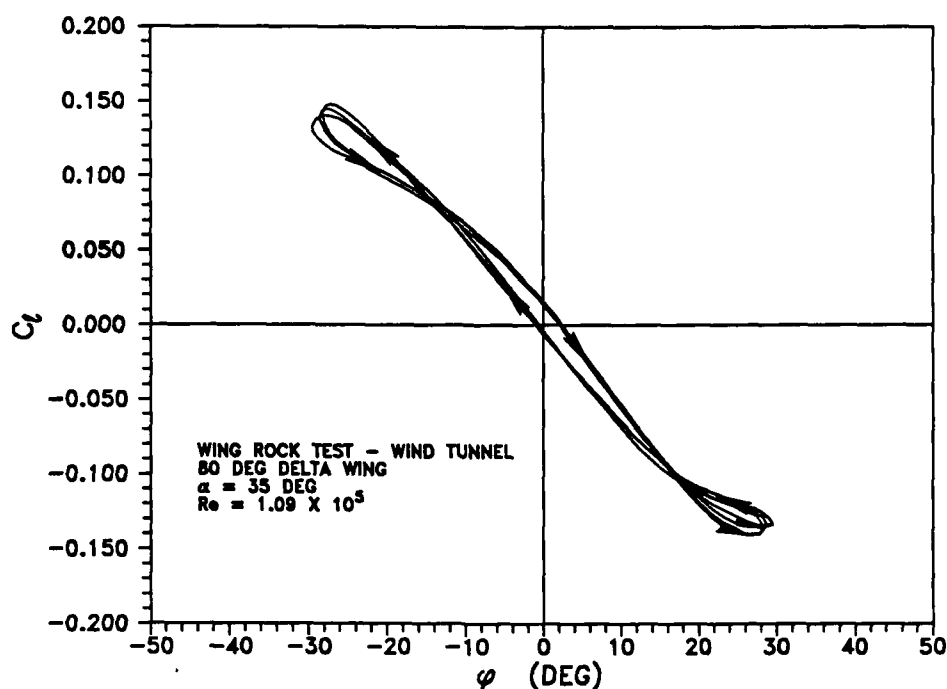


Fig. 110 Aerodynamic rolling moment versus ϕ , $\bar{q} = 0.5$ psf.

The most extensively investigated test condition was $\alpha = 35^\circ$ and $\bar{q} = 1.0$ psf, where $V_\infty = 29$ fps and $Re = 1.54 \times 10^5$. While $\bar{q} = 0.5$ psf demonstrated repeatable results and most closely matched the water tunnel flow conditions, there was some concern about the capability of the wind tunnel to maintain steady flows for $\bar{q} < 1.0$ psf. Additionally, at $\bar{q} = 0.5$ psf, the dynamic pressure could only be set within $\pm 10\%$, while that range was cut in half at $\bar{q} = 1.0$ psf. It was important to accurately know \bar{q} , since whatever percentage of uncertainty existed in its value also existed in the calculation of C_ℓ from equation (12).

These tests also required either the introduction of an upstream flow disturbance or an initial non-zero roll angle setting to initiate wing rock. In addition to examining the wing rock limit cycle characteristics, the results presented here provided excellent information regarding the initiation and build-up of the limit cycle oscillation.

An initial roll angle of -9.5° gave sufficient asymmetry for development of the limit cycle oscillations (Fig. 111). Once the model was released, it took approximately 3.5 seconds to reach

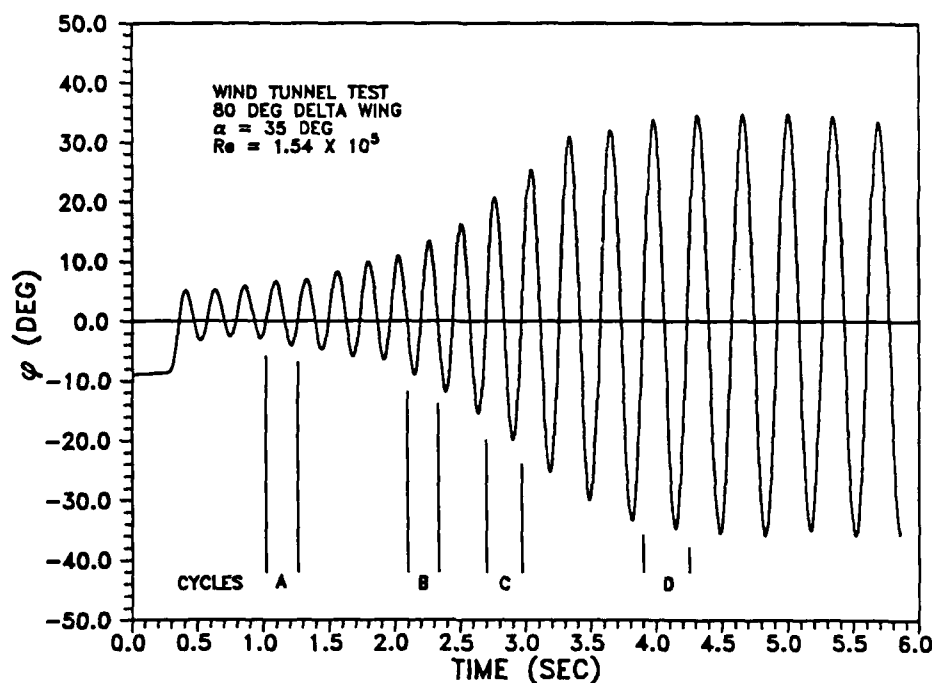


Fig. 111 Wing rock roll angle time history, $\bar{q} = 1.0$ psf.

steady wing rock. The average limit cycle amplitude was 34.8° with maximum cycle to cycle and test to test deviations of less than $\pm 1^\circ$. In over 10 different runs at this test condition, the period only varied from 0.332 sec to 0.344 sec, with an average value for all tests of 0.335 sec. This excellent repeatability established confidence in the accuracy of the data. The corresponding average frequency and reduced frequency were 18.8 rad/sec and 0.095, respectively. The roll rate time history (Fig. 112) showed the build-up to a constant maximum value. The roll acceleration profile is presented in Fig. 113. Despite the compressed time scale, the skewed acceleration peaks in the limit cycle region of Fig. 113 ($t > 3$ sec) indicated hysteresis with roll angle, as observed in other tests. The phase portrait (Fig. 114) clearly showed the wing rock build-up into a steady limit cycle. For comparison purposes, the limit cycle predicted by the fourth order Runge-Kutta algorithm using average values of $C_{l\beta}$, C_{lp0} , $C_{lp\beta}$, and C_{lpp} was also presented. The average $C_{l\beta}$ values were taken from static wind tunnel tests²³ on an 80°

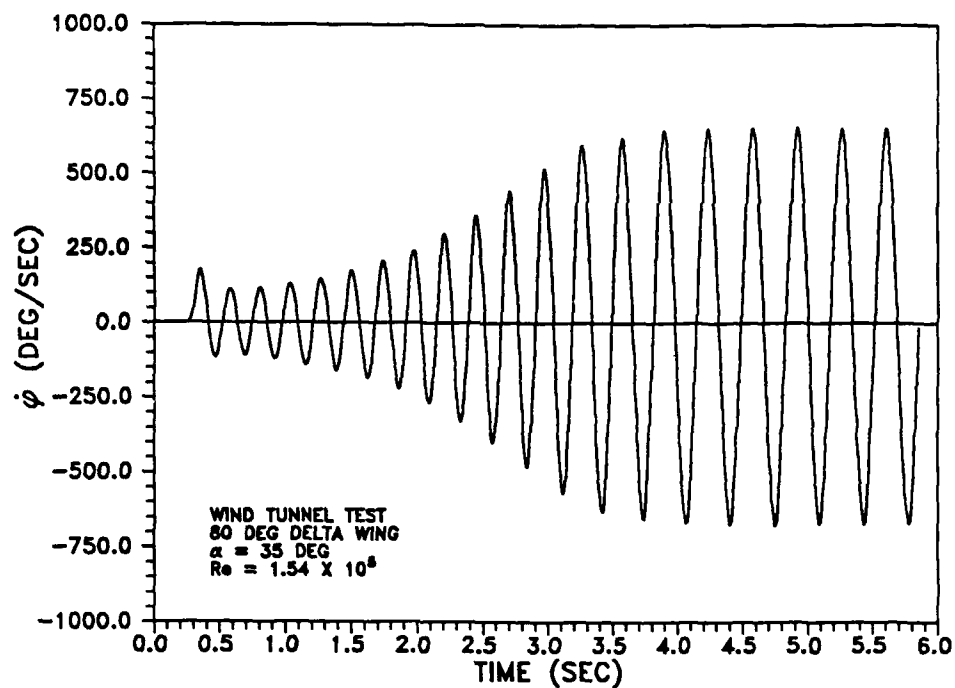


Fig. 112 Wing rock roll rate time history, $\bar{q} = 1.0$ psf.

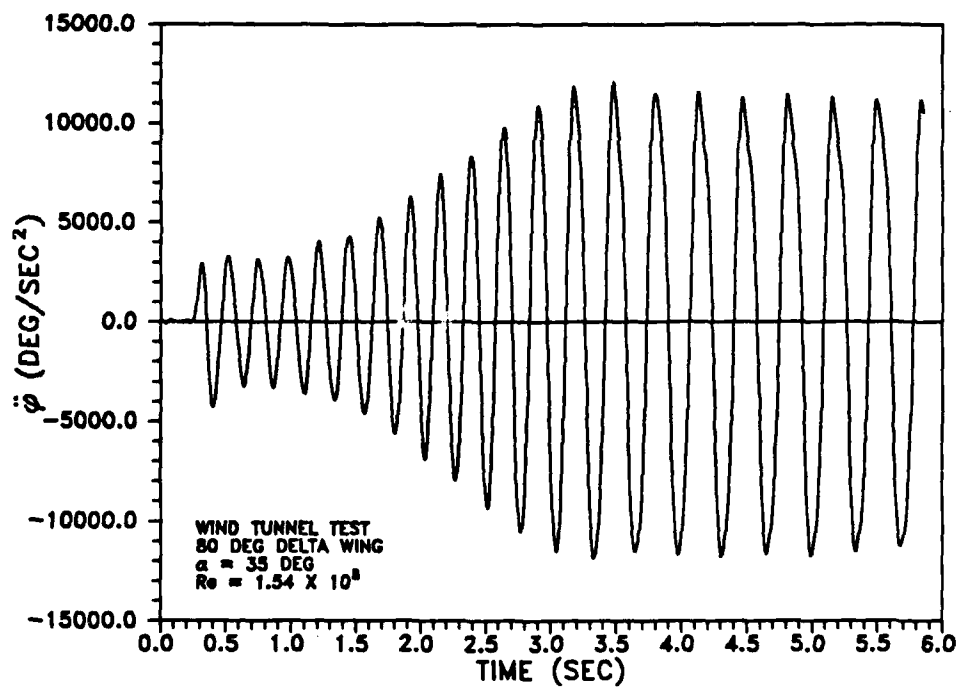


Fig. 113 Wing rock roll acceleration time history, $\bar{q} = 1.0$ psf.

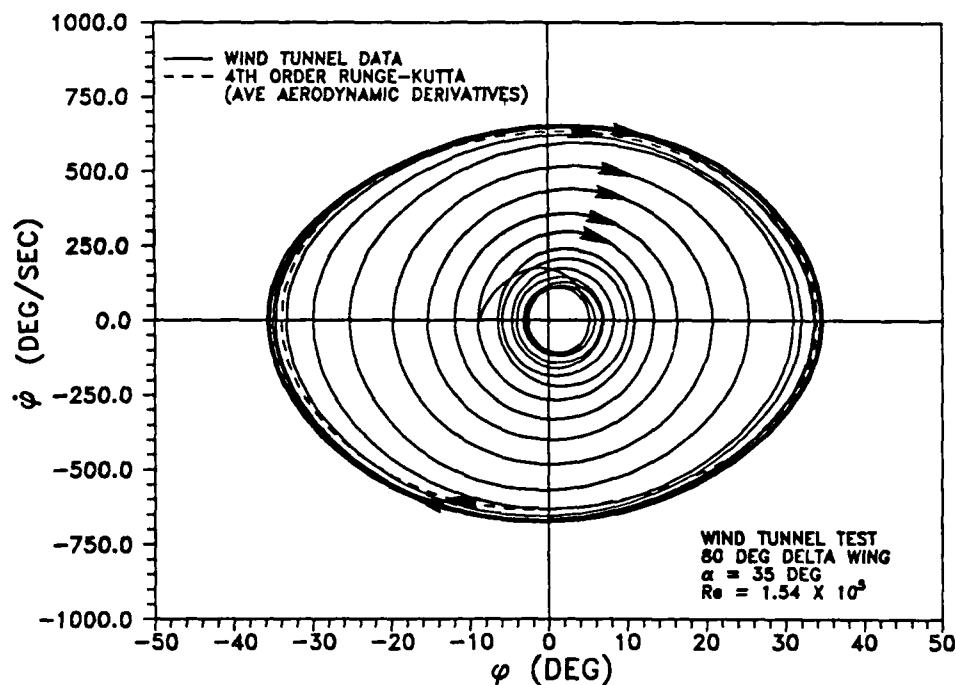


Fig. 114 Wing rock phase portrait, $\bar{q} = 1.0$ psf.

delta wing and are shown for different angles of attack in Fig. 115. The other aerodynamic damping derivatives were calculated by Hsu and Lan using the VORSTAB code^{29,30} (Fig. 116). Overall, the simulation agreed well with the data. The shape of the predicted phase portrait was very similar to the experiment; however, the roll angles and roll rates were slightly underestimated. The Runge-Kutta integration gave a limit cycle amplitude of 33.9° which was 2.6% below the average roll angle magnitude of the experiments. The mathematical model predicted an amplitude of 33.3° which was identical to the value estimated by the Runge-Kutta algorithm using the β approximation of equation (18), but 4.3% below the measured $|\phi|$. The average maximum roll rate magnitude from the tests was $660.6^\circ/\text{sec}$ compared to a simulated value of $626.5^\circ/\text{sec}$. The Runge-Kutta and the mathematical model predicted periods of 0.39 sec and 0.335 sec, respectively, both in excellent agreement with measured periods. Based on these results, the average $C_{l\beta}$ determined from static tests agreed extremely well with results

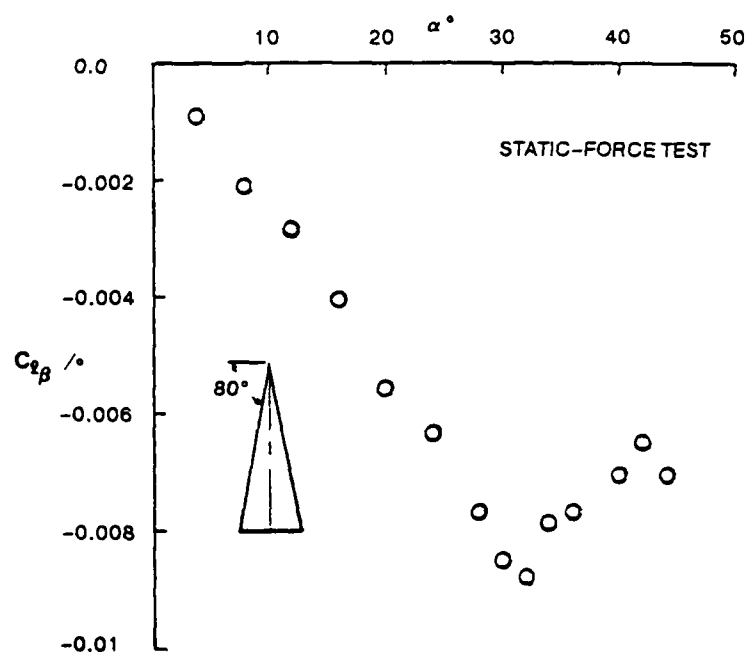


Fig. 115 Average $C_{l\beta}$ versus α for 80° delta wing.³⁰

from dynamic experiments. Average roll damping derivatives also gave a reasonable estimate of limit cycle amplitude at this dynamic pressure.

Analyzing $C_{l\beta}$ versus ϕ during the transient build-up of the limit cycle provided very useful information on the development of wing rock in the wind tunnel. This analysis was accomplished by examining individual cycles during the wing rock build-up. Four such cycles were identified in Fig. 111. The rolling moment histograms are plotted for each cycle in Fig. 117. First, cycle A (Fig. 117a) showed a single small clockwise loop. The loop was not centered at the origin since the initial oscillations were not purely about $\phi = 0^\circ$. Analyzing the energy exchange with equation (29), the clockwise loop represented the addition of energy to the wing and was destabilizing. This condition was indicative of unstable roll damping, positive $C_{l\beta}$, and resulted in an increase in roll amplitude. Cycle B (Fig. 117b) showed a continued increase in the amplitude of the oscillation with a substantial increase in the

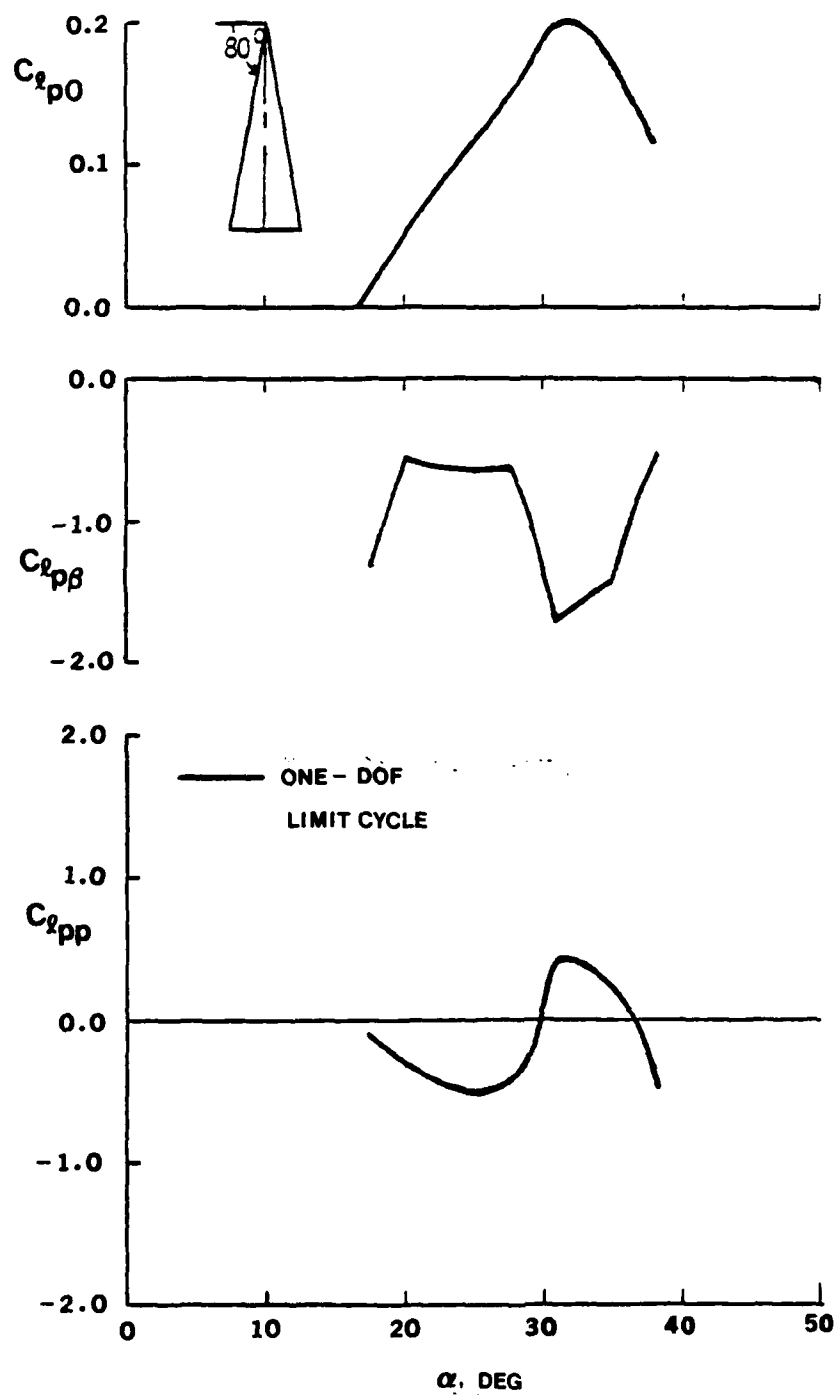


Fig. 116 Theoretical variation of roll damping derivatives with angle of attack.³⁰

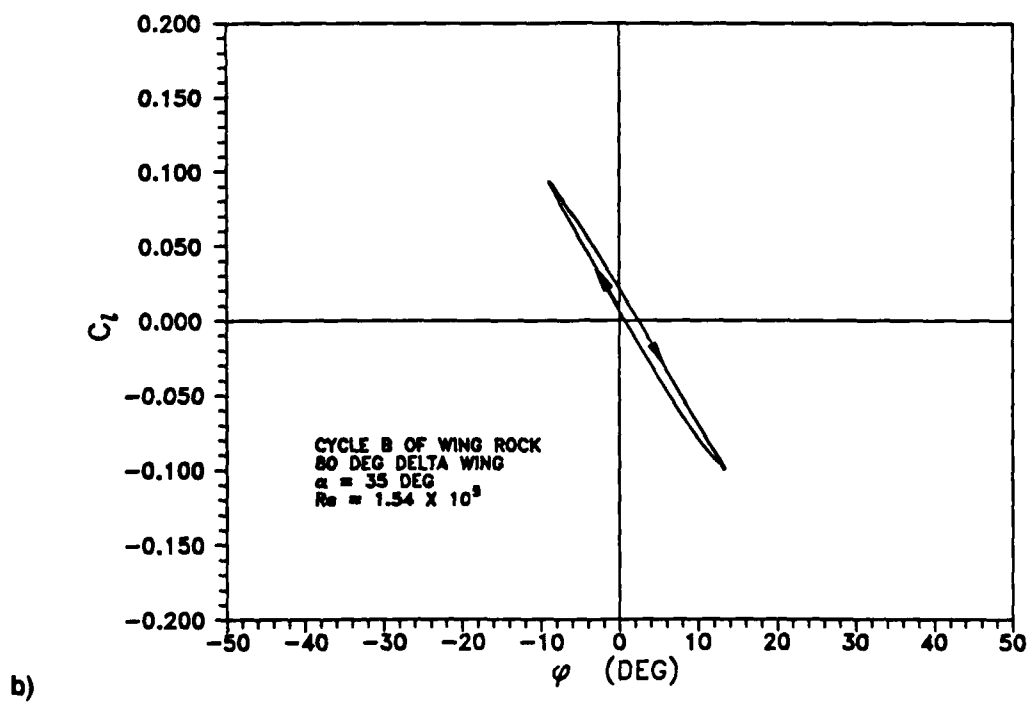
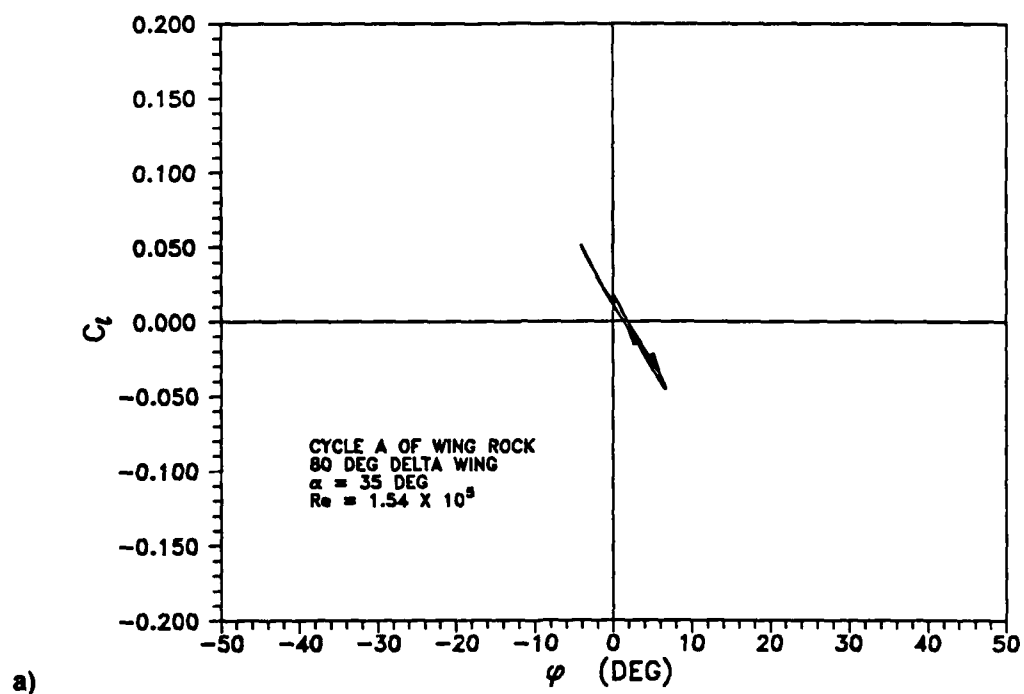
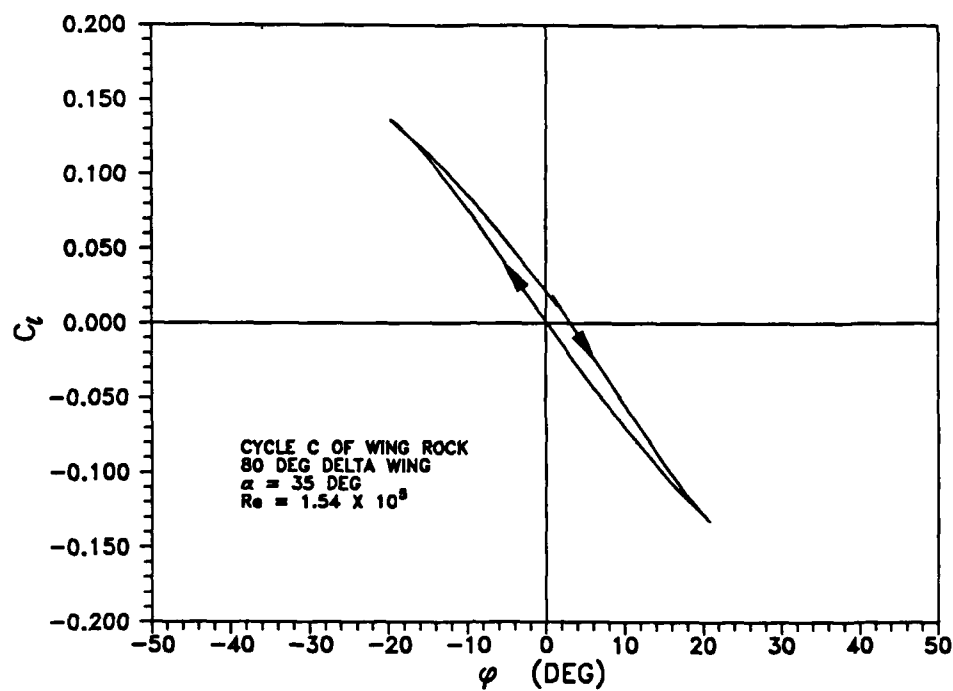
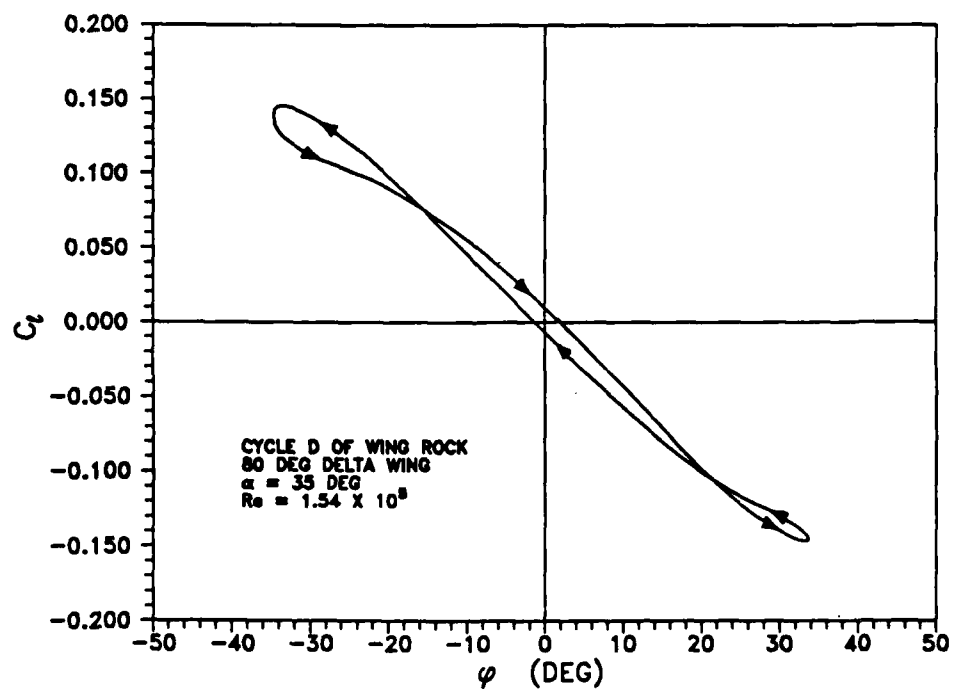


Fig. 117 Aerodynamic rolling moment versus ϕ , $\bar{q} = 1.0$ psf for a) cycle A, b) cycle B, c) cycle C, and d) cycle D.



c)



d)

Fig. 117 Continued

magnitude of the rolling moments. The C_{ℓ} versus ϕ plot was still a single clockwise hysteresis loop, with unstable roll damping, and the roll amplitude continued to grow. Cycle C (Fig. 117c) also demonstrated a clockwise hysteresis loop; however, the loop was very narrow at the larger roll (or sideslip) angles, indicating that the unstable roll damping was small at that point. At cycle D (Fig. 117d), the wing rock just reached its limit cycle amplitude. This cycle revealed a crossover in the rolling moment hysteresis, with a clockwise loop between $\phi = -18^\circ$ and $\phi = +20^\circ$ and counterclockwise loops on each end at the larger positive and negative roll angles. The clockwise loop indicated destabilizing roll damping at the lower roll angles, as discussed above. The counterclockwise loops represented stable roll damping, negative $C_{\ell p}$, which tend to limit wing rock amplitude. Note that crossover roll angles corresponded to $\beta \approx -10^\circ$ and $\beta \approx 11^\circ$. Rotary tests performed by Nguyen, Yip, and Chambers²³ on an 80° delta wing showed that at $\alpha = 30^\circ$, the roll damping changed from unstable to stable at $|\beta| \approx 10^\circ$, which is in good agreement with these measurements. Multiple cycles taken for $t > 4$ sec (Fig. 111) during the steady limit cycle oscillation showed the same destabilizing loops at small roll angles and the stabilizing loops at large roll angles (Fig. 118). It is important to note the excellent repeatability of the data from cycle to cycle. From an energy exchange standpoint, the amount of energy added to the wing in the clockwise loop must exactly balance the energy extracted from the wing in the two counterclockwise loops for a limit cycle to exist. For this balance to hold, the areas of the two counterclockwise outer loops should exactly equal the area of the center clockwise loop. Qualitatively, it appeared that the criteria was met during the wing rock oscillation; however, it was unrealistic to believe that experimental data involving both smoothing and second derivatives would yield perfect results. This same rolling moment development pattern was exhibited on all of the wind tunnel tests examined at this and other dynamic pressures when the initial ϕ was below the amplitude of the limit cycle. The results obtained here were very similar to those obtained by Nguyen, Yip, and Chambers²³ and seemed to support their theory that unstable roll damping at small roll (or sideslip) angles and stable roll

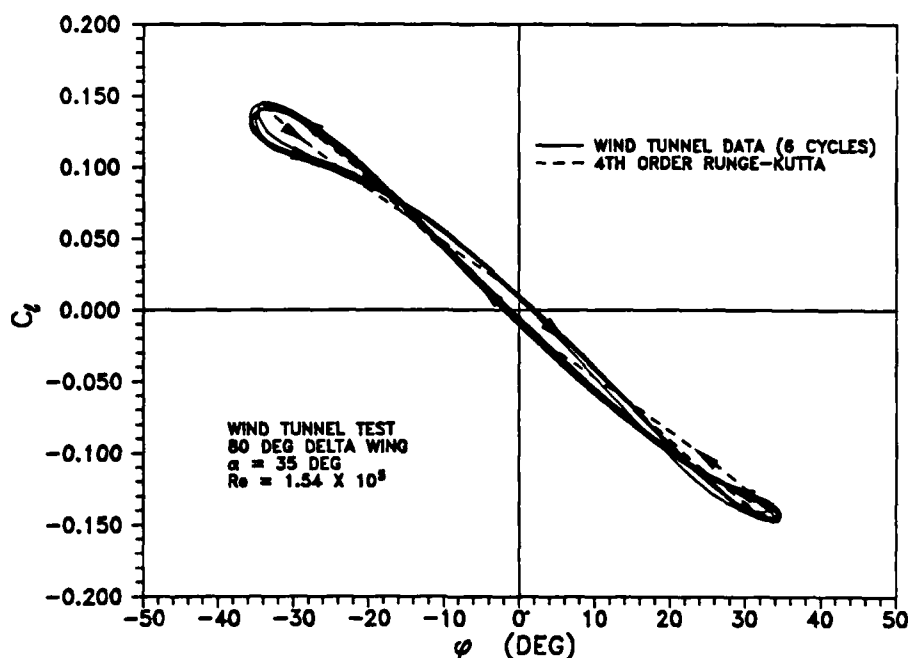


Fig. 118 Aerodynamic rolling moment versus ϕ , $\bar{q} = 1.0$ psf.

damping at large roll (or sideslip) angles are the primary mechanism driving wing rock. Unfortunately, wing rock build-up was not recorded during the water tunnel tests, although the steady state wing rock results showed hysteresis in the opposite direction and C_{ℓ} magnitudes over 15 times smaller than the wind tunnel data. Despite the wind tunnel roll damping results, the water tunnel data cast serious doubt that roll damping actually drives the wing rock oscillations.

A single cycle of the rolling moment coefficient versus ϕ data extracted from Fig. 118 was compared with results from the Runge-Kutta simulation in Fig. 119. As discussed earlier, constant values of $C_{\ell\beta}$ and roll damping derivatives were used in the integration. While roll amplitudes were slightly underestimated in the simulation, the slopes of the plots were in excellent agreement. The hysteresis directions were the same; however, there were some differences in the magnitudes of the hysteresis, especially at the larger negative roll angles. In addition to the Runge-Kutta results, Fig. 119 shows a simulation of equation (14) and (15)

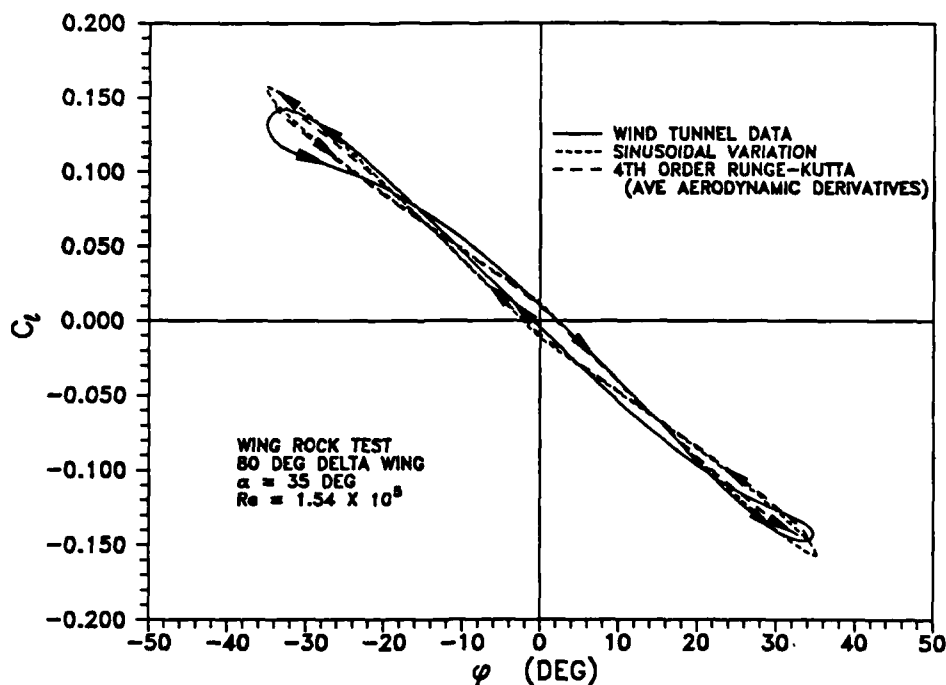


Fig. 119 Aerodynamic rolling moment versus ϕ cycle, $\bar{q} = 1.0$ psf.

assuming sinusoidal variations in the roll angles and roll rates with the roll amplitude and frequency taken from the experimental data. The aerodynamic derivatives used in equations (14) and (15) were the same as used in the Runge-Kutta integration. The simulation and the Runge-Kutta results were in good agreement, especially at small ϕ . Another reasonable simulation was obtained using the same procedures; however, the amplitude and frequency used in the sinusoidal variation were calculated with the mathematical model. This outcome is not shown in Fig. 119; it was also very similar to the Runge-Kutta results.

Tests were also conducted with an initial roll displacement well above the limit cycle amplitude. Fig. 120 illustrates the ϕ time history for a test at the same flow condition of $\bar{q} = 1.0$ psf ($Re = 1.54 \times 10^5$) with an initial roll displacement of approximately -70° . The data presented in Fig. 120 were not smoothed. Once the model was released, roll angle amplitude quickly decreased until the limit cycle was obtained. The phase portrait (Fig. 121) clearly showed

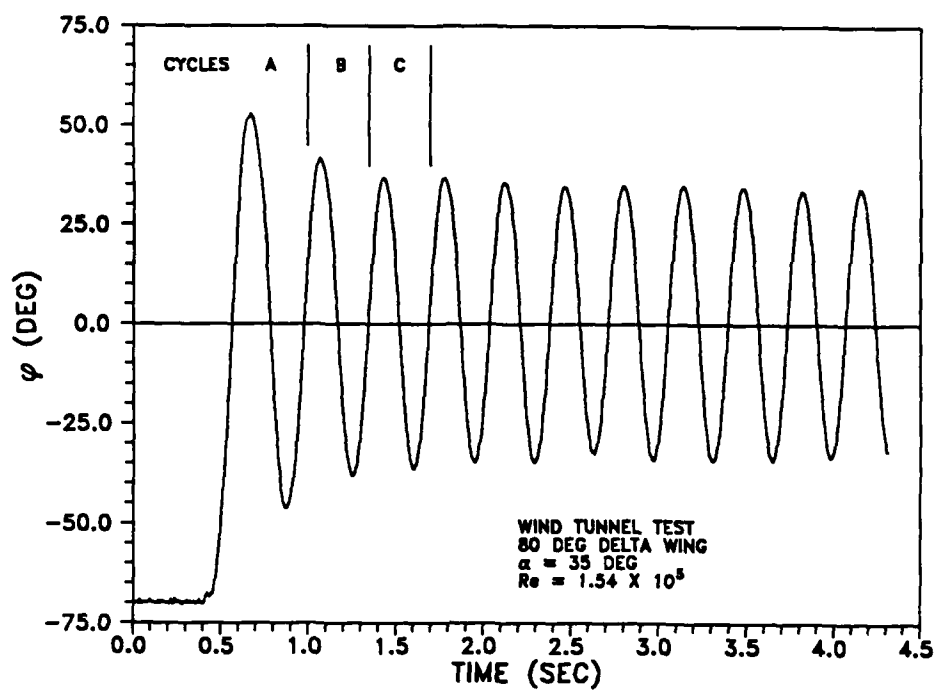


Fig. 120 Wing rock roll angle history, $\bar{q} = 1.0$ psf, $\phi_0 = -70^\circ$.

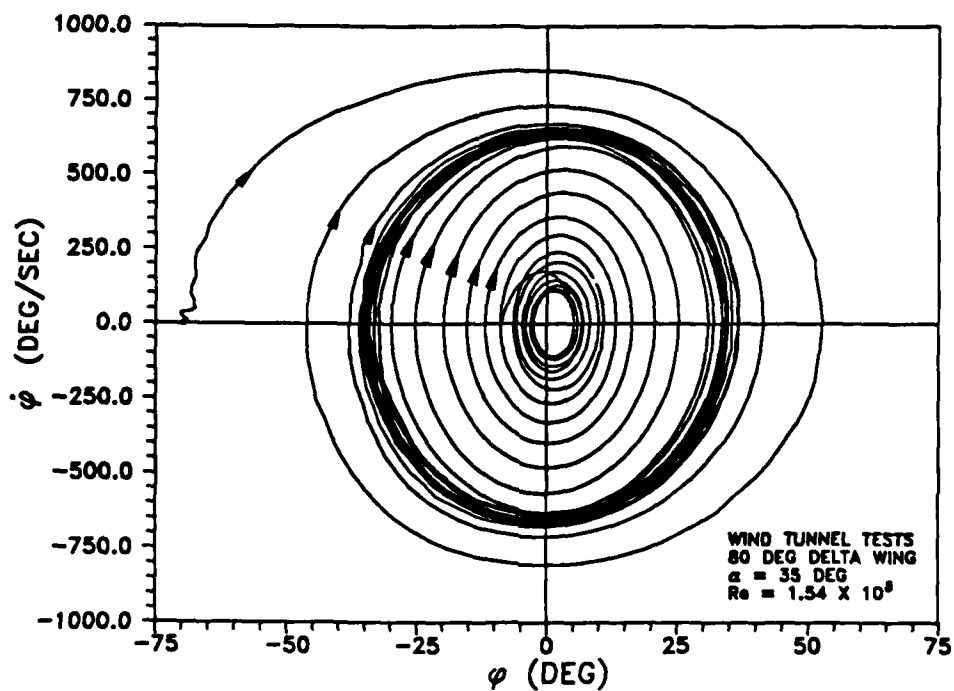


Fig. 121 Wing rock phase portrait, $\bar{q} = 1.0$ psf, $\phi_0 = -70^\circ$.

convergence to the same limit cycle as obtained in the $\phi_0 = -9.5^\circ$ test, which is superimposed. This behavior indicated a stable limit cycle. A stable limit cycle was also predicted by the Runge-Kutta integration, since initial conditions both inside and outside limit cycle converged to the same isolated closed path (Fig. 122), even though roll angles and roll rates were slightly underestimated.

Once again, C_L versus ϕ for the different cycles of the wing rock development in Fig. 120 provided very useful information (Fig. 123). Cycle A (Fig. 123a) showed the first complete cycle of oscillation after the model was released. The C_L versus ϕ had two large counterclockwise loops at the larger positive and negative roll angles, indicating a large amount of roll damping. The same cycle also showed no hysteresis at the smaller roll angles indicating a lack of damping. These loops suggested a decrease in roll amplitude, just as measured. Cycle B (Fig. 123b) was near the start of the limit cycle, as evidenced by the beginning of a clockwise loop (destabilizing roll damping) between $\phi = -16^\circ$ and $\phi = 20^\circ$. Cycle C (Fig. 123c) was a

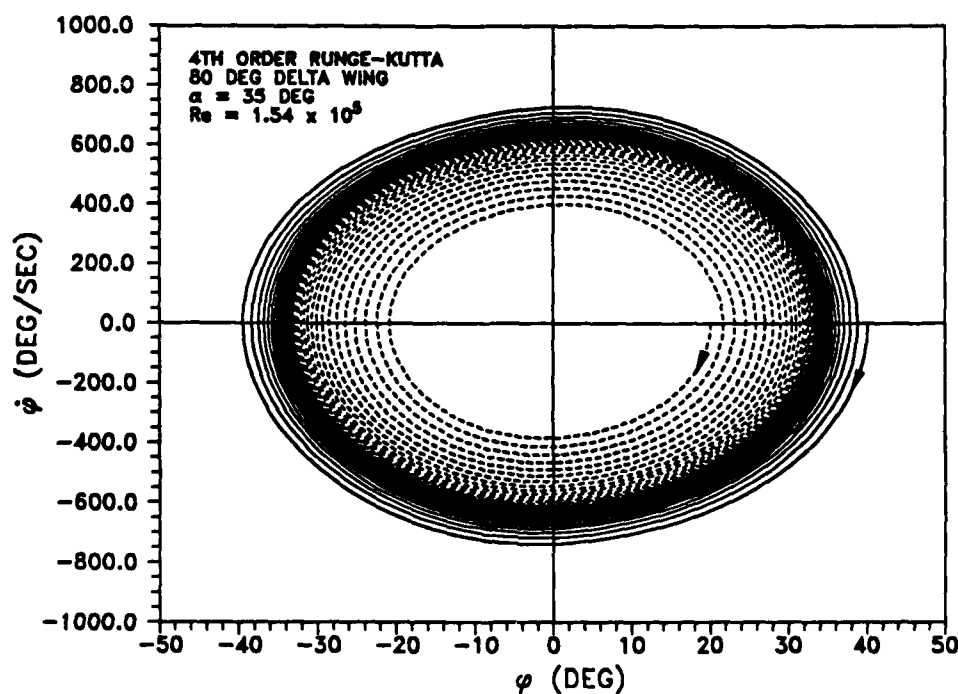
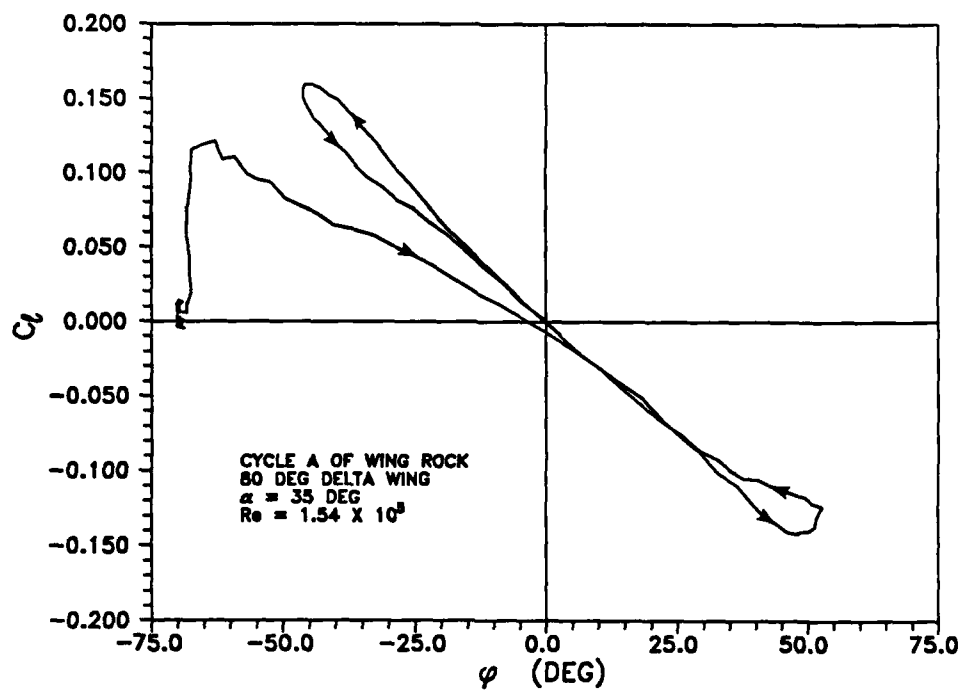
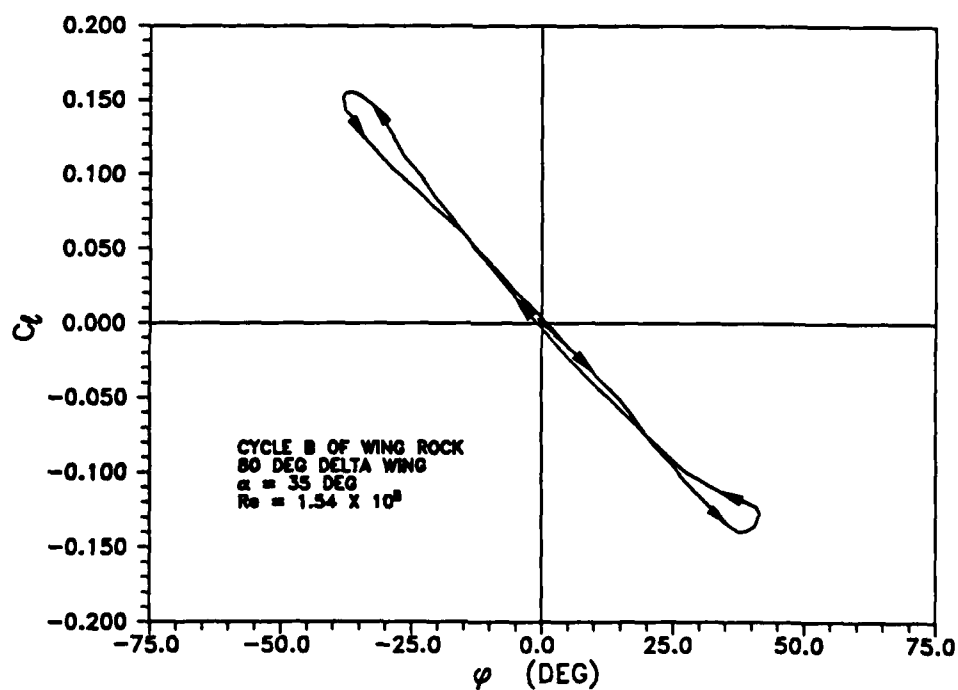


Fig. 122 Wing rock phase portrait from Runge-Kutta integration.

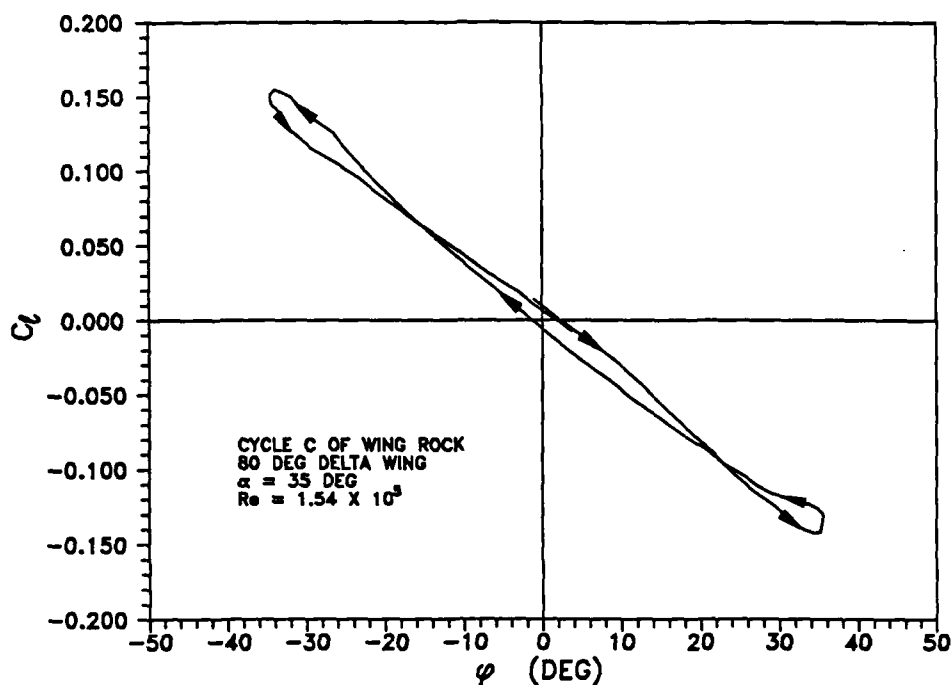


a)



b)

Fig. 123 Aerodynamic rolling moment versus ϕ , $\bar{q} = 1.0$ psf, $\phi_0 = -70^\circ$ for a) cycle A, b) cycle B, and c) cycle C.



c)

Fig. 123 Continued

typical cycle once the limit cycle developed and looked very similar to Fig. 119. The major difference in the two plots is that the roll angles shown in Fig. 123c were raw data with no smoothing, while Fig. 119 had smoothed roll angles. While raw roll angles were shown in all of the data presented at $\phi_0 = -70^\circ$, smoothing was used in obtaining roll rates and roll accelerations.

As the wind tunnel dynamic pressure was increased to $\bar{q} = 2.0$ psf, corresponding to $V_\infty = 41$ fps and $Re = 2.17 \times 10^5$, the period of oscillation decreased to 0.263 sec, while the average limit cycle amplitude grew to 39.6° . The average frequency and reduced frequency of the wing rock were 23.9 rad/sec and 0.856, respectively. The ϕ time history (Fig. 124) increased in magnitude from 2° to the limit cycle amplitude in approximately 3 sec after release of the model. Typical roll rates (Fig. 125) and roll accelerations (Fig. 126) were similar to the $\bar{q} = 1.0$ psf results (Figs. 112 and 113, respectively); however, the magnitudes were larger due to the

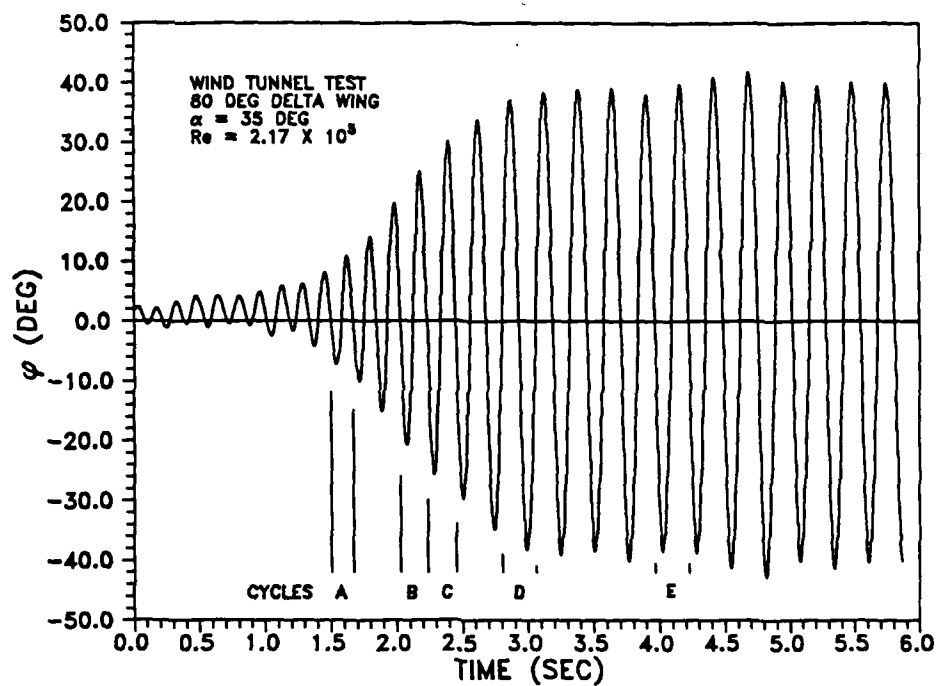


Fig. 124 Wing rock roll angle time history, $\bar{q} = 2.0$ psf.

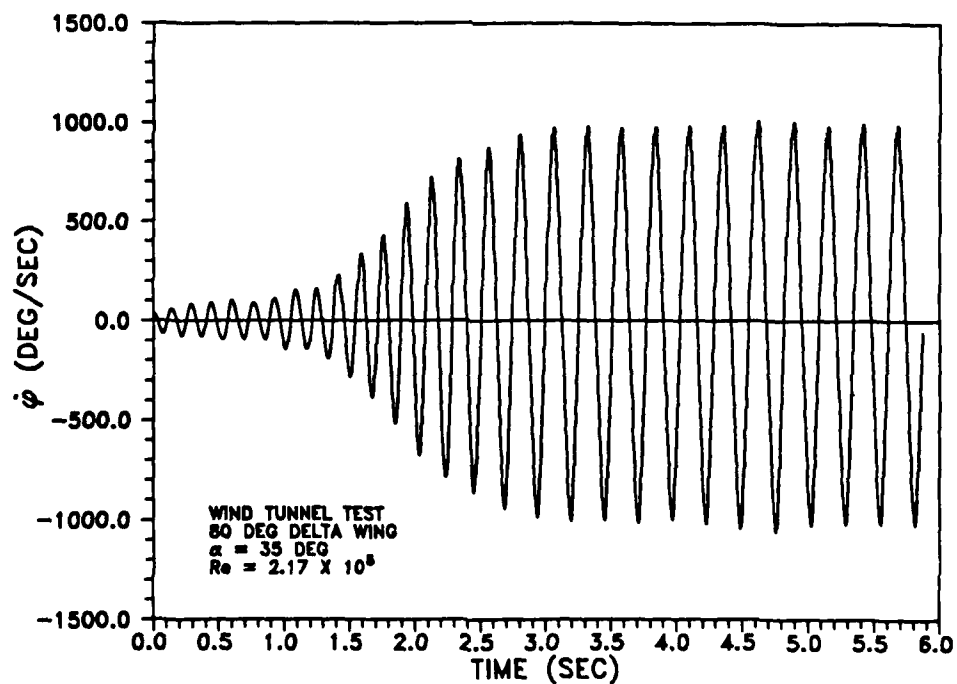


Fig. 125 Wing rock roll rate time history, $\bar{q} = 2.0$ psf.

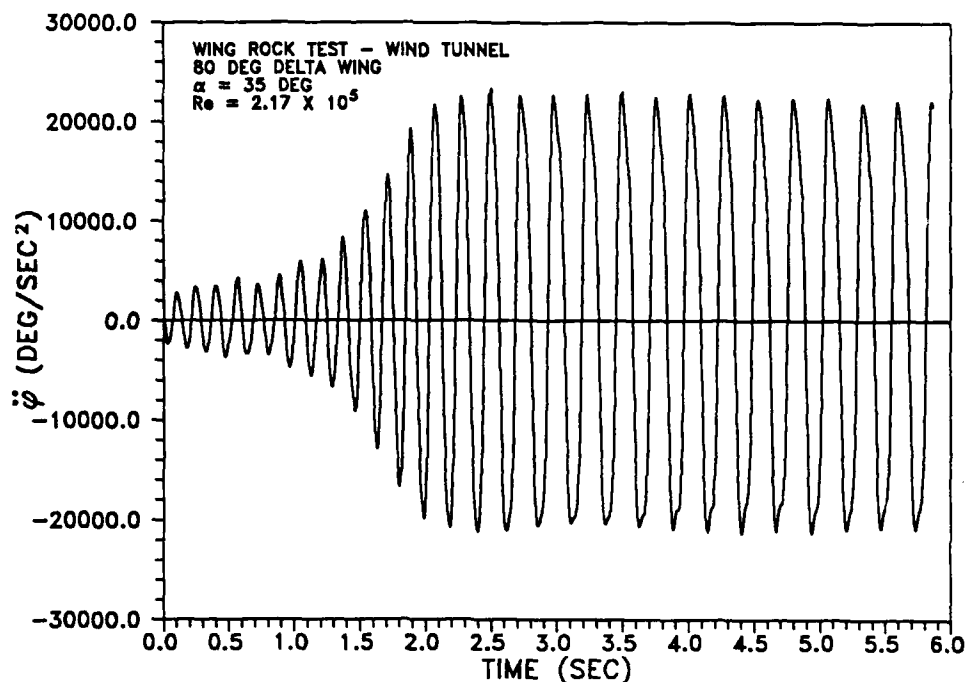


Fig. 126 Wing rock roll acceleration time history, $\bar{q} = 2.0$ psf.

increased roll amplitude and frequency of oscillation. The phase portrait (Fig. 127) also revealed the characteristic growth into the limit cycle. Note that while the average roll amplitude was 39.6° , the maximum ϕ magnitudes varied from 37.9° to 42.7° , which was the widest range of any wind tunnel and water tunnel test. For comparison purposes, the Runge-Kutta simulation of the phase portrait was also shown in Fig. 127. Note that the roll magnitude determined from the simulation was 33.9° , 14% below the experimental limit cycle amplitude. The mathematical model estimated an amplitude of 33.3° using the same average aerodynamic derivatives. A very similar roll magnitude was predicted by Hsu^{29,30} in his simulation of the Nguyen, Yip, and Chambers²³ data; however, that similarity was not surprising since the current study used his roll damping derivatives. The periods predicted from the Runge-Kutta integration and the mathematical model were 0.24 sec and 0.238 sec, respectively, approximately 9% below the measured value.

The C_l versus ϕ for cycles A through E of the $\bar{q} = 2.0$ psf test (Fig. 128) illustrated the same hysteresis patterns which were observed and discussed for the $\bar{q} = 1.0$ psf results. Cycle A

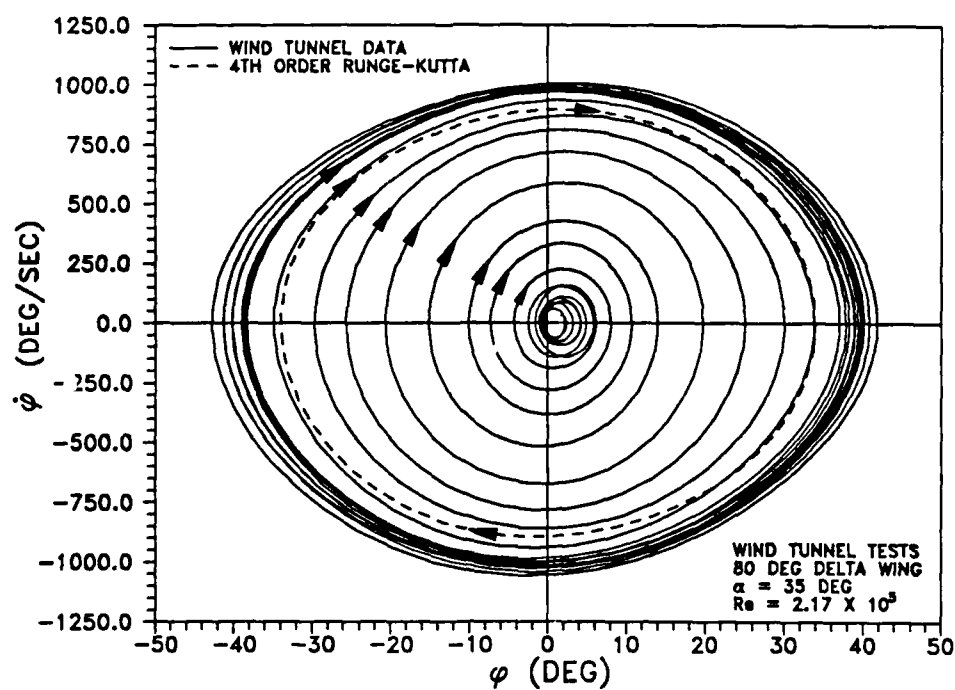
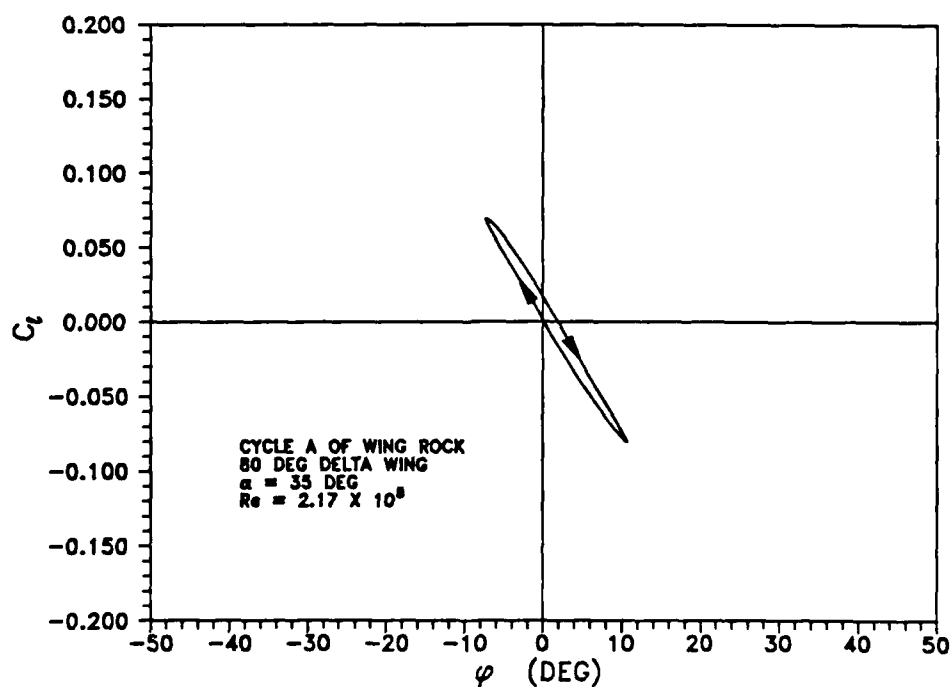
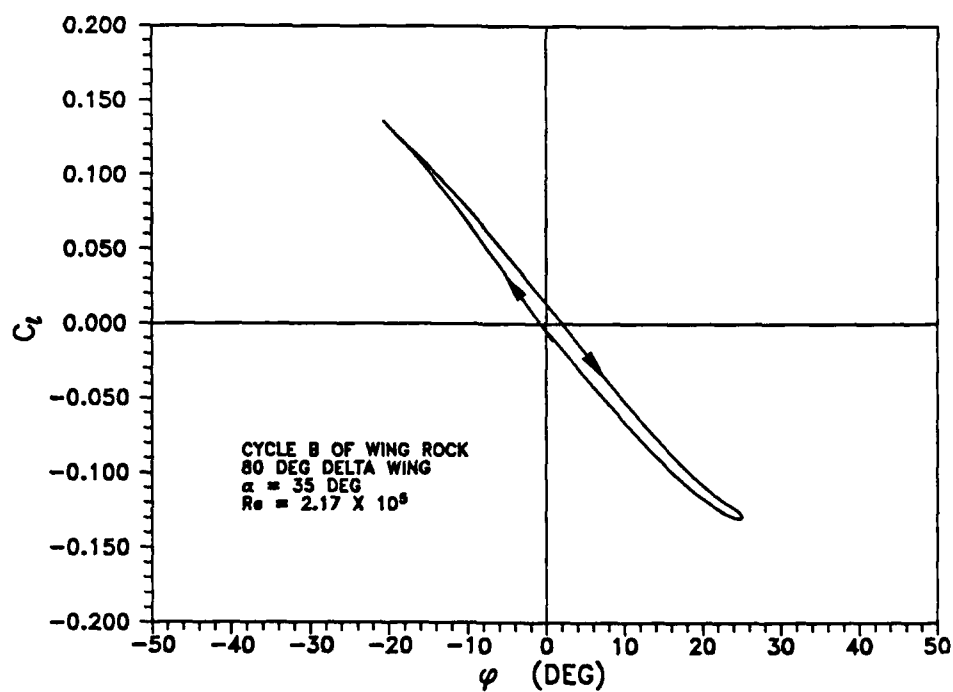


Fig. 127 Wing rock phase portrait, $\bar{q} = 2.0$ psf.

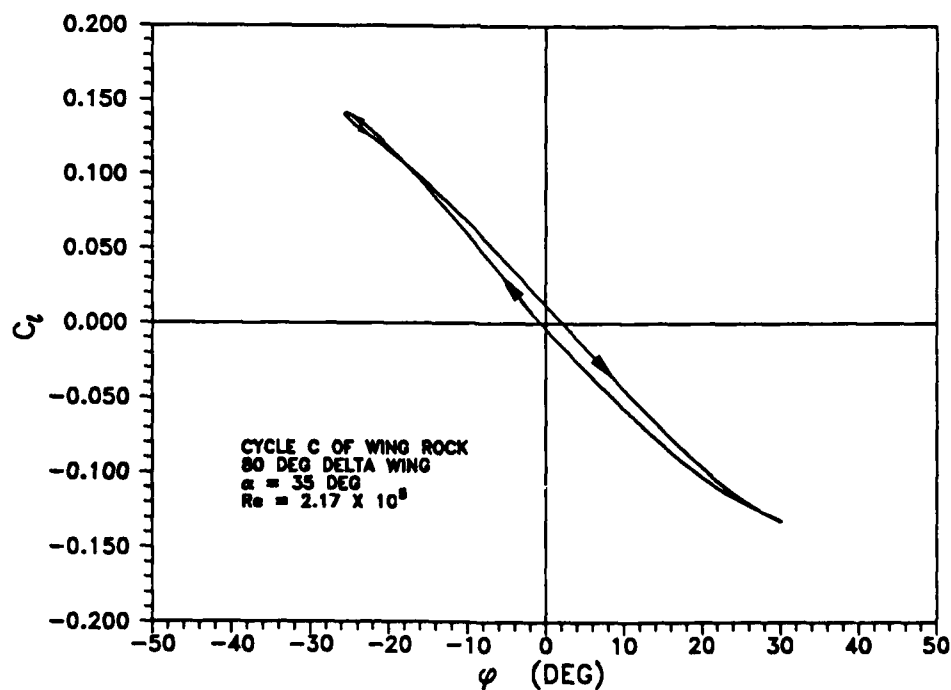


a)

Fig. 128 Aerodynamic rolling moment versus ϕ , $\bar{q} = 2.0$ psf, for a) cycle A, b) cycle B, c) cycle C, d) cycle D, and e) cycle E.

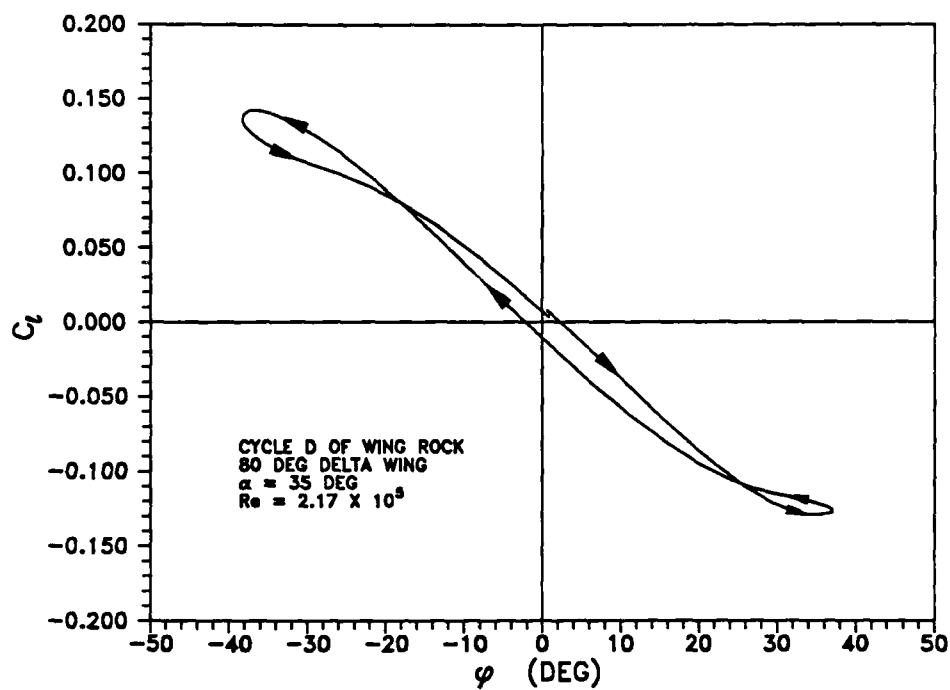


b)

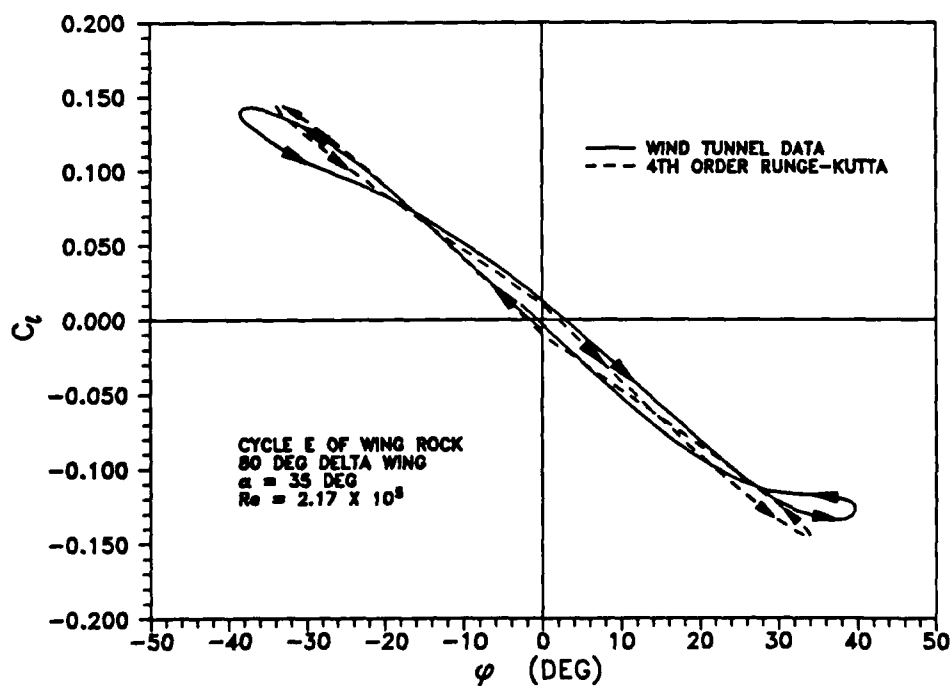


c)

Fig. 128 Continued



d)



e)

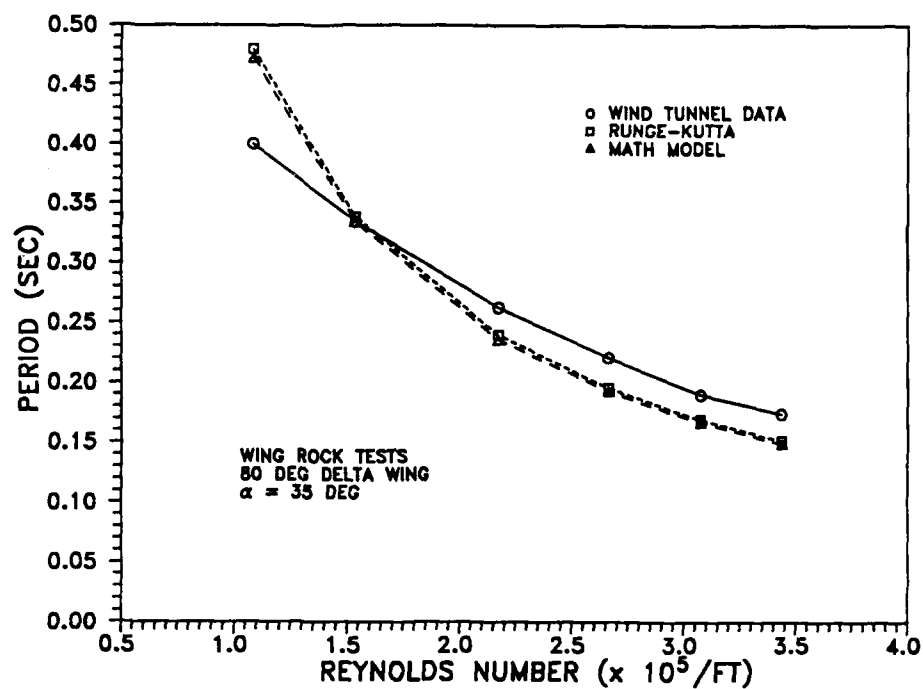
Fig. 128 Continued

(Fig. 128a) and cycle B (Fig. 128b) both occurred early in the ϕ build-up and consisted of single destabilizing clockwise loops. Cycle C (Fig. 128c) was close to the limit cycle and began to display a stabilizing roll damping at the larger roll angles. The stabilizing hysteresis loops became even more evident in cycle D (Fig. 128d) and were completely developed by cycle E (Fig. 128e) where the steady limit cycle had been reached. These results also demonstrated repeatability in the development of the C_{ℓ} versus ϕ hysteresis loops, even at different flow conditions. Similar C_{ℓ} versus ϕ data were also obtained during the wing rock build-up for the other test conditions examined; however, they were omitted from this report for conciseness.

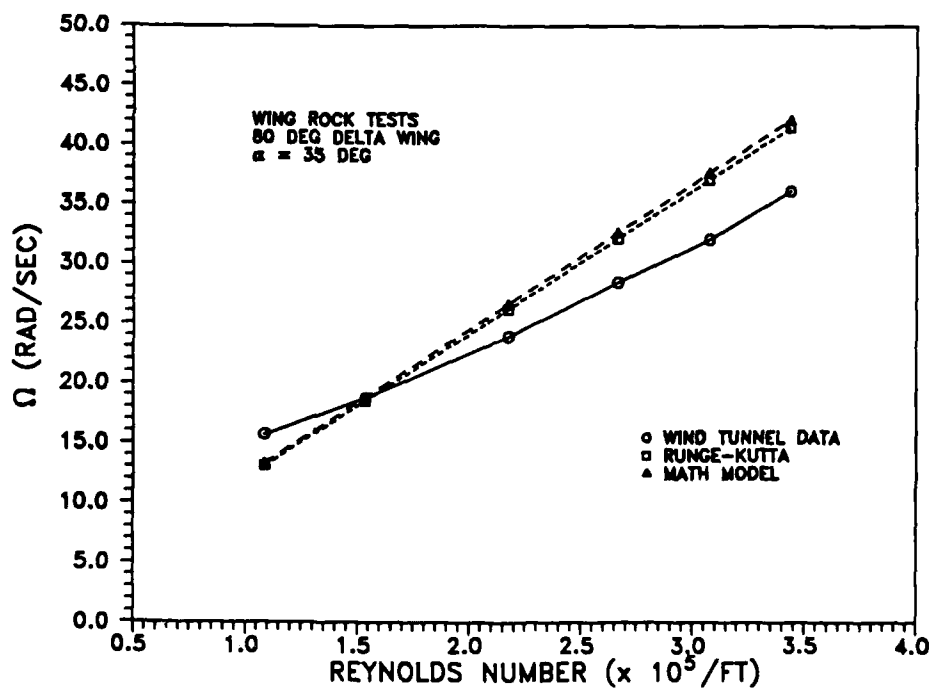
The Runge-Kutta simulation of the C_{ℓ} versus ϕ data (Fig. 128e) agreed reasonably well with experimental data. The slopes of the curves were similar except at the larger roll angles. At these locations, the constant $C_{\ell\beta}$ assumption in the simulation did not account for actual $C_{\ell\beta}$ variation with roll angle. Hysteresis loop directions were the same. Comparing the average slopes of the $\bar{q} = 1.0$ psf and $\bar{q} = 2.0$ psf C_{ℓ} versus ϕ data, $C_{\ell\beta}$ values appeared to be very close. A more detailed discussion of this derivative will be given later.

Other dynamic pressures examined at $\alpha = 35^\circ$ were 3.0 psf, 4.0 psf, and 5.0 psf. Rather than discuss each of these test conditions in detail individually, they will be discussed collectively to illustrate the effects of increased velocities and Reynolds numbers on wing rock behavior. In general, the same phenomena were observed in these tests as were reported for lower \bar{q} .

One of the most obvious effects of increasing dynamic pressure (hence velocity and Reynolds number) was a decrease in period and an increase in frequency (Fig. 129). As shown in Fig. 129a, changing Reynolds number had less effect on the period at the larger Reynolds numbers. While not proven, it appeared likely that the period was approaching some lower limit with increasing Reynolds number. Both the mathematical model and the Runge-Kutta integration predicted the same trend; however, the changes in period with Reynolds number were more abrupt at Reynolds numbers less than $2.17 \times 10^5/\text{ft}$ than in the measured data. The



a)



b)

Fig. 129 Wing rock variations with Reynolds number: a) period variations, and b) frequency variations.

results of the two were very similar as shown in the plots. Above $Re = 2.17 \times 10^5/ft$, the slopes of the predicted and experimental data plots were very similar (Fig. 129a), with the predicted periods ranging from 10% to 15% below the actual values. Both the mathematical model and Runge-Kutta predicted a linear relationship between the frequency and Reynolds number (Fig. 129b). The relationship between frequency and Reynolds number for the experimental data was almost linear with a smaller slope than the predicted results. The water tunnel data also revealed a near linear increase in frequency with increasing velocity, even though the slope of the data was significantly different (Fig. 83). The reduced frequency of the experimental data decreased with increasing Reynolds number up to $Re = 2.17 \times 10^5/ft$ and remained relatively constant at higher Reynolds numbers (Fig. 130). This change in reduced frequency indicated that the frequency versus Reynolds number data (Fig. 129b) was not truly linear since the reduced frequency, k , is

$$k = \frac{\Omega b}{2 V_{\infty}} \quad (40)$$

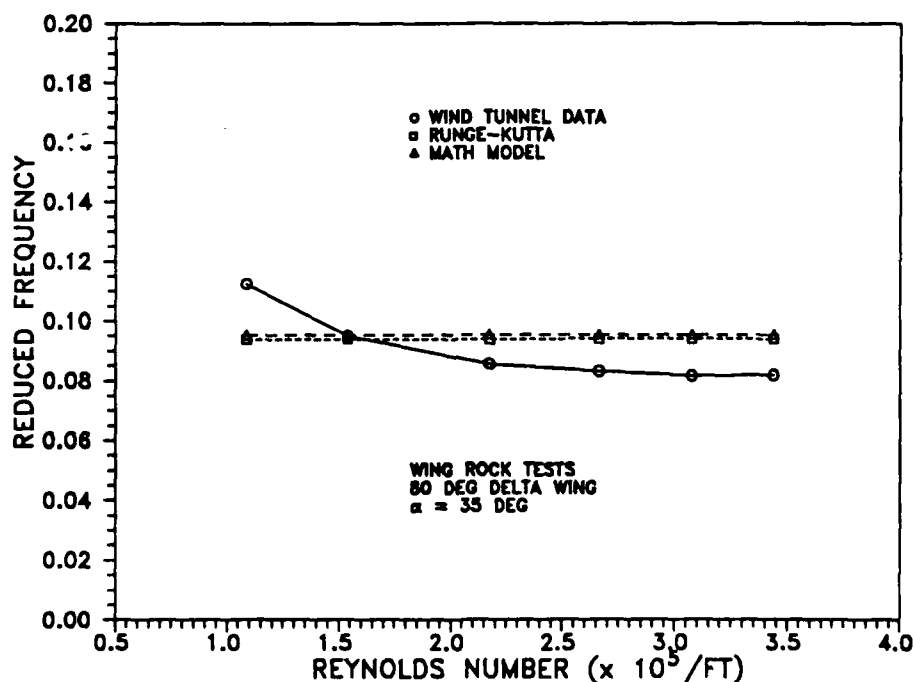


Fig. 130 Wing rock reduced frequency variation with Reynolds number.

and if k is not constant, Ω/V_∞ cannot be constant. The mathematical model predicted a constant reduced frequency of 0.0954, compared to a constant value of 0.0939 for the Runge-Kutta integration. At $\alpha = 35^\circ$, Levin and Katz²⁴ obtained reduced frequencies of 0.1076 to 0.1152 for Reynolds numbers ranging from $4.4 \times 10^5/\text{ft}$ to $8.8 \times 10^5/\text{ft}$. Jun and Nelson²⁶ wind tunnel tests exhibited a reduced frequency of 0.091 at $\text{Re} = 3.15 \times 10^5/\text{ft}$.

As the dynamic pressure increased from $\bar{q} = 0.5$ psf to 5.0 psf (Re went from $1.09 \times 10^5/\text{ft}$ to $3.44 \times 10^5/\text{ft}$), the average limit cycle amplitude increased from 28.7° to 42.1° (Fig. 131). The amplitude growth was relatively dramatic up to $\text{Re} = 2.17 \times 10^5/\text{ft}$, an increase of 10.93° , and then very gradual up to $\text{Re} = 3.44 \times 10^5/\text{ft}$. The bands shown on each data point indicated the range of amplitudes experienced from cycle to cycle and test to test. The mathematical model and Runge-Kutta integration results predicted that roll amplitude would not change with Reynolds number. However, those calculations were based on the assumption that roll damping derivatives ($C_{\ell_{p0}}$, $C_{\ell_{p\beta}}$, and $C_{\ell_{pp}}$) did not change with Reynolds number, which evidently was not valid. Despite this discrepancy, the model and simulation still predicted

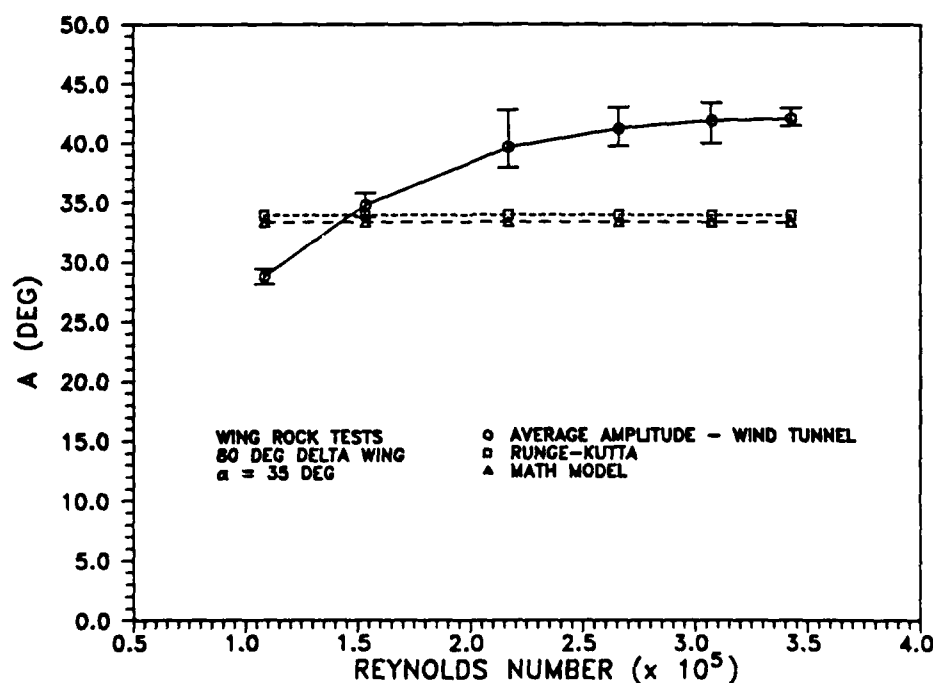


Fig. 131 Wing rock roll amplitude variation with Reynolds number.

amplitude within 20% at the worst case. Levin and Katz reported amplitude growths from approximately 18.5° to 34° in going from $Re = 4.4 \times 10^5/\text{ft}$ to $8.8 \times 10^5/\text{ft}$. While the magnitudes were considerably different from those in the present tests, their results still showed a substantial amplitude growth with increasing Reynolds number. The large differences in the magnitudes were not especially worrisome, given the differences between the two 80° models tested. As discussed in Chapter II, the model used in the Levin and Katz study had a large centerbody to house the free-to-roll bearings and potentiometer (Fig. 13). It was interesting that while there was a factor of 2.5 increase in Reynolds number during the water tunnel tests, the limit cycle amplitude was essentially unchanged. Additionally, in going from $Re = 7.5 \times 10^5/\text{ft}$ in water to $Re = 1.09 \times 10^5/\text{ft}$ in air, the roll amplitude decreased from 36.7° to 28.7° . The wing rock amplitude then grew to 42.1° in the wind tunnel as Reynolds number was increased to $3.44 \times 10^5/\text{ft}$. This difference strongly suggested that Reynolds number was not the only cause of the differences in wing rock behavior between the two media.

A summary of phase portraits for $\bar{q} = 0.5 \text{ psf}$ through $\bar{q} = 5.0 \text{ psf}$ underscored the effects of dynamic pressure (or velocity and Reynolds number) on roll amplitude and roll rate (Fig. 132). As dynamic pressure increased, the phase portrait expanded in all directions. The large increase in roll rates occurred due to the increase of both amplitude and frequency for the oscillation. While magnitudes changed, the shapes of the closed path remained similar. The $\bar{q} = 5.0 \text{ psf}$ plot reflected a limitation of the current video camera system which was mentioned earlier. At this higher velocity, the frequency of oscillation was so large that even 200 frames per second did not capture enough data points for a smooth curve. This limitation resulted in a rougher plot than obtained at the lower dynamic pressures. Note that this condition was most obvious at the top and bottom of the phase portrait where the roll rates were large, while the curve was much smoother on each end where the roll rates were smaller. While the smaller number of data points was noticeable here, it made results from the second derivative of ϕ highly suspect.

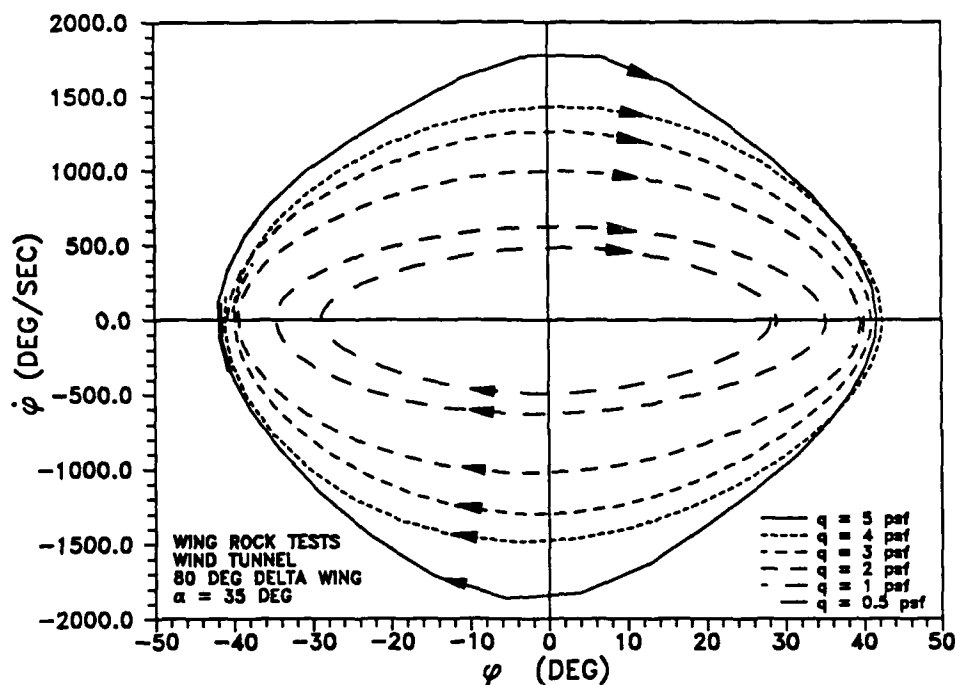


Fig. 132 Wing rock phase portrait comparison, wind tunnel.

The $\ddot{\phi}$ versus $\dot{\phi}$ phase portrait (Fig. 133) showed that the closed paths moved away from the origin with increasing \bar{q} (or V_{∞}). While similar results existed in the water tunnel tests (Fig. 81), those curves had a different shape. The wind tunnel data revealed that at $\dot{\phi} \approx 0$ (near maximum positive or negative ϕ), the magnitude of the roll acceleration was decreasing. On the other hand, the water tunnel data showed that the magnitude of the roll acceleration was increasing at small roll rates. This point once again illustrated the difference in roll acceleration hysteresis between the water tunnel and the wind tunnel experiments.

Another useful comparison was that of C_l versus ϕ (Fig. 134). Dynamic pressures of 0.5, 1.0, and 2.0 psf (Re of $1.09 \times 10^5/\text{ft}$, $1.54 \times 10^5/\text{ft}$, and $2.17 \times 10^5/\text{ft}$, respectively) are presented in Fig. 134a and values of 3.0 and 4.0 (Re of $2.56 \times 10^5/\text{ft}$ and $3.07 \times 10^5/\text{ft}$) are provided in Fig. 134b. These plots display some very important information. First, with the

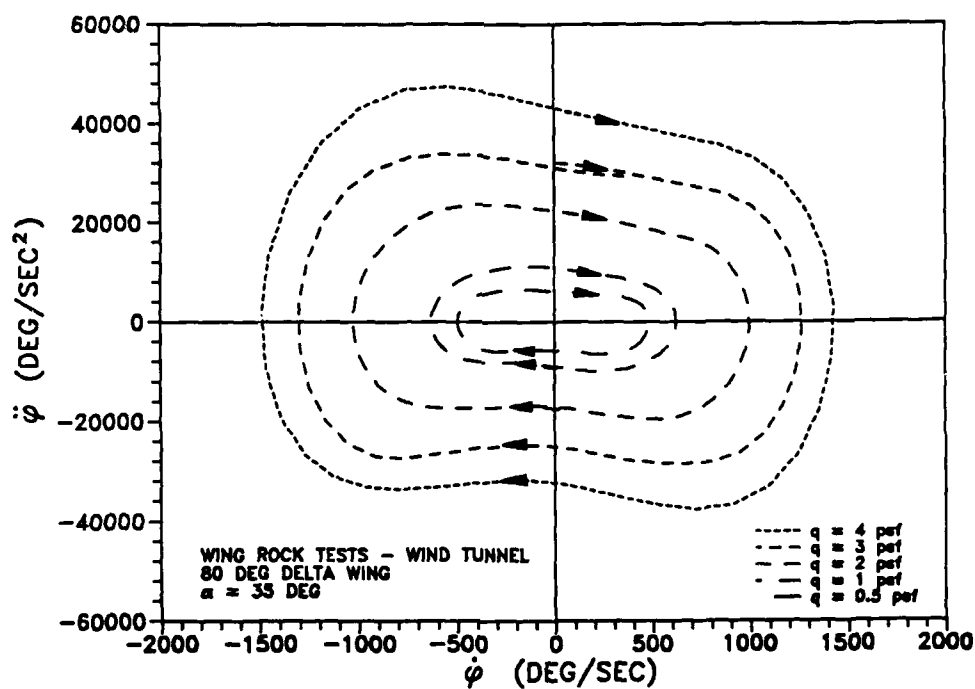
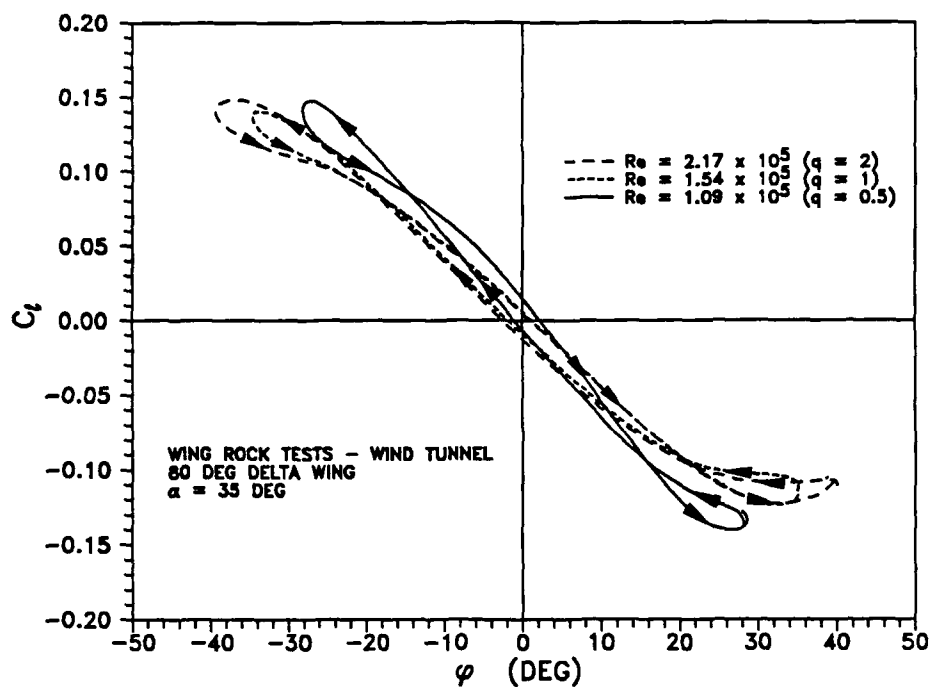
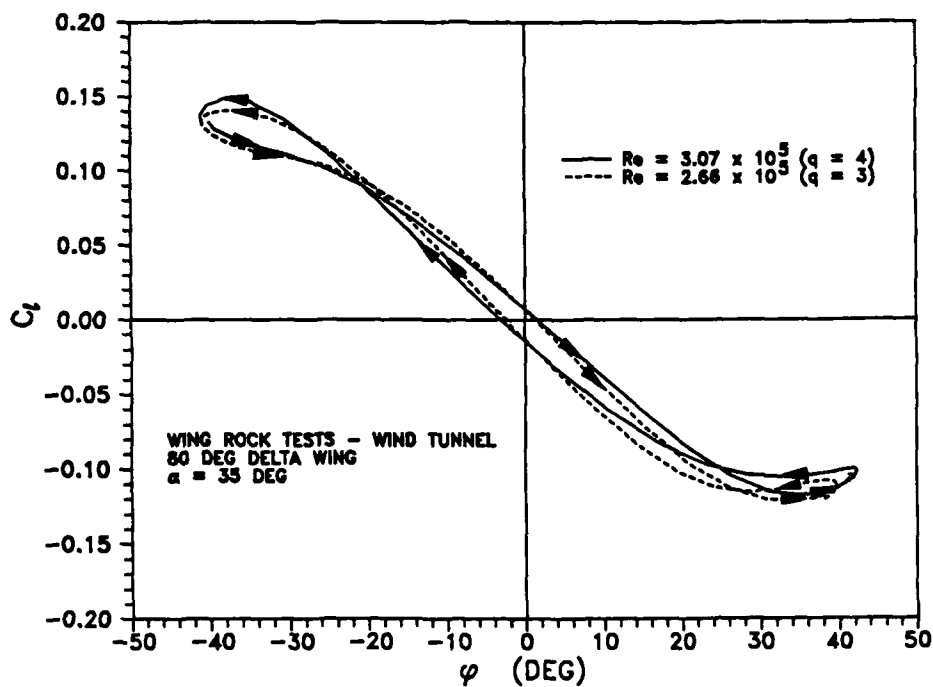


Fig. 133 Roll acceleration versus roll rate comparison, wind tunnel.

exception of the $Re = 1.09 \times 10^5/ft$ data, the slopes of the curves were very similar. This fact indicated that $C_{l\beta}$ changed very little with Reynolds number from $1.54 \times 10^5/ft$ to $3.07 \times 10^5/ft$. The reason for the increased slope at $Re = 1.09 \times 10^5/ft$ is not known; however, it was supported by the large difference between the actual period from the data and the predicted values. Part of the differences could be due to difficulties in precisely setting the dynamic pressures at $\bar{q} < 1$ psf. Also, variations in \bar{q} may be occurring due to the high turbulence levels. Curiously, the largest slope difference between the water and wind tunnel results occurred between the closest Reynolds numbers. This fact emphasized that something other than Reynolds number accounted for the marked difference between the results from the two media. The second important result was the hysteresis bands. In all cases, the outer loops were counterclockwise



a)



b)

Fig. 134 Aerodynamic rolling moment versus ϕ comparison for a) $\bar{q} = 0.5, 1.0, 2.0$ psf, and b) $\bar{q} = 3.0, 4.0$ psf.

and the center loop was clockwise. There were differences in the magnitudes of the hysteresis, primarily in the outer loops, which could lead one to believe that roll damping derivatives changed with Reynolds number. This hypothesis possibly explained the lack of agreement between measured and predicted amplitudes. This suggestion must be tempered by the fact that the size of the loops varied from cycle to cycle.

Other tests were performed at $\alpha = 35^\circ$ to examine the effects of friction, mass asymmetry, and sideslip on the wing rock behavior in the wind tunnel. The discussion of these results will be deferred until later in this chapter.

Angle of Attack Variations

While $\alpha = 35^\circ$ was the most extensively investigated test condition, tests were also performed to determine and examine the wing rock angle of attack range. As shown in Table 7, α was varied from 24° to 55° . At each angle of attack, dynamic pressure was varied to identify its effect on the limit cycle behavior. The following discussion summarizes that data.

The experiments revealed that the range of angles of attack where wing rock occurred was driven by the dynamic pressure of the flow. The widest range occurred at $\bar{q} = 5$ psf ($V_\infty = 64.8$ fps and $Re = 3.44 \times 10^5$) where the 80° delta wing exhibited self-induced roll oscillations from $\alpha \approx 25^\circ$ to $\alpha \approx 50^\circ$ (Fig. 135). An angle of attack of 27° was the lowest value where wing rock was self-initiated; however, once the limit cycle oscillations had started, α was lowered and wing rock was sustained down to $\alpha = 25^\circ$. As α was increased, wing rock amplitude steadily increased until it reached a maximum average value of 42.1° at $\alpha = 35^\circ$. These amplitudes were in good agreement with Nguyen, Yip, and Chambers,²³ they showed peak values of $\phi \approx \pm 40^\circ$ at $\alpha = 32^\circ$ and $\alpha = 37^\circ$. That study also found that the onset of wing rock occurred at $\alpha = 27^\circ$, similar to the current findings. The present results did not agree as well with the amplitudes reported by Levin and Katz²⁴ (Figs. 14 and 135). That study found onset of wing rock at a much lower angle of attack, $\alpha = 19.5^\circ$, and that the maximum limit cycle

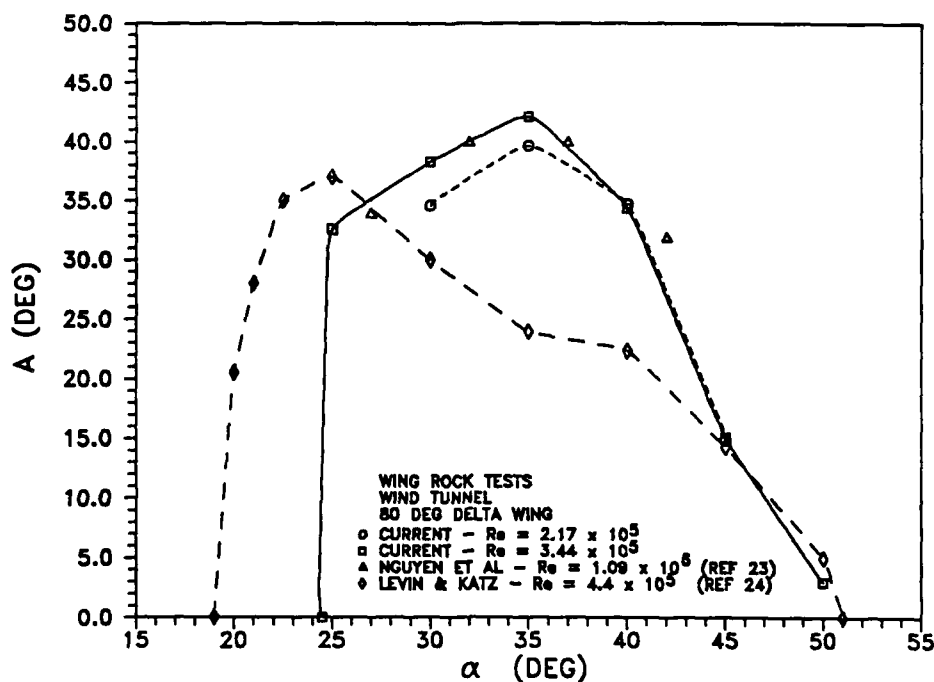


Fig. 135 Wing rock amplitude variation with angle of attack.

amplitude was approximately 37° at $\alpha = 25^\circ$. At $\alpha = 35^\circ$, the amplitude had decreased to less than 25° . At $\alpha = 45^\circ$ and above, the data matched reasonably well, with both studies finding the upper wing rock limit to be in the vicinity of $\alpha = 50^\circ$ to $\alpha = 51^\circ$. While the current study and the Levin and Katz experiments each tested an 80° delta wing, the significant differences in the model configuration are believed to account for the inconsistencies in the amplitude results. The current study tested a delta wing with a slight bulge along the centerline at the aft end of the model, while the Levin and Katz model had a large center-body similar to a fuselage (Fig. 13). Results from the X-29 and F-5 tests,²¹ discussed in Chapter II, demonstrated that a fuselage can provide a strong destabilizing effect favoring the development of the limit cycle oscillations. Those studies also found that a wing and fuselage combination exhibited wing rock at conditions where the wing alone did not. Ericsson^{33,36} showed that in many conventional aircraft, the vortices originating off the forebody initiated wing rock, while vortex interactions with the wings sustained the oscillations. Differences in bearing friction in the free-to-roll apparatus might also

account for some differences in the data. The computational study of Konstadinopoulus, Mook, and Nayfeh²⁷ showed that bearing friction was lower in the Levin and Katz study than in the Nguyen, Yip, and Chambers²³ tests. Lower bearing friction favored the onset of wing rock at a lower angle of attack. Friction tests in the current study qualitatively supported this conclusion. Therefore, while the amplitude differences obtained in the three studies were worrisome at first, there were reasonable explanations for the discrepancies.

The effects of Reynolds number on the limit cycle amplitudes and angles of attack for wing rock were also shown in Fig. 135, comparing $Re = 2.17 \times 10^5/ft$ and $Re = 3.44 \times 10^5/ft$ data. While wing rock occurred at $\alpha = 25^\circ$ at the higher Reynolds number, it was not sustained at the lower value. This result was due to the inability of the lower velocity flow to generate aerodynamic forces large enough to overcome bearing friction. For angles of attack of 30° and 35° , the average roll amplitudes were approximately 3.5° and 2.5° less, respectively, for the lower Reynolds number tests. At $\alpha = 40^\circ$ and $\alpha = 45^\circ$, the magnitudes were very similar. Data were not collected at $\bar{q} = 2$ psf for $\alpha = 50^\circ$. The Reynolds number effect on the limit cycle angle of attack range was further illustrated by the $\bar{q} = 1$ psf ($Re = 1.54 \times 10^5/ft$) tests at $\alpha = 30^\circ$. Under these test conditions, the 80° wing did not exhibit wing rock, even when given an initial roll displacement of -70° .

Fig. 136 shows the variation of wing rock period with angle of attack for Reynolds numbers of $1.54 \times 10^5/ft$, $2.17 \times 10^5/ft$, and $3.44 \times 10^5/ft$. For the higher two Reynolds numbers, the period was relatively constant up to $\alpha = 35^\circ$. In all cases, the period decreased with increasing angles of attack for $\alpha > 35^\circ$. The data also clearly illustrated the decrease in period (increase in frequency) as Reynolds increased. The predicted results from the mathematical model were plotted for each Reynolds number. While not shown, the Runge-Kutta predictions were very similar to mathematical model values. These calculations used average static $C_{l\beta}$ data (Fig. 115) to determine frequency and period. The predictions indicated that the period was almost constant at a given Reynolds number for α above 30° . Despite these differences

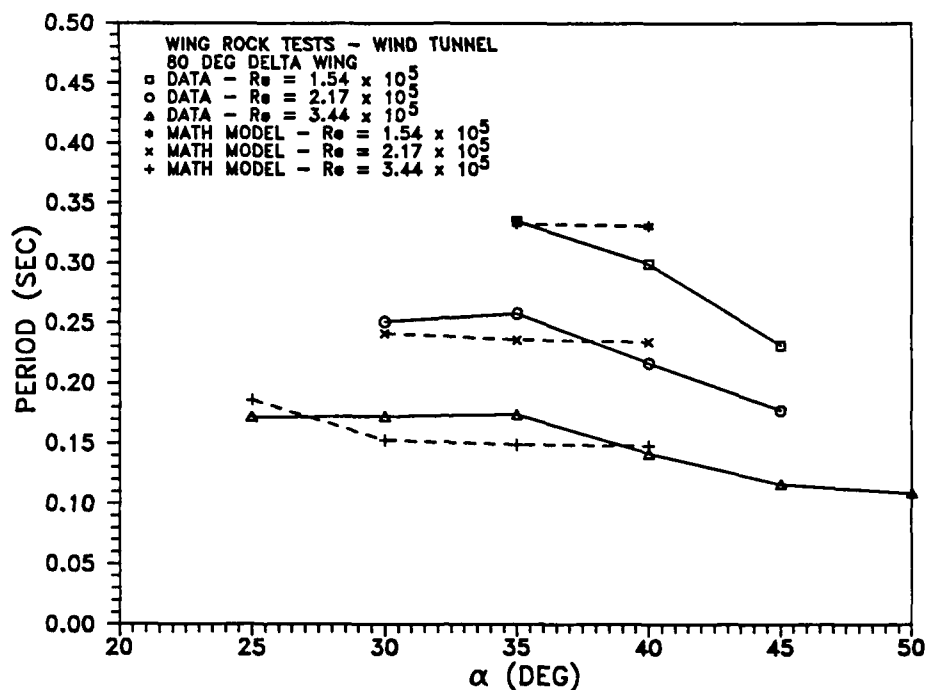


Fig. 136 Wing rock period variation with angle of attack.

between the model results and the experimental data, the simple calculation predicted periods within 13% of the measured values.

Reduced frequency was relatively constant up to $\alpha = 35^\circ$, after which it increased slowly (Fig. 137). The magnitudes of the reduced frequencies were similar to results obtained by Levin and Katz²⁴ and approximately half the value of those obtained by Nguyen et al.²³ Reduced frequency measurements agreed much better with Levin and Katz, while just the opposite was true of the amplitude results. Once again, differences in model geometry and bearing friction are believed to be responsible for these inconsistencies.

Having examined wing rock characteristics, C_L data were examined next to assess the effects of α on C_L magnitudes and hysteresis of the C_L versus ϕ data. Since $C_{L\beta}$ is a function of α , changes in the slopes of the C_L versus ϕ data were expected as α was varied. To address this issue, data from angles of attack of 30° and 40° at $Re = 2.17 \times 10^5$ were analyzed.

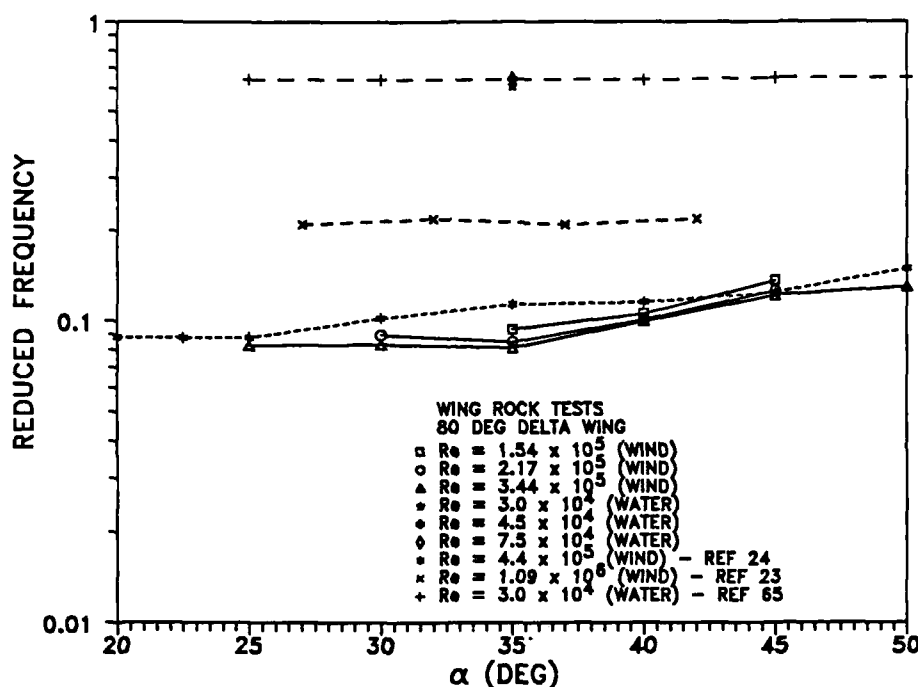


Fig. 137 Wing rock reduced frequency variation with angle of attack.

A typical phase portrait from the $\alpha = 30^\circ$ test at $q = 2$ psf (Fig. 138) shows five cycles of the self-induced oscillations. As previously shown in Figs. 135 and 136, the period of oscillation was approximately 0.25 sec and the average limit cycle amplitude was 35.1° . The C_ℓ versus ϕ graph (Fig. 139) revealed C_ℓ magnitudes very similar to the $\alpha = 35^\circ$ tests discussed earlier. Additionally, hysteresis directions were the same as in the other experiments, with a clockwise loop in the center and two counterclockwise loops at the large roll angles. The Runge-Kutta integration predicted a period of 0.247 sec and a limit cycle amplitude of 40.3° . The period estimate was 1.2% below the experimental value, while the amplitude was 15% above the test results. The mathematical model predicted a period and roll amplitude of 0.241 sec and 39.3° , respectively. C_ℓ versus ϕ from the Runge-Kutta integration was also shown in Fig. 139. Once again, the slope of the data was in good agreement with the average static estimate of

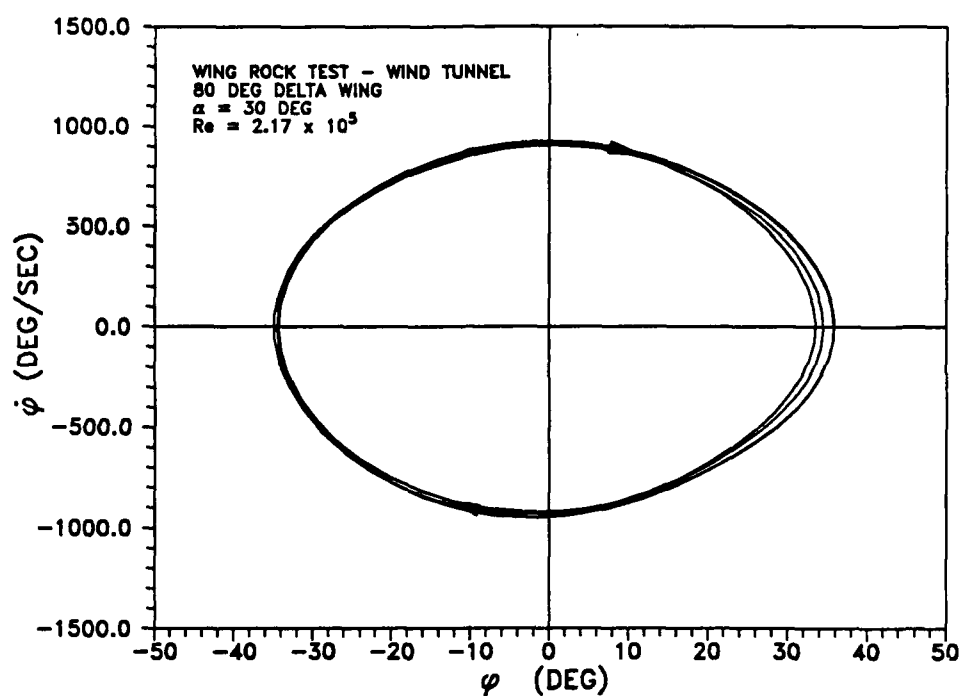


Fig. 138 Wing rock phase portrait, $\alpha = 30^\circ$, $\bar{q} = 2.0$ psf.

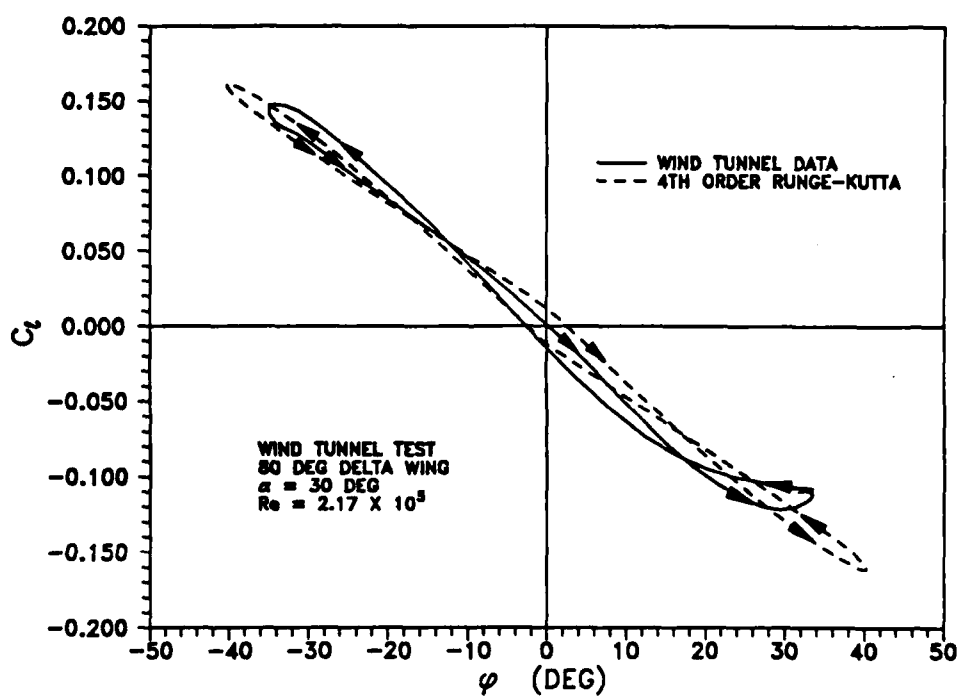


Fig. 139 Aerodynamic rolling moment versus ϕ , $\alpha = 30^\circ$, $\bar{q} = 2.0$ psf.

$C_{\ell\beta} = -0.487$ from Fig. 115. A linear fit to the current data yielded an estimated $C_{\ell\beta} = -0.463$, within 4% of the static value.

Similar results were obtained for the $\alpha = 40^\circ$ tests. The phase portrait (Fig. 140) displayed multiple cycles of oscillation with an average amplitude of 34.8° . The period of oscillation was 0.222 sec, corresponding to a frequency of $28.3^\circ/\text{sec}$ and a reduced frequency of 0.101. C_ℓ versus ϕ (Fig. 141) revealed roll magnitudes and hysteresis directions similar to the other tests. Unfortunately, the VORSTAB code^{29,30} was unable to obtain converged solutions for roll damping derivatives above $\alpha = 38^\circ$, so a Runge-Kutta simulation was not possible using published data. However, the $C_{\ell\beta}$ data from the static force tests (Fig. 115) allowed the calculation of the period using the mathematical model. Based on a $C_{\ell\beta} \approx -0.4$, the calculated period was 0.235 sec, 6% above the experimental value. Additionally, an average slope was determined from the C_ℓ versus ϕ data (Fig. 141) which yielded an estimated $C_{\ell\beta}$ value of -0.427, approximately 7% greater than the average static data.

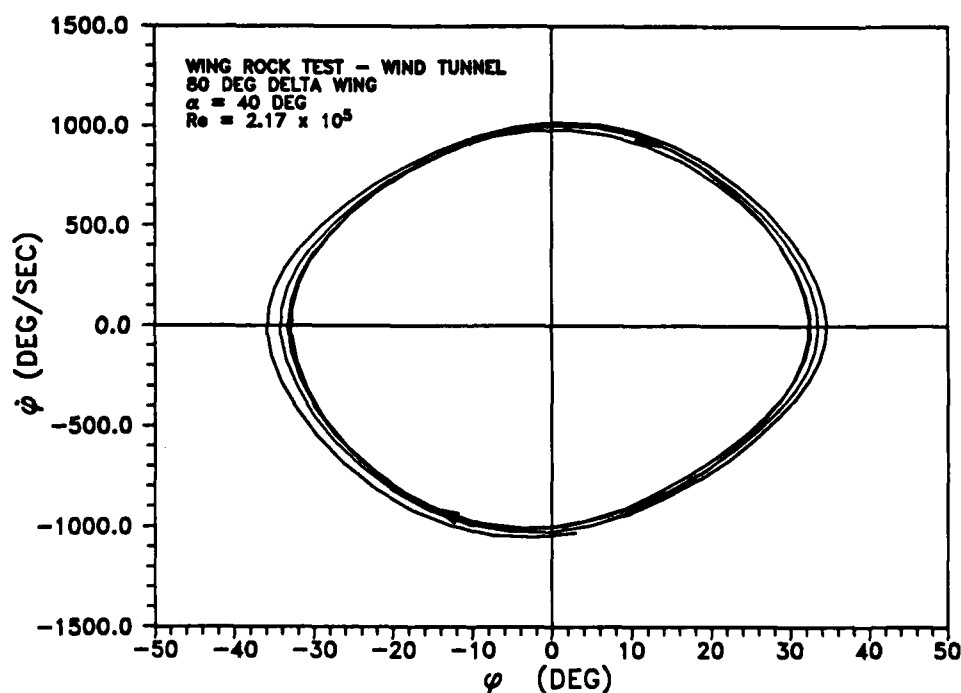


Fig. 140 Wing rock phase portrait, $\alpha = 40^\circ$, $\bar{q} = 2.0$ psf.

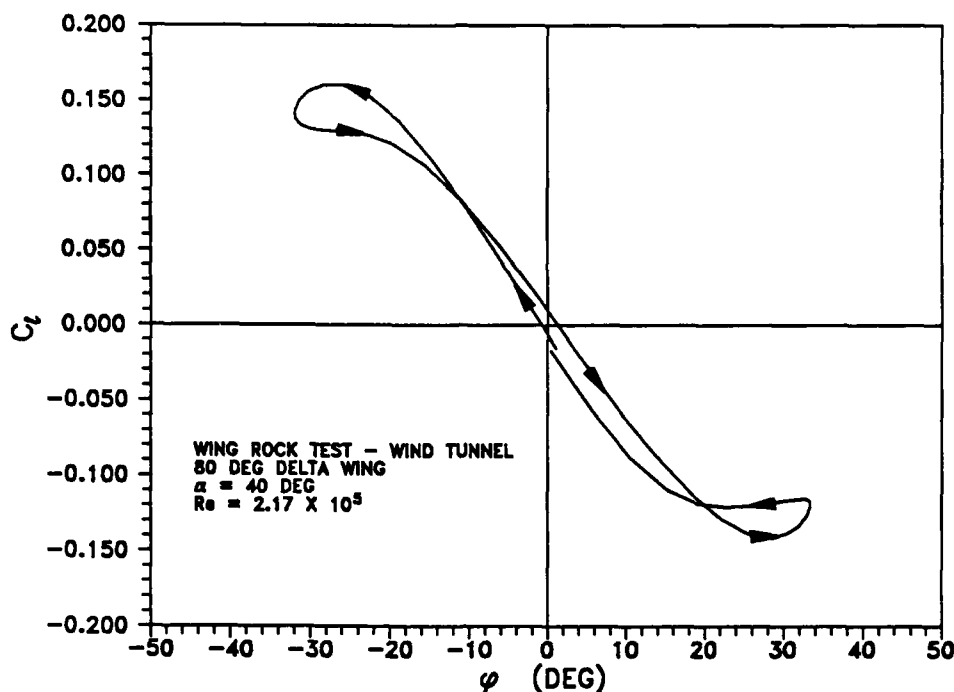


Fig. 141 Aerodynamic rolling moment versus ϕ , $\alpha = 40^\circ$, $\bar{q} = 2.0$ psf.

The results obtained from α variations further support the concept that unstable roll damping existed at small ϕ , while stable roll damping existed at large ϕ . A loss of roll damping has been observed at the onset of wing rock in both flight tests and subscale model tests in the wind tunnel. Despite these results, the water tunnel tests provided data with precisely opposite trends in the roll damping, due to hysteresis direction differences in the $C_{l\beta}$ versus ϕ data. Yet, a similar limit cycle was observed in the water tunnel. Additionally, the large difference in rolling moment coefficients was surprising, since it seemed extremely unlikely that $C_{l\beta}$ would change by a factor of 15 or larger when going from $Re = 7.5 \times 10^4/\text{ft}$ to $1.09 \times 10^5/\text{ft}$, as indicated by the data. This rationale was especially true since $C_{l\beta}$ was relatively constant with Reynolds number in both the water tunnel and the wind tunnel tests. While water and wind tunnel tests both used the same model and bearings, the operating fluid of the bearings was significantly different. To assess the possible effects of large friction differences in the two media due to the viscosity of the

operating fluid, a series of friction tests were performed in the wind tunnel at $\alpha = 35^\circ$. The primary goal of these tests was to identify any changes in C_L magnitudes or hysteresis direction due to changes in bearing friction. It was hoped that this information might help explain the differences in the results from the two media, even though friction was deemed an unlikely candidate. These tests also provided data to support statements made previously regarding the effect of friction on the angle of attack range for wing rock.

Bearing Friction Tests

To assess the effects of bearing friction on the wing rock behavior, experiments were conducted in the wind tunnel which varied the amount of friction. While these tests provided a variation in the bearing coefficient of friction, the actual magnitude of that variation could not be quantified. Therefore, these tests provided only a qualitative assessment of the changes in wing rock behavior due to increases or decreases in friction.

The wind tunnel tests described up to this point used non-lubricated bearings. To alter bearing friction, different lubricants were applied which either decreased or increased resistance to rolling. Bearing friction was first reduced by lubricating the bearings with WD-40. Tests were conducted at the baseline $\alpha = 35^\circ$ conditions for which there was a considerable amount of data using non-lubricated bearings. Following these tests, the bearings were cleaned with freon and alcohol and allowed to dry and the tests repeated. The friction was then increased by soaking the bearings in 10W40 motor oil and tests were conducted at identical flow conditions. A final variation in bearing friction was made by packing the bearings in axle grease.

The results for the different bearing frictions are plotted in Fig. 142. The nominal condition, non-lubricated bearings, is shown as the solid line in the figure. The period of oscillation was approximately 0.335 seconds with an average roll angle amplitude of 34.8° . The WD-40 tests revealed an increase in period to 0.349 seconds with an average amplitude of 37.8° , that is, an increase in roll amplitude of 8.6% and an increase in period of approximately 4% due to the unspecified decrease in bearing friction. Motor oil tests resulted in a decrease in period to

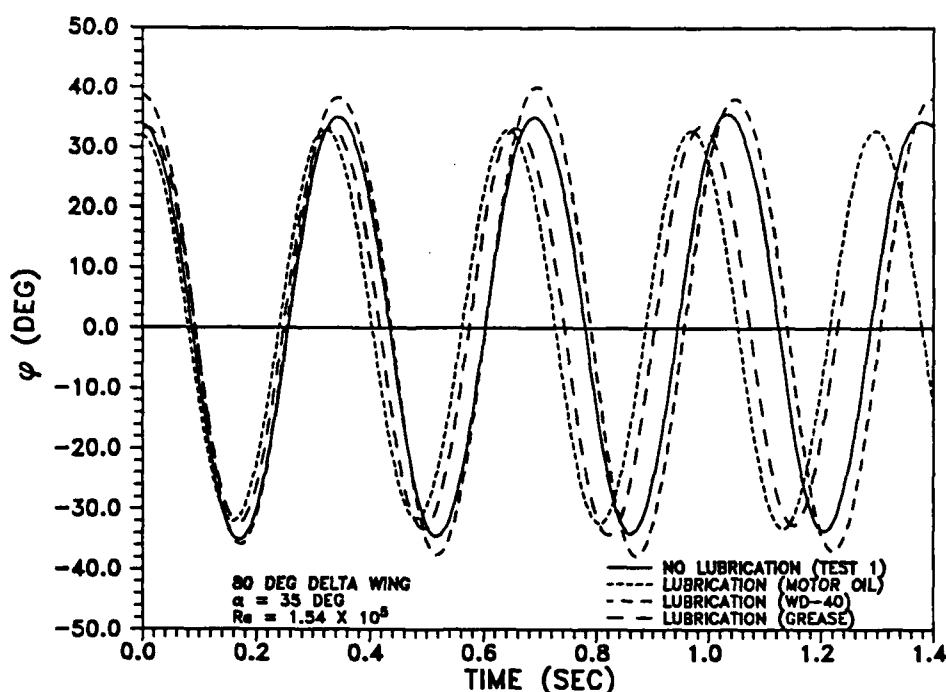


Fig. 142 Bearing friction effects on wing rock response.

approximately 0.328 seconds with an average amplitude decrease to 32.6° , a 2% decrease in period and a 7.3% decrease in amplitude compared to the nominal case. Axle grease yielded a period of approximately 0.328 sec and an average roll amplitude of 33.2° (a 4.8% decrease compared to the nominal condition).

Therefore, both the period and roll amplitude decreased as bearing friction increased. These results were consistent with the analytical predictions of Konstadinopoulos, Mook, and Nayfeh.²⁷ Their computations also indicated that as the bearing friction increased, a value was reached where wing rock no longer developed. Experimentally, this occurred in the motor oil and grease tests at a Reynolds Number of 1.09×10^5 . At that flow condition, the motion damped out for the grease and motor oil tests, while the limit cycle was observed in the non-lubricated and WD-40 tests.

The amount of friction also influenced wing rock build-up (Figs. 143, 144, and 145). The nominal test (Fig. 143) had a more rapid build-up to the limit cycle than the motor oil test

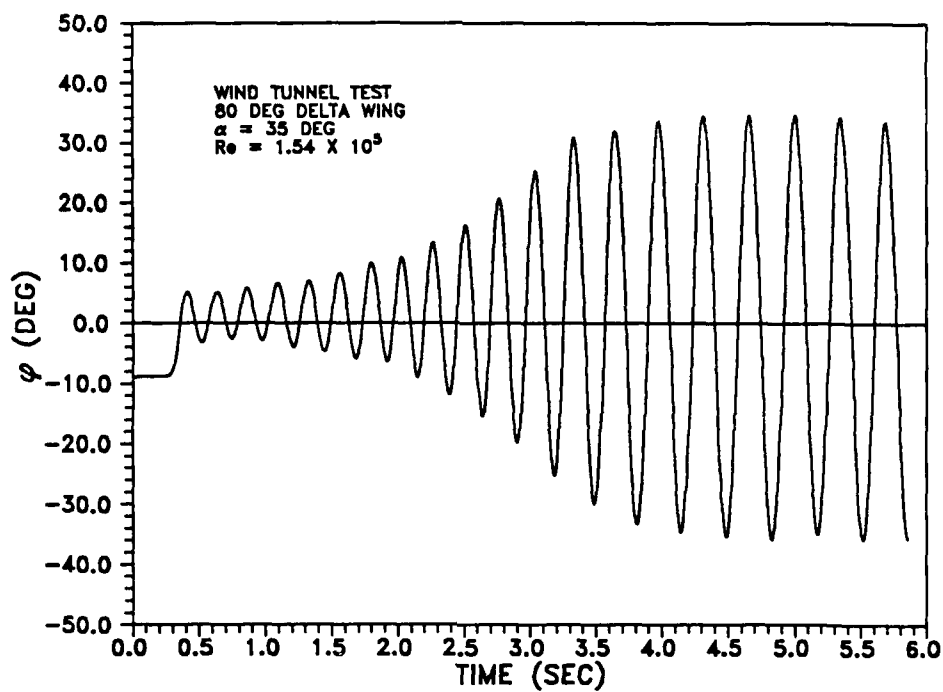


Fig. 143 Wing rock build-up with no lubrication.

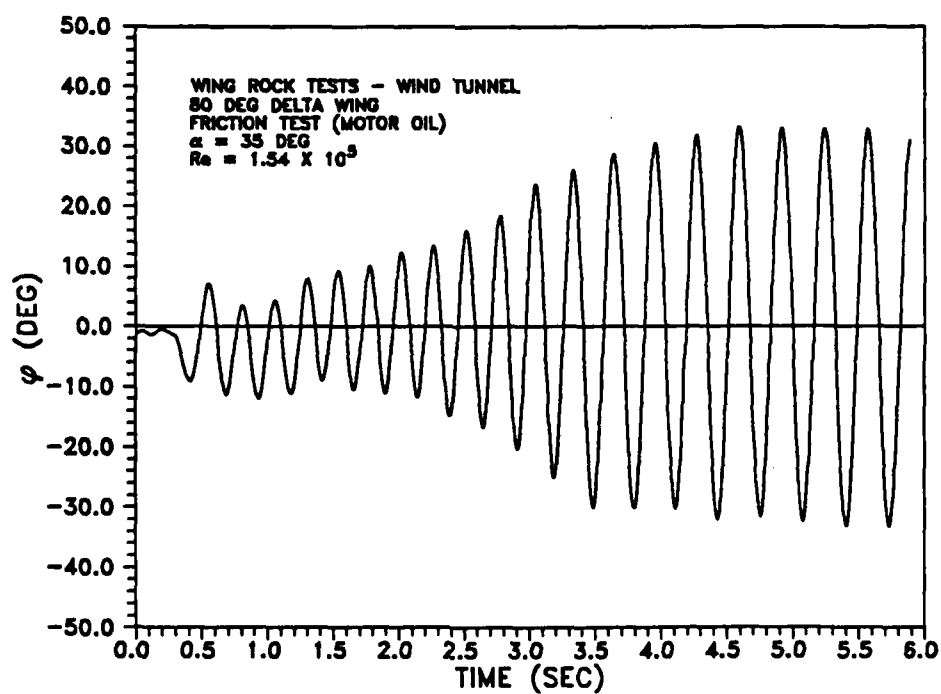


Fig. 144 Wing rock build-up with motor oil lubrication.

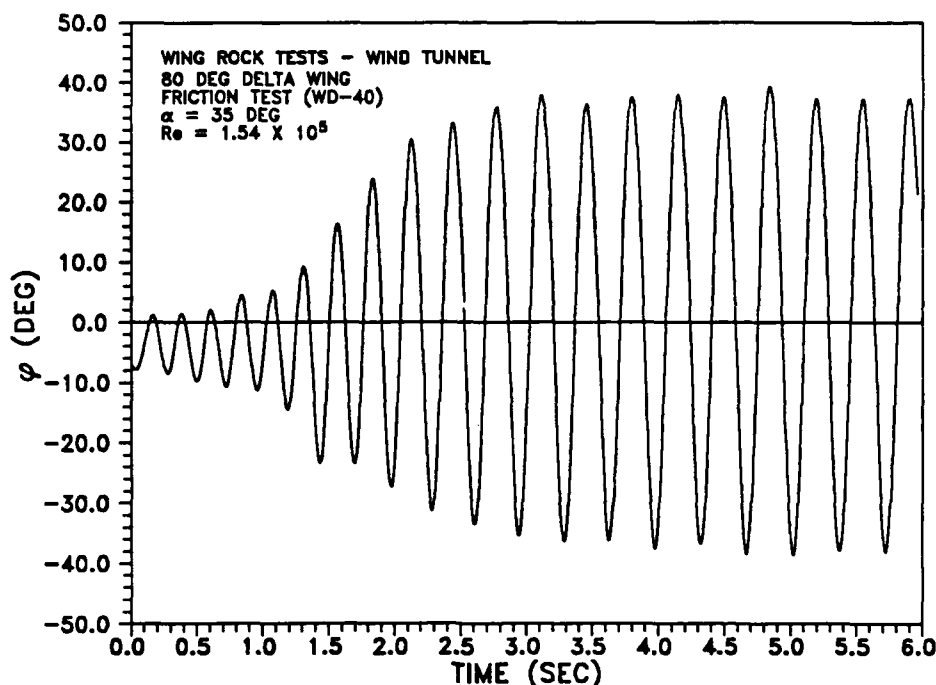
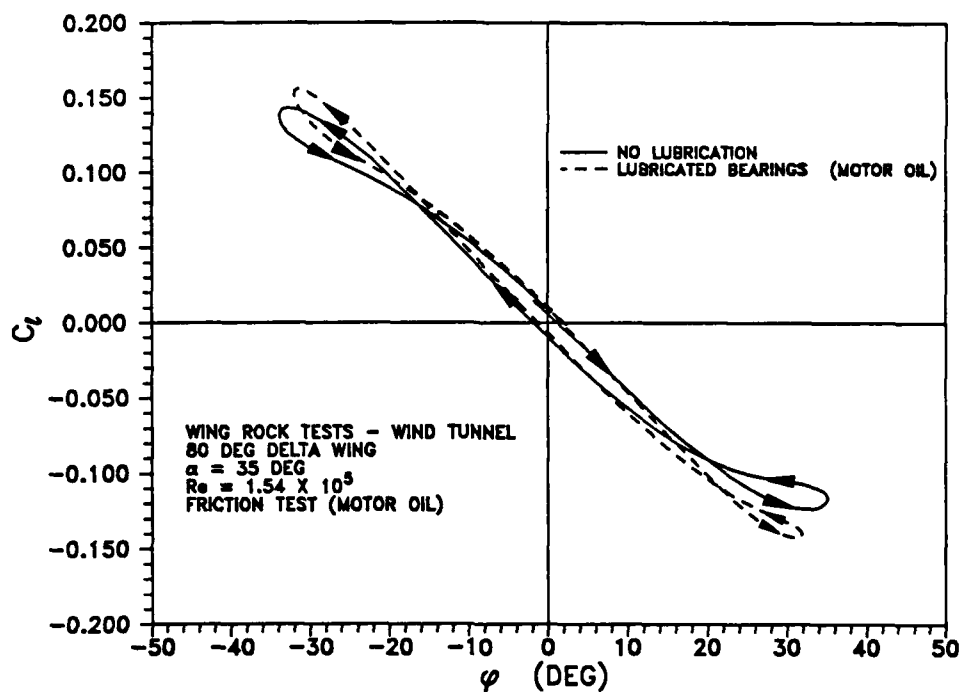
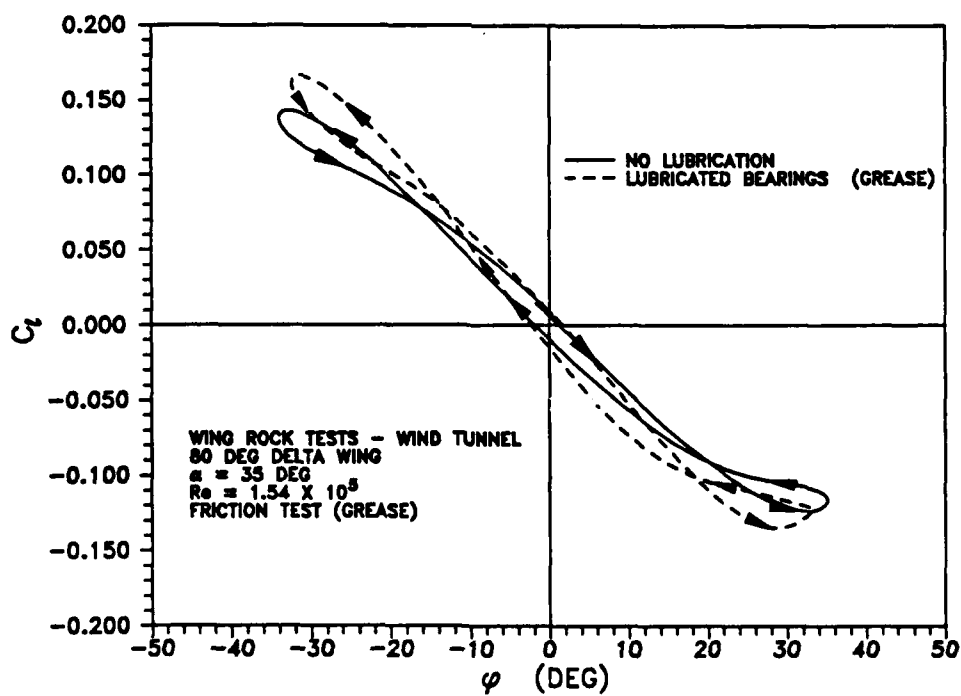


Fig. 145 Wing rock build-up with WD-40 lubrication.

(Fig. 144). The slower initial build-up in the motor oil test was indicative of increased bearing friction and its resistance to the growth of the rolling motion. On the other hand, the WD-40 tests (Fig. 145), with decreased bearing friction, exhibited a faster build-up than the nominal condition.

A decrease in roll angle amplitude with increasing friction was also consistent with equation (24) which showed that as the friction coefficient increased, roll amplitude decreased. The mathematical model failed to predict a change in frequency with friction; however, Fig. 142 shows that frequency was dependent on the friction level. The increased frequency for the higher friction tests could have been partially due to the smaller amplitude of the wing rock. Since the model had a smaller range of motion, it could rotate through one cycle faster. The WD-40 tests, with the larger amplitude, had just the opposite effect.

Figures 146-148 provide comparisons of C_L versus ϕ for the wind tunnel friction tests. The slopes of curves for the motor oil test (Fig. 146) and the grease test (Fig. 147) were slightly higher than the no lubrication case. In both of these tests with higher friction, C_L magnitudes

Fig. 146 Aerodynamic rolling moment versus ϕ , motor oil test.Fig. 147 Aerodynamic rolling moment versus ϕ , grease test.

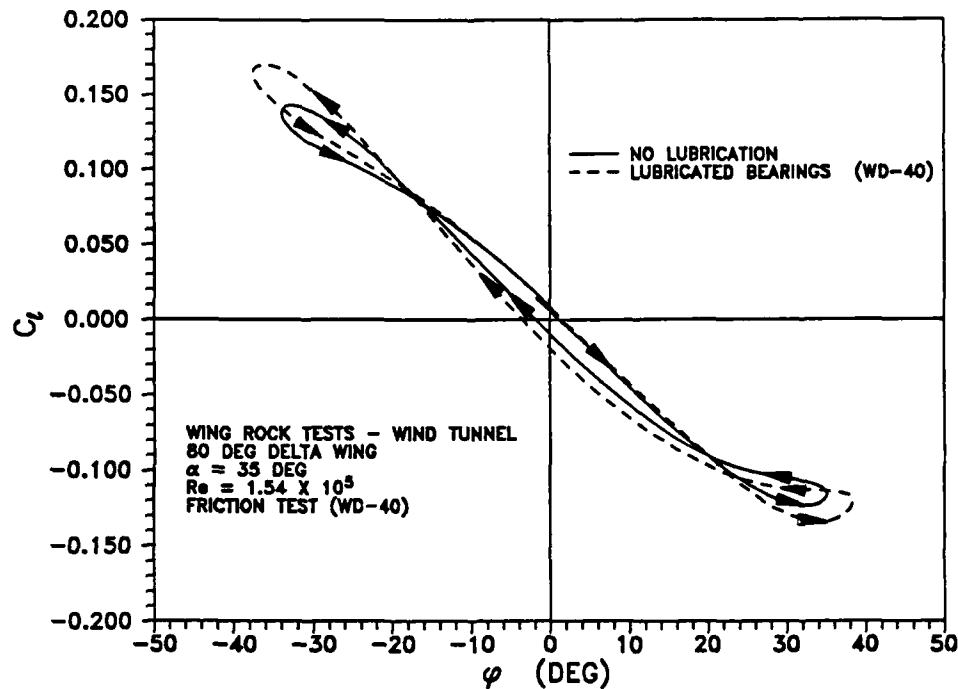


Fig. 148 Aerodynamic rolling moment versus ϕ , WD-40 test.

were about 10% larger than the nominal tests. Therefore, the increased friction actually moved the data even further away from the water tunnel results, just opposite to the trend expected if increased friction in the water tunnel tests were responsible for the large differences in the data between the two studies. The WD-40 test (Fig. 148) had a slope very similar to the nominal test; however, its rolling moment coefficients were larger due to the fact that higher roll amplitudes were obtained. These results also showed that while the size of the hysteresis loops differed somewhat, the hysteresis direction did not change with different levels of bearing friction.

Extrapolating the friction results to the water tunnel tests, it can be concluded that friction cannot account for the substantial differences in wing rock period, C_p , and hysteresis direction. If in fact the differences between the tests in the two media were primarily due to increased bearing friction in water, one would expect a substantial decrease in the roll amplitude. This decrease was not observed in the water tunnel tests; there, an average roll amplitude of

approximately 37° was actually larger than the amplitudes in the $\bar{q} = 0.5$ psf and $\bar{q} = 1$ psf wind tunnel tests. Additionally, the period of the water tunnel tests was much larger than the tests in air, which was inconsistent with the trends of decreasing period with increasing friction experienced in the wind tunnel tests. The friction tests also demonstrated no dependency of hysteresis direction on bearing friction. Based on the above results, it was concluded that some other phenomenon was responsible for the significant differences between the water tunnel and the wind tunnel data. However, the tests did show that differences in bearing friction in the different wind tunnel studies affected wing rock characteristics. Thus, friction was likely to be partially responsible for disagreements in the data of Nguyen, Yip, and Chambers,²³ the Levin and Katz²⁴ experiments, and current tests.

Mass Asymmetry Tests

Tests were also performed on the 80° delta wing with an intentional asymmetric mass distribution about the roll axis. The goal of these experiments was to determine what effects, if any, a small mass imbalance of the model would have on the wing rock behavior, especially rolling moment hysteresis. When the 80° delta wing model arrived at Texas A&M from Eidetics International for the wind tunnel study, four small beads had been added to the left wing, which were not present during the water tunnel tests. These beads had been installed to balance the model about its longitudinal axis for a NASA study⁶⁵ performed after the water tunnel tests for this study. The only reason that could be envisioned for installation of these beads was that the model had been repainted for that study, perhaps slightly altering the mass distribution. However, in the unlikely event that a mass asymmetry had existed during the water tunnel study, several tests were conducted at $\alpha = 35^\circ$ to examine the effects of removing the beads. Without the beads, the right wing dropped down slightly when set at $\phi = 0^\circ$ with no flow, indicating a slight mass asymmetry. However, during the dynamic tests, the C_ℓ versus ϕ data (Fig. 149) showed no major changes to the hysteresis loops with removal of the beads. Some differences can be seen in the size of the loops; however, it must be kept in mind that similar variations were

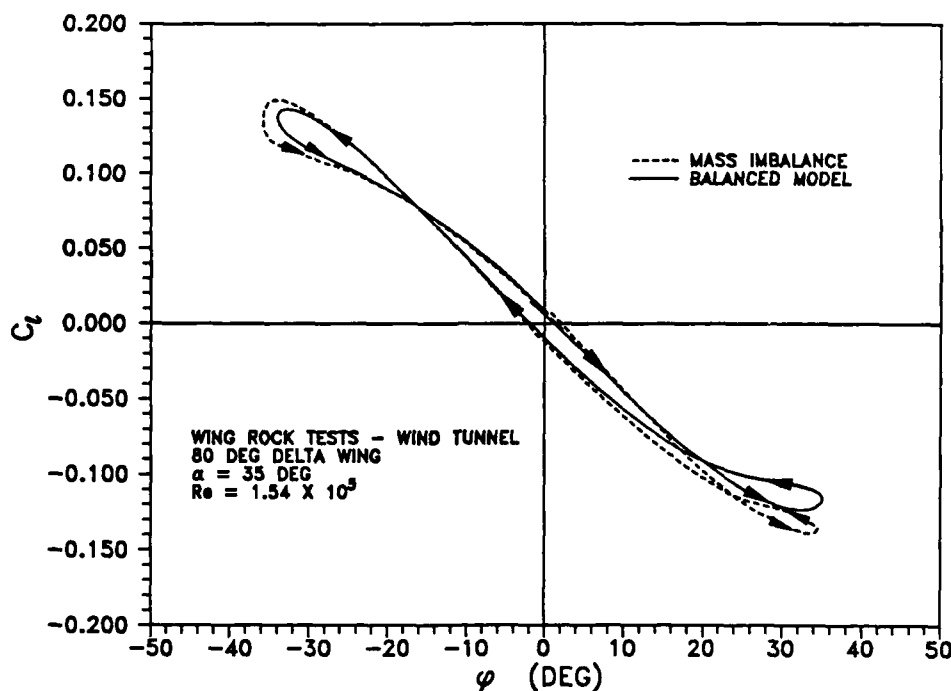


Fig. 149 Aerodynamic rolling moment versus ϕ : mass imbalance test.

noted in different cycles of the same test for many of the experiments. The important result from these tests was that a small asymmetry in mass did not significantly alter the limit cycle oscillations. Therefore, the effects of the mass imbalance were small compared to aerodynamic loads driving wing rock.

Sideslip Tests

In addition to the friction and mass asymmetry tests, several experiments were conducted to evaluate the effects of small sideslip angles on the model response. While considerable care had been taken in both studies to set the model to the correct attitude, these tests were to determine if a small misalignment could explain any of the differences in the water tunnel and the wind tunnel data. If a misalignment had existed, it would have been small, so only small sideslip angles were examined. At $\beta = \pm 2^\circ$, there were no apparent differences in either the C_l magnitudes or hysteresis direction. Therefore, model alignment was not an issue in understanding the differences in the data.

Smoke Tests

In addition to the tests examining the motion of the wing during the self-induced oscillations, several tests were performed to visualize the leading-edge vortices using a smoke wand in the wind tunnel. These runs were conducted at $\alpha = 35^\circ$ at the lowest dynamic pressure possible, $\bar{q} = 0.5$ psf, to give the best hope of tracking the flow. The walls in the tunnel were covered with black particle board to yield the optimum contrast with the white smoke. Unfortunately, due to the high frequency of the oscillations and the relatively small model, it was impossible to obtain video data suitable for reduction with ExpertVision. However, the videotapes did provide a qualitative picture of the vortex movements, which appeared to be similar to results reported by Jun and Nelson.²⁶ The vortex on the downward half of the wing was closer to the surface, while the opposite vortex moved away from the upper half-span of the wing. One of the most significant findings from the videotapes was that the vortices moved in a relatively straight line, markedly different from the water tunnel results, discussed earlier. The movement of the vortices were even better observed by standing inside the wind tunnel against the wall. From that perspective, it was clear that the vortex on the downward moving half-span moved in close to the wing, while the opposing vortex on the upper half-span was displaced well away from the surface. The vortex bursting could not be observed either visually inside the tunnel or on the videotapes. While these results gave only a qualitative assessment of the vortex motion during wing rock, the gross observations did correlate with other available wind tunnel data. More importantly, the fact that the vortices apparently moved in a straight line indicated that there were probably only small phase differences in the vortex positions at different locations along the chord.

Wind Tunnel Summary

A detailed analysis of wing rock on an 80° delta wing in the wind tunnel was presented in the preceding sections. The test results were significantly different from those obtained in the

water tunnel study, but were essentially in agreement with data from other wind tunnel studies. The ability to obtain roll angle data without instrumentation built into or around the model allowed this study to test a true slender sharp-edged 80° delta wing. This advantage was clear from the excellent correlation with $C_{l\beta}$ results from experimental force tests. Further confidence in the data came from the excellent repeatability of the results from run to run.

The tests showed that unstable damping existed during wing rock build-up when starting from initial roll angles less than the limit cycle amplitude. As the steady limit cycle was reached, unstable damping was present at small ϕ and stable damping existed at large ϕ . When starting from initial roll angles larger than the limit cycle amplitude, stable damping was present at large ϕ while no damping existed at small ϕ . This same phenomena existed in all of the tests analyzed for the entire range of α and Re tested. Qualitatively, smoke flow visualization of the leading-edge vortices showed movements similar to those reported in other wind tunnel studies. Of particular significance, the vortices moved in a relatively straight line compared to those observed in the water tunnel.

Comparison of Wind and Water Tunnel Tests

The preceding discussions in this chapter presented the results of both the wind tunnel and the water tunnel studies. This section compares the wing rock characteristics of the two sets of data and provides plausible explanations for the differences. Prior to discussing the major differences in the data, it is worthwhile to review some of the similarities.

Similarities in Water and Wind Tunnel

The most obvious similarity between tests in the two fluids was that wing rock on the 80° delta wing occurred in both cases. This point was extremely significant in that the same model experienced the limit cycle oscillations despite different motion characteristics which have been highlighted throughout this chapter. Roll amplitudes in the water tunnel tests ranged from 36.6° to 37° at $\alpha = 35^\circ$, while they varied from 28.8° to 42.1° in the wind tunnel, depending on Reynolds number. Additionally, a NASA test⁶⁵ conducted in the Eidetics water tunnel, using the

same 80° delta wing model tested in this research, found that wing rock onset occurred at $\alpha \approx 25^\circ$, very similar to the wind tunnel value (Fig. 150). Figure 150 also illustrates that the initial increase in roll amplitude with α in the NASA tests was similar to the current wind tunnel tests, though water tunnel data peaked at $\alpha = 30^\circ$ instead of $\alpha = 35^\circ$. The major difference between the amplitude data occurred at $\alpha > 40^\circ$, where the wind tunnel data showed a rapid drop in amplitude compared to the gradual decrease in the water tunnel results. Wing rock ceased at $\alpha \approx 50^\circ$ in the wind tunnel, compared to $\alpha \approx 55^\circ$ in the water tunnel. As noted in the wind tunnel discussion, as the Reynolds number was decreased, the α range for wing rock decreased. The largest range of α in the wind tunnel occurred at $Re = 3.44 \times 10^5/\text{ft}$, which was an order of magnitude higher than the Reynolds number of the NASA study.

Water and Wind Tunnel Differences

Having listed the similarities in the data, it is even more important to highlight the differences. The most significant differences in the water and wind tunnel data were in C_ℓ versus ϕ results. As pointed out throughout this chapter, the magnitudes of the rolling moment coefficients were substantially different and the C_ℓ versus ϕ hysteresis was in the opposite

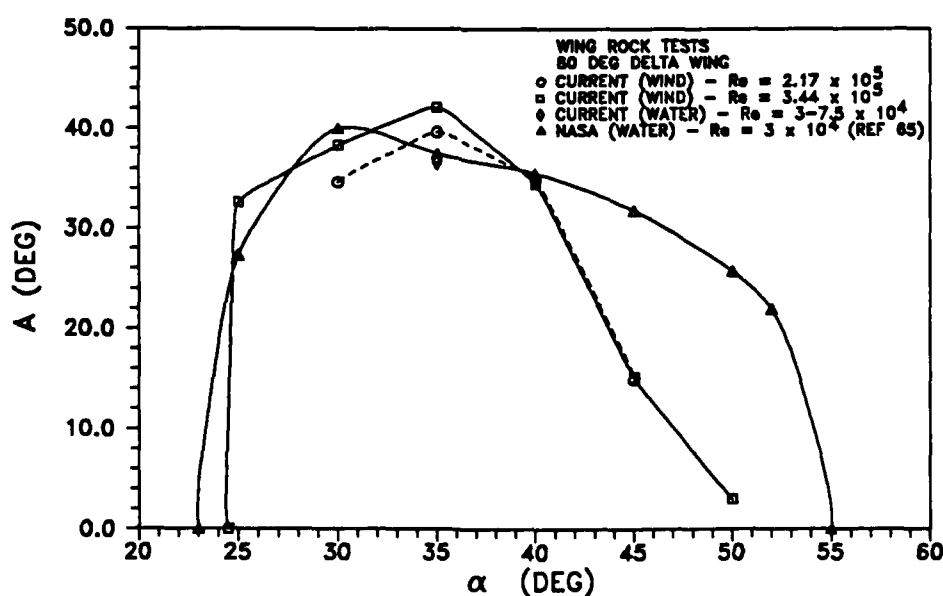


Fig. 150 Angle of attack effect on roll amplitude.

direction. Both of these disagreements in the C_ℓ versus ϕ data are analyzed in the following sections, and plausible explanations given.

Rolling Moment Magnitudes

The large difference in the C_ℓ magnitudes was quite obvious when water tunnel and wind tunnel data were plotted together (Fig. 151). Water tunnel results shown ($Re = 7.5 \times 10^5/ft$) were the data presented in Fig. 79, but plotted on the same scale as the wind tunnel data. With this scale, hysteresis in the water tunnel data was obscure, even though Fig. 79 showed it clearly. Wind tunnel data presented were obtained at $Re = 1.54 \times 10^5/ft$, a factor of 2 higher than the test condition of the water tunnel data. The slope of C_ℓ versus ϕ was relatively constant for the range of Reynolds numbers tested in both the water tunnel and the wind tunnel, but the results from the two series were markedly different. The maximum rolling moment coefficient in the wind tunnel test was approximately 0.145, compared to an equivalent water tunnel value of 0.0085. A large difference was also seen in the values of $C_{\ell\beta}$ derived from the

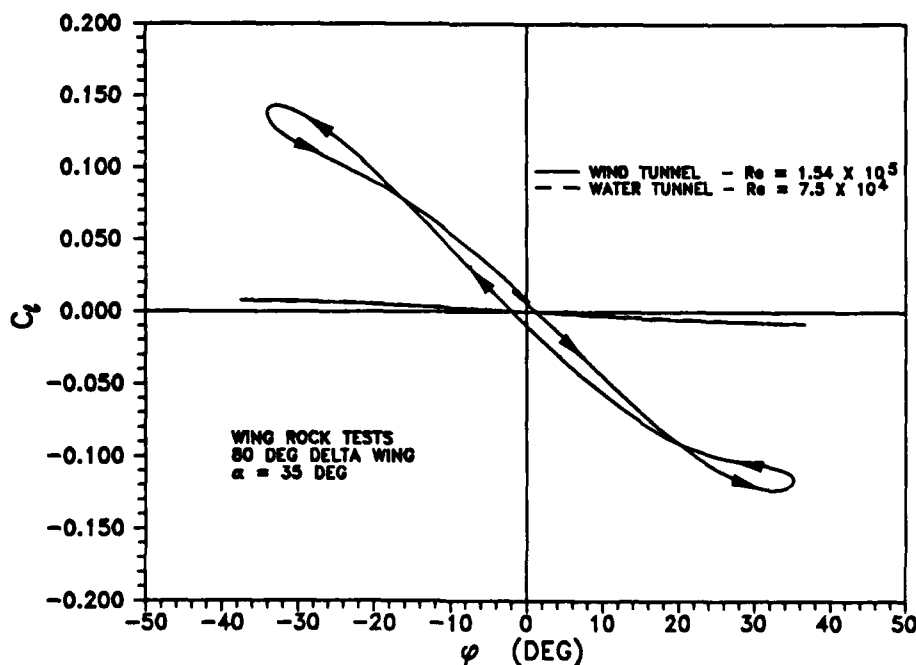


Fig. 151 Comparison of water and wind tunnel C_ℓ versus ϕ .

experimental wing rock measurements. As determined from the water tunnel data, $C_{l\beta}$ was -0.0295, compared to -0.442 in the wind tunnel. This factor of 15 difference in $C_{l\beta}$ was at first surprising, especially since there was only a 25,000/ft difference in Reynolds number at the two closest test conditions.

$C_{l\beta}$ versus ϕ data were also validated by comparing the periods of the water and wind tunnel tests with predictions from the mathematical model. As expected, periods from water tunnel runs were higher than wind tunnel values due to much smaller freestream velocities. Both studies showed that, as flow velocity increased, the period of oscillation decreased (Fig. 152). In addition to the actual periods, Fig. 152 shows the periods predicted by the mathematical model for each test condition using an average value of $C_{l\beta} = -0.444$ from published wind tunnel results on an 80° delta wing.^{23,30} While the agreement with the wind tunnel periods was very good, the predicted water tunnel periods were hopelessly low. These poor estimates showed that, while published $C_{l\beta}$ data were applicable to wind tunnel tests, they were inadequate for

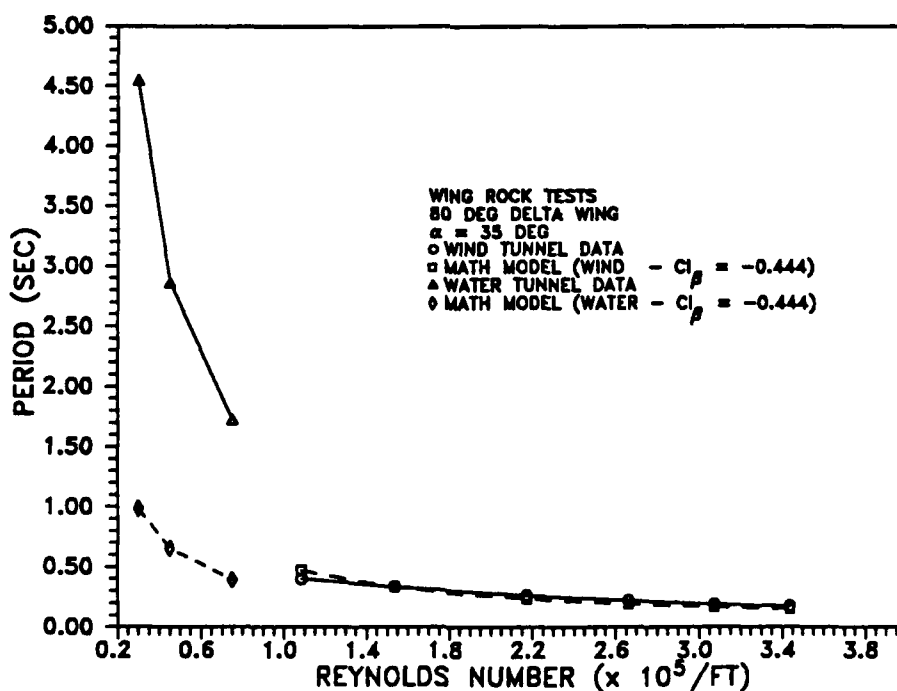


Fig. 152 Comparison of water and wind tunnel wing rock periods.

water tunnel experiments. Using equations (22) and (23) from the mathematical model (water tunnel flow conditions at $V_\infty = 10$ ips and the experimental values of the period or frequency), the calculated $C_{\ell\beta}$ was -0.02307. Performing a similar calculation on the wind tunnel results for $\bar{q} = 1.0$ psf, gave $C_{\ell\beta} = -0.442$, which was only 0.5% below the published value of -0.444. These calculations showed that the wind tunnel $C_{\ell\beta}$ was approximately 19 times larger than the water tunnel value, based on using the experimental periods in the mathematical model. This result was similar to the factor of 15 difference in $C_{\ell\beta}$ determined from the measured C_ℓ versus ϕ data. Therefore, both C_ℓ versus ϕ data and the measured periods revealed that the C_ℓ and the $C_{\ell\beta}$ values for the same 80° delta wing were markedly different between the water tunnel and the wind tunnel. Though Reynolds number usually accounts for differences in density and viscosity between the media, the two sets of measurements indicated that a factor of 15 or greater increase in C_ℓ existed in going from $Re = 7.4 \times 10^5/\text{ft}$ to $Re = 1.09 \times 10^5/\text{ft}$. This large change was especially difficult to accept since $C_{\ell\beta}$ was relatively constant from $Re = 3 \times 10^4/\text{ft}$ to $7.5 \times 10^4/\text{ft}$ in water and changed very little between $1.09 \times 10^5/\text{ft}$ and $3.44 \times 10^5/\text{ft}$ in air.

Considering the low likelihood of such a substantial increase in C_ℓ and $C_{\ell\beta}$ for a 47% increase in Reynolds number, the method of determining of C_ℓ was reevaluated. In air, the single degree-of-freedom rolling equation (12) was derived from aircraft equations of motion in almost any flight dynamics textbook.^{68,69,70} No such application of the equation was found for tests in water. However, several references^{13,71,72,73} suggested that, when dealing with fluids with high densities, apparent mass terms, which are normally negligible in air, must be considered in the calculation of lift and moments. Since water has a density over 800 times that of air, an apparent mass correction was evidently needed. The concept of apparent mass was well-stated by Fung: "If the acceleration of the entire system were produced by an externally applied force or moment, some fraction thereof would go into altering the energy of the liquid, an effect which could be explained physically by imagining the mass or moment of inertia of the

solid to be augmented by a fixed amount. These incremental masses and moments of inertia are known as virtual or apparent masses; they are directly proportional to the density of the fluid but vary, in general, with the orientation of the axis of translation or rotation relative to the solid."⁷¹ Going back to equation (12), any increase in the moment of inertia, I_{xx} , would directly result in an increase in the rolling moment coefficient. Therefore, apparent mass effects were strong candidates to explain water tunnel and wind tunnel data differences.

Application of this concept was more tedious. To estimate apparent mass and moment of inertia of the fluid accelerated by the motion of the model and to include those terms in the calculation of forces and moments required several assumptions. While only two-dimensional examples of the apparent mass concept for pitching motions were found in the literature,^{71,72} extension to rolling motions for the displacement of a three-dimensional volume appeared to be a straightforward, though rather empirical, process.

The apparent mass calculation was started by considering the delta wing as a solid which swept out a cone during a $\phi = \pm 90^\circ$ rolling motion (Fig. 153). Therefore, not only did the model have a moment of inertia, but so did the fluid being accelerated. Acceleration of the fluid added another term to the rolling moment equation (A4)

$$L = I_{xx} \dot{\phi} \quad (41)$$

so that

$$L = I_{xx} \ddot{\phi} + L_a \quad (42)$$

where L_a is the moment due to the apparent mass of the fluid. L_a was found by

$$L_a = I_a \ddot{\phi} \quad (43)$$

where I_a is the apparent moment of inertia. Thus, equation (42) was rewritten as

$$L = (I_{xx} + I_a) \ddot{\phi} \quad (44)$$

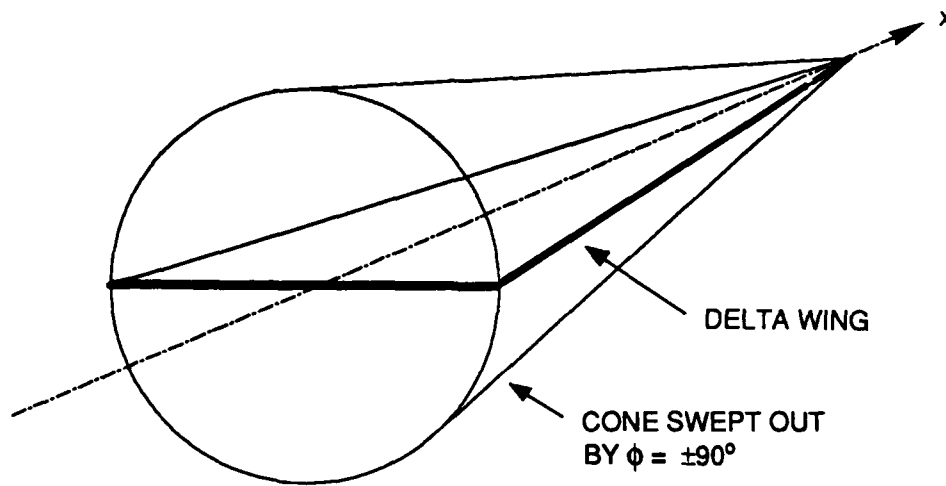


Fig. 153 Volume swept out by delta wing.

Neglecting the effects of gravity, thrust, and elastic forces, equation (44) was rewritten as

$$C_l(t_i) = \frac{(I_{xx} + I_a)}{\bar{q} S b} \ddot{\phi}(t_i) \quad (45)$$

Equation (45) is similar to equation (12); the apparent mass term was simply added. The apparent mass of the fluid was the volume of the cone times the density of fluid, so

$$m_a = \text{Apparent mass} = \frac{\pi (b/2)^2 c}{3} \quad (46)$$

where b is the wing span and c is the wing root chord. For water, this calculation yielded an apparent mass value of 0.036542 slugs, compared to an apparent mass of 4.479×10^{-5} slugs for air. The moment of inertia for the cone was

$$I_{\text{cone}} = \frac{3 m_a (b/2)^2 c}{10} \quad (47)$$

Typically, the apparent moment of inertia is assumed to be 0.25 of the moment of inertia of the fluid.^{71,72} The rationale for this "rule of thumb" was not given in the references; however, it is likely that 0.25 was associated with an assumed magnitude of pitching motions. Based on this assumption, the present analysis used a value based on the fraction of the cone through which the wing rotated. For $\phi = \pm 37^\circ$ from the water tunnel tests, the wing actually rotated through $(37^\circ / 90^\circ)$ or 0.4111 of the cone, so

$$I_a \approx 0.4111 I_{\text{cone}} \quad (48)$$

For water, $I_a = 9.73 \times 10^{-5} \text{ ft}^2\text{-slug}$ compared to an equivalent value of $I_a = 1.19 \times 10^{-7} \text{ ft}^2\text{-slug}$ for air. The 80° delta wing used in this study had an $I_{xx} = 2.417 \times 10^{-5} \text{ ft}^2\text{-slug}$; so augmenting the moment of inertia with I_a actually had the effect of increasing the rolling moment coefficient by a factor of 5.03 in equation (40). This increase led to a $C_{\ell\beta}$ value of -0.148 instead of -0.0295. Substituting the period of oscillation into the math model for the $V_\infty = 10$ ips test and replacing I_{xx} with $(I_{xx} + I_a)$, the calculated $C_{\ell\beta}$ was -0.116. Hence, this crude apparent mass calculation reduced $C_{\ell\beta}$ differences between wind tunnel and water tunnel results from a factor of 15 to a factor of 3. Interestingly, when the apparent mass of air was included in the calculation of C_ℓ in equation (40), C_ℓ increased in magnitude by only 0.5%, so neglecting apparent mass for air was quite reasonable.

The above calculations seemed a good first cut for the inclusion of apparent mass in the equation of motion; however, the vortex trajectory data presented in Figs. 95-103 suggested that the motion of the wing actually accelerated fluid well outside the cone defined by the wing. The difficulty was in assessing how much fluid was affected by the motion of the wing and translating that volume into an apparent mass and moment of inertia. In doing so, the volume of the fluid on top of the wing was modified to include the region affected by the leading-edge vortices. To approximate the volume on top of the wing, the average maximum distance the vortex moved away from the centerline was computed for each of the three locations examined. For example, at $x/c = -0.25$, the vortex moved as far as 0.94 inches from the centerline of the chord in the

spanwise direction and as high as 0.65 inches above the wing surface. Therefore, at this station, the average distance from the centerline was assumed to be approximately 0.795 inches, which corresponded to 1.8 times the local semi-span of the wing. Similar calculations for $x/c = -0.5$ and $x/c = -0.75$ revealed average distances of 1.8 and 1.6 times the local semi-span, respectively. Based on these three chordwise locations, the region of fluid influenced by the upper surface of the wing motion was assumed to be a half-cone with a radius 1.73 times the semi-span of the wing. Therefore, the half-cone swept out by the upper surface was estimated to have a radius of 0.255 ft, instead of 0.147 ft as used in the earlier calculation. The lower surface of the wing was assumed to sweep out a half-cone of the semi-span radius of 0.147 ft. Computing the apparent mass and moment of inertia for the top surface yielded values of 0.0549 slugs and $0.001068 \text{ ft}^2\text{-slug}$, respectively. Using a $\phi = \pm 37^\circ$ variation, the apparent moment of inertia for the top surface was $4.3905 \times 10^{-4} \text{ ft}^2\text{-slug}$. Similarly, I_a was estimated to be $4.89 \times 10^{-5} \text{ ft}^2\text{-slug}$ for the bottom surface. Summing the apparent moments of inertia for the top and bottom volumes yielded a total $I_a = 4.88 \times 10^{-4} \text{ ft}^2\text{-slug}$. Dividing equation (40) by equation (12), C_ℓ was calculated to be approximately 20.1 times larger than reported in the water tunnel results. The $C_{\ell\beta}$ was -0.593, compared to the old value of -0.0295, 1.33 times larger than the wind tunnel results. The mathematical model predicted a $C_{\ell\beta}$ of -0.463 instead of the original estimated value of -0.0230. While admittedly these calculations were relatively crude approximations, they bracket the wind tunnel values of C_ℓ and $C_{\ell\beta}$. This fact clearly indicated the necessity to include apparent mass effects when calculating aerodynamic terms from water tunnel motion data. To include apparent mass effects begs for a more precise calculation of the swept volumes in order to accurately translate acceleration data into rolling moment coefficients. Better approximations to the volume swept out by the wing and vortices need to be obtained; however, the cone approximation forcefully illustrated the point that apparent mass must be considered to quantify water tunnel data in this way.

Cunningham⁷⁴ reported that static lift and pitching moment coefficients obtained from force and moment measurements in the water tunnel were in excellent agreement with wind tunnel data. Additionally, preliminary results from forced pitching experiments in the water tunnel demonstrated reasonable agreement with pitching moment magnitudes obtained in wind tunnel studies on similar wings.^{74,75,76} These results supported the notion that there should be no large discrepancy between the static $C_{\ell\beta}$ and, hence, the rolling moment coefficient magnitudes in the water and wind tunnel wing rock tests. These facts underscore the necessity to include apparent mass terms in the equations of motion when converting acceleration data to force and moment values. Obviously, the problem was avoided by Cunningham by taking measurements directly with a force and moment balance, since there was no conversion of accelerations to forces or moments.

Rolling Moment Hysteresis Directions

Another major difference between the water and wind tunnel results was the opposite hysteresis directions shown in the C_{ℓ} versus ϕ plots. Verifying hysteresis direction in the water tunnel led to an intense and detailed analysis of the data reduction process. As previously discussed, different smoothing techniques were used to insure that the hysteresis was not artificially created during that process. Additionally, different camera views were analyzed to verify the phenomenon from more than one perspective. Based on all of the information collected, hysteresis was real and was in the opposite direction to rolling moment data from wind tunnel tests at Texas A&M and from other published data.^{23,25}

After careful review of the water tunnel vortex data, the most likely explanation for the opposite hysteresis direction in water tunnel and wind tunnel tests was the differences in the dynamic behavior of the leading-edge vortices during wing rock. The leading-edge vortices tended to follow a straight path in the wind tunnel tests, as suggested by the data of Jun and Nelson²⁶ and supported by qualitative smoke flow visualization in the Low Speed Wind Tunnel. This pattern indicated that at any chordwise location, the y and z positions of the vortex core with

respect to the local semi-span were similar. Therefore, only small phase differences existed between the relative vortex positions at various chord locations. But water tunnel flow visualization results presented a markedly different picture; vortices traveled in curved paths with large phase differences in the y and z positions between the different chordwise locations, as spelled out earlier (pages 119 - 131).

Even ignoring the vortex position data from the water tunnel study, significant differences between the water and wind tunnel phase shifts were predicted by a simple calculation involving equation (39). This approach assumed that the positions of the vortices near the apex at time $t = 0$ will not set up at a distance x downstream until time $t = x/V_\infty$.⁶⁷ However, during that elapsed time, the oscillating wing will have moved through some ϕ determined by the frequency or period of oscillation. Therefore, the positions of the vortices relative to the wing will be different at each chordwise location, indicating a phase shift. A phase shift of 0.27 cycles was calculated between vortex locations at $x/c = -0.25$ and $x/c = -0.75$ for the $V_\infty = 4$ ips water tunnel test. Similarly, for $V_\infty = 6$ ips tests with a measured period of 2.863 sec, the phase difference between the same two chordwise locations was estimated to be 0.291 cycles. For $V_\infty = 10$ ips with a period of 1.725 sec, the phase difference was calculated to be 0.289 cycles. Despite the differences in the freestream velocities, the estimated phase differences between $x/c = -0.25$ and $x/c = -0.75$ were very similar since the reduced frequencies did not vary significantly between the tests. The phase shift estimated between the same two chordwise stations was substantially different for the wind tunnel results when equation (39) was applied. For $\bar{q} = 0.5$ psf, $V_\infty = 20.5$ fps, the period was 0.4 sec, which yielded a phase shift of 0.051 cycles between $x/c = -0.25$ and $x/c = -0.75$. Likewise, for $\bar{q} = 1.0$ psf, $V_\infty = 29$ fps, the phase difference was 0.043 cycles. For the \bar{q} tests at 2.0, 3.0, and 4.0 psf, the estimated phase differences between the positions of the vortices were 0.039, 0.038, and 0.038, respectively. Note that the largest change in phase difference occurred between $\bar{q} = 0.5$ psf and $\bar{q} = 1.0$ psf, which corresponded to the largest change in reduced frequency.

Comparing these approximations clearly indicated a significant difference in the behavior of the leading-edge vortices between the wind tunnel and the water tunnel tests. Near the apex, the same relative vortex positions probably existed, but the relative positions became further apart as the chordwise location increased. Since the vortex positions were out of phase between the two test series, it was only reasonable for the rolling moments to be out of phase. Comparing the water tunnel test at $V_\infty = 4$ ips to the $\bar{q} = 1.0$ psf, $V_\infty = 29$ fps wind tunnel test, the phase shift between $x/c = -0.25$ and $x/c = -0.75$ was 0.227 cycles larger for the water tunnel experiment. Similar results existed in comparing the phase differences of any of the water and wind tunnel tests. The phase differences were half that value in going from $x/c = -0.25$ to $x/c = -0.5$. Since Fig. 105 showed that vortex bursting occurred throughout almost half a cycle of oscillation, the effects of the vortices on rolling moment were probably minimal for chordwise locations aft of $x/c = -0.75$, since one vortex had burst and the other was either well above the surface or outside of the wing.

Examining actual data, the same phase effect lent credence to this hypothesis. Due to differences in the positions of the vortices at each chordwise location, the incremental change in C_ℓ at each station was different. This difference was evident in Fig. 104, which qualitatively suggested differences in local C_ℓ contribution due to the vortex positions at $\phi = -37^\circ$. At $x/c = -0.25$, the right vortex was both well above the wing and outside of the local wing edge, indicating the loss of vortex lift on that side. On the other hand, the left vortex was inboard and close to the wing, generating considerable vortex lift. The net effect of this asymmetry was a positive rolling moment contribution due to the vortices at that chordwise location. At $x/c = -0.75$, the right vortex was closer to the surface than the left one. In this case, the right vortex was still outboard compared to the left vortex, but since it was above the wing (inside of the local wing edge), it probably created an even stronger negative rolling moment due to the larger moment arm. So at the same instant of time, the vortices at these two chordwise locations provided opposite contributions to the overall C_ℓ . For completeness, the $x/c = -0.5$ (not shown in Fig. 104, but available in Fig. 100) indicated that the left vortex was also inboard and close to

the wing, while the right one was well outside the edge of the wing, generating a positive rolling moment similar to $x/c = -0.25$. This pattern led to the conclusion that the overall contribution of the vortices created a positive C_{ℓ} , especially since little effect occurred aft of $x/c = -0.75$, as previously discussed. This positive rolling moment did provide the necessary spring to reverse the direction of motion at $\phi = -37^\circ$, yielding the observed limit cycle.

The above discussion illustrates the complexity of analyzing moments based on vortex positions. Not only is the closeness to the wing surface an important parameter, but the spanwise position must also be considered. Whether or not the vortex is inside or outside of the local wing edge is very important. If it is outside the edge of the wing, it is unlikely that vortex lift exists on that semi-span and even a weak influence from the opposite vortex will generate a rolling moment. If it is inside the wing edge, the moment arm becomes important, in addition to the other parameters. Burst point must also be considered, since it is characterized by an increase in local pressure and the loss of vortex lift. Another effect which has not been considered is the relative strengths of the two vortices. The strengths must be understood if the quantified position results are to be used to accurately assess the changes in C_{ℓ} due to phase shifts in the vortex positions.

A more quantitative analysis of vortex positions revealed the same information described in Fig. 104; however, with actual phase shifts determined from the vortex position data for the three chordwise locations. As stated previously, a very important parameter was the spanwise position of the vortex, whether it was inside or outside of the local wing edge. With this point in mind, the right vortex was examined at each of three chordwise locations (during the part of the oscillation where it was closest to the wing surface) to see when it moved outboard of the local wing edge. At $x/c = -0.25$, the right vortex was outside the local wing span at $\phi > -11^\circ$, for $\dot{\phi} < 0$ (Fig. 97). For $x/c = -0.50$, a similar result occurred at $\phi > -29^\circ$, for $\dot{\phi} < 0$ as shown in Fig. 100. Finally, at $x/c = -0.75$, the vortex was outside of the local wing span at $\phi = -37^\circ$, for $\dot{\phi} > 0$ (Fig. 103). In relating the ϕ time history to this information, at $x/c = -0.5$, the vortex had moved off the wing 0.5 sec later than it would have if the vortex positions were in phase. This

corresponded to a phase lag of 0.11 cycles. Similarly, the vortex at $x/c = -0.75$ moved off the wing approximately 1.2 sec after it did at $x/c = -0.25$, corresponding to a phase lag of 0.26 cycles, very close to the 0.27 cycles value predicted using equation (39) and the measured period of oscillation.

The preceding discussion showed the significance of phase differences existing between the positions of the vortices in water tunnel and wind tunnel tests. This phasing has been demonstrated by both simple calculations and experimental data on the vortex positions. The simple calculations suggested that the larger the reduced frequency, the larger the phase difference in vortex positions with chordwise location. Therefore, since the reduced frequency of the water tunnel tests was from 6 to 8 times larger than the wind tunnel results, larger phase differences were predictable. The forced oscillation water tunnel tests on the 70° delta wing (Figs. 55, 56, 57, and 59) also showed that the lag of the vortex burst point location with ϕ increased with increased reduced frequency. This increase was further substantiated by wind tunnel data from Jun and Nelson²⁶ which had a reduced frequency of 0.091, very similar to these current wind tunnel results.

While it is difficult to completely review all of the characteristics of the vortices which generate aerodynamic rolling moments, it is clear that a phase difference in C_ℓ did exist between the tests in the two media. The difference in the phase shifts between the two test series is the most plausible explanation for the opposite hysteresis directions in roll acceleration versus ϕ results. A simple example for a pure sinusoidal motion further illustrated this. For a sinusoidal motion where the roll acceleration was just the second derivative of the ϕ time history, C_ℓ versus ϕ was a straight line (Fig. 154). However, if the roll acceleration led the roll angle time history by $+10^\circ$, 0.0278 cycles, a counterclockwise hysteresis loop in the C_ℓ versus ϕ data existed (Fig. 154). If the roll acceleration lagged ϕ by -10° , 0.0278 cycles, a clockwise hysteresis loop resulted (Fig. 155). Therefore, any alteration to the relationship between the rolling acceleration (or C_ℓ) and ϕ , as occurred due to differences in vortex positions between the wind tunnel and the water tunnel tests, significantly affects both the magnitude and the direction of hysteresis.

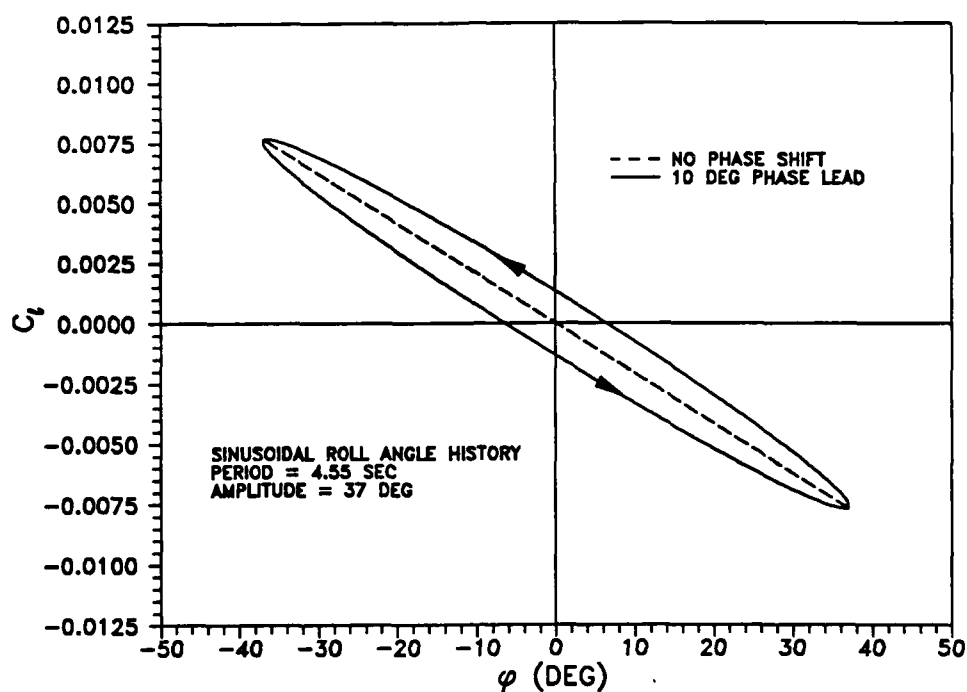


Fig. 154 C_l versus ϕ for sinusoidal motion, with phase lead.

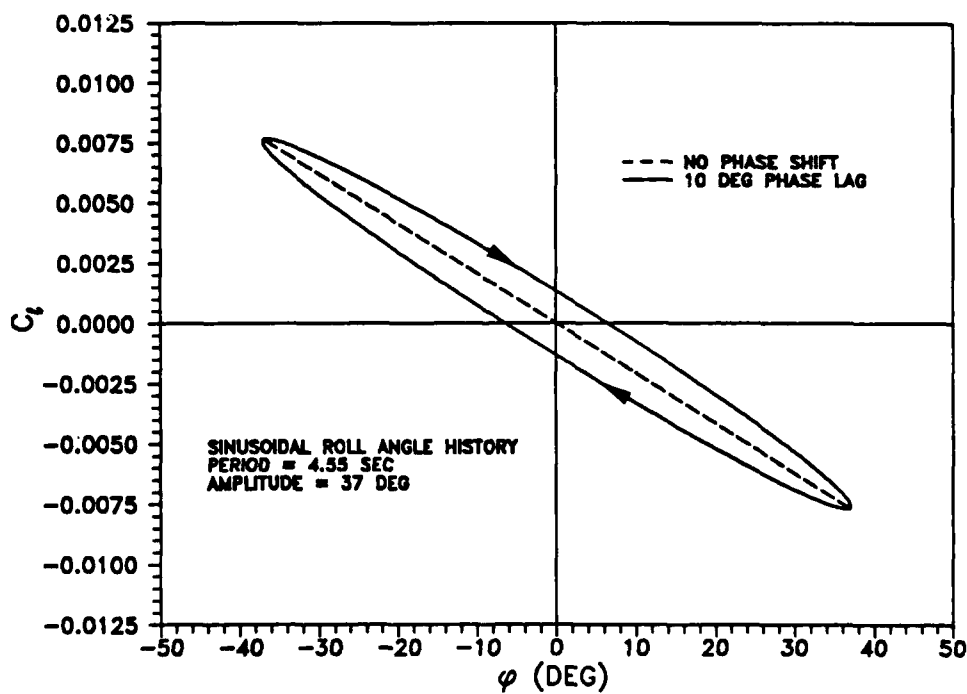


Fig. 155 C_l versus ϕ for sinusoidal motion, with phase lag.

From the detailed discussions of the water and wind tunnel results presented in this chapter, a number of conclusions were drawn. These conclusions, along with recommendations for future work, are summarized in Chapter VI.

CHAPTER VI

CONCLUSIONS AND RECOMMENDATIONS

Based on the results discussed in Chapters IV and V, the following conclusions and recommendations are made. The conclusions are discussed in chronological order since the ability to completely analyze and interpret wing rock data was contingent upon both the validation of the motion analysis system, ExpertVision, and understanding the scaling between water and wind tunnel wing rock results. In addition to providing an explanation of the cause of wing rock, the study uncovered significant differences between the dynamic response of a wing in the water tunnel and the wind tunnel. Recommendations for future research are also given.

Conclusions

ExpertVision Validation

As shown throughout Chapter IV, the current research demonstrated the capability of the video-based motion analysis system, ExpertVision, to nonintrusively provide high quality quantified position information on both the leading-edge vortices and the motion of a model under dynamic conditions. The vortex trajectories and burst points obtained on the 70° and 80° delta wings in the water tunnel were in good agreement with other published data. These data not only verified that the system could be used to quantify the positions of the vortex flows, but comparisons with wind tunnel data further demonstrated the independence of static aerodynamic parameters on Reynolds number for the ranges tested. Two orthogonal planar views were successfully combined to provide the three-dimensional behavior of the vortices. The derived velocity and acceleration data represented a significant addition to the delta wing data base and clearly demonstrated a unique capability to monitor an individual group of fluid particles throughout its path. Such a capability was especially impressive in that all data were obtained using only video cameras and recorders. The laser velocimeter can also nonintrusively measure flow field velocities; however, it is more time consuming, expensive, and requires thoroughly

trained personnel to operate. Moreover, the laser velocimeter cannot track individual fluid element trajectories; it must map out fluid motion in a volume fixed in space.

Dynamic forced oscillation tests proved that the system could simultaneously track the movements of the leading-edge vortices and the motion of the oscillating model. The measured frequencies and amplitudes of the forced oscillations were in excellent agreement with the prescribed values set on the mechanism driving the rolling motion. Vortex burst point locations were determined throughout the oscillations and were directly related to the ϕ time history. These results demonstrated a capability to precisely determine phase and amplitude relationships of the vortex flows with the model motion. The tests also showed that subtle characteristics, such as hysteresis in the forced oscillation rig, could be consistently identified. Obtaining velocity measurements of the vortex core during an oscillation also represented a significant achievement of the current study. The laser velocimeter cannot track this Lagrangian motion since its results are based on the time averaged velocity of particles passing through a fixed control volume.

The study showed that careful attention to lighting was essential to acquire high quality data. While it was relatively easy to obtain the correct lighting for optimum contrast on stationary wing tests, it was not easy for dynamic experiments. As the model rolled during the forced oscillation and wing rock tests, reflections caused marked changes in the contrast. These changes in contrast made digitizing the vortices very difficult since a single threshold setting on the video processor was not adequate. Therefore, the necessity to continually alter the threshold setting during a roll oscillation required that vortex data be digitized frame by frame, making the process extremely slow and tedious. The tests also showed that it is very important to have reference points in the field of view for scaling of the video frame and to verify test parameters, like angle of attack.

Scaleability of Water and Wind Tunnel Results

The study uncovered and reemphasized some very important scaling issues between water tunnel and wind tunnel testing. The free-to-roll experiments revealed significant differences

in the wing rock response of the model in two media. The rolling moment coefficients and lateral stability derivative, $C_{\ell\beta}$, obtained from the water tunnel study were underpredicted by a factor of 15 or greater when converting the roll accelerations into C_{ℓ} with the single degree-of-freedom equation of motion, equation (12). Careful study of the dynamic results showed that the discrepancies were primarily due to the much greater density of the water. In air, the model was relatively heavy compared to the fluid so the volume of air accelerated due to the motion of the wing was negligible. In water, the model motion accelerated a significant fluid mass that could not be neglected. This fluid mass increased the model's resistance to rolling and required the inclusion of apparent mass terms in the equations of motion in order to provide the correct relationship between accelerations and forces and moments. This finding was significant in that it emphasizes that density and dynamic pressure values in aircraft equations of motions do not account for media differences in dynamic tests. This conclusion was further supported by the limited amount of water tunnel force and moment measurements available which were in good agreement with wind tunnel data. While the requirement for the inclusion of apparent mass in the equations of motion was established, it was very difficult to determine the magnitude of those terms. The volume of fluid influenced by the model motion must be precisely calculated if accurate aerodynamic rolling moment coefficients were to be obtained. Therefore, the appropriate volume to use for a given configuration deserved careful attention.

The study also revealed that leading-edge vortices behaved differently in water tunnel tests than in wind tunnel experiments during wing rock. Although the positions of the vortices were similar near the apex of the wing, significant phase shifts developed as the vortices moved aft. These differences were observed in comparing the limited amount of wind tunnel data available on the 80° delta wing with water tunnel measurements for this project. The positions of the vortices at $x/c = -0.25$ in the water tunnel tests were similar to the $x/c = -0.75$ data from the wind tunnel study.²⁶ The phase differences in vortex positions with chordwise location was also predictable from simple calculations which related freestream velocity and oscillation period (or frequency). The current study indicated that for phasing of the vortices to be similar for two tests,

the reduced frequencies must be close. Therefore, the large differences in the reduced frequencies, approximately 0.64 for water tunnel experiments, compared to an average value of 0.09 for the wind tunnel experiments, were indications that the phasing of the vortex positions with chordwise locations was different. This point was further substantiated by the Jun and Nelson²⁶ data to which the water tunnel data were compared. Their tests had a reduced frequency of 0.091, similar to the current wind tunnel values. It is important to note that the large difference in reduced frequency was primarily due to the media, since k was relatively constant for each test series. Since the behavior of the vortices were different, the rolling moments coefficients were also different. It was this difference in vortex behavior which was most likely responsible for the hysteresis direction differences in the C_{ℓ} versus ϕ plots between the water and wind tunnel tests.

Based on results from this research, care must be exercised in using water tunnel dynamic results directly as an indication of a models' behavior in air. In order to determine aerodynamic rolling moment coefficients from the roll acceleration data from water tunnel experiments, equation (40) must be used instead of equation (12). Additionally, $(I_{xx} + I_a)$ must be substituted into the mathematical model instead of I_{xx} in order to obtain reasonable periods and frequencies when $C_{\ell\beta}$ values from wind tunnel static force tests are used in the calculation. While very useful information is available from dynamic tests in the water tunnel, the researcher must understand and apply the scaling relationships applied in this study.

Wing Rock Conclusions

Wing rock is caused by the alternating lift-off and reattachment of the leading-edge vortices. Despite the phase differences noted between the water and wind tunnel tests, it is the positions of the leading-edge vortices which generate incremental changes in the aerodynamic rolling moment favoring wing rock. The relative positions of the leading-edge vortices with respect to the wing determine the imbalance in lift and, therefore, the rolling moments which give rise to self-induced oscillations. The closer a vortex is to the wing surface, the larger the effect of

the low pressure zone on the upper surface, and the greater the vortex lift. As the vortex moves away from the upper surface the low pressure region has a smaller effect on the wing and generates less vortex lift. The vortex lift effect is also lost as the vortex moves outside of the local wing edge, so any lift generated by the opposite vortex is sufficient to create a moment favoring an upward movement of that wing semi-span. It must be remembered that the vortex lift effect is only 10 to 15% of the overall lift on the wing, so the effects due to the vortices are seen as incremental increases or decreases in the overall aerodynamic rolling moment.

Having established the relationship between vortex positions and vortex lift, the following describes the history of a wing rock cycle. Initially, if the wing is at zero roll angle it remains in that orientation until an asymmetry is created in the leading-edge vortices. Once an asymmetry occurs, one vortex is displaced away from the upper surface resulting in a decrease in the vortex lift on that side. The decrease in lift on that semi-span causes it to drop down, while the opposite semi-span moves up. It continues to move down until the lifted-off vortex is blown inboard and close to the wing surface, while at the same time, the opposite vortex has been displaced above the surface and outboard of the local wing edge. In addition to moving inboard and close to the surface, the vortex on the downgoing wing semi-span bursts slightly upstream of the half chord location, resulting in a partial loss of vortex lift on that side. However, the opposing vortex is outboard of the local wing edge, in addition to being far from the surface, generating little or no vortex lift. Therefore, the downward semi-span still has a larger lift which forces it up, reversing the direction of the rolling motion. Increased lift is maintained on that wing semi-span as it rolls through wings level and becomes the upper semi-span. As it continues to move up, the vortex on that side is pushed outboard of the local wing edge and away from the surface, while the opposite vortex moves close to the surface and inboard on the downward semi-span. As before, the lower wing has the greater lift which reverses the motion back toward wings level. The motion continues as long as the alternating lift-off and reattachment of the vortices occur. This phenomenon is clouded somewhat by the vortex positions measured at $x/c = -0.75$ in the water tunnel, which show both vortices inboard of the local wing edge at $\phi = -37^\circ$, with the vortex on the upper semi-span side closer to the surface and with a longer moment arm. This chordwise

location actually generates a moment in the opposite direction of the $x/c = -0.25$ and $x/c = -0.5$ locations. Based on the large lags in the vortex positions, these aft regions of the leading-edge vortices are actually following the motion of the model and their effects on rolling moment are secondary to the larger upstream moments which drive the model motion. They do change the overall magnitude of the rolling moment coefficient, and evidently are responsible for the different hysteresis direction from the wind tunnel results.

Although the movements of the vortices and their effect on rolling moment caused wing rock in both the water tunnel and the wind tunnel tests, the effects of roll damping were less clear. In the wind tunnel, the energy analysis of the C_l versus ϕ data indicated that unstable roll damping existed at small roll angles and stable roll damping existed at larger roll angles. This result was consistent with other free-to-roll wind tunnel tests, as well as forced oscillation roll damping results.²³ It was also in agreement with actual aircraft results which have shown that roll damping was unstable at flight conditions where wing rock occurred. Applying the same energy analysis to the water tunnel measurements revealed a different picture, with unstable damping at the larger roll angles and stable damping at the smaller roll angles. The differences in the hysteresis direction, which indicated the opposite roll damping behavior, have been attributed to lags in the vortex positions with chordwise locations. Assuming that the roll damping results of the water tunnel study were correct (given that the roll damping trends have been verified in the wind tunnel measurements), this behavior further confirmed the conclusion that wing rock occurred due to movement of the vortices and the inherent static stability of the wing. This reasoning also indicated that roll damping was caused by the vortex movements and was secondary to the actual causes of wing rock—that is, vortex locations relative to the model.

Mathematical Model and Simulation

While the mathematical model used was not an original development, results from this research have validated the Beecham-Titchener approach as well as demonstrated the usefulness of the model. As shown in Chapter V, amplitude and period predictions from this model were almost in exact agreement with direct numerical integration of the nonlinear equation

of motion using a fourth order Runge-Kutta algorithm with the same aerodynamic derivatives and approximation for β . Additionally, results from the model were in fair to good agreement with measurements from wing rock tests. The mathematical model also helped give insight into the scaling issues between the water tunnel and the wind tunnel results.

The fourth order Runge-Kutta integration provided a good simulation of the wing rock tests. Not only did it yield predicted wing rock characteristics, but it identified the stable limit cycle by converging to the same solution from initial conditions both inside and outside of the closed path. The Runge-Kutta algorithm also allowed the nonlinear equations to be integrated without requiring the β approximation, increasing the accuracy of the simulation. And as stated above, it provided an excellent validation of the Beecham-Titchener approach.

Both the mathematical model and the Runge-Kutta simulation allowed quick evaluation of the effects of changes in test conditions or aerodynamic derivatives. Both also predicted differences in wing rock behavior between the water tunnel and the wind tunnel tests. The mathematical model and Runge-Kutta integration supported the need to include apparent mass terms in the equations of motion in order to convert water tunnel acceleration measurements to C_2 .

Summary

Overall, the approach employed in this study permitted one of the most detailed examinations of wing rock known to exist. For the first time both leading-edge vortices and model motion were quantified simultaneously. The capabilities of ExpertVision were exploited to obtain data not previously available. The research also provided a substantial contribution to experimental fluid dynamics by identifying significant differences in the dynamic behavior of a model in wind tunnels and in water tunnels.

Recommendations

Although the objectives of the current study were met, a number of recommendations are made for future research. These recommendations are broken into three major categories:

further analysis of wing rock, dynamic scaling between water tunnel and wind tunnel tests, and enhancements to ExpertVision. Recommendations are discussed in order of importance within each category.

Further Analysis of Wing Rock

The first category provides recommendations for further analysis of wing rock based on issues raised during the current research. One of the most important questions concerns the relationship between wing rock and aerodynamic roll damping. While other researchers^{23,29,30} have claimed that roll damping is the major cause of wing rock, the current water tunnel data suggests otherwise. To further analyze roll damping behavior in the water tunnel, free-to-roll experiments should be conducted to monitor wing rock build-up, as performed in the wind tunnel tests. Force and moment forced oscillation experiments should also be conducted in the water tunnel to determine roll damping variations with roll amplitude, similar to the wind tunnel tests conducted by Nguyen, Yip, and Chambers.²³

Efforts should be made to develop new or apply existing flow visualization techniques in the wind tunnel that would allow the movement of the leading-edge vortices during wing rock to be quantified using ExpertVision. A technique that could provide high quality visualization similar to the dye flow technique used in the water tunnel would permit correlation of model dynamics and vortex movements. This information is crucial to verifying the phase differences for vortex movements and their effects on hysteresis.

Forced oscillation flow visualization tests in the water tunnel should be conducted over a wide range of reduced frequencies on the 80° delta wing to assess the effects of oscillation frequency on phase lag of the vortex movements. As a minimum, the forced oscillation tests should be conducted at reduced frequencies from near zero to wing rock values. This work would provide further insight into the effects of reduced frequency on phase differences of vortex movements. Likewise, forced oscillation tests should be performed on the 70° delta wing at additional reduced frequencies to further define the shape of the curves in Figs. 58 and 59.

Experiments should be performed to isolate the aerodynamic derivatives of $C_{\ell p}$ and $(C_{\ell \dot{\beta}} \sin \alpha)$ in both the water tunnel and the wind tunnel. These measurements could be accomplished by subjecting the model to pure $\dot{\beta}$ oscillations at fixed α and measuring the forces and moments. These tests would help determine the significance of the $\dot{\beta}$ derivative to the rolling motion. This information is important in fully understanding the relationship between $C_{\ell p}$ and wing rock oscillations.

Dynamic Scaling Between Water Tunnel and Wing Tunnel Tests

The second major category provides recommendations for further investigation of the dynamic scaling between water tunnel and wind tunnel data. A research study should be performed with the primary objective of examining this scaling. A more detailed analysis of apparent mass corrections could greatly improve the ability to obtain accurate rolling moment coefficients and stability derivatives from free-to-roll water tunnel experiments. C_{ℓ} and $C_{\ell \dot{\beta}}$ should be obtained from actual force measurements in the water tunnel for direct comparison with wind tunnel data to help validate apparent mass corrections. It is extremely important to appropriately modify the equations of motion in order to obtain meaningful information from water tunnel data.

Enhancements to ExpertVision

The third major category includes recommendations to improve the capability and use of ExpertVision. One of the top priorities should be to expand the ExpertVision system to three-dimensional capability with the acquisition of upgraded software and hardware. This upgrade would allow multiple cameras to be used in the data collection process in other than orthogonal arrangements. The improved software would also provide statistical redundancy to improve accuracy and confidence in the data. This redundancy would help reduce data loss which occurs due to poor contrast between the target and background or obstruction of the target from

view by providing different camera perspectives. The software should cross-correlate the data between multiple cameras to determine the three-dimensional trajectory of the target.

The operation of ExpertVision could be greatly improved by better automation of the data reduction process. Algorithms that streamline the editing process by requiring less frame-by-frame editing are necessary to increase the efficiency and productivity of data reduction.

The acquisition of cameras operating at frame rates beyond 200 frames per second will be required for future wind tunnel applications. This fact was highlighted by the $\bar{q} = 5$ psf wind tunnel test which needed a higher frame rate to obtain useful C_ℓ versus ϕ plots.

Summary

In summary, the tests showed that wing rock of highly swept delta wings is caused by the positions and relative movement of the leading-edge vortices with respect to the wing. ExpertVision was validated for use in fluid flow applications and successfully used to simultaneously quantify the movements of the vortices and model motion. Significant scaling differences between dynamic experiments in the water tunnel and the wind tunnel were uncovered in the investigation. Plausible explanations were provided for the causes of these differences. Follow-on efforts have been recommended to further address issues identified by the current research.

REFERENCES

¹Greaves, J.O.B., Wilson, R.S., and Walton, J.S., "A Video-Based Image Analysis System for Rapid Non-Intrusive Collection and Reporting of Motion Data," *Transducer Technology for Physical Measurements*, Proceedings on the 1985 SEM Conference on Experimental Measurements, Society for Experimental Mechanics, 1985, pp. 163-169.

²Nguyen, L.T., Gilbert, W.P., Gera, J., Iliff, K.W., and Enovoldson, E.K., "Application of High- α Control System Concepts to a Variable-Sweep Fighter Airplane," AIAA Paper 80-1582, Aug. 1980.

³"Manoeuvre Limitations of Combat Aircraft," AGARD-AR-155A, Aug. 1979.

⁴Chambers, J.R., Gilbert, W.P., and Nguyen, L.T., "Results of Piloted Simulator Studies of Fighter Aircraft at High Angles of Attack," Paper 33, AGARD-CP-235, May 1978.

⁵Johnston, D.E., "Identification of Key-Maneuver-Limiting Factors in High Angle of Attack Flight," Paper 36, AGARD-CP-235, May 1978.

⁶Chambers, J.R. and Anglin, E.L., "Analysis of Lateral-Directional Stability Characteristics of a Twin-Jet Fighter Airplane at High Angles of Attack," NASA TN D-5361, Aug. 1969.

⁷Grafton, S.B. and Libbey, C.E., "Dynamic Stability Derivatives of a Twin-Jet Fighter Model for Angles of Attack from -10° to 110° ," NASA TN D-6091, Jan. 1971.

⁸Schiff, L.B. and Tobak, M., "Some Applications of Aerodynamic Formulations to Problems in Aircraft Dynamics," Lecture 16, AGARD-LS-114, Mar. 1981.

⁹Ross, A.J., "Flying Aeroplanes in Buffet," *Aeronautical Journal*, Vol. 81, Oct. 1977, pp. 427-436.

¹⁰Ross, A.J., "Lateral Stability at High Angles of Attack, Particularly Wing Rock," Paper 10, AGARD-CP-260, Sept. 1978.

¹¹Ross, A.J., "Investigation of Nonlinear Motion Experienced on Slender-Wing Research Aircraft," *Journal of Aircraft*, Vol. 9, Sept. 1972, pp. 625-631.

- ¹²Hwang, C. and Pi, W.S., "Some Observations on the Mechanism of Aircraft Wing Rock," *Journal of Aircraft*, Vol. 16, June 1979, pp. 366-373.
- ¹³Erickson, G.E., "Vortex Flow Correlation," AFWAL-TR-80-3143, Jan. 1981.
- ¹⁴Orlik-Ruckemann, K.J., "Aerodynamic Aspects of Aircraft Dynamics at High Angle of Attack," *Journal of Aircraft*, Vol. 20, Sept. 1983, pp. 737-752.
- ¹⁵Titiriga, A., Jr., Ackerman, J.S., and Skow, A.M., "Design Technology for Departure Resistance of Fighter Aircraft," Paper 5, AGARD-CP-199, Nov. 1975.
- ¹⁶Grafton, S.B., Gilbert, W.P., Croom, M.A., and Murri, D.G., "High Angle-of-Attack Characteristics of a Forward Swept Wing Fighter Configuration," AIAA Paper 82-1322, Aug. 1982.
- ¹⁷Malcolm, G.N., "Impact of High-Alpha Aerodynamics on Dynamic Stability Parameters on Aircraft and Missiles," Lecture 2, AGARD-LS-114, March 1981.
- ¹⁸Orlik-Ruckemann, K.J., "Effects of High Angles of Attack on Stability Parameters," Paper 1, AGARD-CP-247, Oct. 1978.
- ¹⁹Skow, A.M. and Titiriga, A., Jr., "A Survey of Analytical and Experimental Techniques to Predict Aircraft Dynamic Characteristics at High Angles of Attack," Paper 19, AGARD-CP-235, May 1978.
- ²⁰Ross, A.J. and Nguyen, L.T., "Some Observations Regarding Wing Rock Oscillations at High Angles of Attack," AIAA Paper 88-4371-CP, Aug. 1988.
- ²¹Fratello, D.J., Croom, M.A., Nguyen, L.T., and Domack, C.S., "Use of the Updated NASA Langley Radio-Controlled Drop-Model Technique for High-Alpha Studies of the X-29A Configuration," AIAA Paper 87-2559, Aug. 1987.
- ²²Chambers, J.R., Dicarlo, D.J., and Johnson, J.L., Jr., "Applications of Dynamic Stability Parameters to Problems in Aircraft Dynamics," Lecture 17, AGARD-LS-114, March 1981.
- ²³Nguyen, L.T., Yip, L., and Chambers, J.R., "Self-Induced Wing Rock of Slender Delta Wings," AIAA Paper 81-1883, Aug. 1981.
- ²⁴Levin, D. and Katz, J., "Dynamic Load Measurements with Delta Wings Undergoing Self-Induced Roll-Oscillations," *Journal of Aircraft*, Vol. 21, Jan. 1984, pp. 30-36.

- ²⁵Katz, J. and Levin, D., "Measurements of Canard-Induced Roll Oscillations," AIAA Paper 85-1830, Aug. 1975.
- ²⁶Jun, Y.W. and Nelson, R.C., "Leading Edge Vortex Dynamics on a Delta Wing Undergoing a Wing Rock Motion," AIAA Paper 87-0332, Jan. 1987.
- ²⁷Konstadinopoulos, P., Mook, D.T., and Nayfeh, A.H., "Subsonic Wing Rock of Slender Delta Wings," *Journal of Aircraft*, Vol. 22, March 1985, pp. 223-228.
- ²⁸Elzebda, J.M., Mook, D.T., and Nayfeh, A.H., "The Influence of an Additional Degree of Freedom on Subsonic Wing Rock of Slender Delta Wings," AIAA Paper 87-0496, Jan. 1987.
- ²⁹Hsu, C.H., and Lan, C.E., "Theory of Wing Rock," *Journal of Aircraft*, Vol. 22, Oct. 1985, pp. 920-924.
- ³⁰Hsu, C.H., "Theory of Wing Rock," Ph.D. Dissertation, University of Kansas, Lawrence, Feb. 1984.
- ³¹Schmidt, L.V., "Wing Rock Due to Aerodynamic Hysteresis," *Journal of Aircraft*, Vol. 16, March 1979, pp. 129-133.
- ³²Ericsson, L.E., "The Fluid Mechanics of Slender Wing Rock," *Journal of Aircraft*, Vol. 21, May 1984, pp. 322-328.
- ³³Ericsson, L.E., "The Various Sources of Wing Rock," AIAA Paper 88-4370-CP, Aug. 1988.
- ³⁴Ericsson, L.E., "Analytic Prediction of Slender Wing Rock," AIAA Paper 87-2496, Aug. 1987.
- ³⁵Ericsson, L.E., "Vortex-Induced Effects on Aircraft Dynamics," AIAA Paper 86-2279-CP, Aug. 1986.
- ³⁶Ericsson, L.E., "Further Analysis of Wing Rock Generated by Forebody Vortices," AIAA Paper 88-2597-CP, June 1988.
- ³⁷Beecham, L.J. and Titchener, I.M., "Some Notes on an Approximate Solution for the Free Oscillation Characteristics of Non-Linear Systems Typified by $\ddot{x} + F(x, \dot{x}) = 0$," British Aeronautical Research Council, R & M No. 3651, London, Aug. 1969.

³⁸Lan, C.E. and Hsu, C.H., "Effects of Vortex Breakdown on Longitudinal and Lateral-Directional Aerodynamics of Slender Wings by the Suction Analogy," AIAA Paper 82-1385, Aug. 1982.

³⁹Lan, C.E., "The Unsteady Suction Analogy and Applications," AIAA Paper 81-1875, Aug. 1981.

⁴⁰Tobak, M. and Schiff, L.B., "Aerodynamic Mathematical Modeling - Basic Concepts," Lecture 1, AGARD-LS-114, Mar. 1981.

⁴¹Polhamus, E.C., "A Concept of the Vortex Lift of Sharp-Edge Delta Wings Based on a Leading-Edge Suction Analogy," NASA TN D-3767, 1966.

⁴²*ExpertVision User's Manual*, Motion Analysis Corporation, Santa Rosa, California, 1986.

⁴³Malcolm, G.N., Lewis, L.C., Ward, D.T., and Morris, S.L., "An Innovative Approach to Nonintrusive Quantitative Measurements of Vortex Flows," Eidetics International TR 88-101, Torrance, California, February 1988.

⁴⁴Morris, S.L., Ward, D.T., Malcolm, G.N., and Lewis, L.C., "Nonintrusive Measurements of Vortex Flows on Delta Wings in a Water Tunnel," AIAA Paper 88-2595-CP, June 1988.

⁴⁵*Low Speed Wind Tunnel Facility Handbook*, Texas A&M University, College Station, Jan. 1985.

⁴⁶Brown, C.E. and Michael, W.H., Jr., "On Slender Delta Wings with Leading-Edge Separation," NACA TN 3430, 1955.

⁴⁷Smith, J.H.B., "Improved Calculations of Leading-Edge Separation from Slender, Thin Delta Wings," Proceedings of the Royal Aeronautical Society, A. 306, London, 1968, pp. 67-90.

⁴⁸Lambourne, N.C. and Bryer, D.W., "The Bursting of Leading-Edge Vortices—Some Observations and Discussion of the Phenomenon," Aeronautical Research Council TR-RM-3282, London, 1961.

⁴⁹Malcolm, G.N. and Nelson, R.C., "Comparison of Water Tunnel Flow Visualization Results on a Generic Fighter Configuration at High Angles of Attack," AIAA Paper 87-2423, Aug. 1987.

⁵⁰Erickson, G.E., "Water Tunnel Flow Visualization: Insight into Complex Three-Dimensional Flow Fields," AIAA Paper 79-1530, July 1979.

⁵¹Lowson, M.V., "Some Experiments with Vortex Breakdown," *Journal of the Royal Aeronautical Society*, Vol. 68, May 1964, p. 343.

⁵²Erickson, G.E., Peake, D.J., Del Frate, J., Skow, A.M., and Malcolm, G.N., "Water Facilities in Retrospect and Prospect—An Illuminating Tool for Vehicle Decision," Lecture 1, AGARD-CP-413, Oct. 1986.

⁵³Poisson-Quinton, P., Werle, H., "Water Tunnel Visualization of Vortex Flow," *Astronautics and Aeronautics*, June 1967, pp. 64-66.

⁵⁴Polhamus, E.C., "Prediction of Vortex-Lift Characteristics by a Leading-Edge Suction Analogy," *Journal of Aircraft*, Vol. 8, April 1971, pp. 193-199.

⁵⁵McKernan, J.F. and Nelson, R.C., "An Investigation of the Breakdown of the Leading Edge Vortices on a Delta-Wing at High Angles of Attack," AIAA Paper 83-2114, Aug. 1983.

⁵⁶Johnson, J.L., Grafton, S.B., and Yip, L.P., "Exploratory Investigation of the Effects of Vortex Bursting on the High Angle of Attack Lateral-Directional Stability Characteristics of Highly Swept Wings," AIAA Paper 80-0463, 1980.

⁵⁷Wentz, W.H. and Kohlman, D.L., "Vortex Breakdown on Slender Sharp-Edged Wings," *Journal of Aircraft*, Vol. 8, March 1971, pp. 156-161.

⁵⁸Boyden, R.P., "Effects of Leading-Edge Vortex Flow on the Roll Damping of Slender Wings," *Journal of Aircraft*, Vol. 8, July 1971, pp. 543-547.

⁵⁹Shanks, R.E., "Low-Subsonic Measurements of Static and Dynamic Stability Derivatives of Six Flat-Plate Wings Having Leading-Edge Sweep Angles of 70° to 84°," NASA TN D-1822, 1963.

⁶⁰Nelson, R.C., "Flow Visualization of High Angle of Attack Vortex Wake Structures," AIAA Paper 85-0102, Jan. 1985.

⁶¹Payne, F.M., Ng, T.T., Nelson, R.C., and Schiff, L.B., "Visualization and Flow Surveys of the Leading Edge Vortex Structure on Delta Wing Planforms," AIAA Paper 86-0330, Jan. 1986.

⁶²Bird, J.D., "Tuft-Grid Surveys at Low Speed for Delta Wings," NASA TN D-5045, Feb. 1969.

⁶³Wilson, J.D., "Calculation of Vortex Breakdown Locations for Flow Over Delta Wings," *Journal of Aircraft*, Vol. 14, Oct. 1977, 1020-1022.

⁶⁴Malcolm, G.N. and Skow, A.M., "Enhanced Controllability Through Vortex Manipulation on Fighter Aircraft at High Angles of Attack," AIAA Paper 86-2277-CP, Aug. 1986.

⁶⁵Ng, T.T., Malcolm, G.N., and Lewis, L.C., "Flow Visualization Study of Delta Wings in Wing-Rock Motion," Submitted to AIAA 7th Applied Aerodynamics Conference, Aug. 1989.

⁶⁶Coe, P.L., Graham, A.B., and Chambers, J.R., "Summary of Information on Low-Speed Lateral-Directional Derivatives Due to Rate of Change of Sideslip β ," NASA TN D-7972, Sept. 1975.

⁶⁷Lambourne, N.C., Bryer, D.W., and Maybrey, J.F.M., "The Behavior of the Leading-Edge Vortices Over a Delta Wing Following a Sudden Change of Incidence," British Aeronautical Research Council, R & M No. 3645, London, March 1969.

⁶⁸Lang, J.D., *Aircraft Performance, Stability, and Control*, United States Air Force Academy, Colorado, 1974.

⁶⁹Etkin, B., *Dynamics of Flight*, John Wiley & Sons, Inc., New York, 1959.

⁷⁰Roskam, J., *Airplane Flight Dynamics and Automatic Flight Controls*, Roskam Aviation and Engineering Corporation, Lawrence, Kansas, 1979.

⁷¹Fung, Y.C., *An Introduction to the Theory of Aeroelasticity*, John Wiley & Sons, Inc., New York, 1955.

⁷²Bisplinghoff, R.L., Ashley, H., and Halfman, R.L., *Aeroelasticity*, Addison-Wesley Publishing Co., Cambridge, Massachusetts, 1955.

⁷³Dryden, H.L., Murnaghan, F.D., and Bateman, H., *Hydrodynamics*, Dover Publications, Inc., New York, 1956.

⁷⁴Cunningham, A.M., Private Communications, 1989.

⁷⁵Den Boer, R.G. and Cunningham, A.M., Jr., "A Wind Tunnel Investigation at Low Speed of the Flow About a Straked Delta Wing Oscillating in Pitch," AIAA Paper 87-2493, Aug. 1987.

⁷⁶Brandon, J.M. and Shah, G.H., "Effect of Large Amplitude Pitching Motions on the Unsteady Aerodynamic Characteristics of Flat-Plate Wings," AIAA Paper 88-4331-CP, Aug. 1988.

APPENDIX A

APPROXIMATE ANALYTIC SOLUTION TO ONE DEGREE-OF-FREEDOM MODEL

An approximate analytic solution to the single degree-of-freedom nonlinear equation describing wing rock was originally derived and reported by Nguyen, Yip, and Chambers.²³ The model was extended by Hsu and Lan^{29,30} to include roll damping variations with roll rate. This Appendix further extends the model to include the effects of bearing friction which is present in wind and water tunnel tests. The inclusion of friction provides insight into some of the differences which exist between results obtained from different wind tunnel studies for geometrically similar models. Obviously, for actual flight conditions, the friction term is zero. The Beecham-Titchener method³⁷ is used in development of the solution. This method has been used with excellent success in analyzing other examples which include nonlinear terms.

Equations of Motion

In developing any analytical solution to the single degree-of-freedom wing rock problem, it is important to first understand the equations of motion. Since wing rock is examined for cases where there is no translational acceleration (freestream velocity is constant), only the moment equations are needed to determine the governing equations of motion. In a body-axis system, the moment equation for an aircraft or wing is expressed as

$$\Sigma \bar{M}_B = (\dot{\bar{H}} + \bar{\omega} \times \bar{H})_B \quad (A1)$$

The left hand side of the equation includes all pertinent moments which act about the aircraft center of gravity. The components of the moment vector are defined as

$$\Sigma \bar{M}_B = \begin{bmatrix} L \\ M \\ N \end{bmatrix} \quad (A2)$$

The resulting three scalar moment equations are:

$$\begin{aligned} L &= I_{xx} \dot{p} - (I_{yy} - I_{zz}) q r - I_{xz} (\dot{r} + p q) \\ M &= I_{yy} \dot{q} - (I_{xx} - I_{zz}) p r - I_{xz} (p^2 - r^2) \\ N &= I_{zz} \dot{r} - (I_{xx} - I_{yy}) p q - I_{xz} (\dot{p} + q r) \end{aligned} \quad (A3)$$

For a motion constrained to pure roll (q , r , and \dot{r} are zero), the moment equation reduces to

$$L = I_{xx} \dot{p} \quad (A4)$$

Neglecting the effects of gravity, thrust, and elastic forces, equation (A4) can be written as

$$C_l(t_i) = \frac{I_{xx} \dot{p}(t_i)}{\bar{q} S b} \quad (A5)$$

where I_{xx} is the moment of inertia of the wing about the body fixed x-axis, b is the wing span, S is the reference area, \bar{q} is the dynamic pressure, \dot{p} is the angular acceleration about the longitudinal axis, and $C_l(t)$ is the time varying aerodynamic rolling moment coefficient. For the single degree-of-freedom approximation the kinematic relationships are

$$p = \dot{\phi} \quad (A6)$$

and

$$\beta = \sin^{-1} (\sin \alpha_s \sin \phi) \quad (A7)$$

Equations (A5), (A6), and (A7) form a nonlinear second-order differential equation in ϕ , with the coefficients varying with time. Equation (A7) can be approximated by

$$\beta = \phi \sin \alpha_s \quad (A8)$$

This approximation is extremely useful in the development of an analytic solution to the nonlinear equation. The analysis assumes that freestream velocity, density, Reynolds number, and mass distributions are constant during the rolling motion.

Analytical Formulation

In the development of the analytic solution, the total aerodynamic rolling coefficient is described as a simplified nonlinear function. Such a representation is necessary in order to address the aerodynamic nonlinearities present at high angles of attack where wing rock is experienced. Nguyen, Yip, and Chambers²³ expressed the rolling moment coefficient as

$$C_{\ell}(t) = C_{\ell\beta} \beta + C_{\ell p} \bar{p} \quad (A9)$$

where

$$C_{\ell p} = C_{\ell p0} + C_{\ell p\beta} |\beta| \quad (A10)$$

Hsu expanded the rolling moment coefficient to

$$C_{\ell}(t) = C_{\ell0} + C_{\ell\beta} \beta + C_{\ell p} \bar{p} + C_{\ell\delta_A} \delta_A \quad (A11)$$

where

$$C_{\ell p} = C_{\ell p0} + C_{\ell p\beta} |\beta| + C_{\ell pp} |\bar{p}| \quad (A12)$$

The absolute value signs in equations (A10) and (A12) permit the use of a single averaged value of $C_{\ell p\beta}$ and $C_{\ell pp}$ in the formulation. The current study uses the same function in equations (A11) and (A12) for the rolling moment; however, equation (A4) is modified to include friction; it becomes,

$$L - \mu p = I_{xx} \dot{p} \quad (A13)$$

Equation (A5) is then replaced by

$$C_{\ell}(t_i) - \frac{\mu p}{\bar{q} S b} = \frac{I_{xx} \dot{p}}{\bar{q} S b} \quad (A14)$$

where μ is a damping coefficient due to bearing friction in the free-to-roll mounting bracket. While the friction contribution does not exist in free flight, it is present in the wind and water tunnel studies used in evaluating wing rock. Having obtained an expression for the aerodynamic rolling moment coefficient which represents the nonlinear aerodynamics, the second order nonlinear equation can be written by substituting equations (A6), (A8), (A11), and (A12) into (A14). This substitution yields

$$\begin{aligned} \frac{I_{xx} \ddot{\phi}}{\bar{q} S b} = & C_{\ell 0} + C_{\ell \delta_A} \delta_A + \sin \alpha_s C_{\ell \beta} \beta + \dots \\ & \dots + (C_{\ell p0} + \sin \alpha_s C_{\ell p\beta} |\phi| + C_{\ell pp} \left| \frac{\dot{\phi} b}{2V} \right|) \frac{\dot{\phi} b}{2V} - \mu \frac{\dot{\phi} b}{2V} \end{aligned} \quad (A15)$$

Equation (A15) can be expressed in a more convenient form in terms of dimensional derivatives as

$$\begin{aligned} \ddot{\phi} = & L_0 + L_{\delta_A} \delta_A + \sin \alpha_s L_{\beta} \phi + \dots \\ & \dots + (L_{p0} + \sin \alpha_s L_{p\beta} |\phi| + L_{pp} |\dot{\phi}|) \dot{\phi} - \mu_1 \dot{\phi} \end{aligned} \quad (A16)$$

where the dimensional derivatives are defined by:

$$\begin{aligned} L_0 &= \frac{\bar{q} S b}{I_{xx}} C_{\ell 0} \text{ (sec}^{-2}\text{)} & L_{\delta_A} &= \frac{\bar{q} S b}{I_{xx}} C_{\ell \delta_A} \text{ (sec}^{-2}\text{)} \\ L_{\beta} &= \frac{\bar{q} S b}{I_{xx}} C_{\ell \beta} \text{ (sec}^{-2}\text{)} & L_{p0} &= \frac{\bar{q} S b^2}{2 V I_{xx}} C_{\ell p0} \text{ (sec}^{-1}\text{)} \end{aligned}$$

$$L_{p\beta} = \frac{\bar{q} S b^2}{2 V I_{xx}} C_{\ell_{p\beta}} \text{ (sec}^{-2}\text{)} \quad L_{pp} = \frac{\bar{q} S b^3}{4 V^2 I_{xx}} C_{\ell_{pp}}$$

$$\mu_1 = \frac{\bar{q} S b^2}{2 V I_{xx}} \mu \text{ (sec}^{-1}\text{)} \quad (\text{A17})$$

The nonlinear second order equation (A16) is the equation of motion representing the wing rock motion to be solved using the Beecham-Titchener method

Approximate Solution to Single Degree-of-Freedom Equation of Motion

To solve the second order nonlinear equation (A16), a time-dependent solution

$$\phi(t) = a(t) \cos \nu(t) \quad (\text{A18})$$

is assumed where $a(t)$ is a time-varying amplitude to a sinusoidal motion with a time-varying argument $\nu(t)$. Terms ω and λ are defined as

$$\omega = \dot{\nu} = \frac{d\nu}{dt} \quad (\text{A19})$$

$$\lambda = \frac{\dot{a}}{a} = \frac{1}{a} \frac{da}{dt} \quad (\text{A20})$$

Additionally, the following relationships exist

$$\dot{\omega} = \left(\frac{\dot{a}}{a}\right) a \left(\frac{d\omega}{da}\right) = \lambda a \omega' \quad (\text{A21})$$

$$\dot{\lambda} = a \left(\frac{\dot{a}}{a}\right) \left(\frac{d\lambda}{da}\right) = a \lambda \lambda' \quad (\text{A22})$$

$$\dot{a} = a \lambda \quad (\text{A23})$$

$$\ddot{a} = \dot{a} \lambda + a \dot{\lambda} = a \lambda \lambda' a + \lambda \lambda a = a \lambda (a \lambda' + \lambda) \quad (\text{A24})$$

where the superscript prime (') denotes differentiation with respect to amplitude. Differentiating equation (A18) with respect to time and combining with equations (A19) and (A23) yields

$$\dot{\phi} = a (\lambda \cos \nu - \omega \sin \nu) \quad (\text{A25})$$

Differentiating equation (A25) with respect to time yields

$$\begin{aligned} \ddot{\phi} &= (\dot{a} \lambda + a \dot{\lambda} - a \dot{\omega} \nu) \cos \nu - (\dot{a} \omega + a \lambda \dot{\nu} + a \dot{\omega}) \sin \nu = \dots \\ \dots &= a \{ [\lambda (\lambda + a \lambda') - \omega^2] \cos \nu - \lambda (a \omega' + 2 \omega) \sin \nu \} \end{aligned} \quad (\text{A26})$$

Rewriting equation (A16) without the control deflection term and substituting equation (A25) for $\dot{\phi}$ results in

$$\begin{aligned} \ddot{\phi} &= L_0 + \sin \alpha_s L_\beta a \cos \nu + [L_{p0} + \sin \alpha_s L_{p\beta} \operatorname{sgn}(\phi) a \cos \nu + \dots \\ \dots &+ L_{pp} \operatorname{sgn}(\dot{\phi}) a (\lambda \cos \nu - \omega \sin \nu)] a (\lambda \cos \nu - \omega \sin \nu) + \dots \\ \dots - \mu_1 a (\lambda \cos \nu - \omega \sin \nu) &= F(\nu) \end{aligned} \quad (\text{A27})$$

Combining equations (A26) and (A27)

$$F(\nu) = a [\lambda (\lambda + a \lambda') - \omega^2] \cos \nu - a \lambda (a \omega' + 2 \omega) \sin \nu \quad (\text{A28})$$

Equation (A28) is a Fourier expansion for $F(\nu)$, so

$$F(\nu) = A_n \cos \nu + B_n \sin \nu \quad (\text{A29})$$

where the Fourier coefficients are

$$A_n = \frac{1}{\pi} \int_0^{2\pi} F(\nu) \cos \nu \, d\nu \quad (\text{A30})$$

$$B_n = \frac{1}{\pi} \int_0^{2\pi} F(\nu) \sin \nu \, d\nu \quad (\text{A31})$$

Therefore

$$\lambda (\lambda + a \lambda') - \omega^2 = \frac{1}{\pi a} \int_0^{2\pi} F(\nu) \cos \nu \, d\nu \quad (\text{A32})$$

$$\lambda (a \omega' + 2\omega) = \frac{1}{\pi a} \int_0^{2\pi} F(\nu) \sin \nu \, d\nu \quad (\text{A33})$$

The desired relationships for wing rock amplitude and frequency can be obtained by evaluation of equations (A32) and (A33). First, equation (A32) will be evaluated by substituting $F(\nu)$ from equation (A27) into it. This substitution yields

$$\begin{aligned} \lambda (a \lambda' + \lambda) - \omega^2 &= \frac{1}{\pi a} \int_0^{2\pi} \{ L_0 + \sin \alpha_s L_\beta a \cos \nu + \dots \\ &\dots + [L_{p0} + \sin \alpha_s L_{p\beta} \operatorname{sgn}(\phi) a \cos \nu + \dots \\ &\dots + L_{pp} \operatorname{sgn}(\dot{\phi}) a (\lambda \cos \nu - \omega \sin \nu)] a (\lambda \cos \nu - \omega \sin \nu) + \dots \\ &\dots - \mu_1 a (\lambda \cos \nu - \omega \sin \nu) \} \cos \nu \, d\nu \end{aligned} \quad (\text{A34})$$

Carrying out the multiplications in equation (A34) and separating into 11 individual terms results in the expression

$$\begin{aligned} \lambda (a \lambda' + \lambda) - \omega^2 &= \frac{1}{\pi a} \int_0^{2\pi} L_0 \cos \nu \, d\nu + \dots \\ &\dots + \frac{1}{\pi a} \int_0^{2\pi} \sin \alpha_s L_\beta a \cos^2 \nu \, d\nu + \dots \\ &\dots + \frac{1}{\pi a} \int_0^{2\pi} a L_{p0} \lambda \cos^2 \nu \, d\nu + \dots \end{aligned}$$

$$\begin{aligned}
& \dots - \frac{1}{\pi a} \int_0^{2\pi} a L_{p0} \omega \sin \nu \cos \nu d\nu + \dots \\
& \dots + \frac{1}{\pi a} \int_0^{2\pi} a^2 \lambda \sin \alpha_s L_{p\beta} \operatorname{sgn}(\phi) \cos^2 \nu \cos \nu d\nu + \dots \\
& \dots - \frac{1}{\pi a} \int_0^{2\pi} a^2 \omega \sin \alpha_s L_{p\beta} \operatorname{sgn}(\phi) \cos^2 \nu \sin \nu d\nu + \dots \\
& \dots + \frac{1}{\pi a} \int_0^{2\pi} L_{pp} \operatorname{sgn}(\dot{\phi}) a^2 \lambda^2 \cos^2 \nu \cos \nu d\nu + \dots \\
& \dots - \frac{2}{\pi a} \int_0^{2\pi} L_{pp} \operatorname{sgn}(\dot{\phi}) a^2 \lambda \omega \cos^2 \nu \sin \nu d\nu + \dots \\
& \dots + \frac{1}{\pi a} \int_0^{2\pi} L_{pp} \operatorname{sgn}(\dot{\phi}) a^2 \omega^2 \sin^2 \nu \cos \nu d\nu + \dots \\
& \dots - \frac{1}{\pi a} \int_0^{2\pi} a \mu_1 \lambda \cos \nu \cos \nu d\nu + \dots \\
& \dots + \frac{1}{\pi a} \int_0^{2\pi} a \mu_1 \omega \sin \nu \cos \nu d\nu
\end{aligned} \tag{A35}$$

Equation (A35) must be evaluated term by term to simplify the right hand side of the equation. In order to evaluate these integrals, the $\operatorname{sgn}(\phi)$ and $\operatorname{sgn}(\dot{\phi})$ must be understood. To illustrate the appropriate values, Figs. 156 and 157 are provided, based on the assumed solution of equation (A18). Note that these figures assume $a(t)$ is a constant and $\lambda = 0$.

Table 9 provides the appropriate values of $\operatorname{sgn}(\phi)$ and $\operatorname{sgn}(\dot{\phi})$ needed to evaluate the integrals in equation (A35).

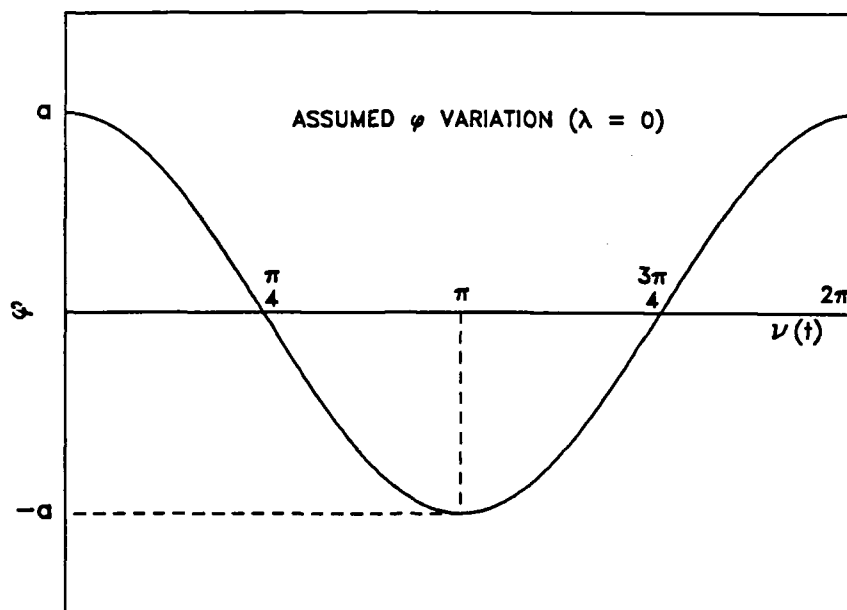
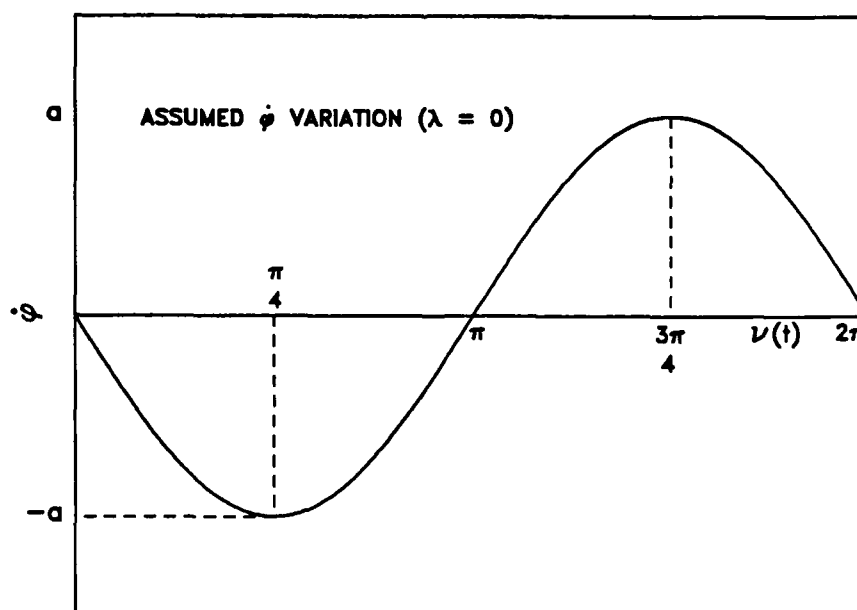
Fig. 156 Assumed ϕ variation.Fig. 157 Assumed $\dot{\phi}$ variation.

Table 9 Evaluation of $\text{sgn}(\phi)$ and $\text{sgn}(\dot{\phi})$

Quadrant	$\text{sgn}(\phi)$	$\text{sgn}(\dot{\phi})$
$0 - (\pi/2)$	+1	-1
$(\pi/2) - \pi$	-1	-1
$\pi - (3\pi/2)$	-1	+1
$(3\pi/2) - 2\pi$	+1	+1

The results of the integration of each of the 11 terms are provided below. Integrals with $\text{sgn}(\phi)$ and $\text{sgn}(\dot{\phi})$ had to be broken into subintervals for evaluation based on the values provided in Table 9.

$$\frac{1}{\pi a} \int_0^{2\pi} L_0 \cos \nu \, d\nu = 0 \quad (\text{A36})$$

$$\frac{1}{\pi a} \int_0^{2\pi} \sin \alpha_s L_\beta a \cos^2 \nu \, d\nu = \sin \alpha_s L_\beta \quad (\text{A37})$$

$$\frac{1}{\pi a} \int_0^{2\pi} a L_{p0} \lambda \cos^2 \nu \, d\nu = \lambda L_{p0} \quad (\text{A38})$$

$$-\frac{1}{\pi a} \int_0^{2\pi} a L_{p0} \omega \sin \nu \cos \nu \, d\nu = 0 \quad (\text{A39})$$

$$\frac{1}{\pi a} \int_0^{2\pi} a^2 \lambda \sin \alpha_s L_{p\beta} \text{sgn}(\phi) \cos^3 \nu \, d\nu = \frac{8}{3\pi} a \lambda \sin \alpha_s L_{p\beta} \quad (\text{A40})$$

$$-\frac{1}{\pi a} \int_0^{2\pi} a^2 \omega \sin \alpha_s L_{p\beta} \text{sgn}(\phi) \cos^2 \nu \sin \nu \, d\nu = 0 \quad (\text{A41})$$

$$\frac{1}{\pi a} \int_0^{2\pi} L_{pp} \operatorname{sgn}(\dot{\phi}) a^2 \lambda^2 \cos^2 \nu \cos \nu d\nu = 0 \quad (\text{A42})$$

$$-\frac{2}{\pi a} \int_0^{2\pi} L_{pp} \operatorname{sgn}(\dot{\phi}) a^2 \lambda \omega \cos^2 \nu \sin \nu d\nu = \frac{8 \lambda \omega a}{3\pi} L_{pp} \quad (\text{A43})$$

$$\frac{1}{\pi a} \int_0^{2\pi} L_{pp} \operatorname{sgn}(\dot{\phi}) a^2 \omega^2 \sin^2 \nu \cos \nu d\nu = 0 \quad (\text{A44})$$

$$-\frac{1}{\pi a} \int_0^{2\pi} a \mu_1 \lambda \cos \nu \cos \nu d\nu = -\mu_1 \lambda \quad (\text{A45})$$

$$\frac{1}{\pi a} \int_0^{2\pi} a \mu_1 \omega \sin \nu \cos \nu d\nu = 0 \quad (\text{A46})$$

Summing the terms in equations (A36) through (A46) and equating to the left hand side of equation (A35) yields

$$\begin{aligned} \lambda (a \lambda' + \lambda) - \omega^2 &= \sin \alpha_s L_\beta + \lambda L_{p0} + \frac{8}{3\pi} a \lambda \sin \alpha_s L_{p\beta} + \dots \\ \dots + \frac{8}{3\pi} a \lambda \omega L_{pp} - \mu_1 \lambda \end{aligned} \quad (\text{A47})$$

Since the Beecham-Titchener method assumes ω and λ are nearly constant during an oscillation, a , λ , ω , and the amplitude derivatives are considered fixed and assigned the values at midcycles. As a result, λ' in equation (A47) is taken to be zero. Therefore,

$$\begin{aligned} \lambda^2 - \omega^2 &= \sin \alpha_s L_\beta + \lambda L_{p0} + \frac{8}{3\pi} a \lambda \sin \alpha_s L_{p\beta} + \dots \\ \dots + \frac{8}{3\pi} a \lambda \omega L_{pp} - \mu_1 \lambda \end{aligned} \quad (\text{A48})$$

Having evaluated equation (A32), it is now necessary to do the same with equation (A33). This is accomplished by substituting equation (A27) into (A33) which yields

$$\begin{aligned}
 \lambda (a \omega' + 2\omega) = & -\frac{1}{\pi a} \int_0^{2\pi} \{ L_0 + \sin \alpha_s L_{p\beta} a \cos \nu + \dots \\
 & \dots + [L_{p0} + \sin \alpha_s L_{p\beta} \operatorname{sgn}(\phi) a \cos \nu + \dots \\
 & \dots + L_{pp} \operatorname{sgn}(\dot{\phi}) a (\lambda \cos \nu - \omega \sin \nu)] a (\lambda \cos \nu - \omega \sin \nu) \\
 & \dots - \mu_1 a (\lambda \cos \nu - \omega \sin \nu) \} \sin \nu d\nu
 \end{aligned} \tag{A49}$$

Carrying out the multiplication results in 11 terms in the right hand side of the equation, so that

$$\begin{aligned}
 \lambda (a \omega' + 2\omega) = & -\frac{1}{\pi a} \int_0^{2\pi} L_0 \sin \nu d\nu + \dots \\
 & \dots - \frac{1}{\pi a} \int_0^{2\pi} \sin \alpha_s L_{p\beta} a \cos \nu \sin \nu d\nu + \dots \\
 & \dots - \frac{1}{\pi a} \int_0^{2\pi} a L_{p0} \lambda \cos \nu \sin \nu d\nu + \dots \\
 & \dots + \frac{1}{\pi a} \int_0^{2\pi} a L_{p0} \omega \sin^2 \nu d\nu + \dots \\
 & \dots - \frac{1}{\pi a} \int_0^{2\pi} a^2 \lambda \sin \alpha_s L_{p\beta} \operatorname{sgn}(\phi) \cos^2 \nu \sin \nu d\nu + \dots \\
 & \dots + \frac{1}{\pi a} \int_0^{2\pi} a^2 \omega \sin \alpha_s L_{p\beta} \operatorname{sgn}(\phi) \sin^2 \nu \cos \nu d\nu + \dots \\
 & \dots - \frac{1}{\pi a} \int_0^{2\pi} a^2 \lambda^2 L_{pp} \operatorname{sgn}(\dot{\phi}) \cos^2 \nu \sin \nu d\nu + \dots
 \end{aligned}$$

$$\begin{aligned}
& \dots + \frac{2}{\pi a} \int_0^{2\pi} a^2 \lambda \omega L_{pp} \operatorname{sgn}(\dot{\phi}) \cos \nu \sin^2 \nu \, d\nu + \dots \\
& \dots - \frac{1}{\pi a} \int_0^{2\pi} a^2 \omega^2 L_{pp} \operatorname{sgn}(\dot{\phi}) \sin^3 \nu \, d\nu + \dots \\
& \dots + \frac{1}{\pi a} \int_0^{2\pi} a \mu_1 \lambda \cos \nu \sin \nu \, d\nu + \dots \\
& \dots - \frac{1}{\pi a} \int_0^{2\pi} a \mu_1 \omega \sin^2 \nu \, d\nu \tag{A50}
\end{aligned}$$

Equation (A50) must be evaluated by performing term by term integrations as in equation (A35).

The result of each integration is:

$$- \frac{1}{\pi a} \int_0^{2\pi} L_0 \sin \nu \, d\nu = 0 \tag{A51}$$

$$- \frac{1}{\pi a} \int_0^{2\pi} \sin \alpha_s L_\beta a \cos \nu \sin \nu \, d\nu = 0 \tag{A52}$$

$$- \frac{1}{\pi a} \int_0^{2\pi} a L_{p0} \lambda \cos \nu \sin \nu \, d\nu = 0 \tag{A53}$$

$$\frac{1}{\pi a} \int_0^{2\pi} a L_{p0} \omega \sin^2 \nu \, d\nu = L_{p0} \omega \tag{A54}$$

$$- \frac{1}{\pi a} \int_0^{2\pi} a^2 \lambda \sin \alpha_s L_{p\beta} \operatorname{sgn}(\dot{\phi}) \cos^2 \nu \sin \nu \, d\nu = 0 \tag{A55}$$

$$\frac{1}{\pi a} \int_0^{2\pi} a^2 \omega \sin \alpha_s L_{p\beta} \operatorname{sgn}(\dot{\phi}) \sin^2 \nu \cos \nu \, d\nu = \frac{4}{3\pi} \omega a \sin \alpha_s L_{p\beta} \tag{A56}$$

$$-\frac{1}{\pi a} \int_0^{2\pi} a^2 \lambda^2 L_{pp} \operatorname{sgn}(\dot{\phi}) \cos^2 \nu \sin \nu \, d\nu = \frac{4}{3\pi} a \lambda^2 L_{pp} \quad (\text{A57})$$

$$\frac{2}{\pi a} \int_0^{2\pi} a^2 \lambda \omega L_{pp} \operatorname{sgn}(\dot{\phi}) \cos \nu \sin^2 \nu \, d\nu = 0 \quad (\text{A58})$$

$$-\frac{1}{\pi a} \int_0^{2\pi} a^2 \omega^2 L_{pp} \operatorname{sgn}(\dot{\phi}) \sin^3 \nu \, d\nu = \frac{8}{3\pi} a \omega^2 L_{pp} \quad (\text{A59})$$

$$\frac{1}{\pi a} \int_0^{2\pi} a \mu_1 \lambda \cos \nu \sin \nu \, d\nu = 0 \quad (\text{A60})$$

$$-\frac{1}{\pi a} \int_0^{2\pi} a \mu_1 \omega \sin^2 \nu \, d\nu = -\mu_1 \omega \quad (\text{A61})$$

Summing the terms in equations (A51) through (A61), equation (A50) becomes

$$\begin{aligned} \lambda (a \omega' + 2\omega) &= L_{p0} \omega + \frac{4}{3\pi} \omega a \sin \alpha_s L_{p\beta} + \frac{4}{3\pi} a \lambda^2 L_{pp} + \dots \\ &\dots + \frac{8}{3\pi} a \omega^2 L_{pp} - \mu_1 \omega \end{aligned} \quad (\text{A62})$$

Since ω is assumed constant during an oscillation, $\omega' \approx 0$, equation (A62) becomes

$$2 \lambda \omega = L_{p0} \omega + \frac{4}{3\pi} \omega a \sin \alpha_s L_{p\beta} + \frac{4}{3\pi} a \lambda^2 L_{pp} + \frac{8}{3\pi} a \omega^2 L_{pp} - \mu_1 \omega \quad (\text{A63})$$

The preceding analysis has converted the nonlinear second-order differential equation in equation (A16) into two coupled nonlinear first-order equations in equations (A48) and (A63).

In the case of a limit cycle, such as wing rock, the amplitude, a , is constant, so $\dot{a} = 0$ and $\dot{a}/a = \lambda = 0$. The constant values of ω and a can be denoted as Ω and A , respectively, where Ω is the frequency and A is the amplitude of the wing rock oscillation. Therefore, equations (A48) and (A63) reduce to

$$-\Omega^2 = \sin \alpha_s L_\beta \quad (\text{A64})$$

and

$$0 = L_{p0} \Omega + \frac{4}{3\pi} \Omega A \sin \alpha_s L_{p\beta} + \frac{8}{3\pi} A \Omega^2 L_{pp} - \mu_1 \Omega \quad (\text{A65})$$

The aerodynamic derivatives in equations (A64) and (A65) are evaluated at average conditions, either from experimental data or computational methods. The results obtained in equations (A64) and (A65) are the same as developed by Hsu, except for the last term (a bearing friction term) in equation (A65). Solving for Ω and A provides the solutions

$$\Omega = (-\sin \alpha_s L_\beta)^{1/2} \quad (\text{A66})$$

and

$$A = -\frac{3\pi}{4} \frac{L_{p0} - \mu_1}{\sin \alpha_s L_{p\beta} + 2 \Omega L_{pp}} \quad (\text{A67})$$

in terms of the dimensional derivatives. Rewriting in terms of nondimensional aerodynamic derivatives yields

$$\Omega = \left[-\frac{\bar{q} S b}{I_{xx}} \sin \alpha_s C_{l_\beta} \right]^{1/2} \quad (\text{A68})$$

and

$$A = -\frac{3\pi}{4} \frac{C_{l_{p0}} - \frac{\mu_1 (2 I_{xx} V)}{\bar{q} S b^2}}{\sin \alpha_s C_{l_{p\beta}} + \frac{\Omega b}{V} C_{l_{pp}}} \quad (\text{A69})$$

or

$$A = -\frac{3\pi}{4} \frac{C_{\ell p0} - \mu}{\sin \alpha_s C_{\ell p\beta} + \frac{\Omega b}{V} C_{\ell pp}} \quad (A70)$$

Determining the proper value of μ might not be possible; however, equations (A69) and (A70) do show that the amount of bearing friction does affect the limit cycle amplitude.

Equations (A66) through (A70) provide a method to approximate the wing rock amplitude and frequency, if the aerodynamic derivatives for the aircraft or wing are known. The equations also predict the relative effect of bearing friction on these parameters given a friction variation with roll rate, $\dot{\phi}$.

APPENDIX B

ENERGY ANALYSIS OF SINGLE DEGREE-OF-FREEDOM WING ROCK

Nguyen, Yip, and Chambers²³ showed that the total aerodynamic energy added to the model ($\Delta E > 0$) or extracted from it ($\Delta E < 0$) during a wing rock oscillation could be related to aerodynamic roll damping and model motion. They found that $\Delta E > 0$ corresponds to unstable roll damping ($C_{\ell_p} > 0$) and $\Delta E < 0$ corresponds to stable roll damping ($C_{\ell_p} < 0$). Hsu³⁰ performed a similar analysis relating the transfer of energy to rolling moment coefficient. His analysis is presented here since it provides an excellent understanding of the relationship between ΔE and C_{ℓ_p} .

Nguyen, Yip, and Chambers²³ showed that the total energy exchanged in a limit cycle oscillation is given by

$$\Delta E = \bar{q} S b \int_{C(t)} C_{\ell}(t) \dot{\phi}(t) dt \quad (B1)$$

or

$$\Delta E = \bar{q} S b \int_{C(\phi)} C_{\ell}(\phi) d\phi \quad (B2)$$

where $C(t)$ and $C(\phi)$ are the curves obtained from plots of C_{ℓ} versus t and C_{ℓ} versus ϕ , respectively. For steady wing rock, $C(\phi)$ is a closed curve for a cycle of oscillation. A C_{ℓ} versus ϕ plot for the one degree-of-freedom simulation of a wind tunnel test research shows a typical contour (Fig. 158). This simulation used the C_{ℓ} function given in equations (14) and (15), which are

$$C_{\ell} = C_{\ell_0} + C_{\ell_{\beta}} \beta + C_{\ell_p} \bar{p} \quad (B3)$$

where

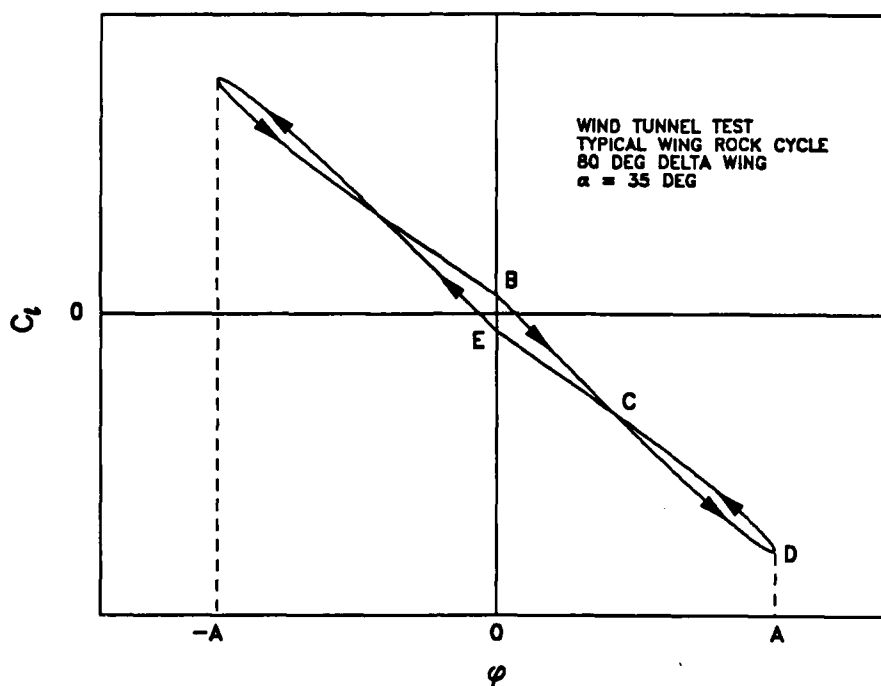


Fig. 158 Typical simulation of C_l versus ϕ .

$$C_{lp} = C_{lp0} + C_{lp\beta} |\beta| + C_{lp\bar{p}} |\bar{p}| \quad (B4)$$

A pure sinusoidal variation of ϕ was also assumed. Since the contours for positive and negative ϕ are identical, equation (B2) can be rewritten as

$$\Delta E = 2 \bar{q} S b \int_{BCDCE} C_l(\phi) d\phi \quad (B5)$$

where the path of integration is shown in Fig. 158. Since

$$\phi = A \cos \nu(t) \quad (B6)$$

and

$$\dot{\phi} = -A \dot{\nu} \sin \nu(t) = -A \Omega \sin \nu(t) \quad (B7)$$

(B6) and (B7) can be combined so that

$$\frac{\phi^2}{A^2} + \frac{\dot{\phi}^2}{A^2 \Omega^2} = 1 \quad (\text{B8})$$

or

$$\phi^2 + \frac{\dot{\phi}^2}{\Omega^2} = A^2 \quad (\text{B9})$$

Therefore,

$$|\dot{\phi}| = \Omega (A^2 - \phi^2)^{\frac{1}{2}} \quad (\text{B10})$$

where A and Ω are the limit cycle ϕ amplitude and frequency, respectively. When ϕ is increasing along path BCD, $\dot{\phi} > 0$ ($p > 0$), so

$$p = \dot{\phi} = \Omega (A^2 - \phi^2)^{\frac{1}{2}} \quad (\text{B11})$$

When ϕ is decreasing along DCE, $\dot{\phi} < 0$ ($p < 0$), so

$$p = \dot{\phi} = -\Omega (A^2 - \phi^2)^{\frac{1}{2}} \quad (\text{B12})$$

Therefore, equation (B5) is rewritten as

$$\Delta E = 2 \bar{q} S b \int_{\text{BCDCE}} (C_{\ell \text{BCD}} + C_{\ell \text{DCE}}) d\phi \quad (\text{B13})$$

or

$$\Delta E = 2 \bar{q} S b \int_0^A (C_{\ell \text{BCD}} - C_{\ell \text{DCE}}) d\phi \quad (\text{B14})$$

where

$$C_{\ell_{BCD}} = C_{\ell_0} + C_{\ell_\beta} \beta + C_{\ell_p} \frac{b\Omega}{2V} (A^2 - \phi^2)^{\frac{1}{2}} \quad (B15)$$

and

$$C_{\ell_{DCE}} = C_{\ell_0} + C_{\ell_\beta} \beta - C_{\ell_p} \frac{b\Omega}{2V} (A^2 - \phi^2)^{\frac{1}{2}} \quad (B16)$$

so that

$$\Delta E = 2\bar{q} S b^2 \frac{\Omega}{V} \int_0^A C_{\ell_p} (A^2 - \phi^2)^{\frac{1}{2}} d\phi \quad (B17)$$

This shows that for $C_{\ell_p} > 0$, $\Delta E > 0$ and for $C_{\ell_p} < 0$, $\Delta E < 0$. From Fig. 158, loop BCE is clockwise, so the area within the loop is positive and $\Delta E > 0$. This implies that the roll damping at small ϕ is positive or destabilizing. The loop CDC is counterclockwise, so $\Delta E < 0$ and the roll damping is negative or dynamically stabilizing. Therefore, the directions of the loops in the C_ℓ versus ϕ plots of a wing rock cycle qualitatively show whether stable or unstable roll damping exists.

Substituting equations (B4) and (B10) into equation (B17) gives

$$\begin{aligned} \Delta E = 2\bar{q} S b^2 \frac{\Omega}{V} \int_0^A \{ [C_{\ell_{p0}} + \sin \alpha_s C_{\ell_{p\beta}} \phi + \dots \\ \dots + \frac{b\Omega}{2V} C_{\ell_{pp}} (A^2 - \phi^2)^{\frac{1}{2}}] (A^2 - \phi^2)^{\frac{1}{2}} \} d\phi \end{aligned} \quad (B18)$$

Carrying out the integrations of equation (B18) yields

$$\begin{aligned} \Delta E = 2\bar{q} S b^2 \frac{\Omega}{V} \left[\frac{\pi}{4} C_{\ell_{p0}} A^2 + \frac{1}{3} \sin \alpha_s C_{\ell_{p\beta}} A^3 + \frac{1}{3} \frac{b\Omega}{V} C_{\ell_{pp}} A^3 \right] \\ = \frac{2}{3} \bar{q} S b^2 A^2 \frac{\Omega}{V} \left[\frac{3\pi}{4} C_{\ell_{p0}} + A (\sin \alpha_s C_{\ell_{p\beta}} + \frac{b\Omega}{V} C_{\ell_{pp}}) \right] \end{aligned} \quad (B19)$$

Combining equation (A24) with $\mu = 0$ developed from the Beecham-Titchener method (Appendix A) and equation (B19)

$$\Delta E = \frac{2}{3} \bar{q} S b^2 A^2 \frac{\Omega}{V} \left[\frac{3\pi}{4} C_{\ell p0} - \frac{3\pi}{4} C_{\ell p0} \right] = 0 \quad (B20)$$

Therefore, for an ideal limit cycle to exist, the net energy exchange during one cycle of oscillation is zero. Thus, the areas of the two outer loops are equal to the area of the inner loop of the C_ℓ versus ϕ curve. Notice that the same result is obtained (i.e., no net change in E) if the hysteresis loop direction in Fig. 158 were reversed; the energy analysis does not require $C_{\ell p} > 0$ for the BCE alone. It merely requires a balance in the overall integration. Therefore, the energy balance is met in both the wind tunnel wing rock results and the current water tunnel tests, despite the opposite hysteresis directions.

VITA

Major Steven Lynn Morris was [REDACTED]. He graduated with honors from the United States Air Force Academy in June 1975 with a Bachelor of Science in Engineering Sciences and received a commission in the United States Air Force. After a two year tour as a Test Engineer at the 6585th Test Group, Holloman Air Force Base, New Mexico, he entered the Air Force Institute of Technology in 1978. Graduating with a Master of Science in Aeronautical Engineering in March 1980, he was assigned to the Air Force Weapons Laboratory (AFWL) at Kirtland Air Force Base, New Mexico. Following the four-year tour at the AFWL, he served as an Assistant Professor of Aeronautics at the United States Air Force Academy from 1984-1986. In August 1986, he entered graduate school at Texas A&M University to pursue a Doctor of Philosophy in Aerospace Engineering.

Major Morris is married to the former Jacqueline Fenter, and they have two sons, Steven and Michael. Among his military decorations are included the Meritorious Service Medal with one Oak Leaf Cluster and the Air Force Commendation Medal. Major Morris can be reached at [REDACTED]